

Study on Flickering Behavior of Interacting Two Jet Diffusion  
Flames

(2つの噴流拡散火炎の干渉による周期変動形態に関する研究)

January, 2021

Doctor of Philosophy (Engineering)

Anek Bunkwang

アネク バンクワング

Toyohashi University of Technology

## **Abstract of the Dissertation**

Appearance of mode change of interacting flickering flames at open normal atmosphere under a gravimetric field is focused on. Fundamentally, the dynamic behaviors regarding the interaction effect of buoyant two flickering flames are found the two modes of flame dynamics: namely, in-phase and anti-phase modes. For present study, the two jet flames are adopted in a systematic manner. The sequence of working series comes up with the goals divided into two research objectives. Firstly, to study about the “transition of the dynamic modes because of the effect of interaction” is paid an attention. Secondly, the application that is the similarity between the different systems (single and two flickering flame(s)) is discussed from scientific point of view. For simplest jet flame model, the interaction effect of two adjacent buoyant fires creates the two modes of flame dynamics; namely, axisymmetric (in-phase mode) and asymmetric (anti-phase mode) motions. Whereas a single fire exhibits the two dynamic modes; so-called, axisymmetric (varicose mode) and asymmetric (sinuous mode) motions. At certain prescribed condition, puffing motion (varicose mode) of fire irregularly exhibits swaying motion (sinuous mode). The flame keeps connecting along the downstream, snake-like creeping motion. In this regard, there must have a critical condition to evoke this instability. Meanwhile, the winding cold-air at the gap between the two identical burners is found with essentially physical similarity. For utilizing this interaction effect of two buoyant fires, the dynamics can well be controlled by systematic parameters. To achieve the transition and similarity of dynamic modes, a well-controllable laboratory experiment was constructed and carefully upgraded for a wide working-range; the factor of 5 of fire scale in term of dealing with the highly non-linear instability. The key parameters; such as fuel flowrate ( $Q$ ), burner diameter ( $D$ ), and burner separation distance

( $L$ ), were examined. Periodicity of flame behaviors was observed and the frequency monitored by thermocouples mounted adjacent to the burner exit. Time-variation of flame shape was recorded by a high speed camera associated with the optical imaging visualization. It was found that the characteristic flickering frequency was insensitive to the fuel flowrate,  $Q$ , implying that jet inertia played the secondary role in transition phenomenon. Instead, the burner critical separation distance for the transition ( $L_{crt}$ ) varied when various burner diameters ( $D$ ) were used, confirming that the difference in distance played an important role in the transition. Thus the critical condition could be summarized by an updated correlation as  $D \times L_{crt}^3 \sim const$ . This is slightly different from the one recently proposed by Yang et al. (2019), which was given under a narrow range of fire scale. Accordingly, the critical condition can also be described by the critical value of the updated global parameter, such as  $\alpha^3 Gr^{4/3}$ , where  $\alpha$  and  $Gr$  denote the length ratio ( $L_{crt}/D$ ) and Grashof number based on the inner diameter. By introducing the numerical method, the influence of gravity on the interaction effect was examined. The results show that the critical separation distance is modified significantly so that the effect of gravity must be taken an account to correct the model. Aside from identifying any similarity in the dynamics, asymmetric motion of both systems was precisely observed. The thermal boundary layer surrounded by the jet flame was visualized, including 3-D numerical prediction. Frequency analysis was executed to determine global parameters to properly describe the observed dynamic motion and the transition phenomenon. The critical Reynolds number ( $Re_{crt}$ ) was discussed as an ideal candidate to characterizing the transition in the system of single fire. The  $Re_{crt}$  is hypothesized to merely describe the transition, not indeed characterize a whole dynamic mode of interacting non-premixed flames.

# Table of Contents

Abstract of the Dissertation	i
Table of Contents	iii
Nomenclature	vi
Acknowledgements	ix
Chapter 1 Introduction	1
1.1 Benefits of Interaction Effect	2
1.2 Physical Description of Hydrodynamic Stability	5
1.3 Waves and Oscillations	13
1.4 Buoyancy and Vorticity in Wake and Jet Flows	18
1.5 Scope of Research	28
1.5.1 Critical Condition of Mode Transition of Twin-flame System	28
1.5.2 Interpretation of Mode Transition of Single-flame System: Similarity Approach	29
Chapter 2 Theoretical Background and Problem	31
2.1 Characteristics of Non-premixed Flames	31
2.2 Transition of Dynamic Modes of Buoyant Non-premixed Jet Flame(s)	39
2.3 Buoyancy Induced Shear Flow Instability	46
2.4 Nondimensional Analysis	54
2.4.1 Reynolds Number, $Re$	59
2.4.2 Froude Number, $Fr$	60
2.4.3 Strouhal number, $St$	62
2.4.4 Grashof Number, $Gr$	63
2.5 Summary	65
Chapter 3 Methodologies and Related Theories	66
3.1 Laboratory Experiments	66
3.1.1 Experimental Apparatus	68
3.1.2 Observation of Influences of Surrounding Mesh	71
3.1.3 Optical Image Photography—Schlieren System	75
3.2 Numerical Experiments	78
3.2.1 Governing Equations	79
3.2.2 Configurations of Numerical Simulation (FDS)	84
3.2.3 Pre-productive Runnings	87
Chapter 4 Mode Transition of Interacting Buoyant Non-premixed Flames	91
	iii

4.1 Introduction	91
4.2 Methodologies	92
4.2.1 Experimental Setup	92
4.2.2 Schlieren Imaging	94
4.3 Experimental Results and Discussion	95
4.3.1 Observation of Dynamic Behavior of an Isothermal (Helium) Experiment	95
4.3.2 Effect of Artificial Ceiling on Dynamic Mode of Interacting Non-premixed Flames	99
4.3.3 Oscillation Mode of Interacting Flames and Its Transition	101
4.3.4 Oscillation Frequency: Modifying of the Experimental Parameters $Q$ , $D$ , $L$	106
4.3.5 Effect of Fuel Flowrate ( $Q$ ) on Overall Oscillation Behavior ( $f$ )	108
4.3.6 Effect of Burner Diameter ( $D$ ) on Overall Oscillation Behavior ( $f$ )	110
4.3.7 Updating the Mode Transition Model	113
4.4 Conclusions	116
Chapter 5 Similarity of Dynamics Behavior of Buoyant Single and Twin Jet-flames(s)	117
5.1 Introduction	117
5.2 Methodologies	118
5.2.1 Experimental Apparatus	118
5.2.2 Schlieren Imaging	119
5.3 Results and Discussion	120
5.3.1 Single Fire Case: Varicose and Sinuous Modes	120
5.3.2 Periodic Axisymmetric/Asymmetric Motions in the Single- and Twin-flame(s) Systems	126
5.3.3 Transition in Single- and Twin-flame(s) Systems	130
5.3.4 Characteristic Frequency of Two Modes of Oscillation	134
5.3.5 Frequency Difference ( $\Delta f$ ) vs given Burner Scale	137
5.3.6 Dynamic Similarity of Buoyant Single- and Twin-flame(s)	140
5.4 Conclusions	142
Chapter 6 Results of Numerical Simulation	144
6.1 Characteristic Frequency of Interacting Two Buoyant Jet Flames	144
6.2 Periodic Axisymmetric/Asymmetric Motions in the Twin-flame System	148
6.3 Structures during the Transition Event in Twin-flame System	151
6.4 Effect of Gravity on Transition in Twin-flame System	158
6.5 Conclusions	164
Chapter 7 Conclusions	166
References	168

Appendix	1
A) Experimental Devices	1
A-1 Cylindrical Tube Selection for Burner Design	1
A-2 Hand-made of Manometer	3
A-3 Calibration Graphs of Methane and Helium Flows	5
A-3 Volume Expansion Coefficient	9
A-4 Drawings of Some Burner Fabrication (Examples)	10
B) Analysis of Oscillation Frequency	1
B-1 Physical Description of Fourier Transform	1
B-2 Image Analysis Software: Spotlight-16	9

## Nomenclature

Symbol	Description	Unit
A	area, amplitude, pre-exponential factor	m <sup>2</sup> , - , ((mol/cm <sup>3</sup> ) <sup>1-n</sup> )/s
c, C	speed, concentration	m/s, rad/s, -
d, D	diameter	m
E <sub>a</sub>	activation energy	J/mol
f, F	frequency, force	Hz, N
g	gravity	m/s <sup>2</sup>
h, H	height	m
k	wavenumber, thermal conductivity	m <sup>-1</sup> W/m
l, L	length, separation distance	m, m
m, M	mass, unit mass	kg
N	sampling point	-
P	pressure	Pa,
Q	flowrate	cc/min
r R	radius	m
s	solid angle	
t	time	s
T	temperature, period	°C, K, s
u, U, V	velocity	m/s

W	width	m
x, X	spatial coordinate	m
y, Y	spatial coordinate	m
z, Z	spatial coordinate	m
Greek symbols		
$\Gamma$	circulation	-
$\Lambda$	critical condition	-
$\alpha$	diffusivity	m <sup>2</sup> /s
$\beta$	expansion coefficient	1/K
$\delta$	thickness, cell size	m
$\phi$	phase	-
$\kappa$	absorption coefficient	-
$\lambda$	wavelength	m
$\mu$	dynamic viscosity	kg/m s
$\nu$	kinematics viscosity	m <sup>2</sup> /s
$\theta$	phase	-
$\rho$	density	kg/m <sup>3</sup>
$\tau$	convective time scale, shear stress	s, N/m <sup>2</sup>
$\omega$	angular frequency, vorticity vector	rad/s
$\zeta$	vorticity quantity	-
Subscripts		
adi	adiabatic temperature	
A	air	

b	buoyancy, blackbody	
crt	critical	
c	closed surface	
g	group, gravity	
I	inertia	
L	spacing distance	
m	maximum	
p	phase	
r	raditation	
w	wall, surface	
v	viscous	
$\infty$	infinity	

## **Acknowledgements**

This work is supported by the joint scholarship program of Pathumwan Institute of Technology (PIT), Thailand and Toyohashi University of Technology (TUT), Japan.

I would like to extend my sincerest gratitude for supervisor great effort, Professor Yuji Nakamura, Professor Hideki Yanada, and Professor Akiyoshi Iida. They tirelessly supported my work from day one, through the good and the bad. They always made time for me and his invaluable time to all everything supports and discussion till dissertation completed. I will forever admire the passion and enthusiasm and I am truly fortunate to have had him as an advisor.

Sincerely acknowledge Professor Hideki Yanada, Professor Kentaro Doi and Professor Kazunori Kuwana; they dedicate their great effort to review the dissertation and provide fruitful comments to learn more issues to improve myself.

I am very thankful to Professor Tsuneyoshi Matsuoka at Energy-Conversion Engineering Laboratory (ECE-LABO) at TUT, who dedicates his valuable time to advise and let me understand the academic world as well as professionals.

Lastly, author would also like to sincerely thank to technical assistance and fruitful discussions provided by Dr. Takuya Yamazaki, including the help of many individuals of the present students, and former student (Mr. Mochizuki) of ECE-LABO at TUT.

# Chapter 1

## Introduction

In this introductory chapter, the basic fundamental knowledge, terminologies and definitions necessitated that are summarized, including preliminary justification of the dynamic mode of flame behaviors. Two unique objectives of doctoral research pointed out in this dissertation are focused on: *first*, the behaviors of interacting flickering non-premixed flame in twin-flame system; and *second*, interpretation of the transition phenomenon in the system of single fire. By means of learning the instability and the transition from the laminar to turbulent fashion, five more-or-less distinct classes are: (1) Natural phenomena and laboratory experiments (2) Numerical experiments (3) Linear and weakly nonlinear theory (4) Qualitative theory of bifurcation and chaos (5) Strongly nonlinear theory [Drazin, Introduction to Hydrodynamic Stability (2002) P.6], respectively. Relevance of making the review, two approaches: laboratory and numerical experiments are selected for present study. Majority of investigation is the nature observations, and then directly/indirectly related theoretical concepts are made to describe and interpret these observations to understand the physics of interacting flame behaviors. Precise time-dependence evolution of mode change would be achieved by numerical simulation which is indeed powerful tool where it can rival laboratory investigation. However, validity needs to be confirmed by experiment before exploitation so that the nature phenomena and laboratory experiments are still necessary.

## 1.1 Benefits of Interaction Effect

Literally more than a century, development of human being has been grown by capitalizing the benefits of fire, as well as ushering in the dawn of civilization. Nowadays, almost all activities are dependent on the service of fire, e.g. heating and lighting our house, to powering the processes of transportation of vehicles (not only the inside the Earth but the outside also), including an industry operation from small scale of business to worldwide enterprise. Even though the new role of green technology, i.e. wind-turbine, solar, geothermal, tidal-wave etc., increasingly has become great impact on worldwide economic in a global scale investment and a new national driving force [Lee et al., 2015], the canonical kernel and long traditional fundamental knowledge of combustion science cannot absolutely replaced/disrupted by the new coming technology yet, rather the world will indeed need to have gained more a deep understanding of the combustion science. More specifically, the fire dynamics for controlling purpose is the major interest in this dissertation. For example, the engineering merit under this circumstance of this work is the characteristic merging fire. This phenomenon is dangerous in controlling the fire accident. It makes strong destruction in fire power and the firefighting experiences difficulties. This scenario becomes very serious issue when the city fire occurs in which the area of such big city had grown improperly in the design and construction around the world. This specific area usually appears with many small buildings (houses) densely constructed [Fukuda et al., 2004; Weng et al., 2015], including narrow alleys and paths as shown in Fig. 1.1 (a) and (b). The (a) illustrates the conceptual idea in practical use of the research outcome. The (b) shows such kinds of application and practical importance of this fundamental study.

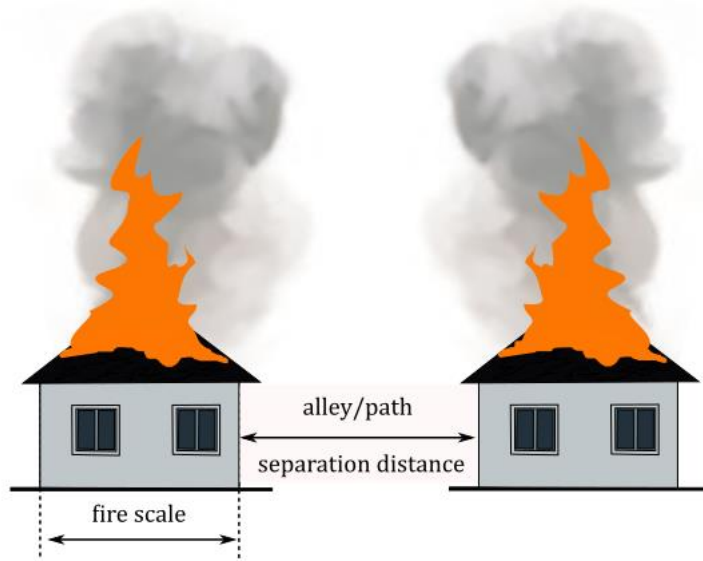


Fig. 1.1 (a) Demonstration of city fire with alley or path between two-fire origins.

The phenomena occur in the real fire accidents around the world which such similar fundamental aspect of flame interaction can obviously be observed. So the interaction of adjacent fires shall be investigated. For example, Fig. 1.1 (b), (iii), merging and non-merging neighboring flames appear. The separation distance under this consideration can be the distance of the windows. This can be found similarly if the city fires is under attention as shown in Fig. 1.1 (b), (i). At a certain value of the distance (alley/path) between house to house, fires can group together. This influence can clearly be observed through the past works (Fig. 1.1 (c), (ii)). Two turbulent diffusion flames become merged when the  $L/D$  value reaches the critical condition which is ranging in the ratio from 1 to 2 for previous study done by other researchers. The height of merging fire increases suddenly as shown in Fig. 1.1 (c), (i). Uncontrollable feature of fires is enhanced; fire becomes strong and it is not easy task to suppress it.



Fig. 1.1 (b) Typical instant photos of the accident of city and building fires with the effect of fire-flume interaction, (i) [GoKunming]; (ii) [MAIL FOREIGN SERVICE (2009), Dailymail.co.uk]; (iii) [BUZZCarrot's NEWS, 2016]; (iv) [News Molbile State Bureau, 2017].

More specifically, if this value is under the critical one, the original fire has more chance to propagate the house/building nearby. On the contrary, if the original two fires are set close to, the interaction effect can reduce fire height and the fires are more controllable when the alley/path is over the critical value. This can be imagined through Fig. 1.1 (b), (ii). Therefore the tremendous damage, catastrophic loss of property, and fatality can be avoided. However, according to the carelessness and unknown factors, tremendous damage and catastrophic loss of property often occur continually, deadly harm human being as well as fatality, i.e.

farm, wildland, urban fires etc. Therefore it is inevitable that the useful information of combustion science is highly necessary.

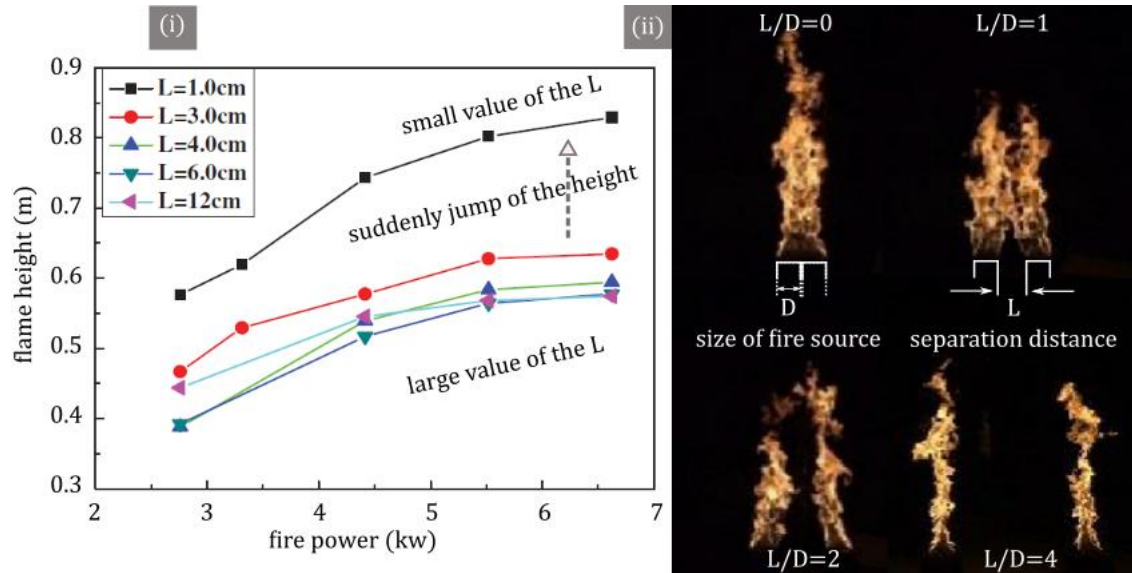


Fig. 1.1 (c) The flame height of flames with different heat release rates and distances (i) [Wang et al., 2017], and Snapshots of two turbulent diffusion behaviors with varying the separation distance (ii) [Wan et al., 2017].

## 1.2 Physical Description of Hydrodynamic Stability

The popular question is “*what the stabilities are and how we study them?*” In the actual world, these phenomena occurring in nature depending upon whether the conditions are satisfied the system or not. Sometimes, their amplitude at the original state is stable with the system satisfactory to small or infinitesimal disturbances of appearance. Theoretically, Figs. 1.2 (a) to (c) demonstrate the system responses during the disturbances shedding onto

through the arbitrary oscillation amplitude (y-axis) growing/decaying in the time-domain [Guyon et al., Physical-Hydrodynamics (2017) P.420].

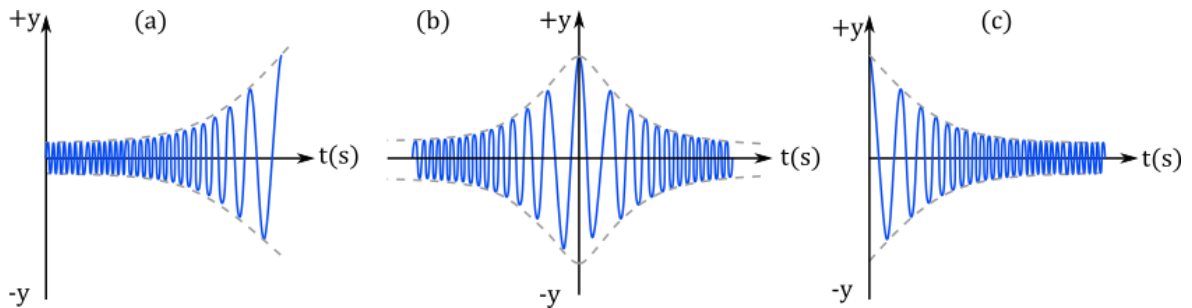


Fig. 1.2 Demonstration of oscillatory amplitude of the stable and unstable of the system.

In considering the unstable model (a), imagine that a resting ball becomes very sensitive to any moves, even slightly touch. Small disturbances can possibly make the original state become unstable and it never returns back. The middle model (b), when the adopted conditions or some jerks are applied to a satisfactory system, small disturbances grow spontaneously to a finite oscillating amplitude; whereas, the growth is damped by stabilizing mechanism until reaching an equilibrium, resulting in a new steady state. The last one (c) demonstrates the stability of the model. For a ball resting on the flat surface is neutral stable and observable. If the surface is concave upwards, a smooth ball gets more stable to any shoves as long as displacement is under the edge limit of a top open hemisphere [Kunda & Cohen, Fluid-Mechanics (2008) P.468].

In fluid dynamics point of view, let's take a quick journey back into 350 BC in a famous physics book; literarily, Aristotle said “*upward motion of fire, clearly an early recognition of the buoyancy force which characterizes the behavior of flames.*” Flame dynamics (both small and large scales) seems greatly be affected by fluid mechanics [Maynard, 2013].

Though this view, the instabilities of non-premixed flame are a phenomenon of fluid dynamics is governed by hydrodynamic mechanism. the hydrodynamic stability had widely been used for investigation of fire instability that the different dynamic modes present in the system of fires [Chen et al., 1988; Coats, 1996; Lingens et al., 1996; Cetegen & Kasper, 1996; Durox et al., 1997; Hu et al., 2015; Moreno-Boza et al., 2016; Xian & Zhang, 2018]. In term of buoyancy-controlled such phenomena here for present study, the evident facts have been sought for identification of the problem; therefore, the preliminary observation had been examined as shown in Figs. 1.3 to 1.4. A single jet-flame system which the methane gas was employed was introduced. Events, i.e. time-variation of flame height and dynamics of buoyant plumes recorded by high speed camera associated with an optical image visualization, reflect the outcome of the instability of perturbed flow-field as illustrated by a shadowgraph image-sequence (Fig. 1.3 (Top)) caused by the growth of small disturbances [Settles & Hargather, 2017]. Measure of flame height as a function of time was also performed as shown in the lower portion of the figure extracted from a specific period of phenomena of interest, when a flickering flame finds an equilibrium state of instability in the system. For case shown here, the buoyant non-premixed jet flame with oscillating in varicose mode returns its initial cycle every 8/100 second with 12.5 Hz of frequency for 18 mm inner-diameter of burner.

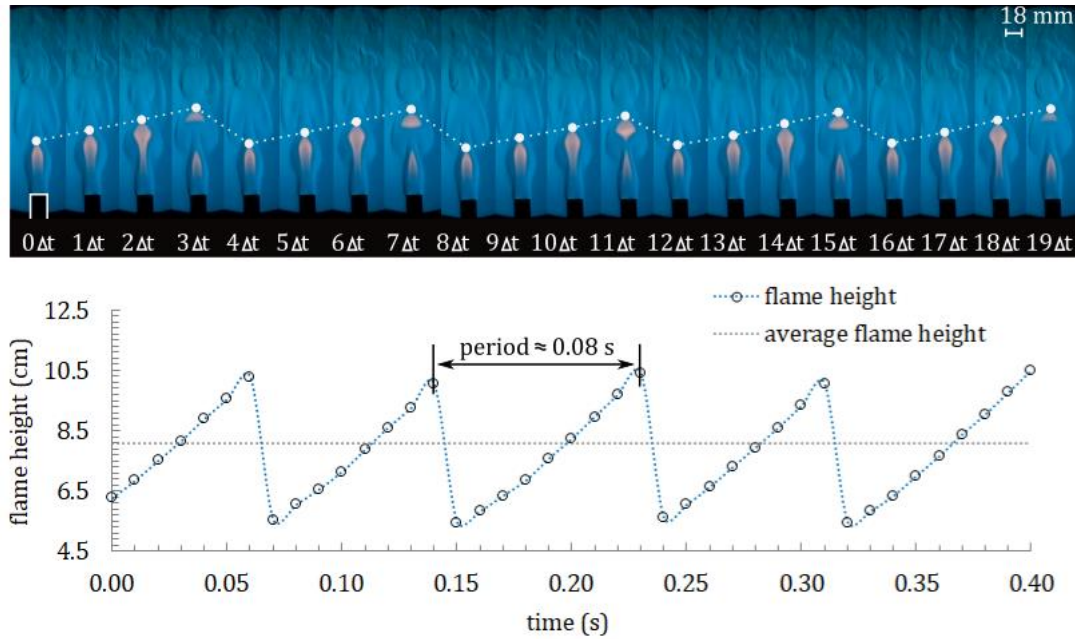


Fig. 1.3 The instantaneous image-sequence of pulsating single-jet methane flame in varicose mode corresponding with Schlieren optical imaging (Top):  $D = 18$  mm,  $Q = 575$  cc/min, time interval ( $\Delta t = 0.02$  s). (Bottom) the measure of flame height varying with time as shown in lower portion.

Let us gain more the detail physics under this circumstance following to the theoretical concept of “*stability/instability*” as depicted in Fig. 1.2. When the system is unsatisfied as shown in (a), any small disturbances grow spontaneously resulting of the infinitive amplitude of oscillation. This scene is similar to the one observed in pretesting case here is Fig. 1.4 (top). The conditions are applied here is unsatisfied the system of steady non-premixed flame behavior. This makes the flame find a new equilibrium state of instability and stay there until the new condition is applied again. In the opposite meaning, the stability is defined as shown in Fig. 1.2 (c); in this case, the adopted condition satisfies the system. Even though appearance of jerk in the system, the amplitude does not grow up in time, rather, the

perturbation is suppressed and its amplitude is damped exponentially. This similar scene can be found in Fig. 1.4 (bottom). The observed time-variation of flame height trends to amplify at earlier stage; however, viscosity as stabilizing mechanism of the system damps the oscillation and the flame finds a new steady state of equilibrium responsible to Fig. 1.2 (b). The perturbation is suppressed; eventually, the luminous flame stops flickering with completing combustion at 5 cm far from the burn exit and the system can find a new equilibrium state in final.

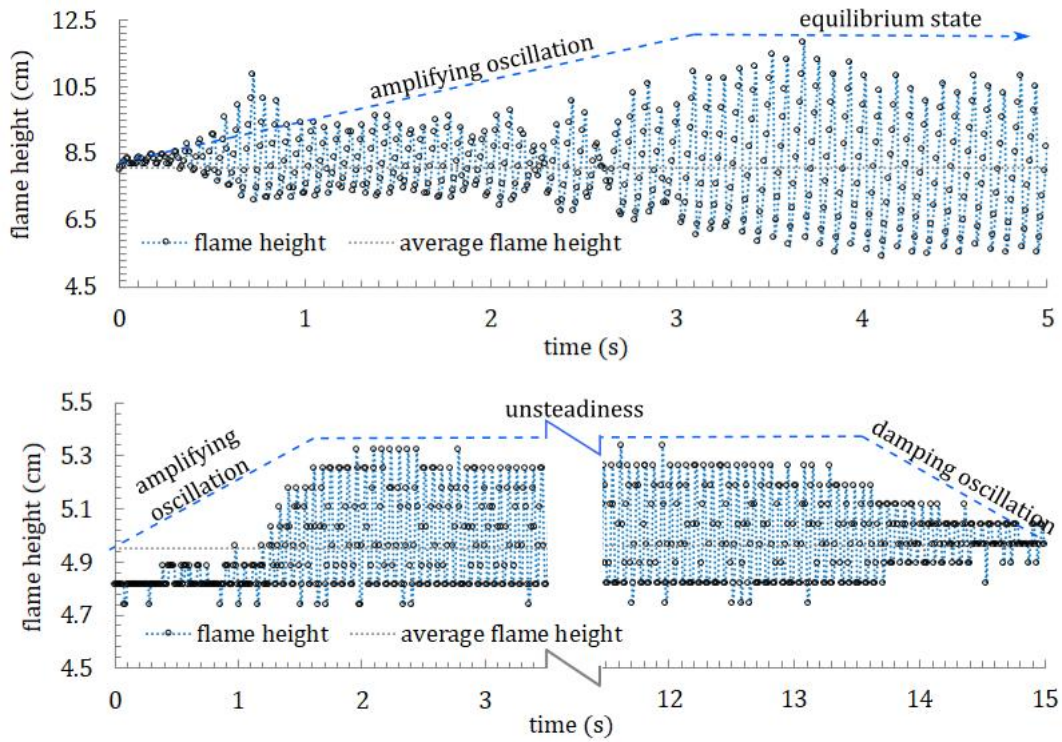


Fig. 1.4 Observations of the temporal variation of flame height evaluated at local oscillation as a function of time. (Top) the adopted conditions:  $D = 18$  mm,  $Q = 575$  cc/min; (Bottom) the adopted conditions:  $D = 18$  mm,  $Q = 330$  cc/min, time interval ( $\Delta t = 0.01$  s).

As mentioned, the instability in fire dynamics investigation is obviously a phenomenon of fluid dynamics is mainly governed by hydrodynamic mechanism, not concerning the chemical energy release or fuel types, or even its apparent shape of sources. Premises under this hypothesis is that oscillating behavior of isothermal buoyant plumes was found as similar to one observed in the reactive case. Finding consistency in the observations such as an isothermal buoyant plumes performed by Cetegen and Ahmed (1993), had been confirmed. In addition, local and global instabilities in spatially developing flows, buoyant reactive plumes absolutely show the intrinsic flow instability caused by the radial density inhomogeneity (density gradient,  $\nabla\rho$ ) subjected to the gravity ( $\vec{g}$ ) sustained by local chemical energy release of combustion reaction ( $\ddot{q}$ ) [Jiang & Luo, 2000]. The term “*local*” refers to the instability of the local velocity profile, conversely, the term “*global*” means the entire flow-field of interest. For more interesting information, the governing theory for this analysis was developed by Huerre and Monkewitz (1990). Some past studies proposed that the onset of flame oscillation involves the shear-layer instability near burner exit, where the buoyancy driven Kelvin-Helmholtz type of instability is evolved, therefore, this type of instability can be able to describe the phenomenon [Kimura, 1965; T. Maxworthy, 1977; Buckmaster & Peter, 1986; Yuan et al., 1994]. Regarding on the concept of this model analysis, the different velocities of fluids play a key role on flow-field development predominating over the difference in density of fluids. Whereas, another group of past works explained this onset of flame oscillation though the Rayleigh-Taylor instability [Lingens et al., 1996; Jiang & Luo, 2000; De Ris, 2013; Hu et al., 2015], which the gravity and viscosity of fluid are the stabilizing/destabilizing mechanism of the system to govern the development of flow-field. Flame is absolutely unstable in dynamical varicose mode of oscillation [Moreno-Boza et al., 2016; Chakravarthy et al., 2018]. Not likely the K-H instability, it is

deemed to be convective instability supposed by Cetegen and Dong (2000) in terms of coexistence bringing the incompatible scaling law of single fire characterization.

Let us make a brief overview on the temporal and spatial of linear stability theory [Huerre & Monkewitz, 1985]. “*Temporal stability*”, is performed by fixing the wavenumber parameters in Eq. (1) as real ( $k_x, k_z \in \mathbb{R}$ ). The desired eigenvalue is the complex frequency ( $\omega \in \mathbb{C}$ ). In two dimensional framework ( $k_z = 0$ ), the perturbation formulation becomes here, alternative form of the complex eigenvalue, the speed of wave ( $c = \omega/k$ ) contains a real part ( $c_r$ ) which is the phase speed and an imaginary part ( $c_i$ ) which is the growth rate (either amplification or decay) of the perturbation.

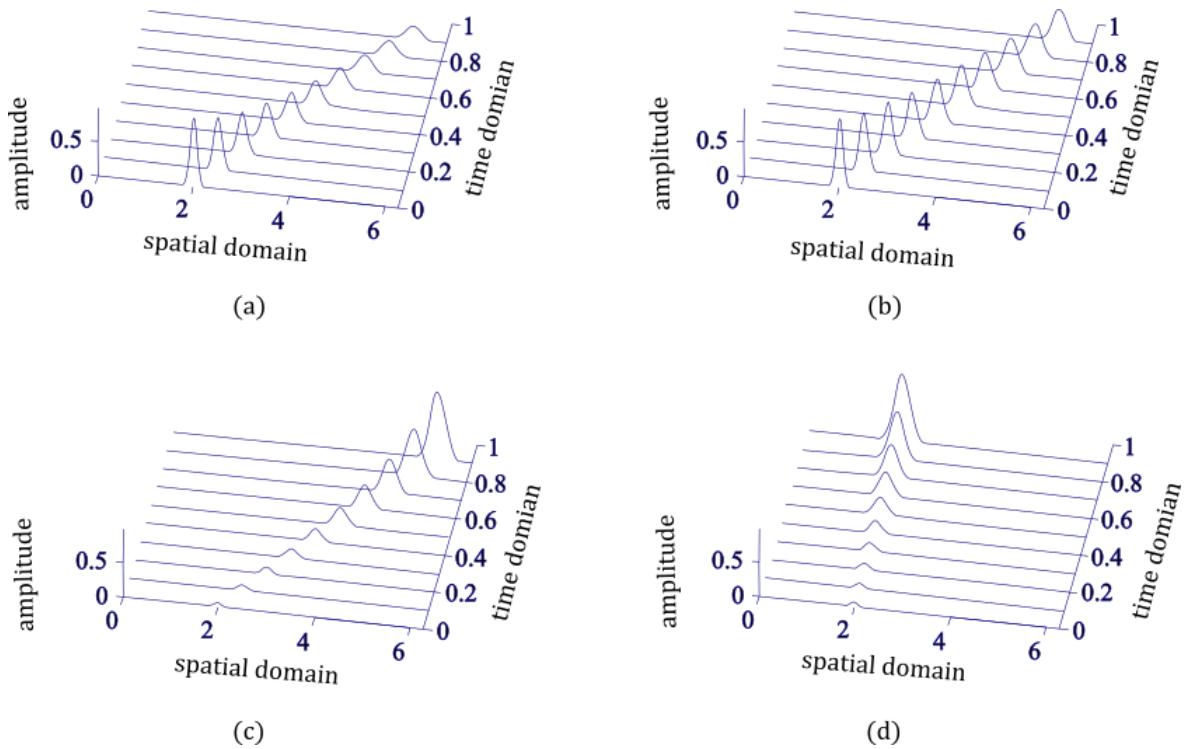


Fig. 1.5 Scenario of plots shows possible stabilities/instabilities for impulse perturbation spreading in system domain: (a) and (b) temporal and absolute stability, (c) convective instability, and (d) absolute instability [Kumar, 2016].

This physically means we consider waves do not grow or decay in the streamwise direction when it moves along the flow from some initial spatial distribution. We then ask whether such waves grow or decay in the time-domain as shown in Fig. 1.5 (a). The eigenvalue sought is angular frequency ( $\omega$ ) of the wave, which is in general complex. When the basic flow is strongly dependent on two spatial directions but homogeneous in the third, the following ansatz is appropriate

$$\hat{q}(x, t) = \eta(y)e^{i(k_x x + k_z z - (\omega_r + i\omega_i)t)} = \eta(y)e^{ik_x(x - (c_r + ic_i)t)} \quad (1.1)$$

In spatial theory, a constant real frequency ( $\omega \in \mathbf{R}$ ) is considered instead and then solve for complex eigenvalue of wavenumber ( $k_x, k_z \in \mathbf{C}$ ). The linear perturbation equation is written as here,  $k_i$  is the spatial growth rate of the wave while  $k_r$  is the wavenumber. The eigenvalue problem to be solved in this framework is nonlinear.

$$\hat{q}(x, t) = \eta(y)e^{i(k_x x + k_z z - \omega t)} = \eta(y)e^{i((k_r + ik_i)x - \omega t)} \quad (1.2)$$

The physical meaning is that we force sinusoidally at a particular point in space and see whether the resulting perturbations grow (negative  $k_i$ ) or decay (positive  $k_i$ ) in space (Fig. 1.5 (b)). This spatial theory is very close to the experimental observations [Chauhan et al., 2003]. For predictions to study of parallel-flow instabilities, i.e. free shear flows and boundary layers, the instability process is very often controlled by periodically forcing the flow at a given angular frequency ( $\omega$ ).

The linear stability analysis begins with deriving a linearized set of equations that satisfy the governing equations subjected to small perturbations  $u'(x, t)$ , and describe the response of a simple basic state. Many of the concepts in local stability analysis, such as “*convective* and

*absolute instabilities*”, are used to provide physical insight into the behavior found in global stability analysis. Saying that the “*local stability analysis*”, is increasingly used as a diagnostic tool for small scale phenomena [Juniper et al., 2014]. Graphically, the “*Convective instability*” shown in Fig. 1.5 (c), a localized pulse on a uniform system can grow and propagate away from the source so that the disturbance decays with time for a fixed point in space. Alternatively, the pulse may grow with time at all the points in space, so called “*absolute instability*” as shown in Fig. 1.5 (d). From numerical simulations of Homem and Erdelyi (2003), applied a fully non-linear adiabatic 2-D hydrodynamic model in open shear layers, they deduced that there factors, e.g. compressibility and viscosity, are significant to decrease the value of the mean flow. The transition from absolute to convective instability of shear-layer flow depends very much on viscosity.

### **1.3 Waves and Oscillations**

Basically the most basic feature of all physical phenomena is the motion of waves by which information is transmitted between two points in space and time [Kunda & Cohen, Fluid-Mechanics (2008)]. Waves are of three main types: (1) mechanical waves (2) Electromagnetic waves (3) Matter waves. In this study, a mechanical waves is concentrated on and it is governed by Newton’s laws and need a medium like materials (i.e. air, water, rock etc.) to travel through [Halliday et al., Fundamentals of Physics (2011)]. Commonly the motion of substance is supposed to be rarely small when the waves is traveling in space. Mass can oscillate around the equilibrium point but it cannot be transferred. The energy, momentum, and phase of disturbance can be transferred from one point to another with the motion of the wave. When the mechanical waves propagates through a medium, it produces

an elastic restoring force because of deformation. “Restoring force” tends to bring the system back to its own undisturbed state, but the “inertia force” causes the overshooting after the system returning the initial state [Ling et al., University Physics Vol.1 (2017)]. Again, as aforementioned above, these waves of which the medium is required are called “*traveling waves*”.

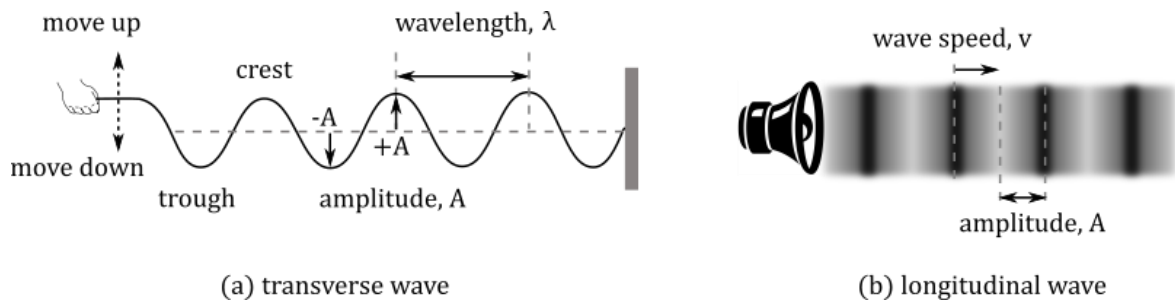


Fig. 1.6 Mechanical traveling waves are schematically shown: (a) a transverse wave, sinusoidal wave-like motion makes the string move up and down continuously along the string; (b) a longitudinal wave, a sound wave caused by a speaker forced the medium air to compress/expand periodically yielding the air element (represented by the dyed-black stripes) are parallel to the direction in which the wave travels.

Traveling waves are both a transverse and a longitudinal waves as shown in Fig. 1.6 (a)(b), respectively. “*Transverse wave*”, we commonly experience free surface wave of a liquid, when a rock has been thrown into a pond, disturbed surface-water making a water wave propagate radially with gravity playing the role of the restoring force. Amplitude,  $A_T$ , is perpendicular to the direction of propagation. In such case shown here, medium (water) is perturbed in the vertical, but the horizontal is the direction of propagation. Observing the trough and crest of the wave in a given duration of displacement, it exhibits a sinusoidal

function of time so that a sine or a cosine curve can befit to characterize its shape. In previous section, this signaling problem is for spatial stability theory. On the contrary, the sound waves is classified as “*a longitudinal wave or compressional wave*”, in which the air is perturbed in the same direction of medium motion moving onto. Saying that the compressed air elements align the horizontal direction which is parallel to the direction of propagation. The amplitude,  $A_L$ , indicates the size of the disturbance, not depending on the speed of propagation ( $c$ ). Oscillatory amplitude is reduced by an external force (case study here is viscosity dissipation) scaled by characteristic length perpendicular to the medium moving direction as results of the oscillatory motion is damped, so-called: *Damping of frequency oscillation*. Mechanical energy of the system decreases as the energy transferring the process of viscous diffusion to the surroundings. Conceptually, varicose mode of non-premixed flames exhibits in this type of oscillation of axisymmetric puffing motion.

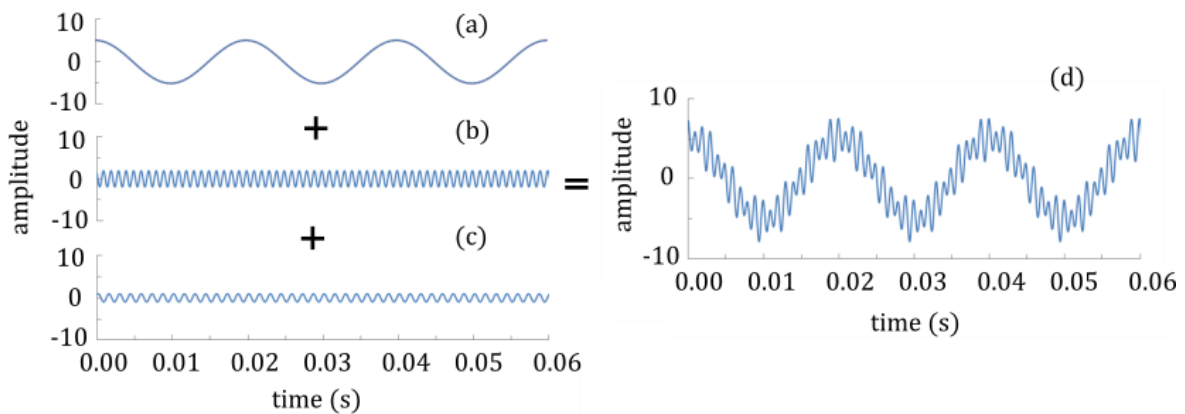


Fig. 1.7 Demonstration concept of wave decomposition: (a-c) single harmonic waves for various frequencies phases and amplitudes, (d) combination waves.

Wave mechanics, phase and group velocity are two important concepts. For 1-D harmonic wave, Fig. 1.7 (a-c), it can be described by the following equation.

$$y(x, t) = A_m \sin(kx - \omega t + \phi) \quad (1.3)$$

Where  $A_m$  is the magnitude of maximum displacement of wave amplitude,  $y(x, t)$ ,  $\omega$  [rad/sec] is the angular frequency of the wave given by  $\omega = 2\pi/T$  by adopting Eq. (1.3) given  $x = 0$  and  $T$  [sec] is the period of oscillation. The angular wavenumber  $k$  [rad/m] is given by  $k = 2\pi/\lambda$  by adopting Eq. (1.3) considering time intervals,  $t = 0$ . An initial constant phase is given by  $\phi$ . The terms in parenthesis ( $kx - \omega t + \phi$ ), sometimes is called the phase  $\theta(x, t)$ . The  $k$  is referred to as the spatial frequency or propagation constant.

$$\frac{d}{dt} \theta(x, t) = k \frac{dx}{dt} - \omega = 0 \quad (1.4)$$

$$\frac{dx}{dt} = \frac{\omega}{k} = V_p \quad (1.5)$$

$$V_p = \frac{\omega}{k} = \frac{2\pi/T}{2\pi/\lambda} = \frac{\lambda}{T} = \lambda f = c \quad (1.6)$$

This  $V_p$  is referred as the phase velocity for each original wave. Being prevalently experiencing the nature, a wave packet is most preferable and useful represented by group velocity ( $V_g$ ). It is considered as a superposition of a set of harmonic waves, in other words a Fourier series or integral. To convey information, amplitude or frequency must be modulated. Conversely, we can use such similar technique to discretize (Fourier decomposition) analyzing the fundamental characteristic nature of instability modes of flame dynamics as shown in Fig. 1.7. In general, this is because at any point in time, it is the summation of each those note of the difference of harmonic waves, which they are either

added together or cancelled out. If we add it more sine wave it becomes more and more complicated (as combination of three frequencies in this instance see appendix B).

$$y(x, t) = y_1 + y_2$$

$$y(x, t) = A_m \sin(k_1 x - \omega_1 t + \phi_1) + A_m \sin(k_2 x - \omega_2 t + \phi_2)$$

$$y(x, t) = 2A_m \cos\left(\frac{k_1 - k_2}{2} x - \frac{\omega_1 - \omega_2}{2} t + \frac{\phi_1 - \phi_2}{2}\right) \sin\left(\frac{k_1 + k_2}{2} x - \frac{\omega_1 + \omega_2}{2} t + \frac{\phi_1 + \phi_2}{2}\right) \quad (1.7)$$

Assume  $k_1 \approx k_2 \approx k$  and  $\omega_1 \approx \omega_2 \approx \omega$ , then we consider group velocity of the envelope as

$$V_g = \frac{\omega_1 - \omega_2}{k_1 - k_2} = \frac{d\omega}{dk} \quad (1.8)$$

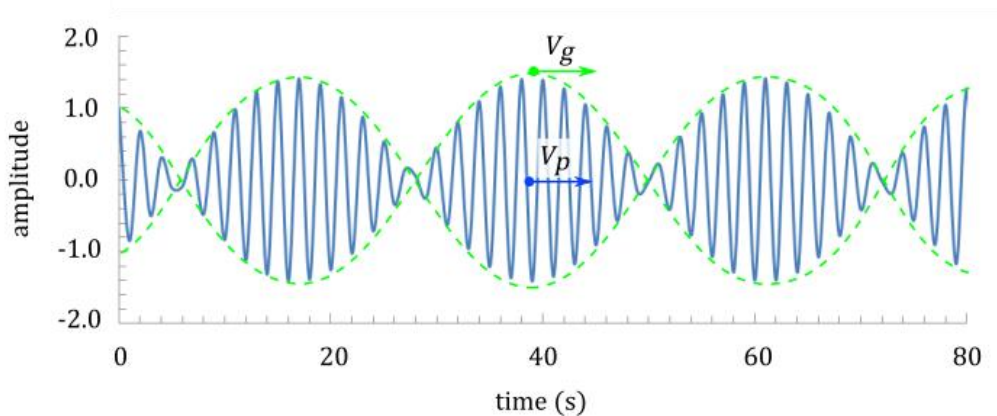


Fig. 1.8 Phase velocity (carrier, blue-line) of each progressive wave and group velocity (envelope, green-line) depicted a packet of progressive waves.

Figure 1.8 presents a concept of group velocity packaging several waves travelling through medium over time domain. The envelope green line is given by  $y_1$  that could be group

velocity ( $V_g$ ) represented at center point of wave packet. It carries on several blue waves given by  $y_2$  that could be  $V_p$  of any waves. Group velocity and phase velocity are not mandatory to necessarily be the same value. They are related through Rayleigh's formula as follows.

$$\frac{\omega_2 - \omega_1}{k_2 - k_1} = \frac{\Delta\omega}{\Delta k} = \frac{d\omega}{dk} = V_g = V_p \left( 1 - \frac{\omega}{V_p} \frac{dV_p}{d\omega} \right)^{-1} \quad (1.9)$$

If the derivative term equals zero, means group velocity equals phase velocity. The pattern of waveform can stay constant; it is on an ideal string of waves. On the contrary, when different wavelengths have different phase velocities ( $d\omega/dk \neq 0$ ), we can have dispersion where the waveform has a sharp peak at one moment in time, but also it is dispersed at another moment in time. In case of different wavelengths (amplitude and speed are same) moving in opposite directions, standing wave can be presented instead.

## 1.4 Buoyancy and Vorticity in Wake and Jet Flows

A fluid is material which flows falling into two categories: gases and liquids. A gas is well-known as highly “*compressible fluid*” and it completely fills any closed spaces encapsulated it. Whereas, the following to the condition ( $Ma < 0.3$ ), gases can be considered as incompressible fluid. Meanwhile, a fluid of which it is sufficiently regarded as “*incompressible fluid*” has a definite volume at constant pressure and temperature placed in an open vessel taken under action of gravity [Milne-Thomson, Theoretical Hydrodynamics (1968)]. Fluid motion at normal atmosphere needs gravity as mechanism driven itself

motions, more specifically, a less dens fluid is driven by buoyancy force. Thus buoyancy effect does not exist in space outside the Earth’s gravitational field.

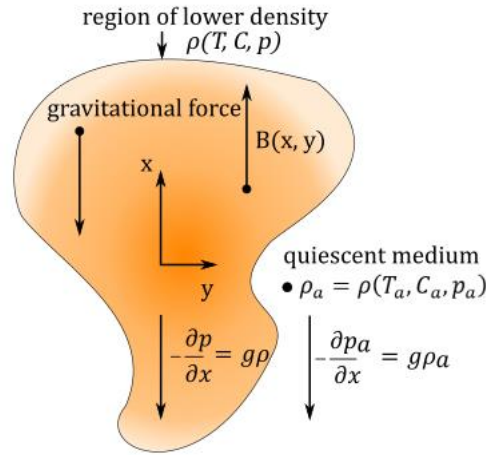


Fig. 1.9 Density disturbance in an extensive and quiescent ambient environment and the resulting transport [Gebhart et al., Buoyancy-induced flows and transport (1988)].

Figure 1.9 shows a considered fluid in 2-D spacing coordinates  $(x, y)$ , whose density  $(\rho)$  depends on temperature  $(T)$  concentration  $(C)$  and static pressure  $(p)$ . In gravimetric field (influence of the  $\bar{g}$ ), a local lighter fluid arises due to buoyancy force  $(\vec{B})$  resulting of the fluid in motion. The motion of lighter fluid is due to the pressure or hydrostatic gradient in the surrounding ambient fluid which is governed by  $\Delta p_a / \Delta x = -\rho_a g$ , this is not same as the lighter fluid because of density variation  $\Delta p / \Delta x = -\rho g$ , where  $\rho$  is the instantaneous local density. The magnitude of buoyancy force is calculated as  $B = B(x, y) = g(\rho_a - \rho)$  where  $B$  is the difference between the two body forces taking positive in case of upward moving direction. This is well-known as Archimedes’ principle [Bahrami, Natural Convection (2015)]. Apparently, the density is a function of temperature. The applied terms

of the volume expansion coefficient  $\beta$  is probably used when a constant pressure is imposed. Therefore, the variation of density of a fluid with temperature are defined as:

$$\beta = -\frac{1}{\rho} \left( \frac{\partial \rho}{\partial T} \right)_p$$

$$\beta \approx -\frac{1}{\rho} \frac{\Delta \rho}{\Delta T} \rightarrow \Delta \rho \approx -\rho \beta \Delta T \text{ at pressure constant} \quad (1.10)$$

Since the buoyancy force is proportional to the density difference, the large temperature difference between the surrounding environment medium and the hot/cold fluid brings more the larger the buoyancy force will be. Whenever two fluid boundaries become in contact and move relative to each other, a friction force develops at the contact surface in the direction opposite to that of the fluid motion. Under steady conditions, let's say the air flow rate driven by buoyancy is established by balancing the buoyancy with frictional forces. Very important nondimensional parameter "Grashof number" is adopted with presenting the ratio of the buoyancy force to the viscous force acting on the fluid.

$$Gr = \frac{g \Delta \rho \forall}{\rho \nu^2} = \beta \Delta T \frac{g L^3}{\nu^2} \quad (1.11)$$

Where  $g$  [ $\text{m s}^{-2}$ ] is gravitational acceleration,  $\beta$  [ $\text{K}^{-1}$ ] is coefficient of volume expansion,  $L$  [m] is characteristic length of the geometry and  $\nu$  [ $\text{m}^2 \text{s}^{-1}$ ] is kinematics viscosity of the fluid. For example, convection is played by the Grashof number in free (natural) convection. Theoretically, the critical Grashof number is observed to be about  $10^9$  for vertical plates as shown in Fig. 1.10. Thus flow becomes turbulent when Grashof member is greater than  $10^9$ . By definition, turbulence is characterized by random fluctuations in fluid properties. As illustrated in Fig. 1.10, when  $Gr$  reaches  $10^9$  the laminar fashion is placed by the turbulence

indicated a high level of disorder of length scales. Sometimes, it is presented as circulation (rotation) in fluid motion.

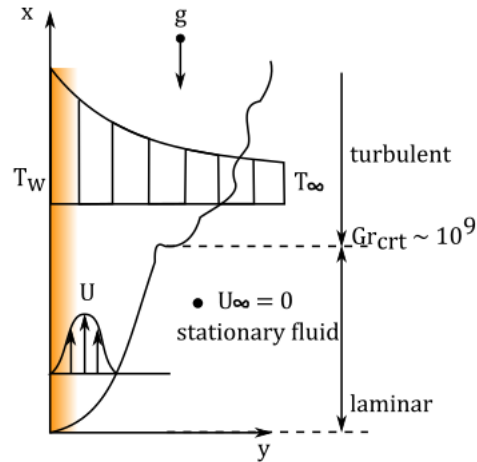


Fig. 1.10 Schematics of velocity and temperature profile for natural convection flow over a hot vertical plate [Bahrami, Natural Convection (2015)].

To study the rotation of fluid, in general, we measure vorticity ( $\vec{\zeta}$ ) or circulation ( $\Gamma$ ). Vorticity ( $\nabla \times \vec{V}$ ) is a vector field that gives a microscopic measure of the rotation at any points in the fluid (see Fig. 1.11 (a)). Meanwhile, Circulation, ( $\Gamma = \oint_C \vec{V} \cdot d\vec{l}$ ), is a scalar integral quantity that gives a macroscopic measure of rotation for a finite area ( $dA$ ) of the fluid (see Fig. 1.11 (b)). A closed contour circled a group of vortices is defined as the line integral which vector velocity ( $\vec{V}$ ) is locally tangent this contour ( $d\vec{l}$ ). Standard notions for the rotation are generally referred to solid objects, however; it seems different for a fluid rotating motion which is represented by the circulation quantity. The fundamental quantity is preferably referred for the analysis of incompressible fluid dynamics. Fig. 1.11 (c) illustrates a shear layer. It is typically demonstrated by means of two types of fluid which

are different of density (concentration), velocity, and phase, and they come in interaction. Shear layer creates by solid wall caused by frictional force (see Fig. 1.11 (d)). Surface of solids moving relative to fluids or extremely close to solid surfaces

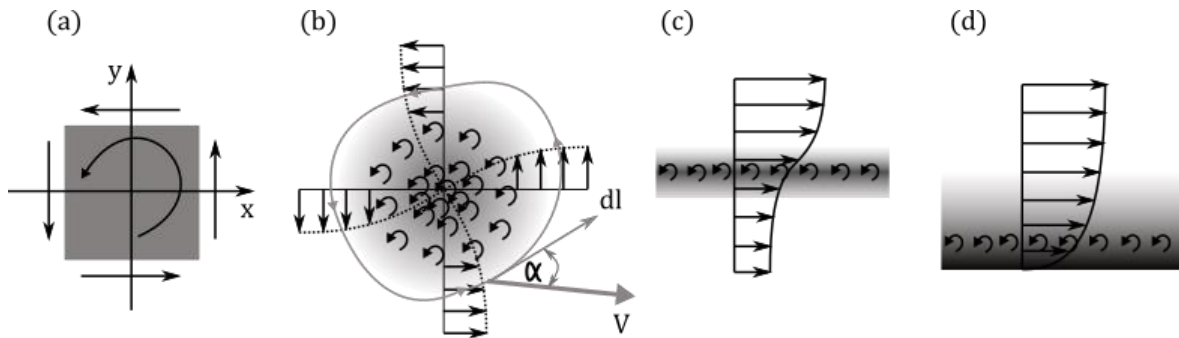


Fig. 1.11 Vorticity corresponds to the local rotation of a fluid particles: (a) vorticity at a point, (b) vortex in a fluid circulation, (c) shear layer invoked vortex and (d) boundary layer invoked vortex. The spatial distribution of vorticity gives rise to different flow structures. An accumulation of vorticity in a compact region corresponds to a vortex; an elongated distribution of vorticity corresponds to a shear layer that, when it is adjacent to the wall, is a boundary layer [Kheradvar & Pedrizzetti, Vortex Formation (2012)].

Circulating region presents at the rear of the solid bluff bodies as shown in Fig. 1.12, is of finite length along the streamwise of the flow, the pressure distribution prevents the high velocity flow from to keep attaching the solid surface (creep flow). Increasing pressure separates the boundary layer and causes eddy shedding in the "wake." Under certain a given flow conditions, a (symmetric) recirculation pattern of flow is established with various types of configuration of bluff body. In real-life problem, we prevalently experience fluid behaviors in wake and jet flows. When wind blows or water flows across bluff bodies, i.e.,

mountains, suspension bridges, tall building, pier of bridge etc., staggering flow pattern can be observed.

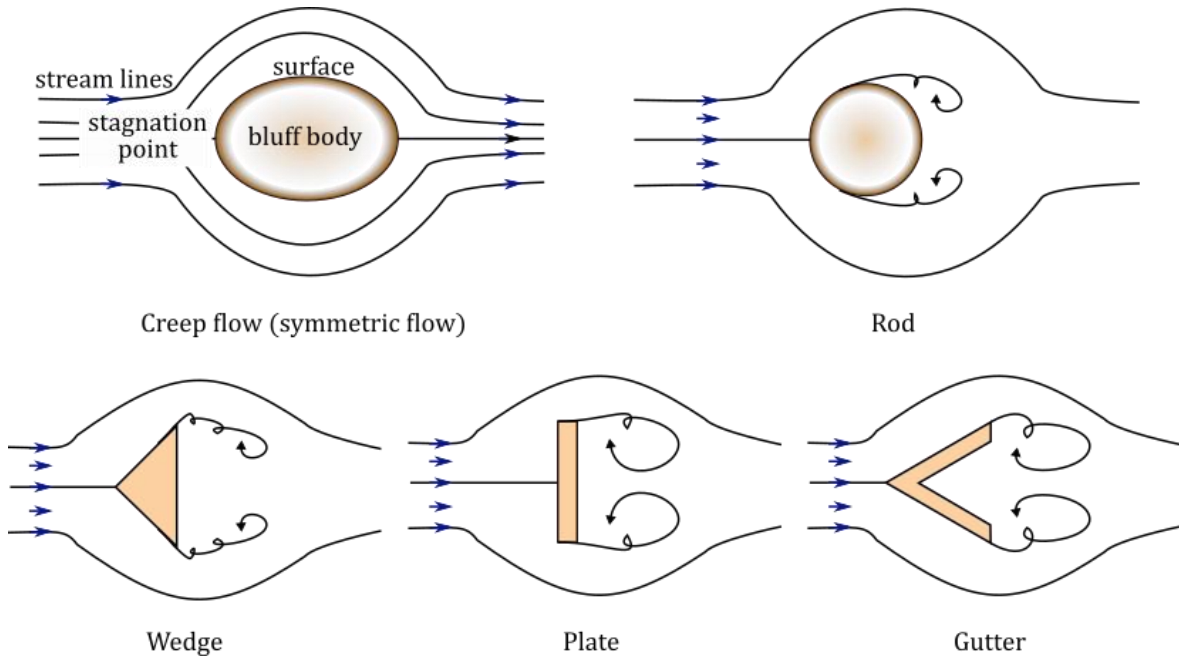


Fig. 1.12 Schematics of flow patterns around various shapes of bluff body [White, Fluid Mechanics (2002) P.458].

For laboratory scale, fluid motion have been studied with various types of bluff body. Wake flow consequently comes up at the downstream region of a moving or stationary bluff bodies which the region of recirculating flow immediately caused by viscosity. Come following to the presence of the flow separation and turbulence, or the wave pattern on the liquid fluid surface at far downstream of an object in a flow-field. It is caused by density differences of the fluids above and below the free surface and gravity (or surface tension). As we have learned in class of fluid mechanics, viscosity distribution creates velocity boundary layer the region at which the flowing fluid contacts the solid surface. Following to Newton’s law of

viscosity, velocity is damped become zero at the solid surface in stationary. In vertical direction (perpendicular to flow-direction), the boundary thickness is defined at the point where the viscous flow velocity is 99% of the freestream velocity. The one major disadvantage of presence of solid bluff bodies in flow-field is the drag that they exert on the flow and the resultant loss of kinetic energy. Thus bluff bodies generated circulation are undertaken of interest on buoyancy induced flame flickering behavior.

Under the effect of gravity, the physical meaning of the three terms are an important sources given as follows: 1) Non-conservative volume forces, e.g., Coriolis forces and Magneto-hydrodynamic forces; 2) Non-barotropic fluids and 3) Viscosity effects [Guyon et al., Physical-Hydrodynamics (2017)]. To study the dynamics of buoyant fire, the last source is very intentional. In overview of dynamics of vorticity, the transport equation is expressed as

$$\frac{\partial \bar{\omega}}{\partial t} + (\bar{V} \cdot \nabla) \bar{\omega} = (\bar{\omega} \cdot \nabla) \bar{V} + \frac{1}{\rho^2} (\nabla \rho \times \nabla p) + \frac{\rho_{\infty}}{\rho^2} (\nabla \rho \times \bar{g}) + \nu \nabla^2 \bar{\omega} \quad (1.12)$$

Through the equation (1.12), we know that when the flow regime is characterized by buoyancy, density gradients play as the dominant contributor to the vorticity generation under the gravitational field (3rd-term, RHS). It is predominating over the pressure gradient demonstrated by second term (Baroclinity) then it can be ignored because there has little effect on buoyant vorticity generation. The first term is the stretching/tilting made by velocity gradients when it is aligned with or orthogonal to the vorticity. On the left hand-side of Eq. (1.12), representing Lagrangian derivatives, changes of the local and convective of vorticity are represented. The second term indicates the rate of volume expansion which is spread out caused by reaction heat release, not changing the overall vorticity and vanishing for incompressible fluid. Annihilation of vorticity is the fourth-term on right hand-side. It is

dissipated by viscous diffusion in a flow field, only the term in here that creates the vorticity is the buoyant term (3rd-term, RHS). For instance of circulation of buoyant fires at the normal atmospheric conditions, vorticity is generated by  $\frac{\rho_\infty}{\rho^2} (\nabla\rho \times \vec{g})$  under the influence of gravity. This scene is prevalently visualized for buoyant type of fires and instability is absolutely sustained itself caused by the radial density gradients. In contrast with the momentum dominated-turbulent fires, the shearing effect of fuel outflow at which vicinity area closed to burner exit (threshold of initiating flow-field instability) generates the external disturbance which turns the entire flow-field to unstable fashion [Lingens et al., 1996; Mell et al., 1996; Jiang & Luo, 2000; De Ris., 2013]. Vortices intensify being proportional to the density difference of hot gases and surroundings. Periodicity of free burning oscillation shown in Fig. 1.13; events: necking-in, bulging, pinching-off, and depleting, are consequently observed over the time. Analysis of kinematic models, e.g., convective time scale ( $\tau$ ) associated toroidal vortex and vortex-dynamical principle were made to gain more understanding the physics of puffing behavior of buoyant non-premixed jet flame. [Cetegen & Ahmed, 1993; Xia & Zhang, 2018]. Globally, characteristic frequency had been reported as function of Richardson and Froude numbers. Vertical length dictated a luminous flame pinched-off is found consistent with numerous past investigations. The length growing strength of vorticity acumination scaled by the (equivalent) diameter of fire source is nearly constant for single-flame system. This scene is similar to the fundamentals of longitudinal wave in mechanical traveling waves described in the previous section.

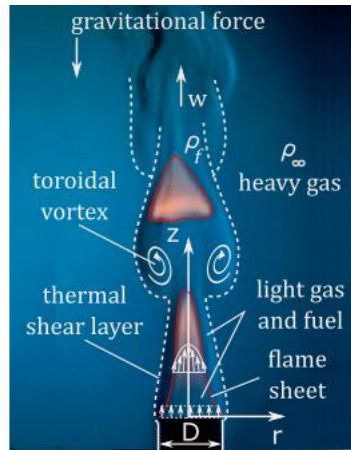


Fig. 1.13 Schematic of toroidal vortex interacting with buoyant flame interface [Ahmed & Cetegen, 1993; Xia & Zhang, 2018].

Again, main focus of the dissertation is on the dynamics of non-premixed flickering flame in global scale. At sufficiently small  $Fr$ , buoyancy plays a great role of entrainment, hereby two inflection points occur in the flow-field. In theory, jet diffusion flame is found to be under control of buoyancy when Froude number is less than 5 [Delichatsios, 1993]. With the fire number is used for a representative one, the value of this number is less than 10 [DiNenno et al., Handbook of Fire Protection (2002)]. For buoyancy induced oscillation, two modes of flame dynamics were observed by Cetegen and Dong (2000); namely, varicose mode (axisymmetric motion) and sinuous mode (asymmetric motion), both modes can occur in single-flame system with the different characteristic frequencies. Based on an extensively several past works, a pool/jet dynamics of flame instability had been studied [Hamins et al. 1992; Malalasekera et al., 1996; Cetegen & Dong, 2000]. The principle topic of fluid dynamics is incorporated into the modern combustion science. Interaction of either flame-to-flame or flame-to-surroundings is of interest of analysis. Different mechanisms have been

proposed. For example, Rayleigh-Taylor (R-T) and Kelvin-Helmholtz (K-H) instabilities are introduced to attribute the nature of mode appearance. Mechanically, R-T instability occurs when gravity overcomes viscosity that mushroom-like shape is generated [Cetegen & Kasper, 1996]. Phenomenologically, the restoring force is the gravity, but the oscillatory amplitude is damped by viscosity. In referring the course of fluid mechanics, viscosity is a transport coefficient which characterizes the transfer of momentum from the regions of higher velocity to those of lower velocity. The effects of viscosity are significant and viscous effects are ubiquitous within the vicinity near reaction zone where the velocity stratification altered are evolved to form the boundary layer. Meanwhile, K-H instability is used to explain growth of disturbance at surface interface as similar as wave-like evolution. The momentum-dominated flows of which the different velocities of fluids meet at surface interface is taking account, but sometimes the density difference still exists and it cannot be ignored [Coats, 1996]. While the adopted of vortex-dynamical principle has also been introduced to explain the nature of such instabilities for both single and dual buoyant diffusion flame(s) [Wang et al., 2012; De Ris 2013; Hu & De Ris 2015; Xia & Zhang, 2018; Yang et al. 2019; Zhang et al., 2020].

## **1.5 Scope of Research**

This dissertation focuses on the transition phenomenon of two modes (axisymmetric and asymmetric motions) of flame dynamics of buoyant non-premixed jet flame.

### **1.5.1 Critical Condition of Mode Transition of Twin-flame System**

Existence of mode change, Figs. 1.14 (a) and (c), of flame dynamics of single (pool) fire was observed and it was pointed by early researchers [Cetegen & Dong, 2000]. Unfortunately, there was difficulty to control this phenomenon (sinuous mode) in a precise manner, hence, precise studies on this matter are rather limited. Many issues including its mechanism remain unknown far thus. So a new trick may bring more chance to approach the transition mechanism which by chance appears in single-flame system as similarly found in twin-flame system (d),(f). Thus the transition (e) of interacting buoyant non-premixed jet flame are precisely studied systematically aiming to understand the mode transition in single-flame system (b). Important systematic parameters (separation distance,  $L$ ; burner diameter,  $D$ ; and fuel flowrate,  $Q$ ) are examined. Results show that the diameter and the separation distance of two identical burners act as a representative characteristic scale to characterize a global flame dynamics, irrespective of the fuel flowrate even of fuel types, even or apparent fire shape. Thus the critical condition can also be summarized/described by the critical value of the updated global parameter which was done by Yang et al., (2019), discussed in chapter 4.

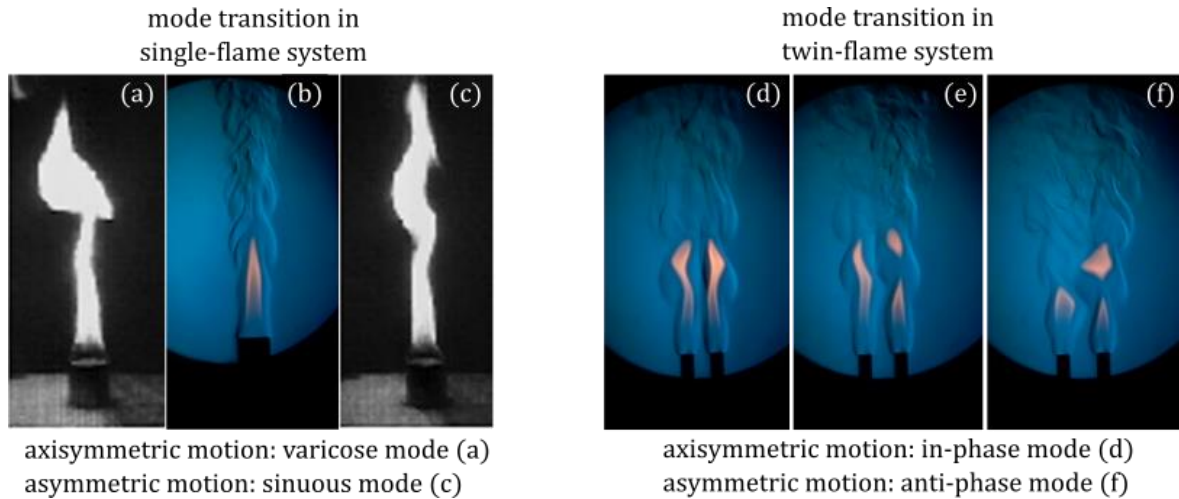


Fig. 1.14 Instant images of a propane buoyant diffusion flame (a) and (c) originated from 25 mm diameter with a fuel flowrate of 570 cc/min; framing rate is 30 fps [Cetegen & Dong, 2000]. Shadow images of 10 mm diameter of burners were observed at  $L= 15$  mm (d) and 25 mm (f), with  $L= 21$  mm for the transition (e). Experiment was performed at a fuel flowrate of 500 cc/min, and 300 fps of framing rate.

### 1.5.2 Interpretation of Mode Transition of Single-flame System: Similarity Approach

According to a whole flame dynamics for twin-flame system, the transition phenomenon found in the single-flame system (Fig. 1.14 (b)) is interpreted by the upgrade correlation done by the twin-flame system. In this regard, hypothesis is made and discussed to provide a proper physical interpretation of mode change of single fire which is generally difficult to control. The similarity is introduced; the optical technique is conducted to see thermal boundary formed/surrounded by jet flame as shown in Figs. 1.15 (a-c) for axisymmetric motion and (d-f) for asymmetric motion. The 3-D simulation is introduced and the frequency analysis is executed, including visible flame dynamics during transient motion. Critical Reynolds number is discussed as an ideal candidate to characterize the change of dynamic

mode having asymmetric motion for both the single- and twin-flame systems. More precise details and discussion are made in chapter 5.

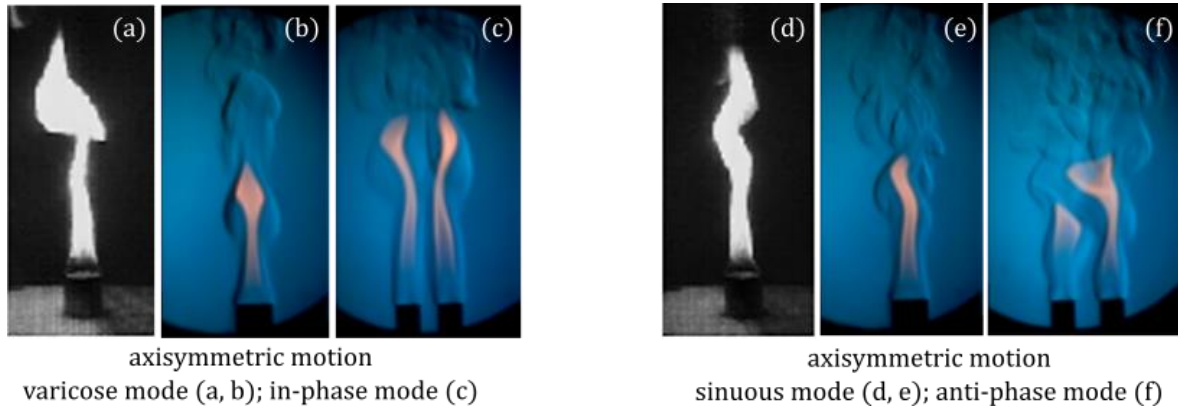


Fig. 1.15 Instant images of a propane buoyant diffusion flame (a) and (d) originated from 25 mm diameter with a fuel flowrate of 570 cc/min; framing rate is 30 fps [Cetegen & Dong, 2000]. Instant luminous methane flame with shadow images recorded at 300 fps of framing rate:  $D = 30$  mm,  $Q = 760$  cc/min; Varicose mode (b) and Sinuous mode (e). And  $D = 18$  mm,  $Q = 1000$  cc/min;  $L = 15$  mm, in-phase mode (c) and  $L = 21$  mm, anti-phase mode (f).

## **Chapter 2**

### **Theoretical Background and Problem**

Having stated research objectives in first chapter, a new strategy to understand the transition phenomenon in single-flame system will be paid an attention. The link should also be clear and highly strong for summarizing and filling this empty fundamentals. Following to this hypothesizing concept, we could be able to approach the mechanism of mode change, which it seems impossible thus far, when the unstable flow structure of buoyant fire have been studied more than a decade since 2000. Therefore, geometrical aspects of non-premixed flames of such single- and twin-flame systems for both reactive and non-reactive cases will be taken into account in the literatures. Potential factors and features, i.e. flame pulsation in term of freely burning in air, locking flame interaction (flame-to-flame, flame-to-cold surroundings), and instability of the unconfined shearing flow layers, are most of interest in this chapter.

#### **2.1 Characteristics of Non-premixed Flames**

In fundamentals of combustion, it has been already known that there are two types of distinctive combustion; firstly: premixed flame, Fig. 2.1 (a); and secondly: non-premixed flame (b). In premixed flames, appearances of flame luminosity are mostly in blue color. The oxidizer is required to supply at earlier stage before reaching combustion location. They are usually mixed prior to ignition by molecular diffusion of oxidizer (pure oxygen or fresh air) and fuel [McAllister et al., 2011]. Not likely the premixed flames, non-premixed

(diffusion) flames, the combustion occurs where the oxygen in the environmental surroundings drawn into the reaction zone due to the entrainment effect. After sufficient natural mixing of fuel and oxidizer, combustion can take place continuously [Drysdale, 2011]. For laminar diffusion flames, oxidizer is primarily moved by the effect of molecular diffusion; whereas, terms either of turbulent eddies in case of highly turbulent fashion or toroidal vortex for moderate turbulence, e.g. flickering flames, draw in the oxidizer to the reaction zone [McCaffrey, 1983]. In this section of literature review, the nature of the global flame characteristics has extensively been discussed. The effects of parameters, i.e. apparent shapes and sizes of fire, fuel flowrate, kind of fuel, radiation and heat release (dilution) etc., will have been of interest.

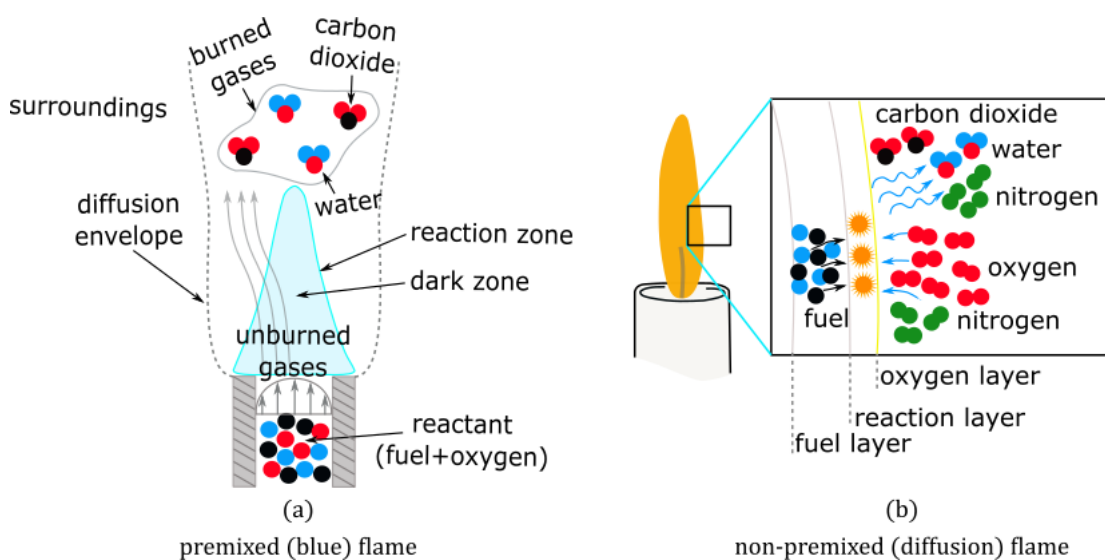


Fig. 2.1 (a) Schematics of premixed flame and (b) Non-premixed (Candle) flame, corresponding with fuel-oxygen-rich layers, and burn (unburned) gas [Lars-Göran, Enclosure fire (2001)].

One striking dynamic feature of non-premixed flames is presenting of flame pocket (the cap: burnable gas encapsulation) when the flame grows over a certain size as observed the trend in Fig. 2.2. In essence of the upper part of flame, the periodic rising-up fashion of pinching-off the cap yields a global characteristic instability of flame dynamics [Carpio et al., 2012; Moreno-Boza et al., 2016; Moreno-Boza et al., 2018]. More specifically, an identical features of flame oscillation can be found irrespective of the source of the flame (jet flame, candle, crib-wood, pool fire etc.), in terms of the dynamic behaviors dominated by the buoyancy. Its “flickering or puffing” frequency becomes an important fundamental quantity summarized in the form  $f \sim D^{-1/2}$ . This scaling relation is valid in a wide range of fire scales in gravimetric flow-field and it has also been confirmed by numerous previous studies [Hamins et al., 1992; Cetegen & Ahmed, 1993; Malalasekera et al., 1996]. In general, classification of flame features depending upon fire scale ( $D$ ) is schematically shown by Fig. 2.2 for freely-burning diffusion flame in gravimetric field. The flames with significant initial momentum are usually jet-like behavior ( $D < 0.01$  m). As further increased the fire scale ( $D \sim 0.1$  m), effect of gravity sheds clearly on the flame shape, the transition to turbulence occurs that it is primarily a function of surface area of fuel issuing, where the observed flames become fully turbulent around at a perimeter of fire, and this makes flame nature as fundamental mode experience a lot of difficulties in practice [Corlett, 1974]. For a very large surface area of fire source, a single flame cannot maintained any longer, effect of gravity becomes substantially influenced to the flame instability; therefore, the fire then breaks up into multi-flickering flames—very high disorder of length scales and highly turbulent fashion. This scene is well-known as a “mass fire” ( $D \sim 1$  m) [Finney & McAllister, 2011]. It is ubiquitous in fireplaces, such as wildland, urban, or even vegetation fires, for which these are quite large scale in reality. The rightmost in figure below, non-premixed turbulent

flames are divided into three zones—continuous flame zone, intermittent flame zone, and buoyant thermal plume [Maynard, 2013].

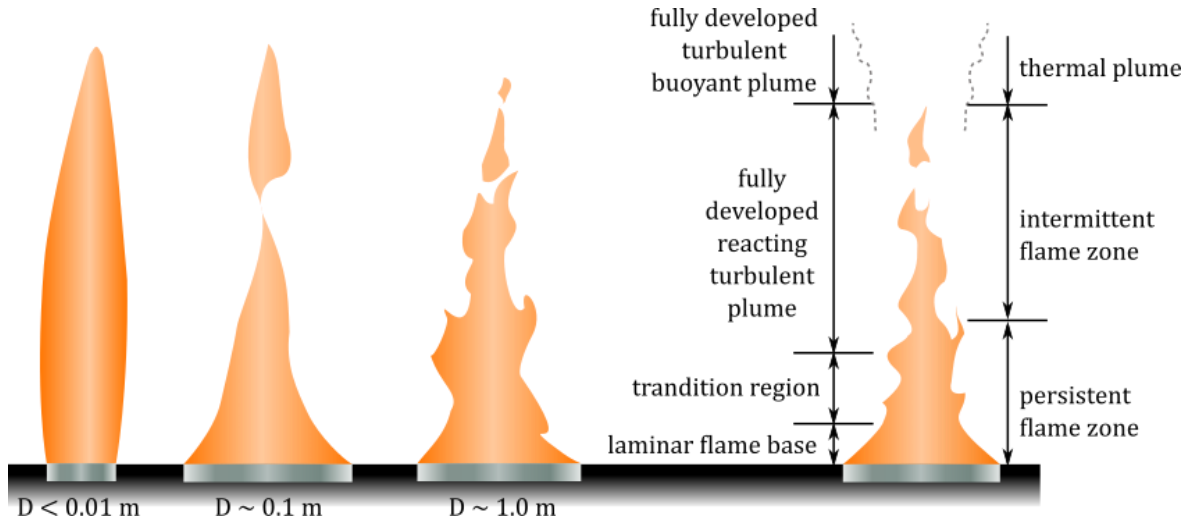


Fig. 2.2 Schematic of transition from laminar to turbulent flame and eventually mass fire adapted from Drysdale, 2011.

For a relatively small fire scale ( $D < 0.01$  m) shown in Fig. 2.2, the steadiness of flame behavior is apparently usually observed when a flow rate of combustible gas does not reach a given condition of turbulence (Fig. 2.3); in such case stated here, Reynolds number could properly tell the state of flow regime. Influence of fuel flowrate was studied to show progressive change in laminar flame length was done by Hottel and Hawthorne (1928). An overall flowing behavior of a wide range of nozzle velocities of ejecting fuel had been determined. The lengths of diffusion flames burning in free air significantly decrease with the increase of the nozzle velocity, but there has no a consequent change in flame length when a transition occurs to fully developed turbulent fashion, and it is substantially independent of further increase in velocity. In other words, once the velocity reaches at a

certain value, the dynamics is completely controlled by momentum (combustible inertia force), rather than the buoyancy-controlled. Regarding on this matter, we could have said that with negligible initiating momentum, the dynamics can also behave as buoyancy-controlled plumes [List, 1982]. The data shown by previous numerous studies indicates that flame dynamics becomes slightly relatively independent of the kinds of fuel issue [Seaba et al., 1988; Hamins et al., 1992; Cetegen and Ahmed, 1993; Malalasekera et al. 1996]. Therefore, this is highly possible that the kinds of fuel might not play a significant role on the global flame dynamics; hence, the characteristic frequency may not present much the difference based on this factor so that this could be ignored in the present study.

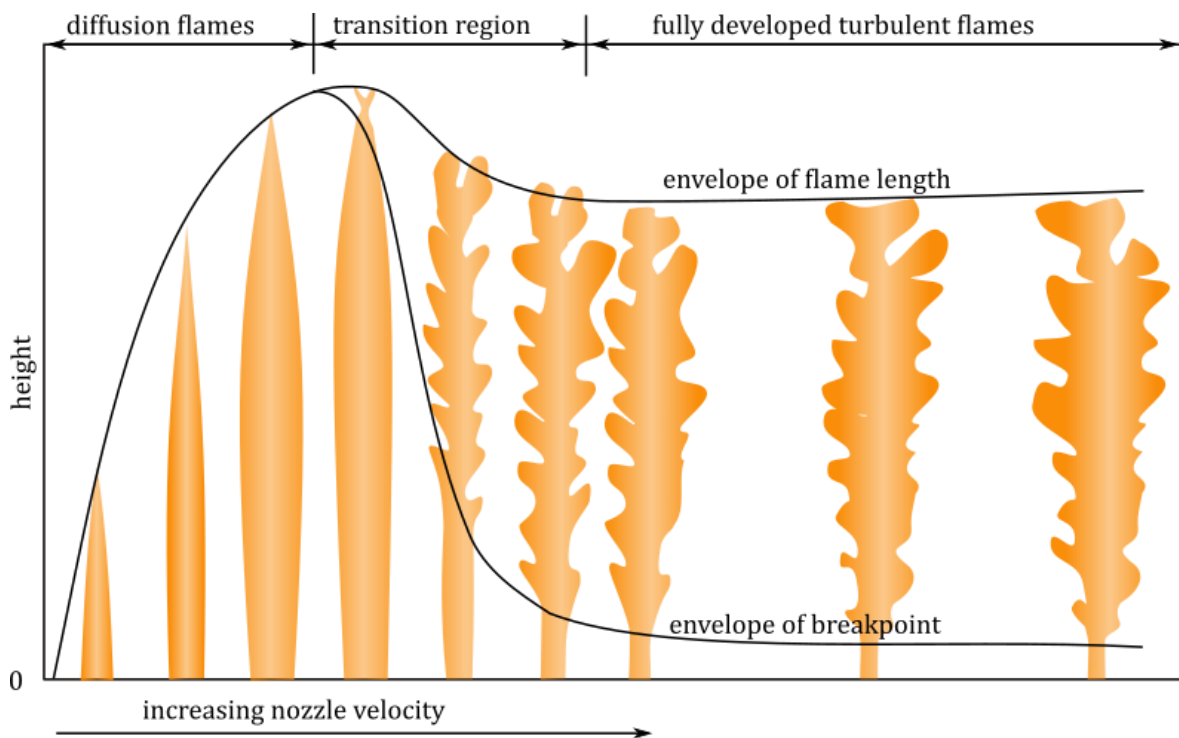


Fig. 2.3 Progressive change in diffusion flame type with increase in nozzle velocity [Hottel & Hawthorne, 1948].

In fundamentals, transport mechanism of laminar flames are primarily controlled by diffusion and convection at the near field of flame edges where coexistence of gaseous fuel and oxidizer from environmental surroundings takes place [Linan et al., 2014]. At very bottom of non-premixed flames, the blue flame can be found in very short length. Coherently, the non-uniform mixture also presents there, the occupancy of which its characteristic yellow color lights from the micrometer-size of carbonaceous soot particles. In case of upsizing more and more, when the size of fire becomes bigger. This scene is very hard to identify, rather, it is no longer observed. So the blue coloring scenario disappears and the burning rate (per unit area) decreases as the flame grows larger [Orloff et al., 1975]. Some studies of the intermediate and larger scales deduced that burning rate becomes increasingly affected by radiation, but it eventually becomes independent upon the apparent size of fire source [Fukuda et al., 2006; De Ris, 2013]. Aside from the vortices contributing the combustion, the rate of fuel consumption is also depending on pumping capacity of toroidal vortex that the air is drawn into the reaction zone by transferring process of plume momentum [Hu & De Ris, 2015]. The most relevant contributions are up to about characteristics of turbulent eddy interacting to the flame. Saying that a big engulfment carries a large amount of fresh air into the reaction zone resulting of a more chemical energy generated by combustion. From some works of Hamins et al. (1992), they had shown the effect of heat release on characteristic frequency and they had pointed out that heat release rate has less effect on flame pulsations, even it is less than the effect of fuel velocity as shown in Fig. 2.4. On the left hand side, characteristic frequency has slightly dependency upon the velocity of ejecting fuel with various diameter of burners. This is similarly consistent with Hottel and Hawthorne examination of the effect of ejecting fuel velocity on the progressive length of laminar diffusion flame, dynamically. The biggest burner in this performing is 10 cm which is still

in the moderate turbulent fashion feasible to fundamental mode identification defined in Fig. 2.2. On the right hand side, the frequencies show insensitiveness with varying heat release rate. So this effect is neglected in this dissertation.

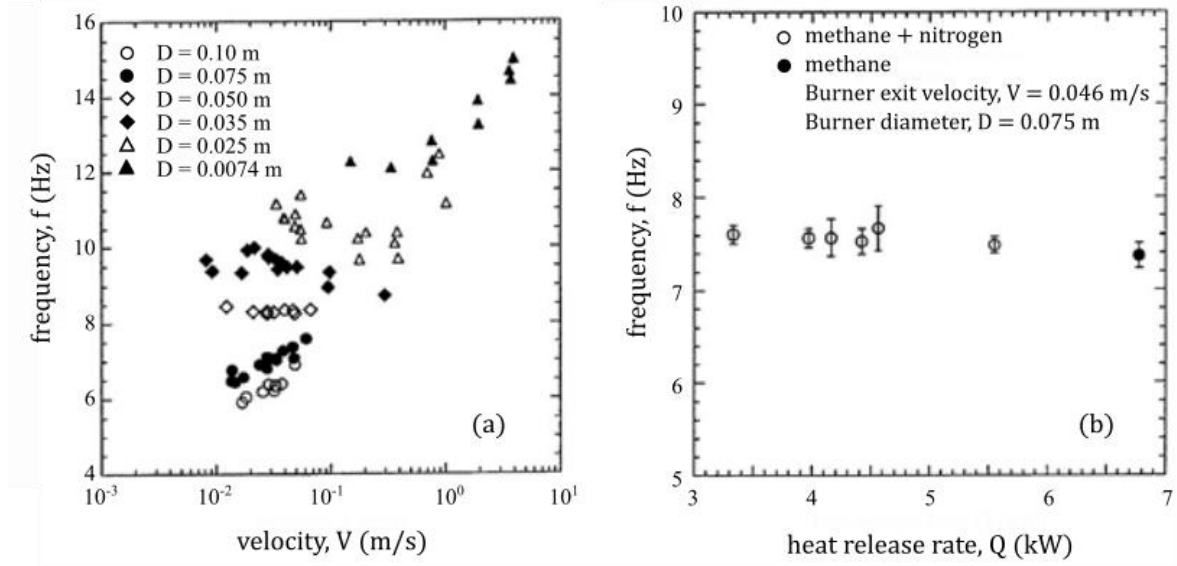


Fig. 2.4 (a) Measurement of oscillation frequency as function of ejecting fuel velocity for various diameters of freely-burning gaseous methane. (b) Measurement of oscillation frequency as a function of the heat release rate for 0.075 m diameter methane flames with constant ejecting fuel velocity (0.046 m/s) diluted by varying amounts of nitrogen with error bars presenting the standard deviation [Hamins et al., 1992].

In case of pool fires such as liquid pool paraffin of candles, burning rate is bound to the ways of energy arriving the pool. Two mechanisms, e.g. radiation and conduction, are controlled the rate of fuel vaporization. Radiant energy transferred by soot emission to the liquid pool is very essential; therefore, amount of soot generated in the flame affects the amount of the radiation. Nevertheless, the change of dynamic mode of flame may not be governed by this

factor. Evidence of this effect had been made experimentally as well as numerically that the puffing frequency was insensitive to modification of this factor. Its influence was revealed by Katta et al. (2009), that the magnitude of flame oscillation was a function of amount of soot radiation. For example, in their study shown that once the radiant energy is increased reaching 80%, puffing behavior is stopped, a steady flame presents instead and vice versa. Wu and Zhao (2020), their prediction also reveals such similar results that an independency of variations in chemistry, soot, and radiation had been confirmed. Saying that sooty flame seems preferable to be steady regime, rather than to exhibit periodically fluctuation.

In terms of multiple fires synchronization, a simple mathematical model including a non-linear effect via radiation energy transfer developed by Kitahata et al. (2009), revealed that such a non-linear effect played a key role on switching to oscillation mode. Together with an overlapped peaks model done by Chen et al. (2019), the deduction of this study claimed that the synchronization of flames was very essential to the thermal radiation. By means of measurement of the temperature between flames, the impact generated by flame radiation can indicate the coupling strength between oscillators. However, regarding the latter our examination on the influence of thermal radiation, a numerical three-dimensional simulation was performed [Mochizuki & Nakamura, 2015; Mochizuki et al., 2017]. The model for interacting two jet burners showed that the radiation effect did not play the primary role in the appearance of two modes. Together with optical imaging technique [Bunkwang et al., 2019], it was confirmed that the fluid dynamics induced by buoyancy played a key role in the appearance of two modes and their transition, we will make a serious discussion on this phenomenon in chapter 4. Even though the radiation found to initiate flame oscillation, from steady flame to puffing behavior in axisymmetric (varicose mode) motion of flame dynamics, this is not concerning the appearance of two dynamic modes in twin-flame system, saying

that the transition. It is merely very essential to enhance the evaporation of liquid fuel for pool fires. From fluid dynamics point of view, when the frequency changes, the orientation of fluid structure is found differently, e.g. streamwise switching to spanwise, in flow-field velocity. Such that switching event is defined as the transition of dynamic mode of non-premixed flickering flames.

## **2.2 Transition of Dynamic Modes of Buoyant Non-premixed Jet Flame(s)**

In section 1.4, types of flame dynamics have been introduced; here, physical description is continued. In this dissertation, the modes of flickering flames are classified as shown in Fig. 2.5 (top images: the drawing schematics of luminous flame behaviors, and bottom images: instantly direct photographs from previous studies). That is: 1) an axisymmetric motion, e.g. varicose mode for single-flame system and in-phase mode for twin flame system; 2) an asymmetric motion, e.g. sinuous mode for single-flame system, anti-phase mode for twin flame system, respectively. The sinuous meandering fashion originates in the contracting region at very upper flame portion showing a steady buoyant diffusion flame envelope without freely-burning flame pocket (b). For puffing oscillatory motion, the varicose mode (axisymmetric motion), which develops very close to the burner exit of surface contracting of flame (a), encountering the periodic burn-out at the flame-top with height fluctuations caused by toroidal vortical interaction.

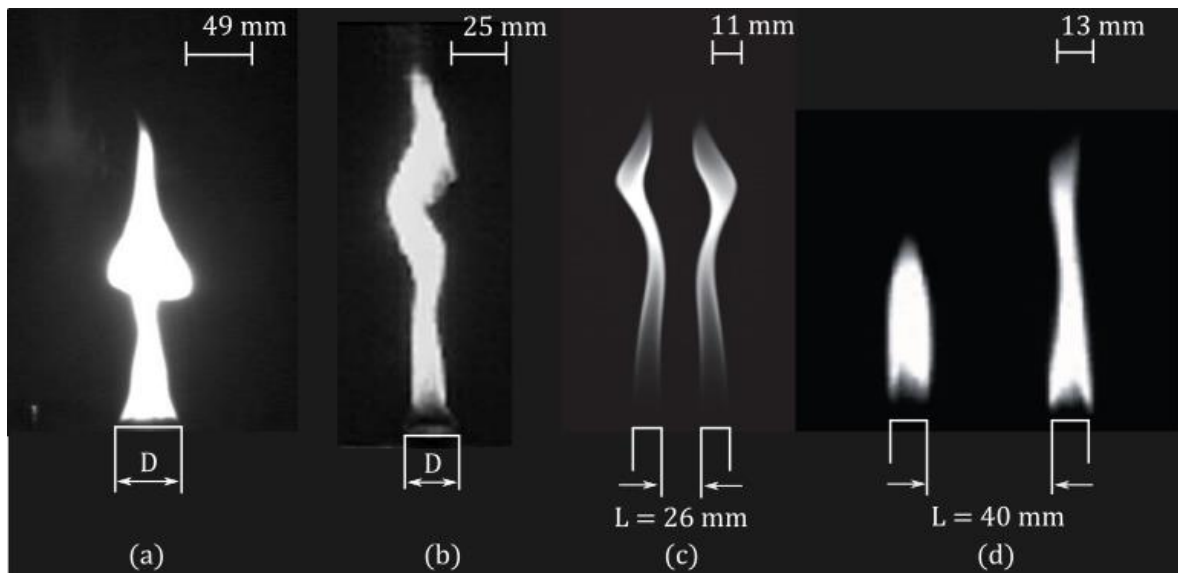
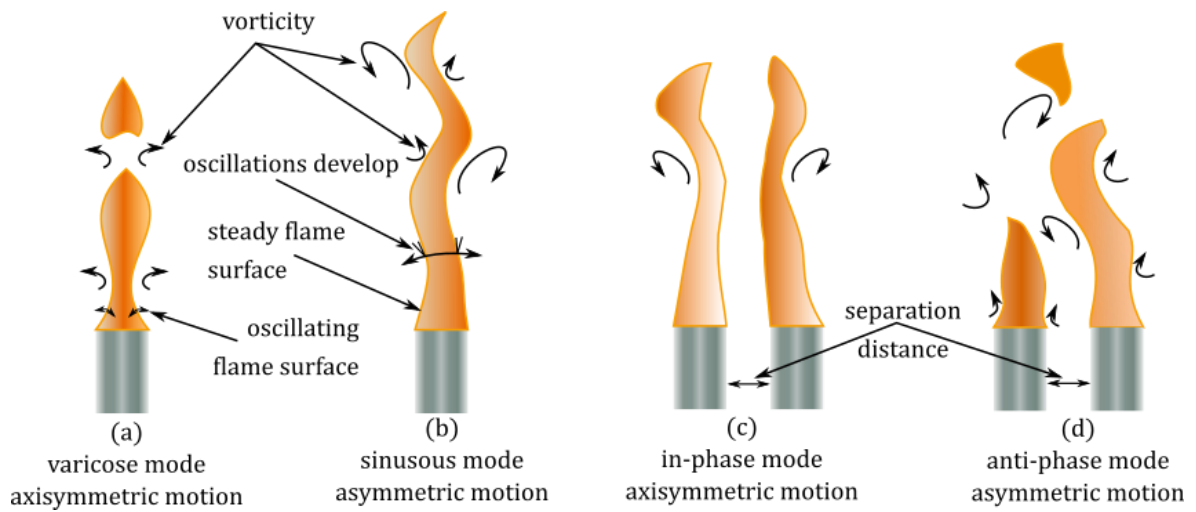


Fig. 2.5 Schematic depiction (top) of the varicose and sinuous dynamic modes of a single-flame system (a), (b). [Cetegen & Dong, 2000]; and the in-phase and anti-phase instability modes of twin-flame system (c), (d) [Toong et al., 1965] in buoyant diffusion flames. Instant snapshot (bottom) of non-premixed flame oscillations: (a) n-heptane pool fire [Fukuda et al., 2006], (b) propane diffusion flame [Cetegen & Dong, 2000], (c) dual jet methane diffusion flames [Fujisawa, 2020], and (d) bound three-candle (paraffin) diffusion flames [Kitahata et al., 2009].

Through the observation of such quick snapshots of flame dynamic behaviors shown in Fig. 2.5 (a), (c) bottom, axisymmetric (varicose and in-phase modes) motion exhibits the mushroom-like shape found in process of flame detachment. Orientation of flame deformation is obviously in vertical; this scene is similar to longitudinal traveling wave as mentioned in section 1.3. Thus the size (equivalent diameter) of fire source can properly characterize this type of flame dynamics. With already well-known from several past works of fundamental study, this prominent relation  $f \sim D^{-1/2}$  is very versatile scaling to describe the oscillation frequency of axisymmetric motion [Hamins et al., 1992; Cetegen & Ahmed, 1993; Malalasekera et al., 1996]. In contrast with axisymmetric motion, the asymmetric (sinuous and anti-phase modes) motion as shown in Fig. 2.5 (b), (d) bottom, the deformation of luminous flame stays contacting and it looks very like the transverse wave (see section 1.3). The size (equivalent diameter) may not be appropriate as characteristic length scale of the system. For further hypothesizing this event, the characteristics changing of buoyant flowing fluid structure would probably be inferred. In essence, flame dynamics exhibits exactly different orientation to the one found in the axisymmetric motion, Together with evidence pointed out by a study of Cetegen and Ahmed (1993), a very striking scattering of frequency analysis was found when relatively small diameters of burners were adopted. Presence of sinuous meandering in single-flame system was found when small Richardson number was employed [Cetegen & Dong, 2000]. This scaling relation,  $f \sim D^{-1/2}$ , deems no longer to be proper in well-correlated with the global dynamics of puffing/flickering flame. Speculation would be the coexistence of two dynamic modes leading to inability of the scaling occurrence.

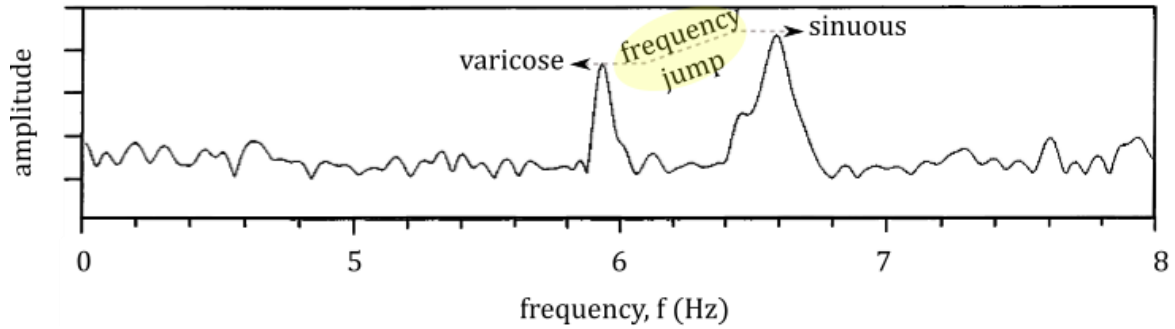


Fig. 2.6 (a) Pulsation frequency spectra of a buoyant propane flame ( $D = 38$  mm,  $Q = 575$  cc/min) showing coexistence both varicose and sinuous modes in transition condition [Cetegen & Dong, 2000].

Figure 2.6 (a), frequency jump is noticeably outstanding physical feature of the transition phenomenon. A very similar feature was found by numerous previous studies in different flame systems [Toong et al., 1965; Cetegen & Dong, 2000; Kitahat et al., 2009; Fuuda et al., 2006; Dange et al., 2019; Changchun et al., 2019; Fujisawa et al., 2020]. More specifically, appearance of this mode of single fire was found by chance, unfortunately, no critical value proposed far thus. Oscillation frequency of varicose mode was pointed out to be lower than the one found in sinuous mode. Axisymmetric (varicose mode) motion has longer cycling period than asymmetric (sinuous mode) motion. Although the transition of buoyant non-premixed flame had been observed since 2000 for single fire and in 1965 for dual fires, there has no more precise details to tell its mechanism and its appearance until the present. Together with the author's knowledge, to control such that dynamic mode to study its structure is not easy task dealing with single fire, not even taking the advantages of powerful computation for simulation. On the other hand, the observed change of dynamic modes of dual diffusion flames was carried out in mid' 60s. Toong and coworkers (1965) had

demonstrated the distinctive two modes by modifying system parameter, the separation distance ( $L$ ), where two identical burners were perfectly aside—positioning side by side (Fig. 2.6 (b), blue diamond). As clearly observed in Fig. 2.6 (b), the modes of flame dynamics are controllable through the modified  $L$  with various apparent sizes of fire and different kind of fuels; moreover, the more clear point of the transition is successfully identified, which has never experienced in single-flame system.

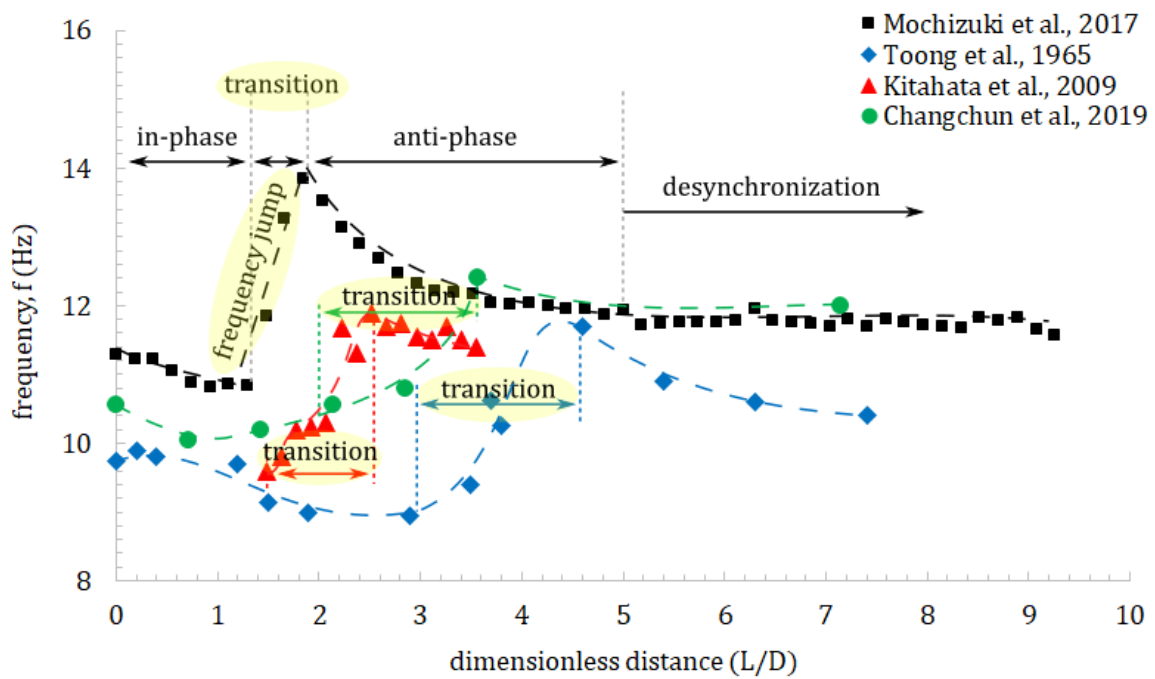


Fig. 2.6 (b) Effect of burner separation distance on flickering frequency of twin-flame system. [□] Mochizuki et al., 2017 (dual jet methane flames); [◇] Toong et al., 1965 (simulated dual propane candle flames); [△] Kitahata et al., 2009 (dual paraffin wax candle flames); [○] Changchun et al., 2019 (dual jet propane flames).

The observed evidence of buoyant plume dynamics reported by Moses et al. (1990), and Cetegen and Ahmed (1993), as similar as Yuan et al. (1994), found such similar oscillatory behavior in visible flames. Merely, the different scale of oscillation frequency presented is because the reactive case has local chemical reaction to sustain the fluid motion continuously accelerating along the visible flame, but deceleration occurs for the case of the non-reactive caused by cooling effect of the contamination of entrained fresh air. More likely, substantial ought to be vortex-dynamical perspective. For merging behavior of dual/multiple flames, configurations of burners were studied and deduction made by Baldwin et al. (1964) and Baldwin (1968), was about the entrained-air controlling aspect. This insinuates the influences of how aligned the vortices in the system behaves. For both of the small and large scale of fires, the degree of their interaction is dependent on their respective timescale [Bray, 1996]. There have many past works dedicated to the changes of height and radiant intensity in term of merging flames [Weng et al., 2004, Weng et al., 2015; Miklavcic & Wichman, 2016; Nagamine et al., 2017], but transition of dynamic modes of flames has less attention. The transition ought to be cause of shear-layer instability so that synchronized configuration of dual jet diffusion flames can be transferred by controlling the stream velocity. By introducing coflow technique, the flame shape could be changed by controlling the inner stream velocity [Ko et al., 2005]. As revealed by Wang and coworkers (2012), the flickering behavior disappears, at certain increment of air flowrate (critical velocity) and visible flame becomes stable, but the critical air flowrate to stop flame oscillating increases with fuel flowrate. By computations of Takahashi and coworkers (2007), the frequency jump occurs caused by the scale of vortex changed at near flame-base when coflow air velocity reaches certain value. Lately, Yang et al. (2019) performed 3-D numerical simulation for pool fires, Fig. 2.7, and proposed that the transition can be summarized by a modified Grashof number.

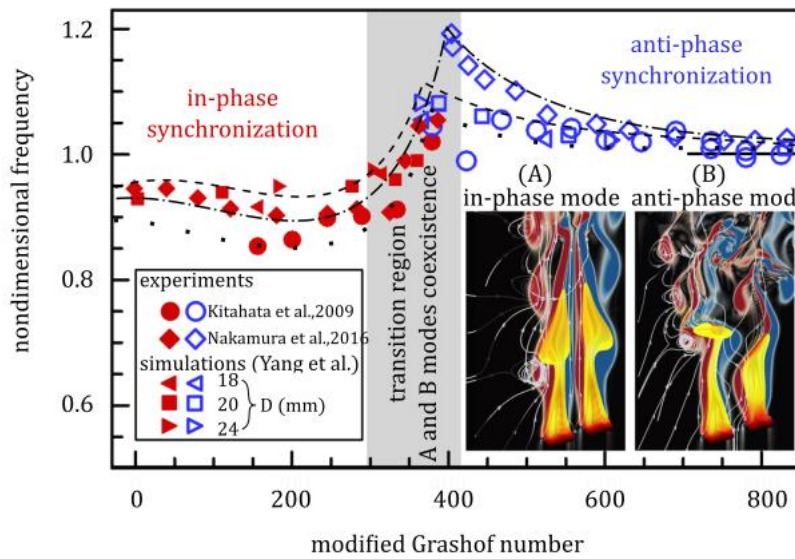


Fig. 2.7 Comparison of normalized nondimensional frequency at different modified Grashof number [Yang et al., 2019]. The red solid and blue empty symbols correspond to in-phase and anti-phase flickering modes, respectively.

Although their model successfully revealed the simple relation between the fire scale ( $D$ : pool/burner (inner) diameter) and separation length ( $L$ ) as  $D \times L^2 \sim const.$  at the transition, their working range was limited, 18 mm to 24 mm apparent diameter of fuel source. For instance, the range of the burner scale is less than factor of 3 because the target phenomena was known as highly non-linear one and the actual trend to be investigated needed a wide range, at least a factor of 5 or higher. Thus, the critical conditions based on Yang's model have been given as a "range", not "value", suggesting that the precision of the proposed strategy needs to be validated further. Further infer that velocity differences driven by buoyancy at the interface plane of inner shear layers would characterize the dynamics modes. As mentioned above, when the flames are separated at a short distance, both flames flicker at an identical phase (in-phase mode). Seemingly, they share thermal thickness and a nearly

constant frequency is found. Whereas when the flames are apart at a certain distance, the flames exhibit an asymmetric motion or anti-phase mode and the frequency decreases with the separation distance. This event shows the impact of this factor to modify velocity field in the thermal shear-layer.

### **2.3 Buoyancy Induced Shear Flow Instability**

As known from previous section, the characteristic frequencies of twin flames are depending on the impact of the modification of the systematic length scales, e.g. spacing distance of fire sources. Flow condition at outer edge of the layer confines the inside velocity field. Viscosity makes friction force slow down the buoyant velocity in flow field, more specifically, the boundary problem would be good example to think about for this instance. The boundary layer in a region of very large velocity gradients according to Newton's shear-stress law, which states that the shear stress is proportional to the velocity gradient, the local shear stress can be very large within the layer. In backdrop of rheology, vorticity reflects the instability of velocity field. It is a physical quantity generated by unstable shear-layer in dynamics of viscous fluid. For the boundary-layer concept as shown in Fig. 2.8, a flow in boundary layer ( $\delta$ ) that pressure increases in streamwise direction is an unpreferable (adverse) pressure gradient which impacts the flow lifting-off fashion, so called: separation [Anderson, 2005]. On RHS, the blowup of boundary layer shows the flow velocity changes as function of the normal distance (spanwise) varying from zero at the surface to the full inviscid-flow value (0.99 of oncoming free-stream velocity) at the outer edge. The boundary-layer separation is promoted by the type of the external inviscid flow. At the point of

separation of boundary layer, there has an inflection point, beyond this point the boundary layer can simply lift off the flow resulting of circulation fashion in fluid motion.

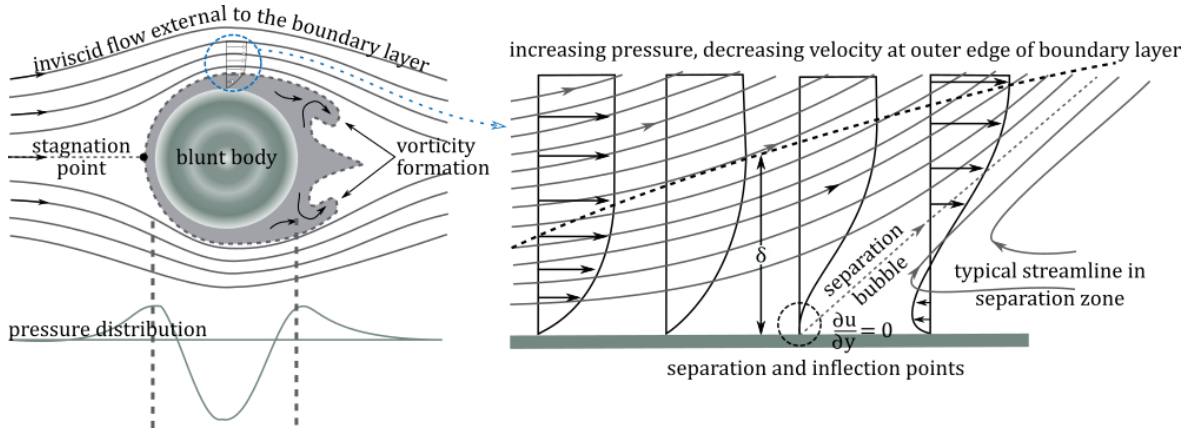


Fig. 2.8 Schematic illustration of boundary-layer separation, the blowup in the figure in on the right hand side [Ebeling, Lecture notes (2018/2019)].

The boundary-layer properties are strongly affected by the outer inviscid flow: indeed, the velocity profile within the layer is dictated by the out flow creates the boundary conditions at the outer edge of the boundary layer. On the other hand, the boundary layer itself has virtually no-effect rule because it is very thin that is if the flow separates; then the outer inviscid flow is greatly modified by the presence of the separation region. Distributions, pressure and shear-stress of which are normally and tangentially acting on the object, are responsible for the force exerting on the interface surfaces. Saying that there is a very large velocity gradients in this region. At certain points fully determined by external conditions, the fluid flow ought to separate from the interface plane that is, there ought to be a layer of fluid which, having been set in rotation by the friction of hot gases, insinuates itself into the free fluid, transforming completely the motion of the latter, and therefore playing there the

same part as the Helmholtz surfaces of discontinuity. Regarding this hypothesis, the boundary properties modified by a middle slot air-jet were experimentally examined as seen the following figure.

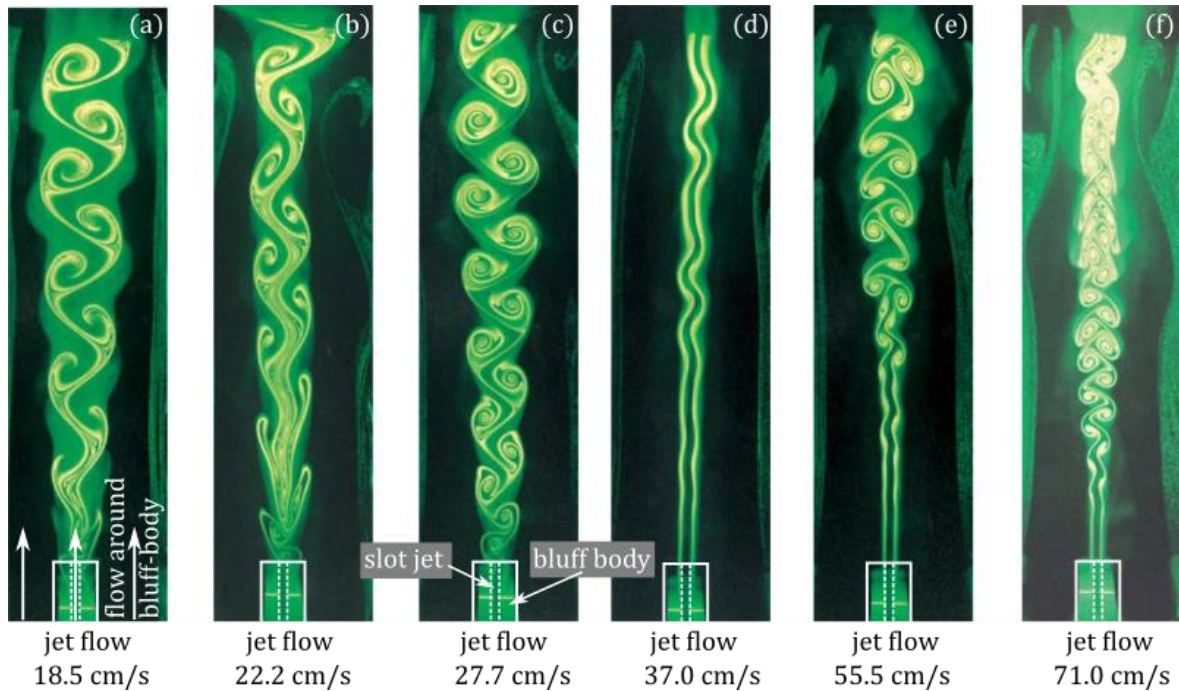


Fig. 2.9 Instantaneous photographs show the vortex structures resulting from the interaction of vortices shed from a 2D bluff body and those shed from a slot jet ( $3 \text{ mm} \times 150 \text{ mm}$ ) is located in the center of the rectangular face of the bluff body ( $15 \text{ mm} \times 240 \text{ mm}$ ) [Samimy et al., 2003].

Figure 2.9 from left to right, the velocity of the slot air-jet increases for all cases shown here, (a) to (c), the velocity of jet is smaller than the velocity of the flow around the bluff-body and vice versa as for such cases: (d) to (f). In the first three photographs starting from the left, the velocity of the jet is smaller than the velocity of the flow around the bluff-body. At

smaller jet velocity, vortex orientation is found in counterclockwise. For an averaged air jet velocity of 18.5 cm/s, the alternating vortex structures shed from the 2-D bluff body are evident after about 5 bluff-body widths downstream. Once the jet velocity is most equal to the flow around the bluff body as demonstrated by the (d) of 37 cm/s jet velocity. The shear layer velocities of the jet and wake are nearly equal and the Kelvin–Helmholtz instability does not grow rapidly, rather, a wavy structure is observed. At this stage, the Vortex Street is altered in switching orientation. The coflow depicted in the preceding, can hinder/promote such that change in flow structures and viscosity is occasionally considered as a primarily stabilizing mechanism for laminar flow [Drazin, Introduction to Hydrodynamic Stability (2002)] At higher velocities (e)(f), the vortex structures from the jet begins to dominate the flow field as noted by the change in the direction of rotation of the vortices, clockwise, the wake from the bluff body is significantly modified. According to what found by Jiang and Luo (2000) studied combustion-induced buoyancy effects of an axisymmetric reactive plume by numerical simulation. Three types of vortical structures were observed: first-case ( $Fr > 5$ ); the jet preferred mode because of the inner vortical structures predominates the instability, second-case ( $Fr < 2$ ); buoyancy induced by combustion the outer vortical structures governed the reactive flow instability, and third-case ( $2 \geq Fr \leq 5$ ); the coexistence of inner and outer vortical structures dominated the flow field. The boundary layer (Fig. 2.10 (top)) of both absolute and convective instabilities had been classified by the linear stability analysis model (bottom). A simple vortex sheet model, both varicose and sinuous of 2-D jets and wakes that allow a quick evaluation of the effect of variable density on their stability characteristics, thereby refers to symmetry of the vortex sheet deformations.

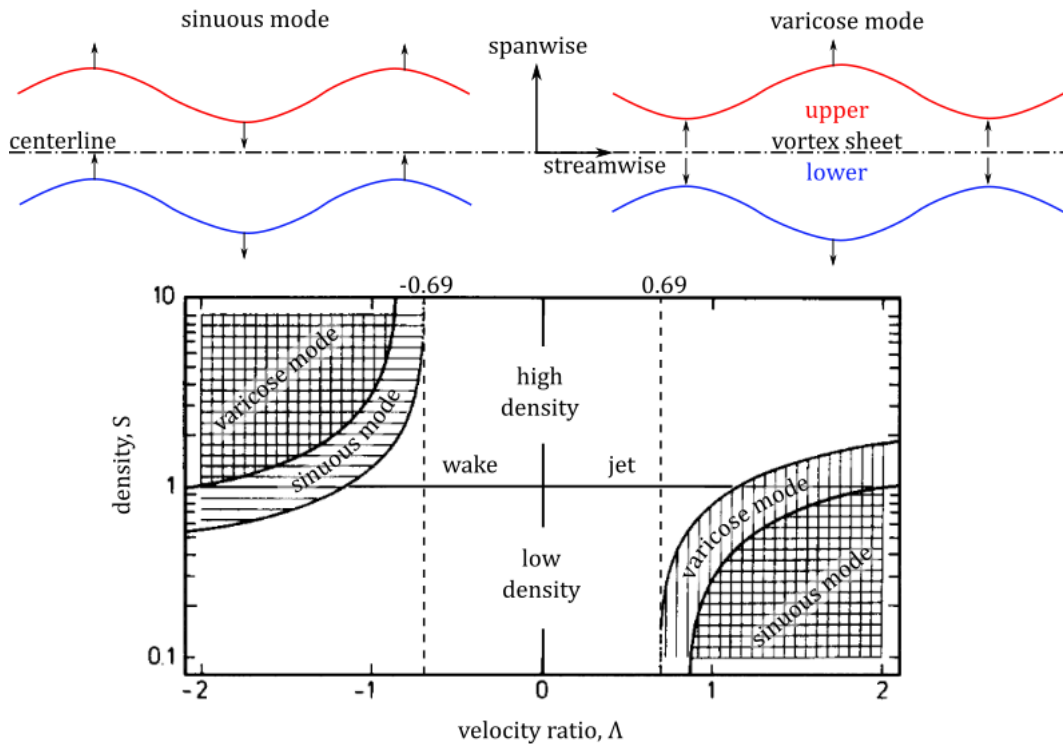


Fig. 2.10 (top) Sinuous and varicose modes defined in terms of vertical perturbation velocity. (bottom) Stability properties of the two-vortex-sheet model as a function of density ratio and velocity ration. Horizontal hatching (absolute instability of sinuous mode); Vertical hatching (absolute instability of the varicose mode) [Yu & Monkewitz, 1990].

For varicose mode, the transverse deformations of the two vortex sheets are in opposite directions, while they are in the same direction for sinuous mode (top). 2-D jets become absolutely unstable as the computed density ratio below  $S = 0.95$  consistent with the experimental observations in round jet. The onset of self-excited oscillations was around  $S = 0.9$  given  $S = \frac{\bar{\rho}_c^*}{\bar{\rho}_\infty^*}$  and  $\Lambda = \frac{\bar{u}_c^* - \bar{u}_\infty^*}{\bar{u}_c^* + \bar{u}_\infty^*}$  where  $c$  represents at the centerline of streamwise and  $\infty$  represents at the free-stream velocity. It clearly displays that the symmetry and allows three broad conclusions qualitatively as well as validly under the continuous velocity and

density profiles. “*First*”, absolute instability is suppressed and it does not appear at any density ratio if  $|\Lambda| \leq 0.69$  because of sufficiently shallow wakes as well as in jets with sufficient coflow. In contrast, when the  $|\Lambda|$  is increased, the absolute instability is promoted corresponding to counterflow either in the wake or exterior to the jet. “*Second*”, in the wake region the sinuous mode first encounters and absolutely unstable, while in the jet region, the varicose mode is first observed. “*Third*”, heating- or lowering-fluid density yields the opposite effects. In the jet, the absolute instability (axisymmetric self-excited oscillation) is enhanced by low density, while the suppression occurs in case of the wake consistent with the observed experimental evidence done by [Monkewitz et al., 1990; Sreenivasan et al., 1989]. Regarding the target phenomena, flow-like wake at low Reynolds number found in first group in Fig. 2.9 (a)-(c), matching wake region in Fig. 2.10 (bottom) for denser-fluid of wake absolute instability, is potential flow characteristics of interest.

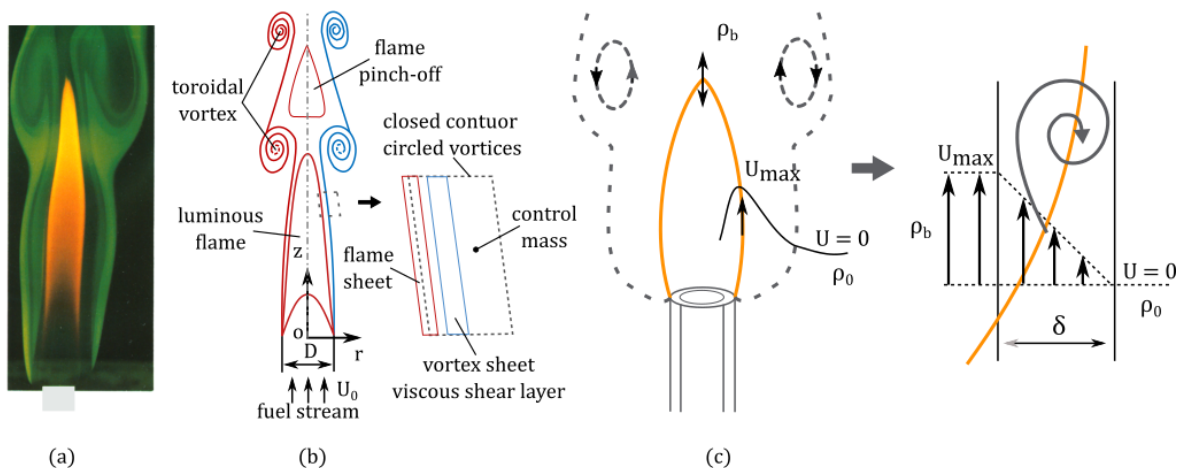


Fig. 2.11 (a ) Instantaneous image photograph of planar visualization of methane jet diffusion flames:  $Re = 110$ ,  $D = 11$  mm [Chen et al., 1988]; (b) Schematic of the vortex sheet for the growth of the toroidal vortex in a laminar diffusion flame, assuming the zero thickness of flame and vortex sheets exaggerated for illustration [Xia & Zhang, 2018]. (c) Sketch of the profile of vertical velocity appearing a maximum close to the reaction zone. Representation of the thermal shear-layer between  $U_{max}$  and the surrounding air [Durox et al., 1997].

In combustion science, dynamics of flickering diffusion flames manifests the absolute instability (low density region in Fig. 2.10) of the hot gases ascending column. This phenomenon is related to buoyancy being characterized in terms of pressure and gravitational force and it had been confirmed by varying the ambient pressure [Yuan et al., 1994; Durox et al., 1997]. These measurements are entirely in agreement with a theoretical model based on the hydrodynamic instability of the layer (thermal-layer thickness as shown in Fig. 2.11 (c)) of burnt gas under the influence of buoyancy. The outer region next to flame

luminosity is thermally boundary layer defined as vortex-sheet where dynamics of viscous fluids is under the law of Newton 'viscosity'. The frequency of shedding toroidal vortex was found to be related to frequency of flame puffing [Chen et al., 1988]. The link between flame dynamics and vortex-dynamical principle was done by Xia and Zhang, (2018). They took this concept to fill this blank and they presented that vorticity formation is only dictated by the vertical distance along which a vortex is formed until emitting point. This is similar to previous suggestion done by Betchov and Szewczyk (1963), the mathematical study of the laminar transitioning to the turbulent of a shear layer away from solid walls found that occurrence of mode change began at the Reynolds number reached order of 150 of a viscous incompressible fluid flow characteristics. The Reynolds number, whose function consists of the flowing length, oncoming free-stream velocity, and kinematic viscosity characterizes the flow-field of fluids. So long as the incident stream-flow is not turbulent, the viscous terms in the equation of motion are negligible, but inside the boundary layer (Euler's equation), and the considered flow has the same profile as for an ideal fluid. The length scale can be any aspects/orientations as long as it can properly characterize the motion of the fluid, i.e. either in the direction of or in perpendicular to a stream. As illustrated by Fig. 2.11 (c), the distance used is in spanwise for studying the thermal layer formed by jet diffusion flame. Past works done by Yuan et al. (1994) and Durox et al. (1997), taken the thermal thickness ( $\delta$ ) for studying toroidal vortex formation. Evidence found inflection points appears in boundary layer of flow field; presence of maximum convective velocity occurs near reaction zone [Buckmaster et al., 1983; Lingens et al., 1996]. Vorticity production due to gravity torque in Eq. (1.12) becomes dominated to strengthen the vortices; meanwhile, the annihilation term must be diminished and eventually come up a consequent rotation in fluid motion.

## 2.4 Nondimensional Analysis

As mentioned in section 2.2, the drawback of their work is the computational cost, saying that large computational domain consuming such huge time required by DNS mode for 3-D numerical computation. The model proposed by Yang and coworkers (2019), will be upgraded by introducing a wider range in order of 5 of fire-size-source through a carefully constructed experiment. For our precise experiment construction for large burner investigation, this purpose could be attained by systematic examination. So a technique of generalizing the experimental results is scale modelling. It is both essential and practical means of obtaining general results. This, in reality, is because the complexities of fire precluding complete mathematical solutions. Consequently, a realistic scale is reduced to laboratory scale for observation. To do so, the significant dimensionless parameters have to be derived from the governing differential equations. The law of scaling for the system considered is established. Even though the exact quantitative results cannot be expected, the insight on the mechanism and behavior of the system phenomena become satisfactory. This one simplest, yet most powerful tools is conducted to study the transition observed in the system of single buoyant flickering flame. At the critical condition, phenomenon is suspected that shear and buoyancy forces ought to be taken in account for analysis. Therefore, the equation of motion to investigate the target phenomena is conservation of momentum. Regarding the dimensionless groups done by James G. Quintiere (1989) for scaling application in fire research corresponding to the combustion theory written by Forman A Williams (1995). Nondimensional form of conservation of momentum is given by:

$$\omega \frac{\partial \hat{\mathbf{u}}}{\partial \hat{t}} + \hat{\mathbf{u}} \cdot \hat{\nabla} \hat{\mathbf{u}} = -\frac{1}{Ma^2} \frac{\hat{\nabla} \hat{p}}{\hat{\rho}} + \frac{1}{Fr} \sum_i Y_i \hat{\mathbf{f}}_i + \frac{1}{Re} \frac{\hat{\nabla} \cdot \hat{\mathbf{T}}}{\hat{\rho}} \quad (2.1)$$

Important characteristics quantities for dimensionless variables to form the nondimensional parameters are listed as follows:

$$\hat{u} = \frac{u}{u_0}; \hat{\rho} = \frac{\rho}{\rho_0}; \hat{x} = \frac{x}{l_0}; \hat{t} = \frac{t}{\tau}; \hat{f}_i = \frac{f_i}{g_0}; \hat{p} = \frac{p}{p_0} \quad (2.2)$$

$$\omega = \frac{l_0}{u_0\tau}: \text{Ratio of flow time to evolution time or Strouhal number } (\tau = 1/f)$$

$$Ma = \frac{u_0}{\sqrt{p_0/\rho_0}}: \text{Mach number (ratio of velocity to speed of sound)}$$

$$Fr = \frac{u_0}{\sqrt{g_0 l_0}}: \text{Froude number (ratio of kinetics energy to gravity potential)}$$

$$Re = \frac{\rho_0 u_0 l_0}{\mu_0}: \text{Reynolds number (ratio of momentum to viscous force)}$$

Section 2.3, the literature shows when flame dynamics purely dominated by buoyancy the outer vortical structures governed the reactive flow instability for single-flame system. Most recently, Xia group (2020) showed the occurrence of flame asymmetry is as a function of Reynolds number. So far Yang group (2019) had proposed an analytical model to characterize the transition of dual pool flames synchronization as found in the following equations. The combined spacing distance and size (equivalent diameter) of fire source were employed as system characteristic length. The nondimensional Grashof number was modified and they were well-characterized the whole phenomena.

$$f = F(D, g, L, v_A) \quad (2.3)$$

$$\frac{f}{f_s} \sim \frac{f}{\sqrt{g/D}} = G\left(\frac{L}{D}, \frac{\sqrt{gD^3}}{v_A}\right) = G(\alpha, Gr^{1/2})$$

Let's say that the condition at the transition is a function of these two nondimensional parameters.

$$\Lambda \sim \alpha^n Gr^m = \left[ \frac{L}{D} \right]^n \left[ \frac{gD^3}{v_A^2} \right]^m \quad (2.4)$$

Apply this at the critical point (crt) and impose mean convective flow ( $U_b$ ) induced by buoyancy is scaled as  $U_b \sim \sqrt{gD} \rightarrow U_b^2 \sim gD$ , and then hypothesize Froude number becomes unity at this stage of flow regime. By considering the exponents of the  $D$ , we can find the  $m$  as a function of the  $n$  so that the  $m$  can be eliminated from the RHS of Eq. (2.4). Then we can be able to write:

$$\begin{aligned} \Lambda_{crt} &\sim \left[ \frac{L_{crt}}{D} \right]^n \left[ \frac{U_b^2 D^2}{v_A^2} \right]^m \sim \frac{L_{crt}^n U_b^{2m} D^{3m}}{D^n v_A^{2m}} \\ \Lambda_{crt} &\sim \frac{U_b^{2(n+1)/3} L_{crt}^n D^{2(n+1)/3}}{v_A^{2(n+1)/3} D^n} \sim \left[ \frac{L_{crt}^{(n-2)/3}}{D^{(n-2)/3}} \right] \left[ \frac{U_b^{2(n+1)/3} L_{crt}^{2(n+1)/3}}{v_A^{2(n+1)/3}} \right] \\ \Lambda_{crt} &\sim \alpha^{(n-2)/3} Re_L^{2(n+1)/3} \end{aligned} \quad (2.5)$$

Exponent “ $n$ ” can be obtained from experimental analysis through  $D$ - $L_{crt}$  plane found in chapter 4. Observe through the analytical above, Grashof number can be transformed to Reynolds number which insinuates the instability of inner shear-layer vortices. Thus thermal thickness formed by jet flames scaled by separation distance and the diameter of burner is suspected to play the role to change the dynamic mode of flames.

For comprehensive understandings, the concept of similarity to link the different systems is made for interpretation of the mechanism of mode change observed in relative single small scale (pool/jet) fire. Similarity in combustion dynamics pertaining of force driving

phenomena is the key. In reality, there are three similarities, e.g. geometric, dynamic, and kinematic, as common rule. Nevertheless it seems impossible to be retrained all of them. Forces driven the target phenomena, e.g. buoyancy and friction, dominate the shear flow structure. Through its viscosity transport property, fluid is accelerated in gravimetric flow-field caused by buoyancy effect (i.e. lighter/hot fluid in term of single flame), but deaccelerating fashion made by heavier/cold surroundings slows down the velocity of flowing fluid. Unbalancing fashion of shear layer velocities crossed the layer possibly perturbed by disturbances (either far downstream or upstream regions) causes fluctuation growing in velocity field when the time goes by. The dynamic similarity is conducted to deals with the transient phenomena measured by characteristic scale, in essence, the equality of all characteristic variables must be retained for two systems. Meanwhile, the characteristic length is used to keep the target phenomena geometrically similar to streamline point of view in velocity field [Saito, JSME TED (2008); Chitsomboon, ME-NETT15 (2001)].

$$Force = G(\rho, L, V, \mu, g, p) \quad (2.6)$$

$$d[M] = d[\rho] d[L]^3 \rightarrow \rho L^3$$

$$d[L] = d[L] \rightarrow L$$

$$d[t] = d[L]/d[V] \rightarrow LV^{-1}$$

$$force = mass \times acceleartion$$

$$F = \frac{MV}{t^2} = MLt^{-2} = (\rho L^3)(L)(LV^{-1})^{-2} = \rho L^2 V^2 \quad (2.7)$$

*pressurer = force/area*

$$P = \frac{F}{L^2} = \frac{MLt^{-2}}{L^2} = ML^{-1}t^{-2} = (\rho L^3)(L)^{-1}(L/V)^{-2} = \rho V^3 \quad (2.8)$$

*viscosity = shear stress/velocity gradient*

$$\mu = \frac{y\tau}{u} = \frac{(L)(\frac{F}{A})}{V} = \frac{(L)(MLt^{-2})}{L^2 V} = \frac{L \rho L^3 L L^{-2} V^2}{L^2 V} = \rho VL \quad (2.9)$$

Primary unit of gravity is same as acceleration so that  $\frac{g}{(V^2/L)} \rightarrow \frac{gL}{V^2} \rightarrow \frac{\sqrt{gL}}{V}$ , however, we usually use this number in  $\frac{V}{\sqrt{gL}}$  as known as Froude number. So we can rewrite the above equation as the following.

$$\frac{F}{\rho L^2 V^2} = G\left(\frac{\mu}{\rho VL}, \frac{V}{\sqrt{gL}}, \frac{p}{\rho V^3}\right) \quad (2.10)$$

In final, we can reduce the number of independent variables by taking this trick of powerful tool. The denominator indicates the characteristic scale saying that forces acting on the target object can be measured by the group of characteristic quantities. Presence of length quantity resulting in the shape of target problem can be geometrically similar. Thus the different scale of the problem can be applied. More specifically, through the world well-known the prominent scaling for a buoyant pool/jet flames under the normal gravity, the frequency ( $f$ ) is well related to the apparent size of fire source, as given by:

$$f \sim D^{-1/2} \quad (2.11)$$

There are two nondimensional parameters: Strouhal number ( $St$ ) and Froude number ( $Fr$ ). The unsteady problem is usually explained through the  $St$  and  $Fr$  is undertaken in account

when the gravitational force dominated the phenomena. For example, numerous past studies suggested that pulsating behavior of buoyant (pool) fires is characterized by the inverse Froude number.

$$St \sim 1/Fr \quad (2.12)$$

So sophisticated engineers had wisely developed this technique which it had been evolved to be the fundamental theory so that there has no longer effort in long run (time-consuming) of repeating the experiments, costly expenses. Dimensionalized method has must more restriction than the nondimensionalization. By introducing the nondimensionalization, every additive term in an equation can be ensured that they are nondimensional. The nondimensional becomes rendered; the dimensions of which those product are same, for which the terms will have been divided by a group of variables and constants. In addition, in terms of the nondimensional terms in the equation are of order of unity, the equation is called “normalized”. Though this concept, the best curved-fitting experimental data may be presented and summarized in a single set or single line which is very fruitful for catching the physics of phenomena [White, Fluid Mechanics (2002)]. Let’s introduce some an important nondimensional parameters as the following topics.

#### **2.4.1 Reynolds Number, $Re$**

The  $Re$  which is the basis of much physical modelling is now universally employed in the correlation of experimental data on frictional pressure drop and heat and mass transfer in convective flow. It is employed to characterize when the viscous flowing fluid changes its flow-regime to transition between the laminar and turbulent. It is always important and this

number cannot be ignored if flow regions of high-velocity gradients are considered. Confined or unconfined flow can be characterized by this number, but it becomes insignificant at which the regions are far away from solid surfaces, jets, or wakes. The  $Re$  characterizes the relative importance of the momentum transport by convection ( $\rho U^2$ ) and by viscous diffusion ( $\mu U/L$ ) [Reynolds, 1883]. In general terms, it is defined as

$$\frac{\text{convective flux of momentum}}{\text{diffusive flux of momentum}} \approx \frac{\rho U^2}{\mu U/L} = \frac{UL}{\nu} = Re \quad (2.13)$$

Alternatively, another way given Reynolds number, it can also considered as the ratio between the characteristic transport times by diffusion and convection along distances of order of magnitude  $L$ . since  $\nu$  represents the diffusivity of momentum of order  $L^2/\nu$  and the characteristic time for convection is then of order  $L/U$  which presents the time for covering the distance  $L$  at the average velocity  $U$  of the flow. Considering altogether, we can find the ratio of the characteristic times as

$$\frac{\text{characteristic diffusion time}}{\text{characteristic convection time}} \approx \frac{L^2/\nu}{L/U} = \frac{UL}{\nu} = Re \quad (2.14)$$

where  $\nu = \frac{\mu}{\rho}$ ,  $\nu$  is kinematic viscosity,  $\rho$  fluid density,  $\mu$  fluid viscosity,  $U$  is fluid velocity and  $L$  the characteristic length [Guyon et al., Physical Hydrodynamics (2017)].

#### 2.4.2 Froude Number, $Fr$

$Fr$ -number becomes significant when we are dealing with free surface flow. This dimensionless number is an important value in flow analysis to which the flow is exposed to

the Earth's atmosphere. Physical meaning of interpretation can be done in the same way as Reynolds number. Generally, we starts to first square it and then multiply it by the density and the area of flowing fluid ( $\rho AVV/\rho ALg$ ). Through the order of magnitude analysis, we can interpret as the value of the inertia against the weight of fluid itself. However, due to the formation of characteristic scale for measuring the gravitational force, it is found that the gravity should be measured by values of  $V^2/L$ , so that  $gL/V^2$  shall be utilized to represent the value of Froude number. In terms of historical reasons, however, it is preferable to measure the square root of the inverse value itself ( $V/\sqrt{gL}$ ) and it should be interpreted that the gravity makes fluid attach to the Earth' surface. In case of value of the characteristic gravity looks too small (Froude number becomes high-value), the surface of the flowing fluid that is open to the atmosphere might jump, e.g., appearing the hydraulic jump. The inertia can overcome the gravity influence [Chitsomboon, ME-NETT15 (2001)].

$$Fr = \frac{F_I}{F_g} = \frac{\rho L^2 V^2}{\rho g L^3} = \frac{V^2}{gL} \quad (2.15)$$

$$\frac{\text{inertial force}}{\text{gravitational force}} \approx \frac{V}{\sqrt{gL}} = Fr \quad (2.16)$$

Where  $F_I$  and  $F_g$  are defined as the inertial and gravitational forces [Somchai & Kaewnai, Fluid Mechanics (2014) P.355]. The system of which the gravity and inertia play an important role predominating over, the phenomena shall be driven by frictional and gravitational forces. We need to logically judge whether the frictional force or gravitational force shall be selected [Cengel & Cimbala, Fluid Mechanics (2006)].

### 2.4.3 Strouhal number, $St$

In general, oscillating flow is physically interpreted by utilizing the Strouhal number. The  $St$  represents the oscillations of the flow due to the inertial forces relative to the changes in velocity due to the convective acceleration of the flow field. To study the oscillating unsteady fluid flow dynamics involves vortex shedding behavior as we often see to investigate von Karman Vortex Street, oscillating flow mechanism.

$$\frac{\text{characteristic flow time}}{\text{period of oscillation}} \approx \frac{fL}{v} = St \quad (2.17)$$

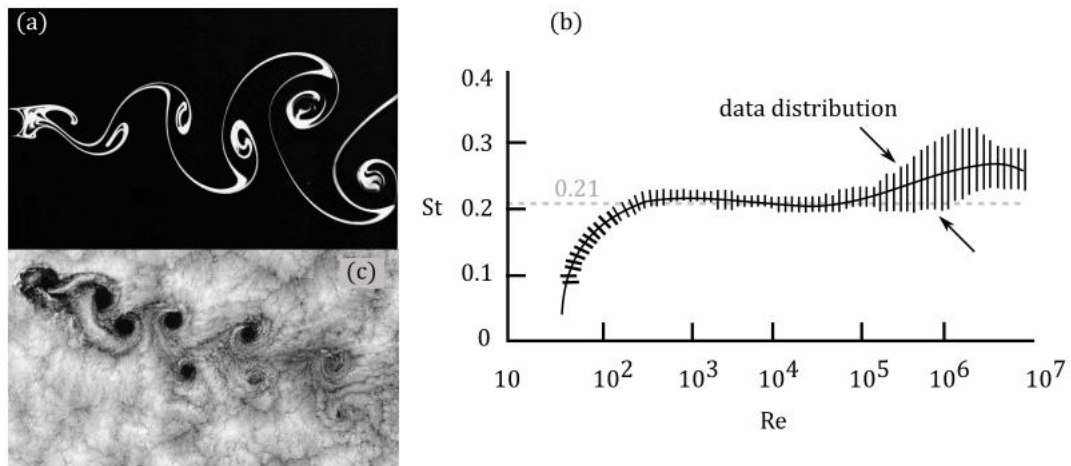


Fig. 2.12 (a) Visualization of “Kármán Vortex Shedding”, flow patterns near a cylinder at various: 10 mm diameter of cylinder, 14 mm/s of water flowing velocity,  $Re = 140$  [Dyke, An album of fluid motion (1982)]. (b) Measurement of flow oscillating frequency presented in nondimensional Strouhal number vs. Reynolds number [White, Fluid Mechanics (2002) P.296; Somchai & Kaewnai, Fluid Mechanics (2014)]. (c) Satellite view of clouds off the Chilean coast show a unique pattern called a “von Karman vortex street”, Image and caption courtesy Bob Cahalan, NASA GSFC [Guyo et al., Physical Hydrodynamics (2017) P.58].

Some flows we think that it is completely steady flow, but it actually becomes a swaying flow which the periodic shedding frequency is depending upon the  $Re$  [Somchai & Kaewnai, Fluid Mechanics (2014) P.346]. As frequently encounter in real-life, periodic flowing fashion is always observed when viscous fluid flowing accord a bluff body formed shearing boundary layers around a solid body; once free stream velocity reaches certain value, the shearing layers become unstable; they are alternatively shed into the far stream region at the downstream and dissipated like the street of vortices, so called von Karman Vortex Street. For example, the flow patterns near the cylinder when free stream velocity is set,  $U$ . Vortex shedding at the rear of cylinder shows periodic motion which falls in  $10^2 < Re < 10^7$ . From the directly measured the Strouhal number from experiment, the value was found that it is approximately 0.21 in averaged ( $fL/2\pi U \approx 0.21$ ) shown in Fig. 2.12. Resonance would be serious if the frequency of vortex emitted behind the cylinder approached the cylinder frequency itself.

#### 2.4.4 Grashof Number, $Gr$

The  $Gr$  is a nondimensional parameter used in the correlation of heat and mass transfer due to thermally induced natural convection at a solid surface immersed in a fluid [Hewitt et al., Process Heat Transfer (1994)]. It is defined as

$$\frac{\text{buoyancy force}}{\text{restraining force}} \approx \beta \Delta T \frac{gL^3}{\nu^2} = Gr \quad (2.18)$$

where  $\beta$  [ $\text{K}^{-1}$ ] is coefficient of expansion of the fluid,  $\nu$  [ $\text{m}^2\text{s}^{-1}$ ] is kinematic viscosity of the fluid,  $g$  [ $\text{m s}^{-2}$ ] is acceleration due to gravity,  $L$  [ $\text{m}$ ] is the characteristic length and  $\Delta T$  [ $\text{K}$ ] is temperature difference between the surface and the bulk of the fluid.

The  $Gr$  plays the same role in free convection that the  $Re$  plays in forced convection. In practice, it is the ratio of forcing (buoyancy) forces, due to spatial variation in fluid density caused by temperature differences, to restraining (viscous) forces due to the viscosity of the fluid

Derivative can be done by considering the forces acting on a small element of fluid of volume  $L^3$ , the buoyancy force,  $F_b$ , on this element has the magnitude  $gL^3\Delta\rho$ , where  $\Delta\rho$  is the difference in density between the element and the surrounding fluid. The order of magnitude of the viscous force,  $F_v$ , on the element is  $\mu UL$ , where  $\mu$  is the dynamic viscosity of fluid, and  $U$  the velocity of the element relative to the surrounding fluid. Hence,

$$\frac{F_b}{F_v} = \frac{gL^3\Delta\rho}{\mu UL} \quad (2.19)$$

By equating viscous and momentum forces, the order of magnitude of the velocity,  $U$ , can be approximated as

$$\mu UL = \rho U^2 L^2$$

$$U = \frac{\mu}{\rho L} \quad (2.20)$$

Substituting velocity into the ratio of buoyancy to viscous forces and using the relationship,  $\Delta\rho = \beta\rho\Delta T$ , then we can derive

$$\frac{F_b}{F_v} = \frac{gL^3\Delta\rho}{\mu\frac{\mu}{\rho}L} = \frac{gL^3\rho\Delta\rho}{\mu^2} = \frac{\Delta\rho}{\rho} \frac{gL^3}{\nu^2} \quad (2.21)$$

$$\frac{F_b}{F_v} = \frac{\beta\rho\Delta T}{\rho} \frac{gL^3}{\nu^2} = \beta\Delta T \frac{gL^3}{\nu^2} \quad (2.22)$$

Since Reynolds number represents the ratio of momentum to viscous forces, the relative magnitudes of  $Gr$  and  $Re$  are an indication of the relative importance of natural and forced convection in determining heat transfer. Forced convection effects are usually insignificant when  $Gr/Re^2 \gg 1$  and conversely natural convection effects may be neglected when  $Gr/Re^2 \ll 1$ . When the ratio is of the order of one,  $Gr/Re^2 = 1$ , the combined effects of natural and forced convection have to be taken into account.

## 2.5 Summary

In considering altogether, the target phenomena, the transition of dynamic mode of non-premixed jet flickering flame(s) in term of buoyancy driven instability, would highly be sensitive to the modification of fire scale ( $D$ ) and fuel flowrate ( $Q$ ), and separation distance ( $L$ ). These three global potential parameters are systematically examined experimentally as well as numerically. The conditions at the edge of boundary layer dictates the inside field of velocity vector. Instability mechanism is buoyant induce velocity and viscous fluid of inner shear layers for twin-flame system which is applicable to describe the change of dynamic mode in single-flame system via similarity concept under scaling law. Pre-examinations are performed and seriously judged to ensure that the target phenomena is primarily dominated by buoyancy, i.e. an isothermal helium flow, artificial ceiling, repeatability check etc., including simplification of the problem.

## Chapter 3

### Methodologies and Related Theories

Based experimental investigation in a systematic manner is selected to gain the insight physics to understand the mode change in twin-flame system. By further interpretation, the transition found in the single-flame system can properly be described. Therefore the dynamics of flame behaviors (both systems) is globally observed by frequency measurement and direct photography accompanied with an optical visualization technique (Schlieren imaging). Characteristic quantity such as frequency is monitored by fine k-type thermocouples mounted at very near burner exit to collect the time signals of temperature variation. The analysis of frequency is done by introducing Fast Fourier Transform (FFT). The numerical simulation (FDS: Fire Dynamics Simulator), version 6.5.3, free and open-source software provided by the National Institute of Standards and Technology (NIST) of the United States Department of Commerce, is responsible for the time-dependent of direct numerical simulation method.

#### 3.1 Laboratory Experiments

Regarding research objectives summarized in the preceding (section 2.5), two approaches are conducted for investigation: first, system of frequency measurement; second, system of optical (Schlieren imaging) photography. The investigation is performed under the condition of  $Fr < 1$  (Table 3.1), suggesting that buoyancy purely controls the phenomena (note that Froude number is defined as jet ejecting velocity, burner diameter and gravity acceleration,

$Fr = V/(gD)^{1/2}$ ). The range of fuel flowrate ( $Q$ ), burner diameter ( $D$ ), and separation distance ( $L$ ), varied in this study is  $Q \leq 3000$  cc/min,  $D \leq 55$  mm and  $0 \leq L \leq 100$  mm, respectively.

Table 3.1 Calculation of Froude number ( $Fr$ ) adopted in this dissertation

$Q$ (cc/min)	$D = 10$ mm	$D = 18$ mm	$D = 30$ mm	$D = 45$ mm	$D = 55$ mm
500	0.279	0.076	0.022	0.008	0.005
1000	0.559	0.152	0.043	0.016	0.010
1500	0.838	0.227	0.065	0.024	0.014
2500	1.397	0.379	0.109	0.039	0.024
3500	1.956	0.531	0.152	0.055	0.033

The order of 7 of fuel flowrate and of 5 of size of fuel source are adopted to examine the target phenomena with highly non-linear instability. In the literatures, the phenomena would be suggested as two-dimensional problem under the considered range of the designed experimental conditions. Thus this hypothesis will also be confirmed before productive performing in order to ensure that thermocouple is placed at the right position, including the camera in the system of optical image visualization. It should be positioned properly to gain the fundamental essence of flame dynamics. Data acquisition set at 100 sampling points per second is sufficient to track flame flickering behavior because the target phenomena are ranging in oscillation frequency from 10 Hz to 20 Hz.

### 3.1.1 Experimental Apparatus

The schematic experimental apparatus used in this work is shown in Fig. 3.1 and instant image photography of single and twin burner(s) shown in Fig. 3.2 (a) and (c) responsible to the adopted cylindrical tubes (b). In Fig. 3.1, the three main parts are separately introduced as follows: first, circular burner(s) and optical stage presented in the black-line; second, the green-line indicates the flowrate controlling section; third, the blue-line represents the wiring set of acquisition.

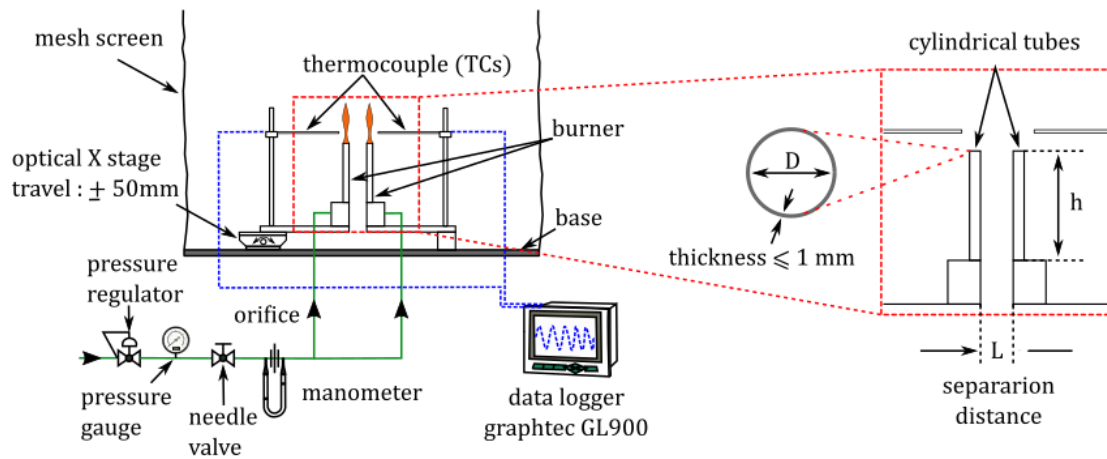


Fig. 3.1 Schematics of experimental apparatus and definition shown in blowup section.

In order to manufacture a hand-made thermocouple, this is most preferably referred to Takuya' dissertation, appendix B (2020). Basically four sizes of circular burner-shape (the inner diameter equals 10-, 18-, 30-, 45 mm shown in Fig. 3.2 (b)) are made of stainless steel (SUS304) with equal to or less than 1 millimeter thickness. For example, the case of 55 mm diameter (e),(f) was done by roll forming of stainless sheet with 0.3 millimeters thickness. Materials is a Japanese JIS standard with 18% Cr and 8% Ni contains. All burners here have

150 millimeters in height. For more details of drawings, please freely browse in appendix-A. All experiments were performed at in the open, quiescent environment surroundings in the laboratory. As shown in Fig. 3.3, the dimension of test section is 0.9 m (width)  $\times$  0.7 m (depth)  $\times$  0.9 m (height).

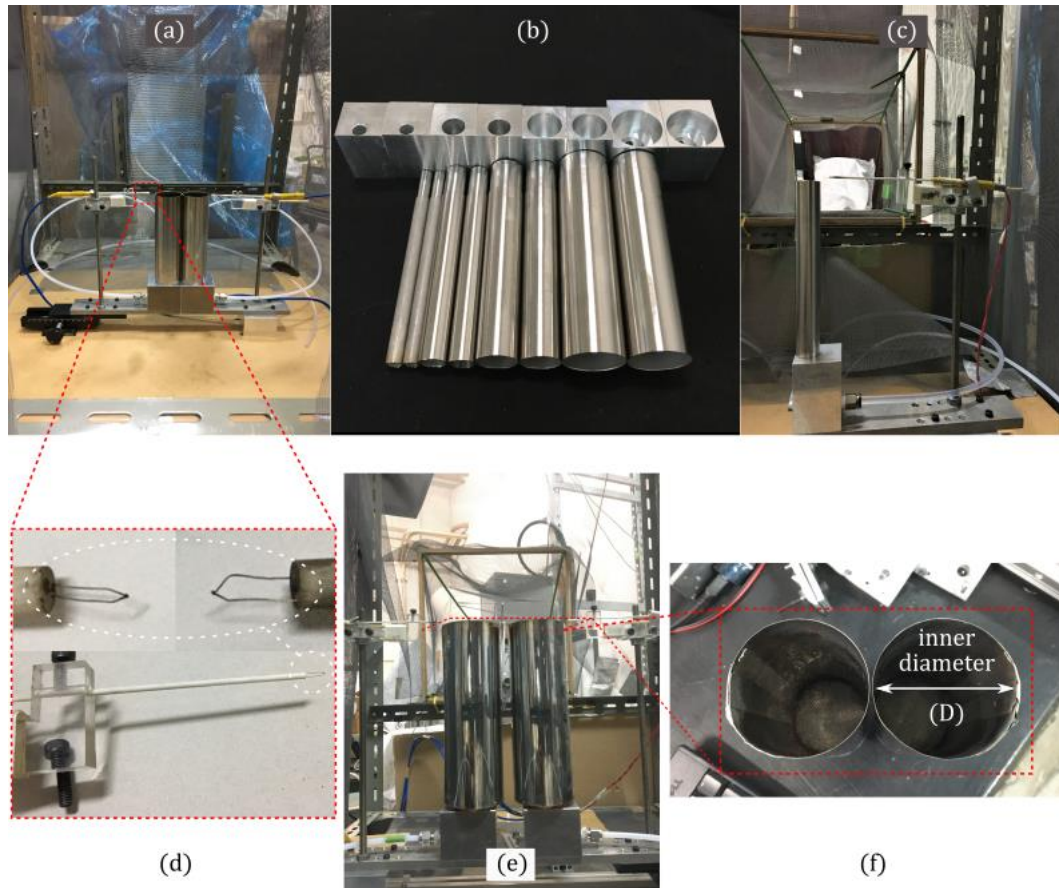


Fig. 3.2 Typical configurations of round-shape burner: (a) twin-flame system; (b) four pairs of identical circular burner made of SUS304 of cylindrical tubes, from left to right  $D = 10$  mm, 18 mm, 30 mm 45 mm; (c) single-flame system; (d) type-k thermocouple; (e) twin burners made of SUS304 sheet metal hand-made forming shape-rolling seaming with gas welding; (f) top-view of 55 mm diameter of cylindrical burners with 0.3 millimeters thickness.

The experiment performing was repeated for least twice to ensure the collected data of very fundamental feature. Repeatability (see Fig. 3.13) was also confirmed in satisfactory level. Sample standard deviation was adopted for uncertainty. Two identical round-shaped burners were located vertically and research grade methane gas (purity: 99.4 %) was issued upward at identical flowrate,  $Q$ . Flowrate of the methane was controlled by a controlling system (see appendix A for more detailed information), which composes of a hand-made monometer with the accuracy being approximately higher than 99%. One burner was fixed at to the floor on cantilever beam and another burner mounted on the optical stage, which enabled us to modify the burner separation length,  $L$ , within a range of 0 - 100 mm. The condition  $L = 0$  mm indicated two burners were perfectly aside in parallel, in other words, the burner axes are at the distance of burner diameter ( $D$ ). Multi-layered mesh screens surrounded the apparatus in order to suppress any disturbance from the ambient surrounding to bother the fundamental physics of flame dynamics. Ignition was made using a burner torch, and the system allowed to stabilize for a while before recording data. The fine thermocouples to capture the time-variation signals by fine thermocouples (TCs: k-type, junction dia.: 0.25 mm, Fig. 3.2 (d)), were equipped near the burner exit to record the time-variation of field temperature signal via data logger (Graphtec GL900) at the sampling rate of 10 millisecond. Harmonized frequencies,  $f$ , were obtained by analyzing the TCs' signal by operating Fast Fourier transformation (FFT).

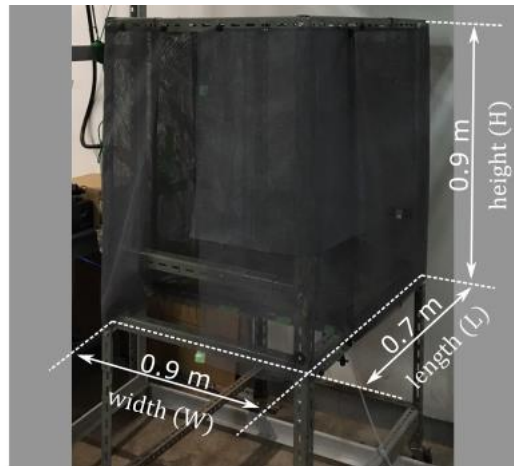


Fig. 3.3 Instantaneous photograph of the experimental test section.

### 3.1.2 Observation of Influences of Surrounding Mesh



Fig. 3.4 Instantaneous photograph of various encompassments of mesh-screen for the experimental test section.

Proper judgment and data acquisition of very fundamental dynamic mode are very important to convey the useful academic information. Hence the compartment size and the number of mesh-screen were precisely performed. Comparison of the present investigation to previous suggested fundamentals was attained. Figure 3.4 typically illustrates the applied dimensions of compartment test-section corresponding to three cases shown in Table 3.2.

Table 3.2 Dimension of experimental test section

case	dimension	layer of mesh	fuel flowrate
	W × L × H	quantity	cc/min
1	0.2 × 0.7 × 0.9	2	1000
	0.4 × 0.7 × 0.9	2	1000
	0.6 × 0.7 × 0.9	2	1000
2	0.6 × 0.7 × 0.9	2	500
	0.6 × 0.7 × 0.9	2	1000
	0.6 × 0.7 × 0.9	2	2000
3	0.2 × 0.7 × 0.9	2	1000
	0.2 × 0.7 × 0.9	4	1000
	0.2 × 0.7 × 0.9	4	2000

Figure 3.5, the characteristic frequency is obviously affected by the modification of compartment dimension as demonstrated by case 1. Meanwhile, weak sensitiveness was found by modifying fuel flowrate and the number of mesh-screen (cases 2 and 3). In case 3, the dimension of compartment is smallest; the frequency slightly increases. This could be the cause of independent distribution of pressure pressurized jet flames in radial direction because thermal boundary is disturbed by surrounding mesh.

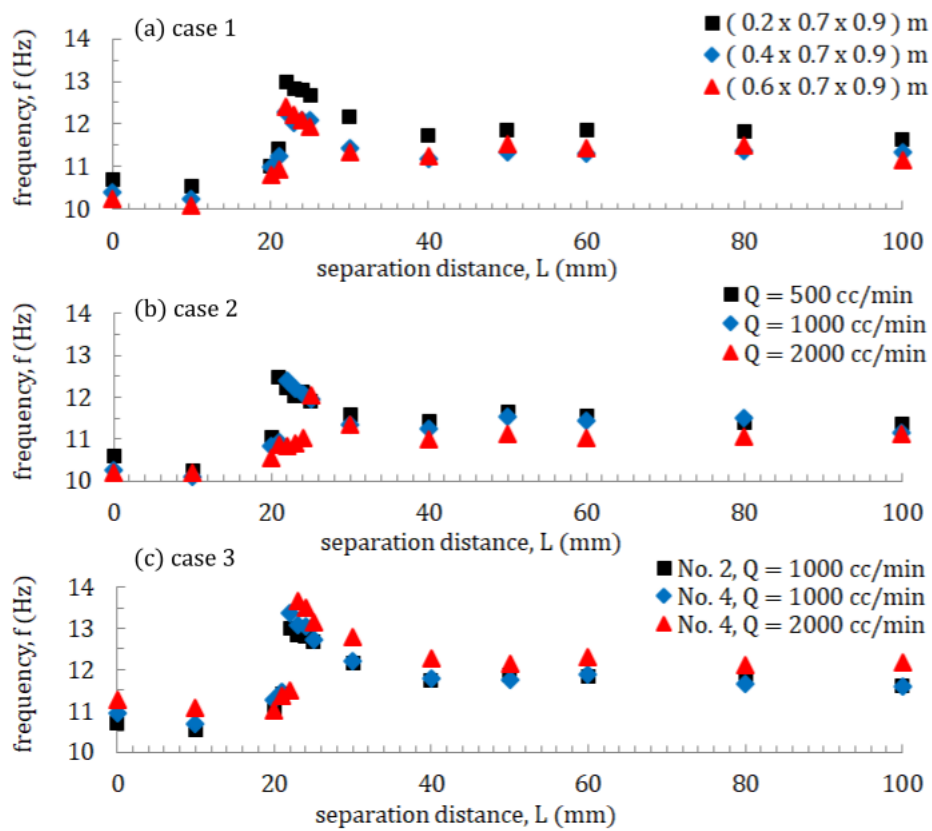


Fig. 3.5 Effect of burner separation distance on flickering frequency for varying dimension of compartment test section, number of mesh-screen and of fuel ejecting velocity at 10 mm diameter of burner.

Acceleration in axial direction comes instead ( $f \sim 1/t$ ), in terms of conservation of mass. Interestingly, the transition point is very solid; it is not altered by those parameters because the target phenomena may be strongly driven by buoyancy. The shear-layer formed by jet flames would highly develop in a relatively strong-acceleration flow field of gravity effect. However, this case is avoided in this study. Noticeably once the dimension of compartment is smaller than  $0.6 \times 0.7 \times 0.9$ , the magnitude of oscillation frequency becomes slightly changed. Thus all productive experiments are decided to go with  $0.9 \times 0.7 \times 0.9$  of compartment dimension (Fig. 3.3).

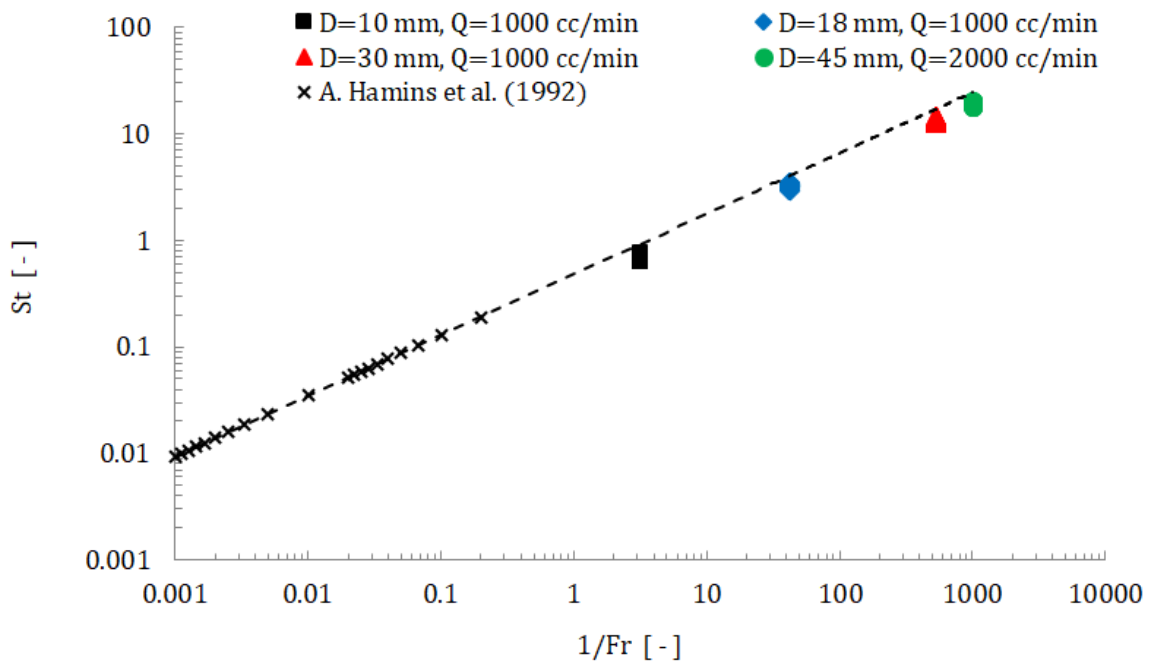


Fig. 3.6 The Strouhal number as a function of the inverse Froude number for studying oscillation of non-premixed jet flickering flame.

Figure 3.6, the measured frequency of various size of burner diameter and fuel flowrate of ejecting methane gas is taken to finish the physical  $St-Fr$  plane. Fundamentally, instability of non-premixed jet flames in present study is dominated by buoyancy force. Saying that this plot of frequencies (for both in-phase and anti-phase modes) can be fitted well with previous study done [Hamins et al., 1992]. Therefore, this scene insinuates the fundamentals is essentially identical as buoyancy dominates phenomena.

### **3.1.3 Optical Image Photography—Schlieren System**

Dynamical flame behavior was directly recorded by a high-speed camera (CASIO EX-F1: 300 fps with 512 x 384 pixels). The camera was only located at front of identical burner(s) corresponding with Fig. 3.7 (a) (corresponding to Fig. 4.1, RHS). To judge whether the target phenomenon is 2-D or 3-D problem, we obtained the orthogonal photography, Fig. 3.7 (b),(c), to check whether the flame moved in front-back direction or not during the interaction event. By observation facts, this is more pronounced that the problem of two-dimensional instability as hypothesis made in chapter 2.

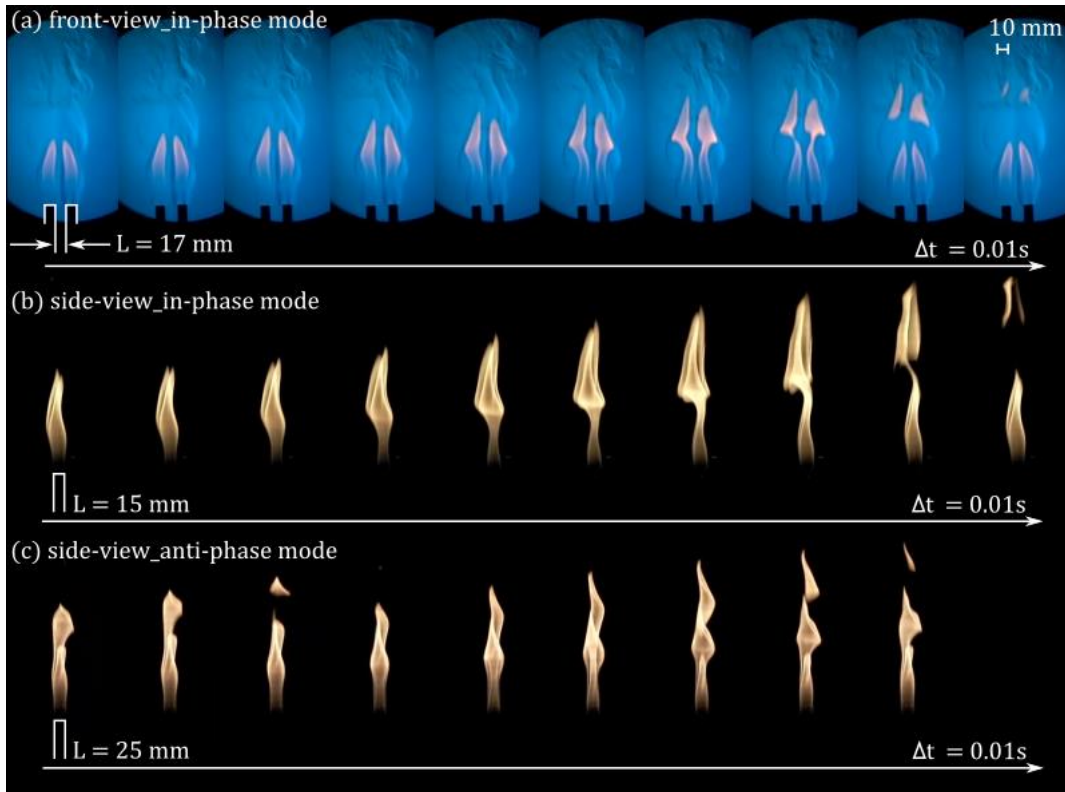


Fig. 3.7 An instantaneous image-sequence of pulsating methane plume: (a) front-directional photography (Schlieren image) of visible flame and density variation ( $D = 10$  mm,  $Q = 900$  cc/min,  $L = 17$  mm); (b), (c) orthogonal (side-view) photography, the middle is in-phase mode ( $D = 10$  mm  $Q = 1000$  cc/min,  $L = 15$  mm) and the bottom is anti-phase mode ( $D = 10$  mm  $Q = 1000$  cc/min,  $L = 25$  mm).

To visualize the formation of the hot plume surrounded by the visible flame, Schlieren imaging technique was conducted [Bunkwang et al., 2019]. Fig. 3.8 shows (a),(b) schematics of the system and the representative visualized images (visible flames with and without thermal layer caused by density variation (c),(d)) for two dynamic modes (in-phase and anti-phase). The object (i.e. visible flames) was positioned between two collimating mirrors, with spacing distance set at approximately 5 meters. A stroboscope (either Flashlamps: xenon, Types: MSX-1A, Metered variac: 0-240V, Flashing range: 100-26000 rpm, and Mini three

modes adjustable focus zoom flashlight and flashing frequency, SWG801130) were used as light-source. The focal length and diameter of the mirrors are 3.5 m and 0.28 m respectively. The cut-off plane and light source were placed at the focusing point of the parabolic mirrors and the high speed camera on a tripod was positioned closely using a 300 mm zoom lens to fill the image plane. The spatial resolution is approximately 0.58 mm/pixel in the imaging plate. Refracted light rays are blocked by a cutting implement, resulting in the grey pixel-intensity level of the background. Adjusting the shoe system, a clear visualization of the both direct flame and hot plume is available to help to understand how the flame start to flicker.

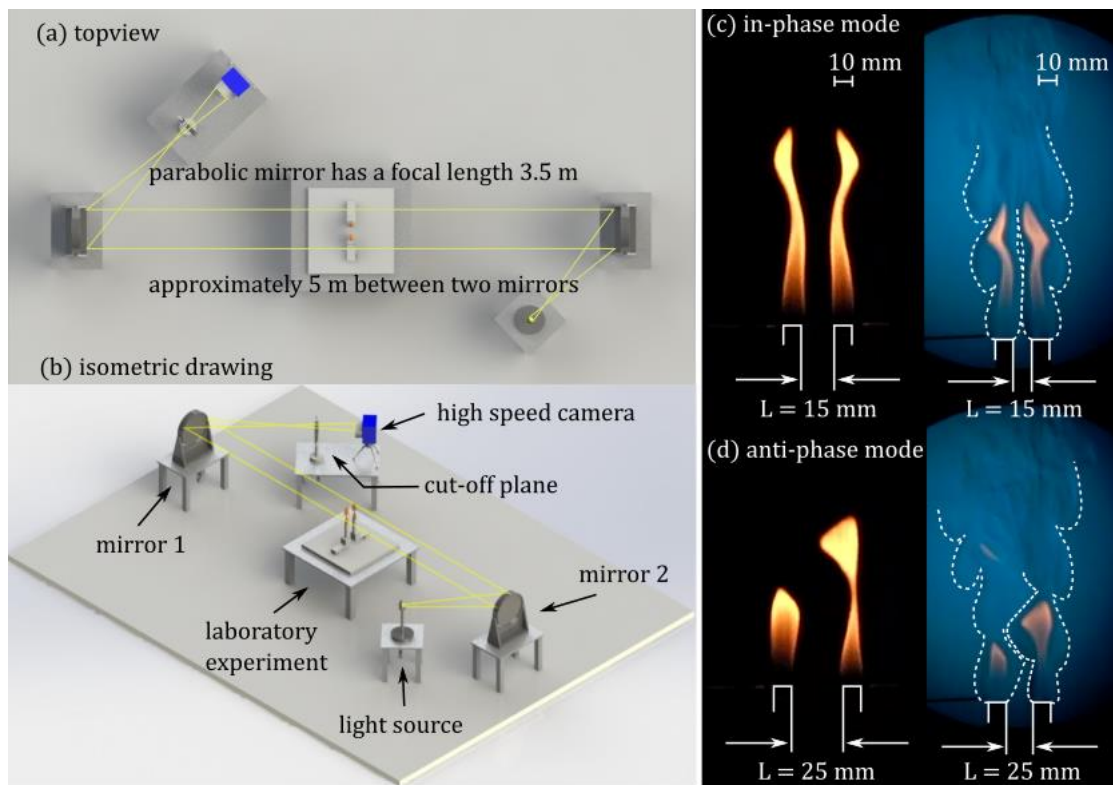


Fig. 3.8 Schlieren optical imaging system (a) and representative images observed at  $L=15$  mm (in-phase) and 25 mm (anti-phase), respectively (b). Broken lines in (c)(d) indicates the representative boundary of thermal layer.

## 3.2 Numerical Experiments

Fire Dynamics Simulator (FDS, version 6.5.3) developed by the National Institute of Standards and Technology (NIST) were used for precise flow visualization of velocity and temperature fields. The software solves numerically a form of the Navier-Stokes equations appropriate for low-speed, thermally-driven flow with focus on smoke and heat transport from fires [McGrattan et al., FDS User Guide 2017]. The FDS, it has been applied in three major areas: basic research in fire dynamics, performance-based design, and forensic reconstructions of actual fires, since first publicly released in 2000 and it has recently undergone its sixth major revision [McGrattan et al., 2014]. In concept of fire triangle, a spontaneous combustion needs the following three things to be present: oxygen, sufficient temperature for ignition and combustible material. Though the perspective seems very simple, in reality, this contains many complex phenomena. For example, the combustion of the combustible gasses, the mass transfer of combustible gasses, even solid material, the heat transfers (conduction, convection, and radiation) from the flame to the combustible material and the surroundings, the buoyancy driven fluid flowing into and out going from the fire,. These complex phenomena must be modelled in computational fluid dynamics software (CFD). The CFD is a numerical tool to solve the governing equations for fluid flow. The governing equations include Navier-Stokes equations, and conservations of mass, energy, and species which can be applied to both laminar and turbulent flows. The area of interest is divided in many small volumes where the equations are discretized into algebraic equations following to the conceptual idea for derivatives over an arbitrary infinitesimal fluid element ( $\Delta x, \Delta y, \Delta z$ ) [Kuo, Principles of Combustion (2005)]. Turbulence models for fire simulation, i.e. Direct Numerical Simulation (DNS), Large Eddy Simulation (LES), and Reynolds-Averaged Navier-Stokes (RANS), are gotten involve. Turbulent models (LES and RANS)

may bring an anomaly to the computational outcome; even though, DNS requires high computational cost for executing time, including fine mesh for fine tune; not likely the LES model, the uniform meshing is preferred. The DNS model is still limited to small *Re*-number [Wen et al., 2007]. Thus DNS is selected in this study fundamentals, because the computational domain of the target is relatively small and the investigation of the target phenomena is set at relatively low *Re*-number. For example, the biggest domain (*X*, *Y*, *Z*) is 0.38 m × 0.16 m × 0.4, and adopted 3-D rectilinear grid is set as default. Moreover, the instability is purely driven by buoyancy force, which suits the purpose of software invention as mentioned very beginning of this section. The governing equations, except the thermal radiation solver which a finite volume technique is employed, are approximated with a finite differences method. They are briefly discussed as the following section.

### **3.2.1 Governing Equations**

In DNS mode, the transport Coefficients: the viscosity, thermal conductivity and material diffusivity, are approximated from kinetic theory. That is because the temperature dependence of each coefficient is important in combustion scenarios. An empirical function of the temperature (*T*) is adopted to obtain the fluid viscosity at a point. Thermal conductivity is set as a function of viscosity and Prandtl number (*Pr*) that can be set by the user as an input property is order of 0.7 to be default value. The molecular diffusivity is based on mixture-averaged binary Fickian diffusion. Postulate the nitrogen gas is the dominant species in any combustion scenario. Thus the diffusion coefficient in the species mass conservation equations is that of the given species diffusing into nitrogen [McGrattan et al., FDS Technical Reference Guide (2017)].

### 3.2.1.1 Continuity

For infinitely small elemental volumes, conservation of mass can be written as the following equation.

$$\frac{\partial \rho}{\partial t} + \nabla \cdot (\rho \mathbf{u}) = 0 \quad (3.1)$$

Where  $\mathbf{u}$  is velocity vector in considered spatial flow and  $\rho$  is filtered fluid density.

### 3.2.1.2 Momentum

$$\frac{\partial \rho \mathbf{u}}{\partial t} + \nabla \cdot (\rho \mathbf{u} \mathbf{u}) = -\nabla \bar{p} - \nabla \cdot \boldsymbol{\tau} + (\rho - \rho_0) \mathbf{g} \quad (3.2)$$

Where  $\mathbf{g}$  is gravity vector, normally (0,0,-g) and variable density fluid is given by  $\rho = \bar{p} \bar{W} / TR_u$ . The inertia force is shown on the LHS and forces acting an infinitesimal volume element is spited into the terms as presented on the RHS. From the left to right, hydrostatic pressure gradient, and force due to viscous stress, and body weight, respectively.

### 3.2.1.3 Energy

$$\frac{\partial}{\partial t} (\rho h_s) + \nabla \cdot (\rho h_s \mathbf{u}) = -\frac{D\bar{p}}{Dt} + \dot{q}''' + \dot{q}_b''' - \nabla \cdot \dot{q}'' \quad (3.3)$$

The LHS represents the changes of the local and convective of sensible enthalpy. First term on the RHS, Eulerian derivatives indicates the pressures in the system: the background

pressure  $\bar{p}(z, t)$  varying with height in gravimetric field and a perturbation pressure  $\tilde{p}(x, y, z, t)$  driving the fluid motion in flow field.

$$\bar{p} = \rho T R_u \sum_{\alpha} \frac{Z_{\alpha}}{W_{\alpha}} = \frac{\rho T R_u}{\bar{W}} \quad (3.4)$$

The thermodynamic (background) pressure may be related in terms of the internal energy and enthalpy ( $e = h_s - \bar{p}/\rho$ ). A given flowing fluid of a control volume per unit mass is defined as total energy ( $e + v^2/2 + gz$ ). The term  $\dot{q}'''$  is the heat release rate per unit volume from a chemical reaction. The term  $\nabla \cdot \dot{q}''$  represents combined heat fluxes: conductive, diffusive, and radiative transfers.

$$\dot{q}'' = -k\nabla T - \sum_{\alpha} h_{s,\alpha} \rho D_{\alpha} \nabla Z_{\alpha} + \dot{q}_r'' \quad (3.5)$$

where  $k$  is the thermal conductivity and  $D_{\alpha}$  is the diffusivity of species  $\alpha$ . The Radiative Transfer Equation (RTE) is adopted to obtain the radiation intensity. Medium is considered as non-scattering medium and a relative small number of bands with a separate RTE derived for each band ( $n$ ); hence, an appropriate mean absorption coefficient  $\kappa_n$  for each band is computed. However, the drawback is if optically thin flames occur, the yield of soot is small compared to the yields of  $\text{CO}_2$  and water vapor, the gray gas assumption (independent on wavelength,  $\lambda$ ) can lead to an over-prediction of the emitted radiation yet, the current computation is fine anyway. The net contribution from the thermal radiation in the conservative energy equation is defined by:

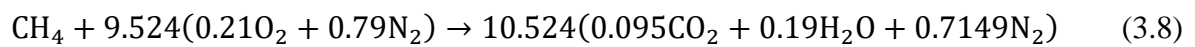
$$\dot{q}_r''' = -\nabla \cdot \dot{q}_r''(\mathbf{x}) = \kappa(\mathbf{x})[U(\mathbf{x}) - 4\pi I_b(\mathbf{x})]; U(\mathbf{x}) = \int_{4\pi} I(\mathbf{x}, \mathbf{s}') ds' \quad (3.6)$$

In real fires, soot is the dominant source and sink of thermal radiation ( $\dot{q}_r'''$ ), not being particularly sensitive to wavelength ( $\lambda$ ), so that the mean absorption coefficient,  $\kappa$ , is a function of species composition and temperature in spatial coordinates, from which a narrow-band model (Radcal) is adopted to obtain its values. In large scale fire simulations, the order of tens of centimeters is typically the size of grid cells. Thus this means flame sheet cannot be resolved so that computed cell-average temperature becomes significantly lower than the temperature one would be expected in the reacting flame. Consequently, the source term is approximated in the grid cells, homogeneity of subgrid temperature field, where the fuel and oxygen react.

#### 3.2.1.4 Species

$$\frac{\partial}{\partial t}(\rho Z_\alpha) + \nabla \cdot (\rho Z_\alpha \mathbf{u}) = \nabla \cdot (\rho D_\alpha \nabla Z_\alpha) + \dot{m}_\alpha''' \quad (3.7)$$

Lumped species is usually referred to the air and products, whereas fuel is defined as a single gas species. Primitive species mass fraction of gases is linearly related to lumped mass fraction given by  $Z_\alpha$ , where subscript  $\alpha$  represents mass fractions: air (oxygen, nitrogen, water vapor, and carbon dioxide), fuel, and product primitive gases. Regarding the combustion model in the current computation, by default, FDS uses a mixing-controlled combustion (Arrhenius model). Consider a single-step reaction mechanism for complete methane combustion as follows:



Then the rate expression for the methane and the rate constant are defined by:

$$\frac{dC_{CH_4}}{dt} = -k \prod C_{\alpha}^{N_{S,\alpha}} ; k = AT^{N_T} e^{-E_a/RT} \quad (3.9)$$

A give parameters are: the pre-exponential factor,  $A$ , [ $((\text{mol}/\text{cm}^3)^{1-n})/\text{s}$ ], where  $n = \sum N_{S,\alpha}$  representing the order of the reaction; the activation energy,  $E_a$  [J/mol]; an array containing the concentration exponents,  $N_{S,\alpha}$ , (default is 1); the temperature exponent,  $N_T$ , (default is 0, meaning no temperature dependence).

In addition, the governing equations that are applied to computational domain governs a combustible (methane) gas for freely-burning in ambient still air at normal atmospheric conditions. So the added mass (evaporating droplets) or subgrid-scale particles (fuel sprays, vegetation etc.); however, it does not exist in current computational model because only mass of primitive species executed is methane. For example, the mass particles ( $\dot{m}_b'''$ ) is generated in the system in mass conservation equation. The external force term ( $f_b$ ) represents the momentum transferred from particles to the gas in conservation of momentum. And the energy transferred to subgrid-scale droplets and particles ( $\dot{q}_b'''$ ) is neglected in this study in conservation of energy.

### 3.2.2 Configurations of Numerical Simulation (FDS)

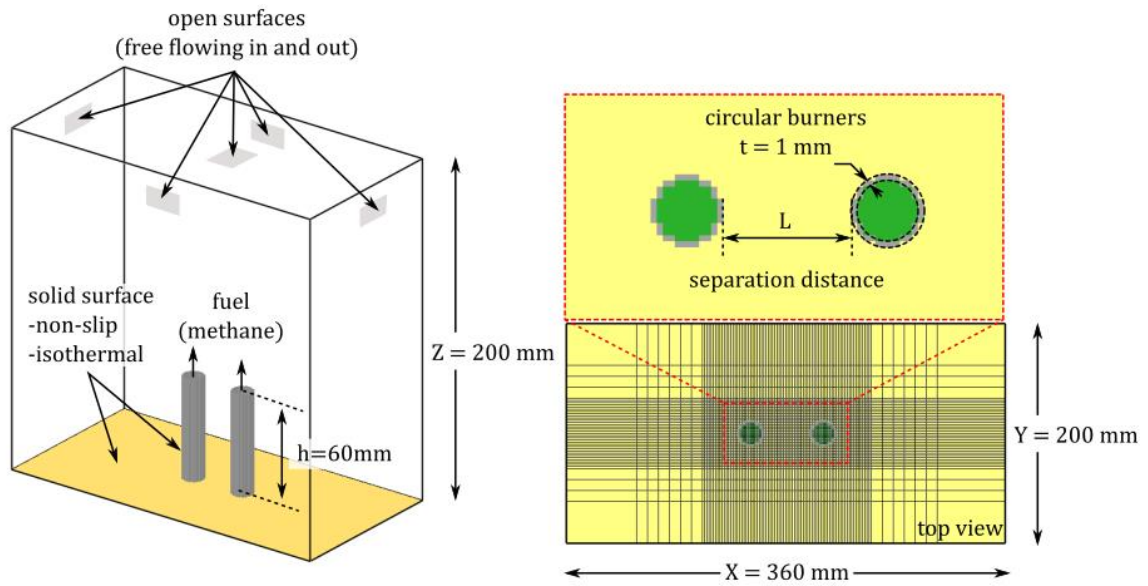


Fig. 3.9 The applied numerical model (for twin-flame system).

The numerical model, time-dependent, 3-D heat and mass transport processes under finite-rate reactions using an Arrhenius model as similar to our previous studies [Mochizuki et al., 2017], was conducted to examine the precise thermal and flow structure during the flickering events as shown in Fig. 3.9. A rectangular computational domain was set with setting dimensions of 0.36 m (width)  $\times$  0.2 m (depth)  $\times$  0.2 m (height) in a Cartesian coordinate, encompassed the object at center of each axis. Simplified chemical model is acceptable for the present purpose since the ignition and extinction is not governing processes on flickering flame dynamics. It is ensured by our preliminary test that periodic flame motions reproduced by the present model is insensitive to the imposed initial condition, instead, characterized by the imposed boundary conditions. All surfaces of the domain boundary are set to “open boundary (i.e., free flow incoming and outgoing)”, except at the bottom surface (non-slip

floor) as indicated in Fig. 3.9 (left). Non-reactive, a smooth inert wall with the temperature fixed at 25°C, non-slip conditions are applied to the burner surface. A fully developed parabolic flow profile was employed at the inlet of the burner. Because the orthogonal structured grid system is employed in FDS, the shape of circulated port is not very smooth. However, this does not cause severe problem as long as the ejecting fuel flowrate is properly imposed because the major dynamics motion of interest is driven by buoyancy and gas dynamics above the jet [Clement, 2000]. Pure methane is ejected through the burners toward the ambient air at the standard state. The temperature at the top surface of the burners is maintained at 1000 °C to promote the ignition and anchoring purposes.

The adopted numerical grid is shown in Fig. 3.9 (right); uniformed grid is applied around the burners, and stretched toward the outer boundaries to save the computational cost. Minimum grid size is 1 mm, which is satisfactory to obtain the buoyancy-driven dynamics. Assuming that characteristic buoyancy flow velocity is  $U = 1$  m/s, the characteristic length in transport system can be estimated by  $U^2/g$  (where  $g$  is gravity acceleration)  $\sim 0.1$  m  $\gg 1$  mm, revealing that the applied grid scale is fine enough to resolve the transport process in the present system. It is true that the adopted grid is not fine enough to resolve the reaction structure in a precise manner so that the maximum temperature might not be correct. With this respect, the quantitative agreement between the simulation and experiment is not expected as observed in next section (3.2.3). Because the purpose of the simulation is to assist to understand the thermal and flow structure at various modes, we believe that the present strategy is satisfactory. However, in FDS User's Guide itself, there has a nondimensional expression,  $\hat{D}/\delta x$ , where  $\hat{D}$  is characteristic fire diameter and  $\delta x$  is the nominal size of a mesh cell. That mesh resolution is preliminarily suggested to accomplish the flow field of buoyant plumes resolved [McGrattan et al., FDS User Guide (2017)].

$$\hat{D} = \left( \frac{\dot{Q}}{\rho_{\infty} c_p T_{\infty} \sqrt{g}} \right)^{2/3} \quad (3.10)$$

Where parameters are given as:  $\dot{Q}$  [kW] is the total heat releases rate of the fire.

A cell size of 10 centimeters may be “adequate”, in some sense, for evaluating the overall flame dynamics, but may not be appropriate to study the inner thermal shear-layer deformation in a very small spacing between two identical burners as already aforementioned above. So fine mesh with small grid cells is always applied at the middle spacing and they must be smaller than 10 centimeters. “Grid sensitivity”, a common question dealing with grid spacing is how size the mesh is. In general, it is depending upon what we are trying to accomplish. Sometimes, trials and error is the easier choices shown in next section. For example, using a relatively coarse mesh to build an FDS input file, and then gradually refine the mesh until the differences in the results are in satisfactory level (see Fig. 3.12). A piecewise-linear mesh stretching-like stair stepping method was applied to transform the uniformly-spaced mesh to a non-uniformly spaced mesh in this study (Fig. 3.10).

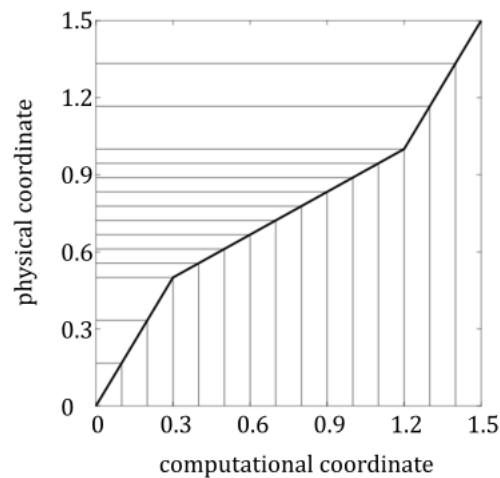


Fig. 3.10 Piecewise-linear mesh transformation [McGrattan et al., FDS User Guide (2017)].

### 3.2.3 Pre-productive Runnings

When using a CFD software, end-user must finish two things, namely, verification and validation. Verification is justifying to mathematical equations; whereas, validation is for checking the accuracy of the numerical results whether they are in good reliability to currently model the real world problem or not. Validation of performance of numerical method (FDS) on single fire pulsation correlation was performed. This scaling relation,  $f \sim 1.5(D)^{-0.5}$ , from the study of Cetegen and Ahmed (1993), is much unified popularly so that it was adopted to achieve this purpose. As shown in the Fig. 3.11, due to the pre-running cases, the numerical results found to be in sufficiency to simulate the target phenomena and the qualification of work can be expected to visualize the velocity and temperature fields of hot substance behavior.

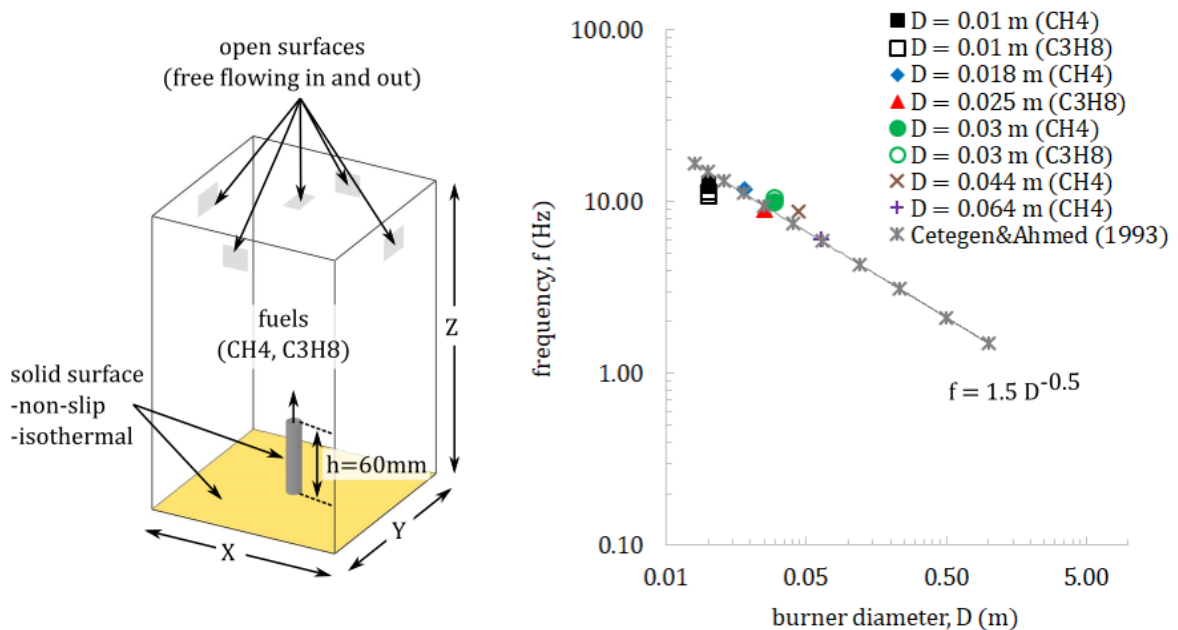


Fig. 3.11 The applied numerical model for single fire.

Grid sensitivity was also checked for the computational domain, whose dimension shown in Fig. 3.9, was applied to simulate the target phenomena. The uniform fine-grid was applied around the burners and the coarser one was applied at farther distance as similarly shown in Fig. 3.9 (right). The impact of mesh sizing on the simulation results was checked. Numerical results are found in Fig. 3.12, summarized in both types: table and graph. It was found that the number of mesh should be higher than 0.6 million cells as expressed by third case of the pre-running (Run 3). The oscillation frequency was found satisfactorily within 2 % difference of deviation. The third, therefore, will be adopted to enable FDS to capture the vorticity caused by disturbances. Satisfaction was fulfilled as found by pre-operative checking.

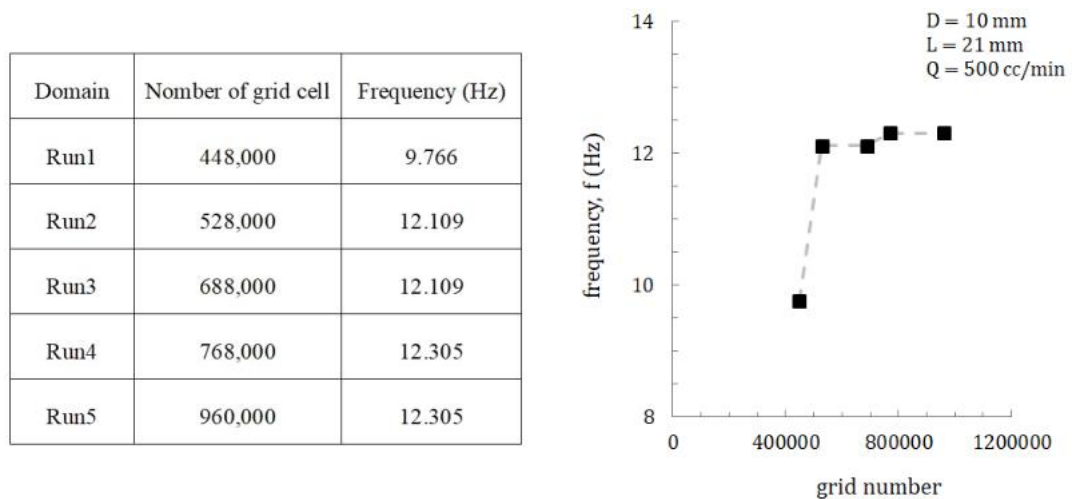


Fig. 3.12 Observation of grid sensitivity.

The experiments, based case:  $D = 10$  mm  $L = 0 - 100$  mm,  $Q = 500$  cc/min, fuel = methane, were conducted in order to provide experimental data which can be used to validate computer models. Forward and backward of moving burner were precisely performed as presented in the red and blue in Fig. 3.13, the whole trend of flame dynamics within the designated working range was accomplished. The observation results are most satisfactory. Under prediction of frequency is not a big surprise to this rival of both; the reason caused of this computational outcome was already described. However the numerical simulation shows good agreement adequately with the experiment in qualitative comparison as expected. Three regions of flame dynamics have been separated: first, “the region of low oscillation frequency”, the two visible flames behave like a single-flame pulsation and frequency of flame dynamics found slightly change, seems independent on the distance. Between the first and second regions, “appearance of frequency jump”, this found with prompt jump showing a prominent peak, within this jumping region, the mode of flame dynamics was very sensitive and difficult to identify. Second, “high frequency region”, the frequency becomes decreasing with the separation distance modified apart farther until no change of oscillation frequency. This was observed in the third region, “desynchronization”, the two flickering flames are not affect each other, and they are isolated at those applied conditions.

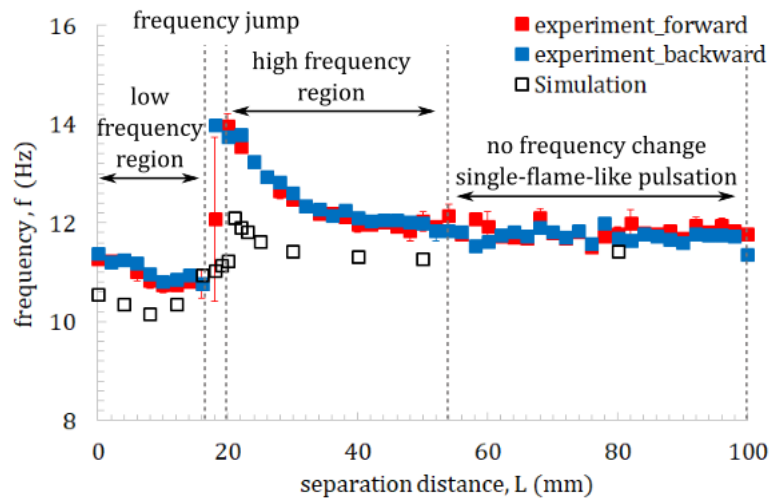


Fig. 3.13 Comparison the experimental observation (both forward and backward to moving optical stage of the burner) with the numerical simulation:  $D = 10$  mm,  $Q = 500$  cc/min, varying the  $L$  (separation distance) from 0 mm to 100 mm.

## Chapter 4

# Mode Transition of Interacting Buoyant Non-premixed Flames

### 4.1 Introduction

In this section, the mode transition observed in twin-flame system for laboratory scale is observed in details. Regarding the first target of research objectives stated in section 1.5, the transition of flame dynamics is revealed and discussed from scientific way. To achieve this goal, the experimental apparatus applied by Toong and coworkers at MIT (1965) is adopted for a precise construction in order to carefully upgrade for a wide working-range. The important systematic parameters: fuel flowrate ( $Q$ ); burner diameter ( $D$ ); and burner separation distance ( $L$ ), are examined. Through the special technique introduced in here, the distinctive two modes of flame dynamics can perfectly be controlled and the instability mechanism is investigated, including discussion from scientific point of view. We attempt to provide the precise data on the transition, including the further validation on the transition model. The correlation between the adopted burner diameter ( $D$ ) and critical burner separation distance ( $L_{\text{crit}}$ ) at prescribed condition is found slightly difference from Yang work (2019). The trend of mode change for a wide working-range of burner diameter is revealed. The exponents of the correlation are corrected and the upgraded of Yang's model is successfully done. The critical value can be described by critical condition through global parameters ( $\alpha$  and  $Gr$ -number). By taking this way of trick for further interpretation, the

transition in single fire could have chance to interpret the detailed physics, which never did because of the natural instability itself. So this will be continued in the next chapter.

## 4.2 Methodologies

### 4.2.1 Experimental Setup

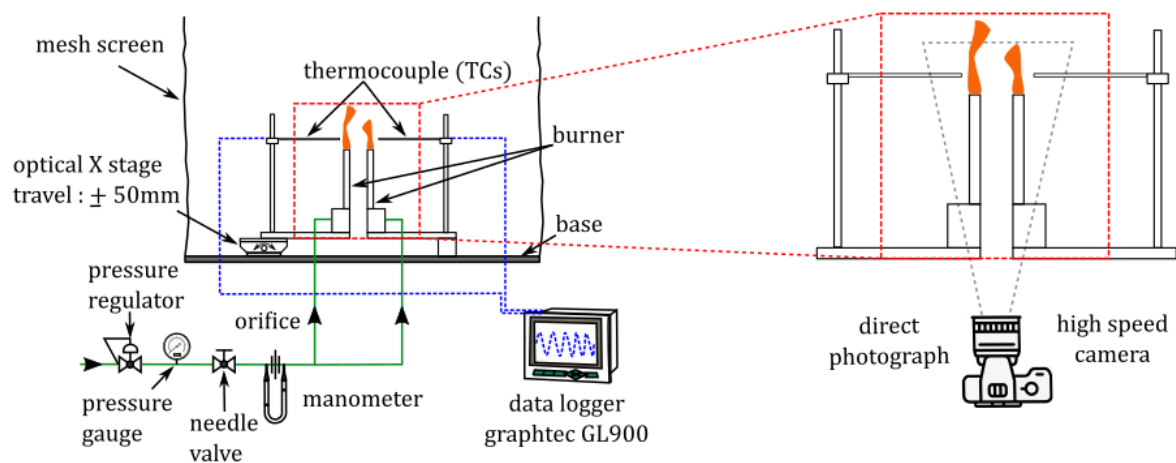


Fig. 4.1 Schematics of experimental apparatus with blowup section of flame photography.

A brief explanation is made here for experimental setup (Fig. 4.1). This is because the main configuration of laboratory experiment is similar to what already explained in section 3.1, to which the transition is studied by introducing the twin non-premixed jet flames in this section. It is little modified to suit the helium flow (isothermal experiment) because working with helium the objective must be positioned in between the optical system shown in Fig. 3.8 (left). Metal meshes (Fig. 4.2) were inserted into the cubic aluminum base of twin cylindrical tubes in terms of ensuring the uniformity of ejecting helium flow at the exit. All experiments

were performed at in the open in the laboratory. The experiment was repeated for least twice, but for some highly turbulent cases, more than five times were needed. Sample standard deviation was adopted for uncertainty prediction. The research grade methane gas (99.4 % of purity) and helium gas, inserted at the cylindrical base were issued upward at identical flowrate,  $Q$ , through two circular burners. The  $Q$  of the methane and helium was controlled by flow controlling system, which composes of a hand-made monometer with the accuracy approximately higher than 99% (see the appendix A). One burner was fixed at to the floor and another one was movable in terms of modifying the separation length,  $L$ . The condition  $L = 0$  mm indicated two burners were perfectly aside placed in parallel. Reading the fundamental mode of flame dynamics, multi-layered mesh screen was surrounded the apparatus in order to eliminate any disturbance.

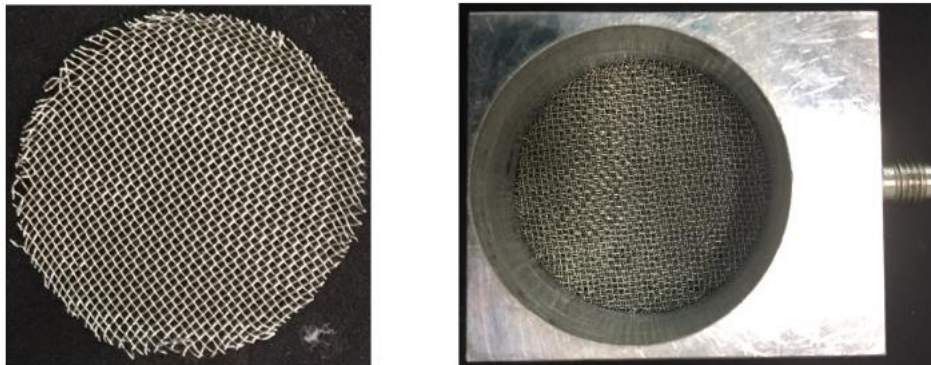


Fig. 4.2 Typical snapshots of metal mesh inserted in the base of circular burner.

The dynamic behaviors of methane flame and helium flow were directly recorded by a high-speed camera. Whereas, in case of helium its behavior was recorded through the optical system and its frequency was analyzed by introducing an image analysis software (see appendix B for more information), in order to prepare the input signals in time domain.

Through the operating of the FFT, the harmonized frequencies,  $f$ , were obtained. This strategy is same purpose of fine thermocouples equipped near the burner exit to record the time-variation of field temperature signal which is described already.

#### **4.2.2 Schlieren Imaging**

To visualize the formation of the hot plume surrounded by the visible flame and density difference in the test of helium flow, Schlieren imaging technique overviewed in section 3.1 was used. So it is briefly discussed here. The apparatus and representative visualized images are shown in Fig. 4.3. The visualized target, such as methane flames and helium flow field, were positioned between two parabolic mirrors. The spacing distance was set at 5 m and the controlled shooting frequency of visible light was employed as light-source in this study. The focal length and diameter of the mirrors were 3.5 m and 0.28 m respectively. Optical devices (knife-edge and light-source) were placed at the focusing point of the mirror and the high speed camera on a tripod was positioned closely using a 300 mm zoom lens to fill the image plane. The spatial resolution was approximately 0.58 mm/pixel in the imaging plate. Refracted light rays were blocked by a cut-off implement, resulting in the grey pixel-intensity level of the background. By adjusting the shoe system, a clear visualization of the both direct flame and hot plume was available to help to understand how the flame start to flicker. The buoyant flow field of helium gas confirms the observed evidence of hydrodynamics instability.

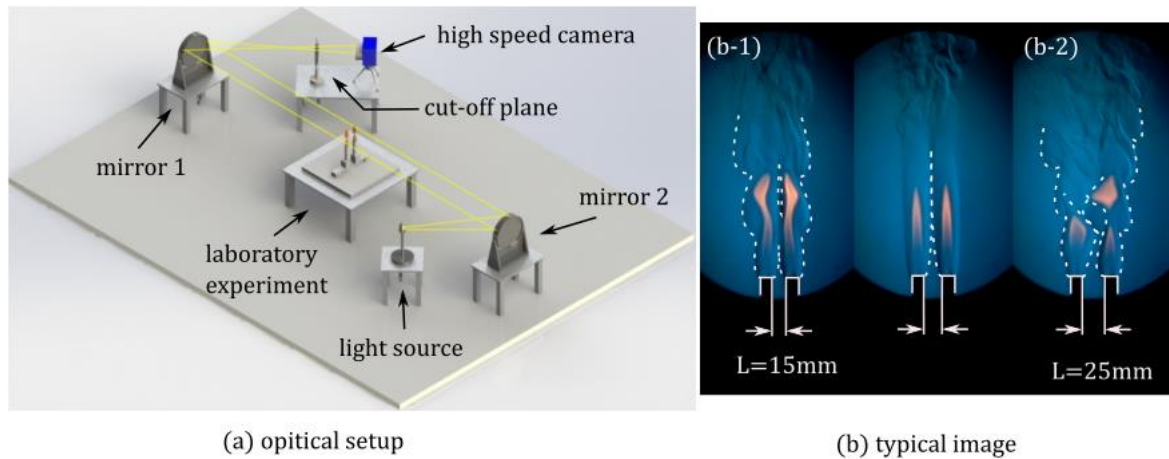


Fig. 4.3 Schlieren optical imaging system (a) and representative images observed at  $L=15$  mm (in-phase) and 25 mm (anti-phase), respectively (b). Broken lines in (b) indicates the representative boundary of thermal layer.

### 4.3 Experimental Results and Discussion

#### 4.3.1 Observation of Dynamic Behavior of an Isothermal (Helium) Experiment

As shown in Fig. 4.4, typically sequential images of helium flow with various flowrate of two sizes of cylindrical tubes:  $D = 18$  mm and 30 mm, are shown. The observed fundamental physics, i.e. isothermal and reactive cases, checking the effect of ceiling, was performed. The useful information was necessitated to make a proper judgement prior to productive performing which conveys by means of the applied methods. Previous fundamental suggested,  $St-Fr$  physical plane, is finished. This is clear that, without chemical energy release, the target phenomenon is still simulated and the transition occurs at a certain separation distance. When the buoyancy force intensifies in the flow, the vorticity can fully form until it alternatively sheds toward the downstream region. This conveys that the

instability of the transition would highly be considered as hydrodynamics problem. The observation fact becomes satisfactory.

On  $f-L$  plane in Fig. 4.5, clear transition is found for 18 mm and 30 mm diameters of cylindrical tubes, but difficulty occurs when 45 mm diameter is adopted. This is because the flow becomes highly turbulent fashion leading to difficulty to identify the transition. Such similar scene is also found in the reactive (methane) case for such relative large diameter ( $\geq 45$  mm), so that we can highly infer that this is purely hydrodynamics problem. Probably, phenomenon is not solid on 2-D plane, rather on the 3-D one which would be considered instead. Through three cases of helium buoyant plume, the observed trend shows slightly inconsistency with previous study of empirical correlation and the critical value of ejecting helium is needed to initiate plume pulsation [Hamins et al., 1992]. In Fig. 4.6, notice that two cases (18 and 30 mm), they can follow the line of the suggested fundamentals, but the case of 45 mm diameter seems to be out of the suggested fundamental relationship. To summarize based on the two cases (18 and 30 mm) of characteristic frequency and the physical observation evidence, the buoyancy induced instability would highly be the cause of mode change in this study [Cetegen & Dong, 2000; Toong et al., 1965].

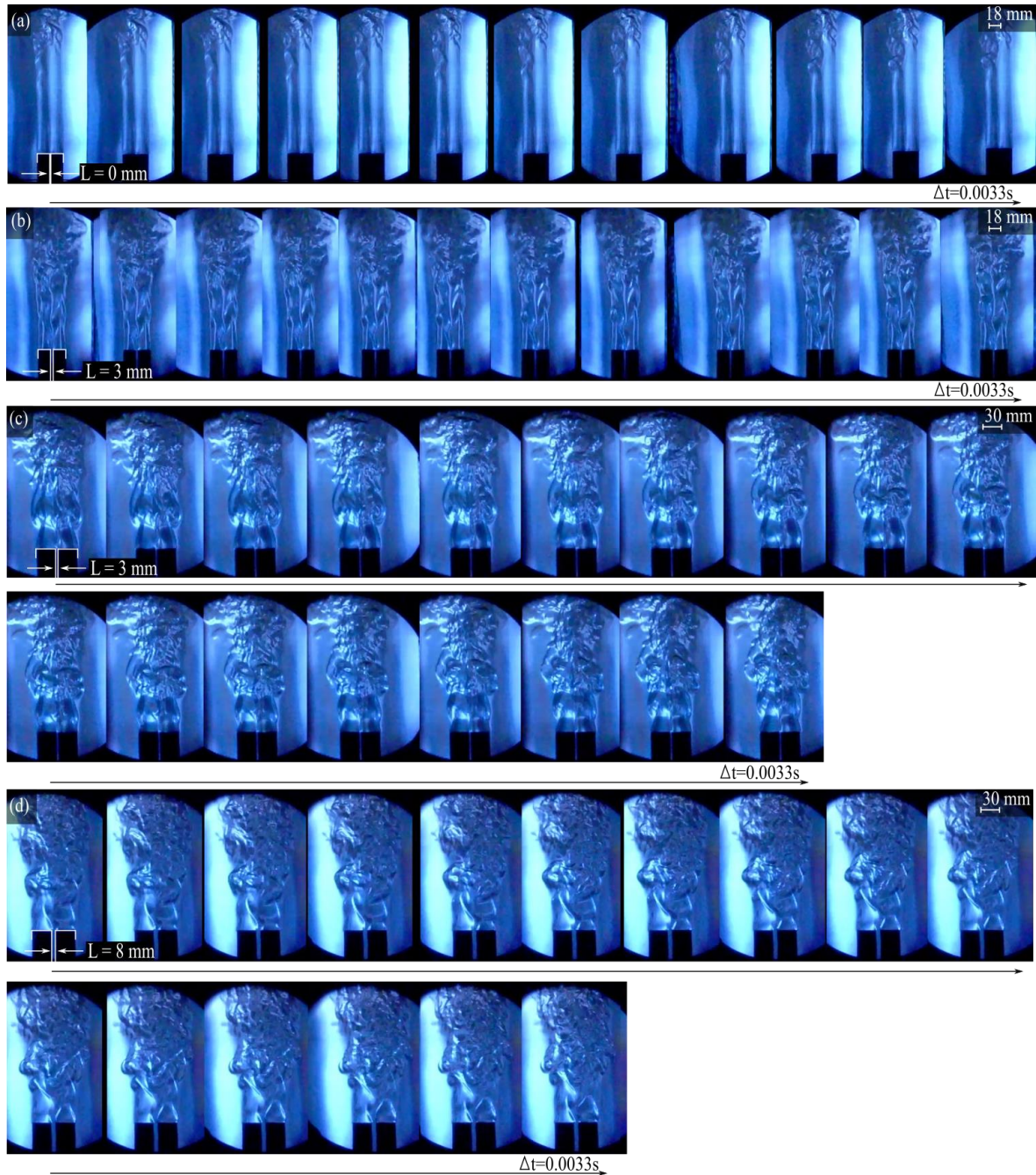


Fig. 4.4 Time-sequential images of pulsating helium of oscillation associated with Schlieren images photography. Conditions are  $D = 18$  mm and  $Q = 15000$  cc/min at which  $L = 0$  mm, plume behaves steadiness (a), and at which  $L = 3$  mm, plume behaves anti-phase mode (b). Conditions are  $D = 30$  mm and  $Q = 40000$  cc/min at which  $L = 3$  mm, plume behaves in-phase mode (c), and at which  $L = 8$  mm, plume behaves anti-phase mode (d). Time interval ( $\Delta t$ ) is 0.0033s.

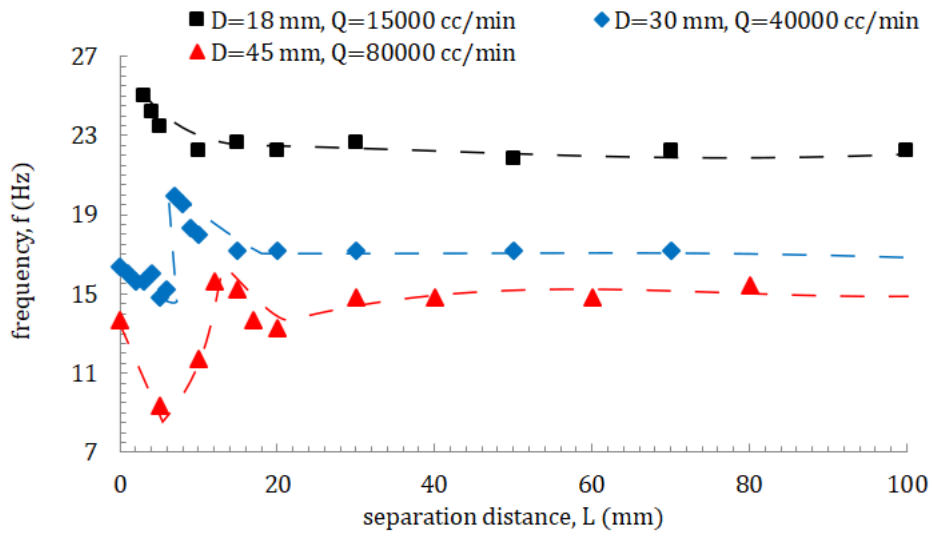


Fig. 4.5 Effect of burner separation distance on flickering frequency for varying of helium flowrate and three adopted diameters of cylindrical tubes.

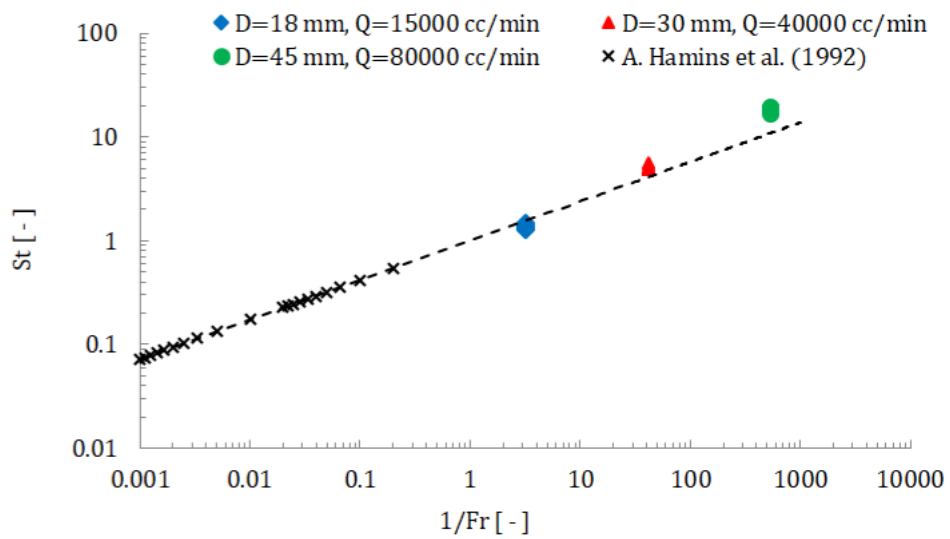


Fig. 4.6 The Strouhal number as a function of the inverse Froude number for studying oscillation of an isothermal buoyant helium flow.

### 4.3.2 Effect of Artificial Ceiling on Dynamic Mode of Interacting Non-premixed Flames

Figure 4.7 shows the drawing concept of experimental test section to simulate the effect of ceiling on flame dynamics of buoyant flickering flame. The results are shown in Fig. 4.8, the characteristic frequencies as a function of burner separation distance with various heights of artificial ceiling. The dimension of test section is same setup as shown in Fig. 3.3. Typical four cases shown here were examined. They are summarized as follows: Case 1: open, no appearance of the ceiling; Case 2: ceiling to burner tip is set at 1.2 m and ceiling to mesh is set 0.6 m; Case 3: ceiling to burner tip is set 0.7 m, and ceiling to mesh is set at 0.1 m; Case 4: ceiling to burner tip is set at 0.6 m, and ceiling to mesh is completely closed at 0 m. All cases considered here, the mesh to burner tip is of 0.6 m, and fuel (methane) flowrate is 500 cc/min, and 10 mm diameter of circular burner.

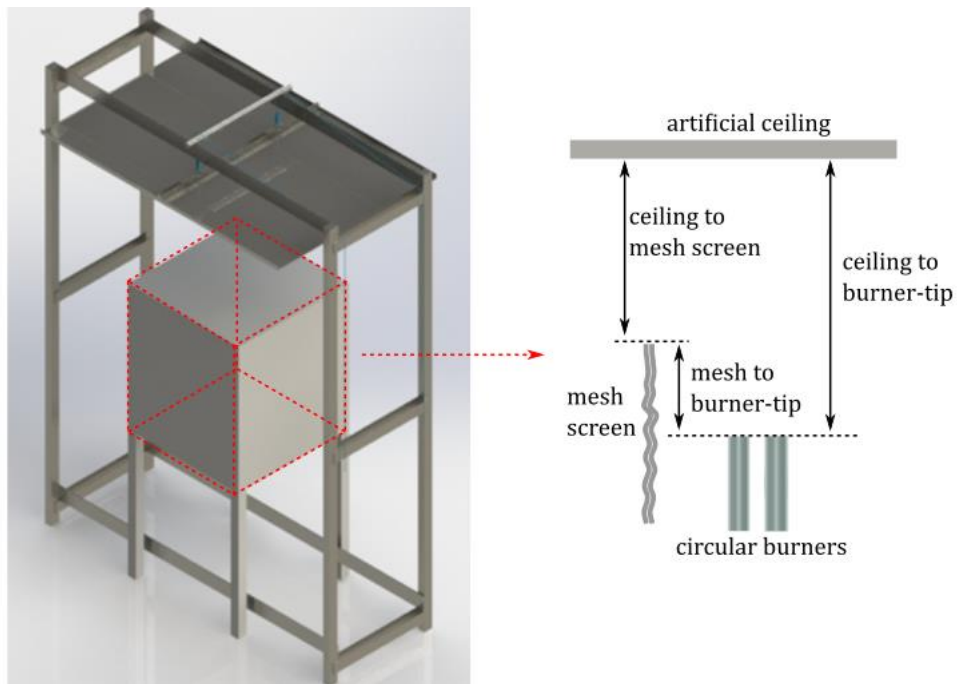


Fig. 4.7 Schematics of the experimental test section for simulating the artificial ceiling.

Notice the experimental results that the transition is insensitive to any modification of ceiling height, whereas, the magnitude of oscillation frequency becomes less influence of this factor. This scene clues that even minor distortion effect from turbulent hot-plume above the visible flames, the dynamics can be triggered by just disturbances shedding onto the upstream region, and then the mode change occurs. The hot plume is important for triggering the two kinds of transition.

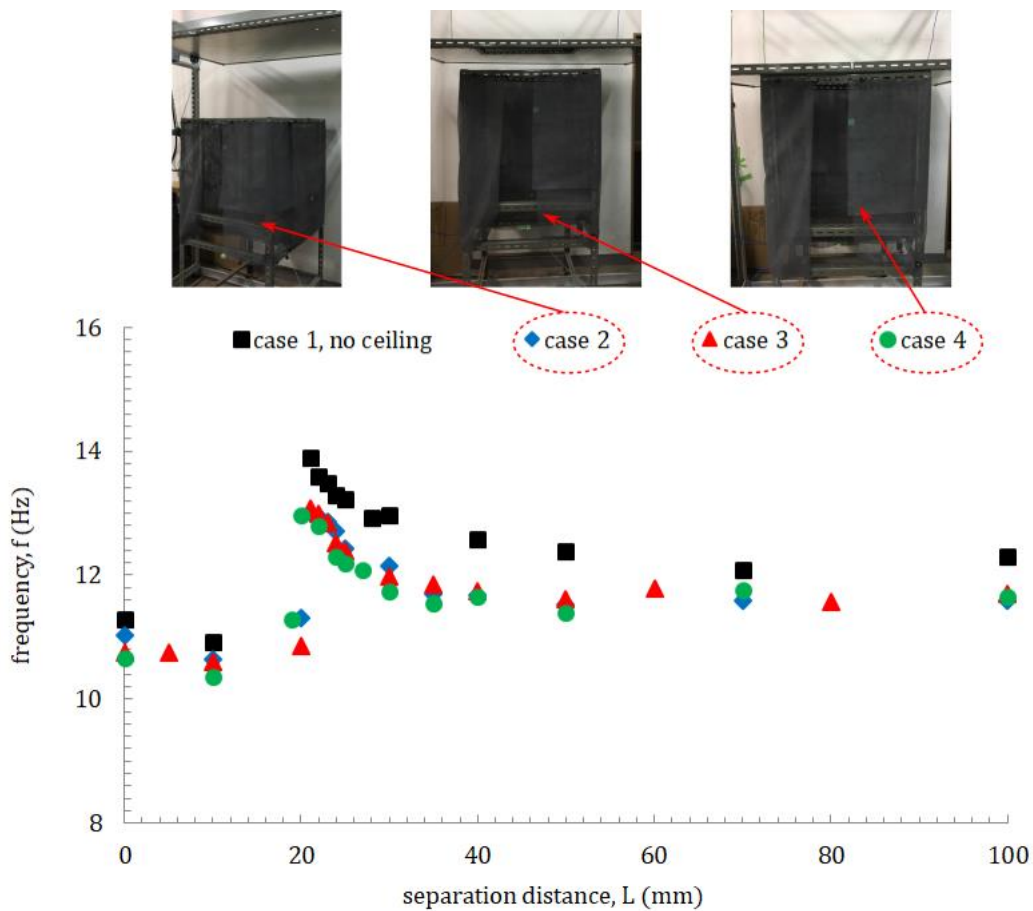


Fig. 4.8 Effect of artificial ceiling on oscillation frequency under the variation of separation distance .

### 4.3.3 Oscillation Mode of Interacting Flames and Its Transition

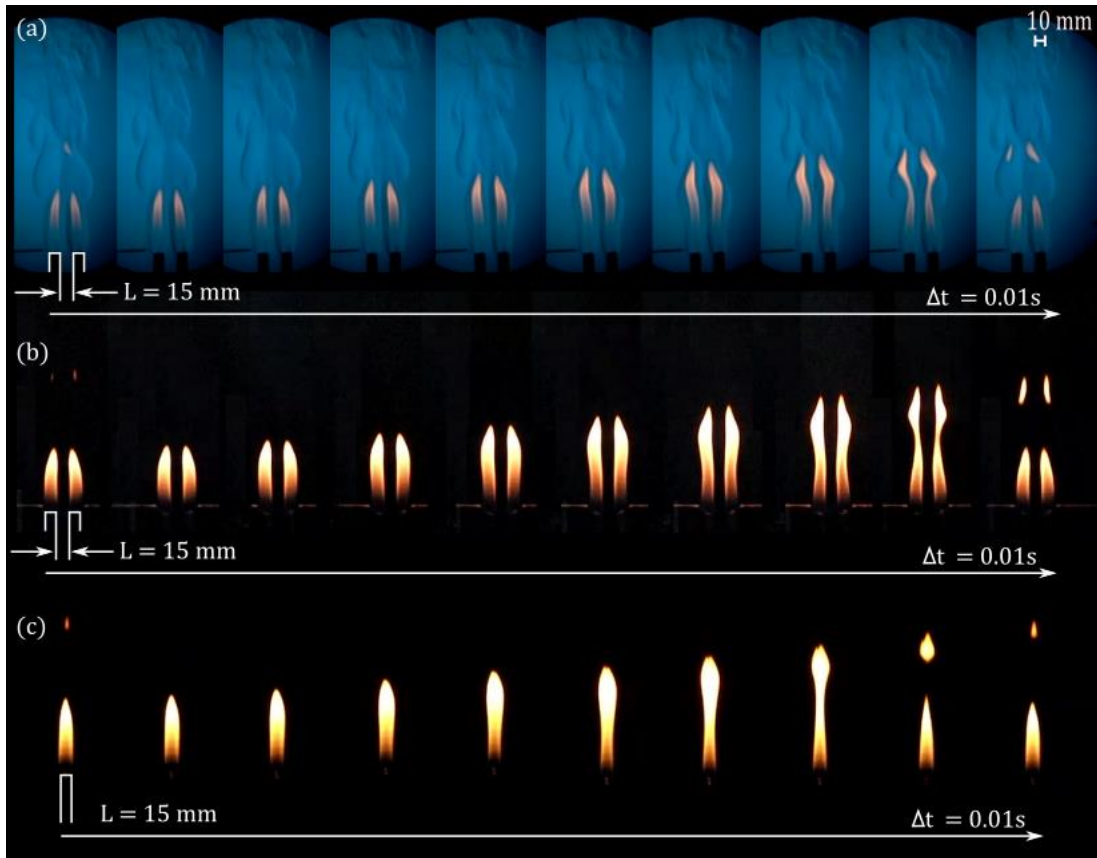


Fig. 4.9 Time-sequential images of pulsating methane plume at in-phase mode of oscillation: Schlieren images (a), and direct photography (b), orthogonal photography (c);  $L = 15$  mm,  $D = 10$  mm,  $Q = 500$  cc/min, and time interval ( $\Delta t$ ) is 0.01s.

Figures 4.9 and 4.10, they show typical sequential pictures (front directional and orthogonal photography) of the pulsating methane-air jet flames obtained with prescribed fuel flowrate ( $Q$ ) and burner separation distance ( $L$ ), together with the corresponding Schlieren images. Previous studies (e.g., Toong et al., 1965; Kitahara et al. (2009); Nakamura et al., (2016) and Mochizuki et al (2017)) identified two kinds of dynamic modes exhibited by the interacting flames, such as in-phase (Fig. 4.9 (a)-(c)) and anti-phase (Fig. 4.10 (a)-(c)) modes.

Corresponding with the optical image visualization [Bunkwang et al., 2019], it is evident that the fundamental modes appear in the gravimetric field as seen in Fig. 2.5 (section 2.2).

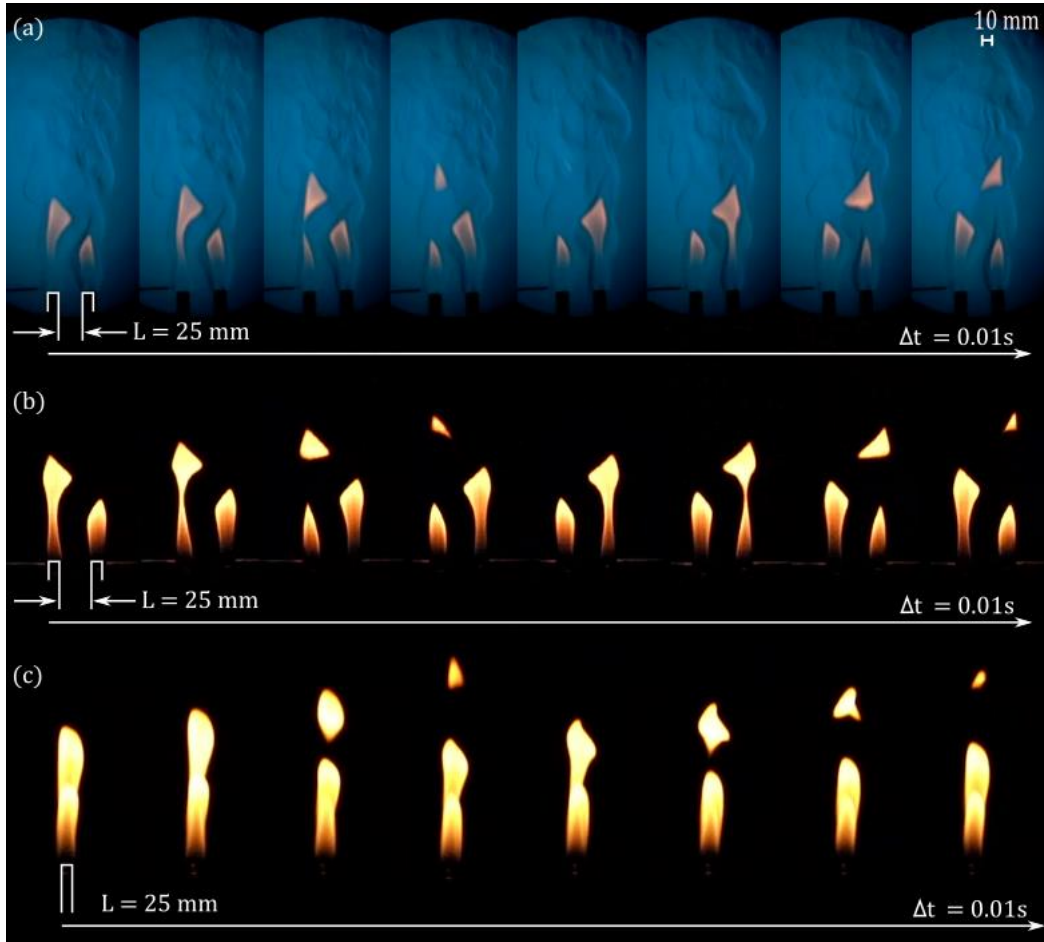


Fig. 4.10 Time-sequential images of pulsating methane plume at anti-phase mode of oscillation: Schlieren images (a), and direct photography (b), orthogonal photography (c);  $L = 25 \text{ mm}$ ,  $D = 10 \text{ mm}$ ,  $Q = 500 \text{ cc/min}$ , and time interval ( $\Delta t$ ) is  $0.01 \text{ s}$ .

As seen in the figures (Figs. 4.9 and 4.10), periodic motion of two synchronized jet flames is very solid on 2-D plane. Based on the orthogonal photographs shown in (c) of Figs. 4.9 and 4.10, pinched off flames at in-phase mode is relatively thicker than in the anti-phase mode. Nevertheless, it is identified that the bottom part of flames for both modes do not

move front-to-back, suggesting that the two-dimensional observation of the flickering phenomena is enough to grasp the overall motion of the flames. In this regard, Schlieren imaging from front view delivered beneficial yet sufficient information of flame dynamics. From Fig. 4.9, it can be understood that the hot plume over the flame fully developed and merged when in-phase mode is attained, then the large hot plume could drive the whole dynamics of the flame. However, when the anti-phase mode is attained as shown in Fig. 4.10, hot plumes made by each jet flame do not merge completely, but rather, are always separated at the flaming zone although they are disturbed and mixed far downstream.

In Fig. 4.11 (a), time-sequential Schlieren images in a transient condition are shown. In this figure, a series of images of the transitions from steadiness to weak flickering motion to in-phase and from the in-phase to anti-phase oscillation are presented. It is true that the time intervals of image-sequence of 0.1 sec cannot capture the complete motion of flame flickering because the typical flickering frequency is 10-15 Hz, using this size of burner. The main purpose of Fig. 4.11 (a) is to illustrate how the hot plume interacts with the flames developing in time. At very earlier stage of development, flames become steadiness ( $0 < t < 0.4$  sec), the hot plume around the flame is rather smooth and forms a steady boundary layer. In this stage, viscosity absolutely prevents the flame from perturbation amplified, the growth of disturbances is completely suppressed. At far downstream, however, the disturbance is identified due to the buoyancy acceleration, and forms a shear stress along the hot plume boundary. However, it gradually turns into in-phase mode, then eventually shift to anti-phase mode.

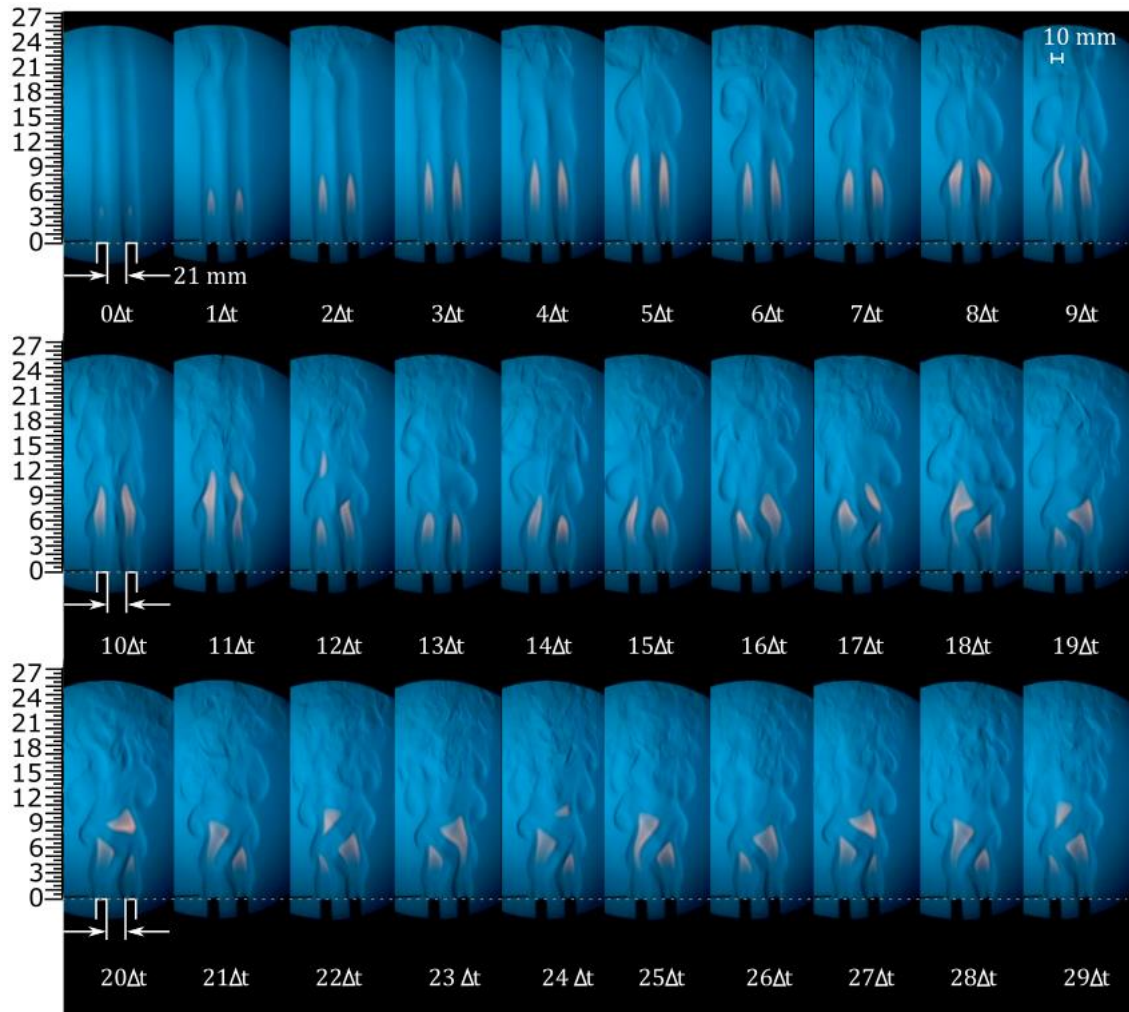


Fig. 4.11 (a) Typically optical image-sequence of mode transition of methane flame from steady to in-phase, and from in-phase to anti-phase:  $D = 10$  mm,  $Q = 500$  cc/min,  $L = 20$  mm,  $\Delta t = 0.1$  s, scale: centimeter.

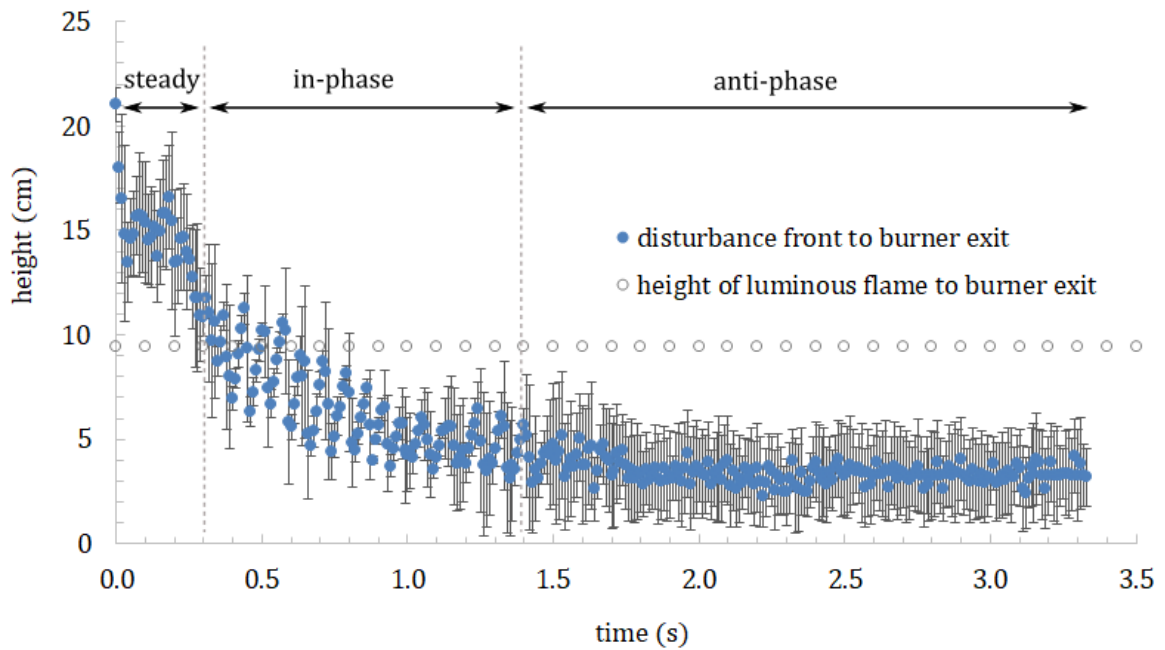


Fig. 4.11 (b) Approximation height of disturbance front to burn exit with time-dependent at the transition condition of methane flame interaction ( $D = 10$  mm,  $Q = 500$  cc/min,  $L = 20$  mm,  $\Delta t = 0.01$  s, scale: centimeter).

As time progresses, the disturbance front travels toward the upstream and eventually reaches the upper part of the flame to promote the deformation of the visible flames. The temporal variation of the observed height of the disturbance front shown in Fig. 4.11 (b), referred to the burner tip. An initiating point of disturbance front is about 20 cm above the burner tip (physically expressed by the dot-line in Fig. 4.11 (a)), while the flame height is around 9 cm represented by the empty circle. By the way, steady flame fails to preserve this stage of dynamic mode then it collapses when the disturbance front propagates toward the flames and it comes close to the flame tips. The flames exhibit in-phase mode observed in the (a) ( $0.4 \text{ sec} < t < 1.2 \text{ sec}$ ). Symmetry oscillation is presented, showing that two flames oscillate

in opposite way. The disturbance keeps squeezing the flames, once the vorticity sheds on the flow closely to the flame location as shown in the (b),  $0.4 \text{ sec} < t < 1.4 \text{ sec}$ . At  $t = 1.1 \text{ sec}$ , the left and right flames give slight asymmetry, then the asymmetry grows in time to achieve the transition to anti-phase mode. Even this is quite low frequency of the shedding oscillation but it seems potentially to accelerate the mode change as shown in the (a),  $t > 1.2 \text{ sec}$ . The disturbance front continuously keeps traveling toward the upstream and eventually passes the flame tip, at which the anti-phase mode appears (the (b),  $t > 1.3 \text{ sec}$ ). Once anti-phase mode is achieved, the flames prefer to stay in that mode and is difficult to back to the in-phase oscillation. From this observation, as previously predicted (Mochizuki et al, 2017), anti-phase mode (flame exhibits asymmetry) seems more stable than in-phase mode. It is obvious that the disturbance can be one of trigger of the appearance of the mode change. It is interesting to notice that we have two-mode change (laminar to in-phase, in-phase to antiphase) and the disturbance only travels toward the upstream. Such disturbance observed in this case is a stabilizing mechanism of this dynamic system of twin flickering flame interaction. Hence, it is expected that the promotion of buoyant-flow intensity may result in modifying the transition condition.

#### **4.3.4 Oscillation Frequency: Modifying of the Experimental Parameters $Q, D, L$**

Time variation of temperature field from thermocouples (TCs) fixed adjacent to the flame base is analyzed to identify the characteristics of the dynamic resonance behavior. Fig. 4.12 shows a representative example of the characteristic frequency obtained by FFT of TC signals, with the apparent peak at a certain frequency, ensuring the dynamic motion shall be characterized by that frequency.

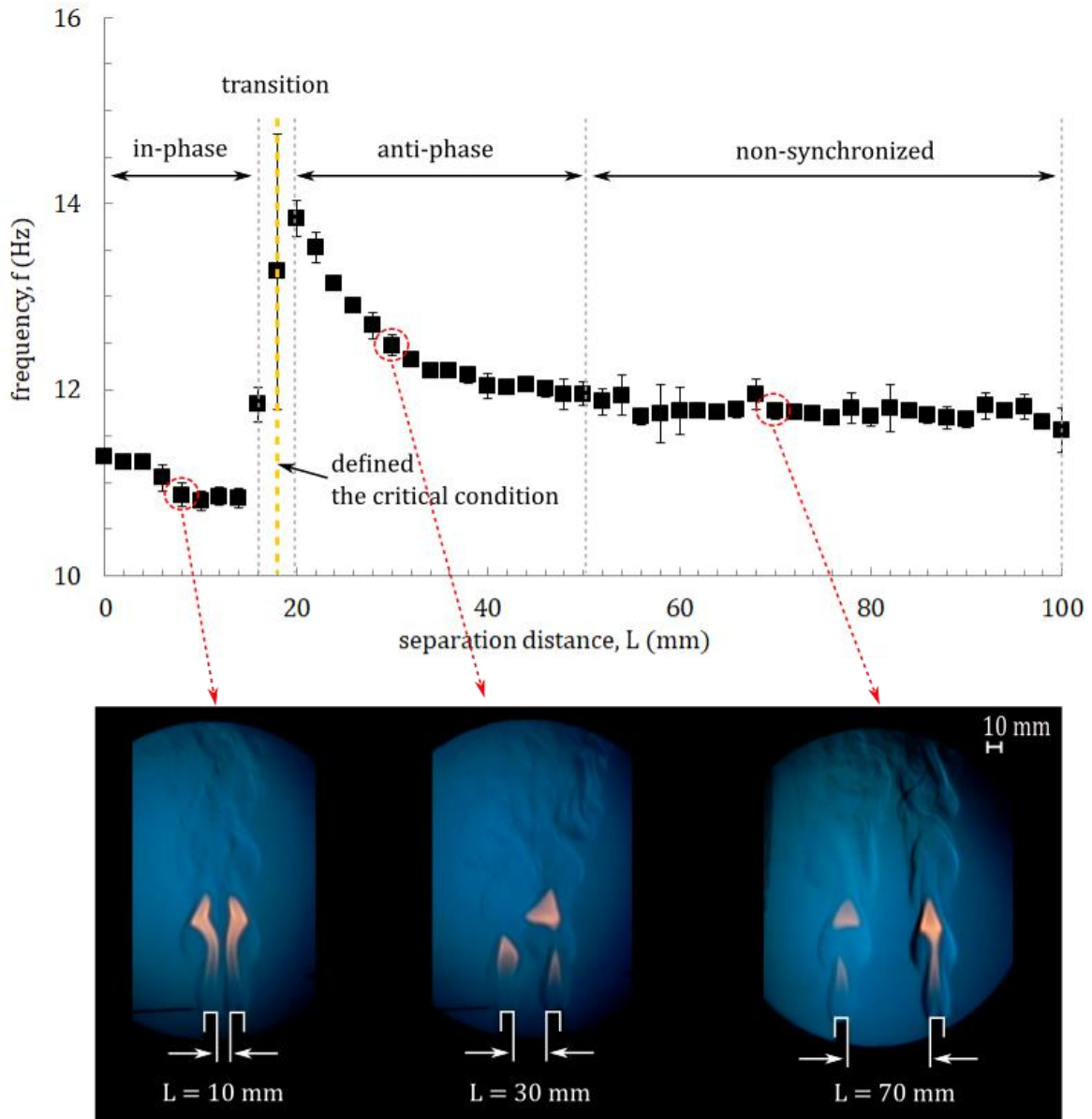


Fig. 4.12 Effect of burner separation distance on flickering frequency and each resonance dynamic modes ( $D = 10$  mm,  $Q = 500$  cc/min).

Characteristic frequencies stay nearly constant with the  $L$  modification, when the in-phase mode of dynamics is experienced, whereas it decays significantly when the anti-phase mode of dynamics comes up instead once the  $L$  is over the  $L_{\text{ct}}$ . The transition from one mode to the other occurs around 20 mm of the burner separation distance, defined as the “critical

condition” for mode change. It is interesting to note that uncertainty at the critical condition becomes extra-ordinarily large compared to other prescribed conditions. This is due to various modes that randomly appear, including two dynamic modes (in-phase and anti-phase), or even stationary (no motion), suggesting that this mode is quite unstable. Hereafter, the critical burner separation distance is denoted as  $L_{\text{crit}}$ . As the response of frequency depending on the separation distance ( $L$ ) provides the characteristics of the oscillation behavior presented in this system, we investigated  $f$ - $L$  curve with various  $Q$  and  $D$ . Note that  $L_{\text{crit}}$  is theoretically solely determined, however, there is certain (even narrow) range as shown in Fig. 4.12. Thus, in this study,  $L_{\text{crit}}$  is defined as the center value of transition range as shown in Fig. 4.12 (top).

#### **4.3.5 Effect of Fuel Flowrate ( $Q$ ) on Overall Oscillation Behavior ( $f$ )**

Figure 4.13 (a)-(c) shows typical Schlieren images at various fuel flowrates ( $Q = 500$  cc/min, 600 cc/min, 700 cc/min, respectively). Fig. 4.13 (d) summarizes the averaged flickering frequency which is considered as the characteristic dynamic measure of the present system, vs. the burner separation distance,  $L$  for  $D = 10$  mm (smaller burner case). In Fig. 4.13 (d), four cases in ranging fuel flowrate from 500 to 3500 cc/min are shown for direct comparison. From Figs 4.13 (a)-(c), a trend for flame height to increase as fuel flowrate increased was found. Further, the shape and the scale of hot-plume above the visible flame did not significantly differ under different flowrates. We deduced that the length of the bottom stem seemed to increase, which is most responsible for the increase of the flame height. In this regard, the fluctuation of the top part of the flame as well as the hot plume.

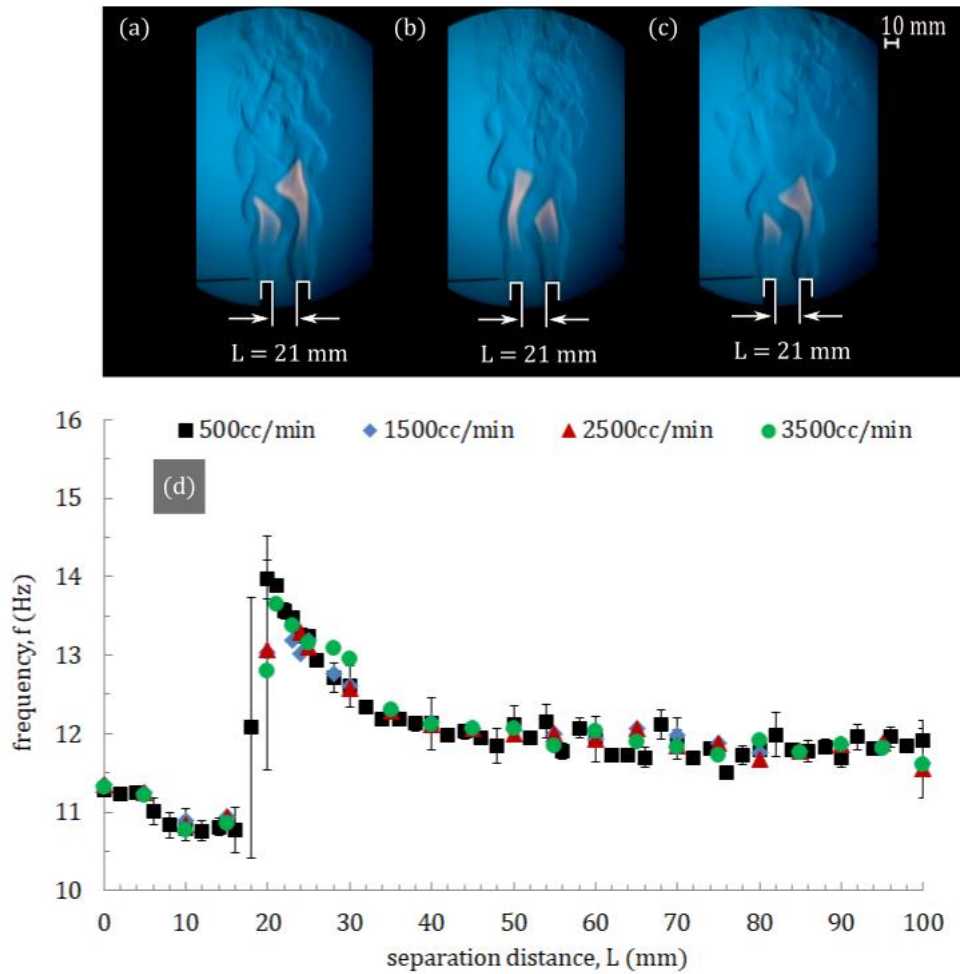


Fig. 4.13 Typical Schlieren images at various fuel flowrates (a):  $Q = 500$  cc/min, (b):  $Q = 600$  cc/min, (c):  $Q = 700$  cc/min, and (d) Effect of burner separation distance on flickering frequency for varying of fuel flowrate. All cases shown here are at burner diameter of  $D = 10$  mm.

In Fig. 4.13 (d), an abrupt frequency jump was clearly identified at the critical separation distance ( $L_{crit}$ ), nearly 20 mm for the wide range of the flowrate. More importantly, not only the jump condition (at transition), but also the overall dependency of frequency on the separation distance was nearly identical. This indicated that the periodic motion of the flame was quite insensitive to the jet momentum, ensuring that the periodical dynamic behavior

observed in this study was mainly governed by the buoyancy, not the inertia (momentum) of the fuel flow jet.

#### 4.3.6 Effect of Burner Diameter ( $D$ ) on Overall Oscillation Behavior ( $f$ )

Figure 4.14 (a)-(c) shows the typical Schlieren images at various burner diameters ( $D = 10$  mm, 18 mm, 30 mm, respectively, with  $Q = 900$  cc/min) and (d) summarizes the averaged flickering frequency which is considered as the characteristic dynamic measure of the present system, vs. the burner separation distance,  $L$ . The adopted fuel flowrate in Fig. 4.14 (d) is  $Q = 1000$  cc/min for smaller burner cases ( $D = 10, 18,$  and  $30$  mm), whereas  $Q = 2000$  cc/min and  $3000$  cc/min for larger burner cases ( $D = 45$  and  $55$  mm, respectively). Because a variation of  $Q$  does not have a significant effect on  $f$ - $L$  plane, as confirmed in the previous section (see Fig. 4.13), applying various  $Q$  values to investigate the effect of  $D$  on flickering frequency,  $f$ , is not really needed. In Fig. 4.14 (d), all five cases of burner diameters from  $D = 10$  mm to  $55$  mm are shown for direct comparison. Figs. 4.14 (a)-(c), show the neck part (eventually pinched off) gradually moving upstream (close to the burner surface) as the burner diameter increases. Obviously, the shape and scale of the hot plume above the visible flame are not constant, but increase as burner diameter increases. Because the gap size is the same for three cases, an interaction of thermal boundary layers formed around each flame as seen earlier for larger burner cases. This suggests that the critical transient condition for separation distance ( $L_{\text{crt}}$ ) is affected when the burner diameter is varied. In Fig. 4.14 (d), an abrupt frequency jump can be clearly identified at the critical separation distance ( $L_{\text{crt}}$ ) for all tested cases of the burner diameter. Frequency jump-gap before/after at the transition becomes smaller as the burner diameter increases, suggesting the difference between in-

phase and anti-phase is no longer clear enough, and the direct flame images tend to give a highly fluctuated appearance (unlike with smaller diameter as shown in Fig. 4.12 (bottom)).

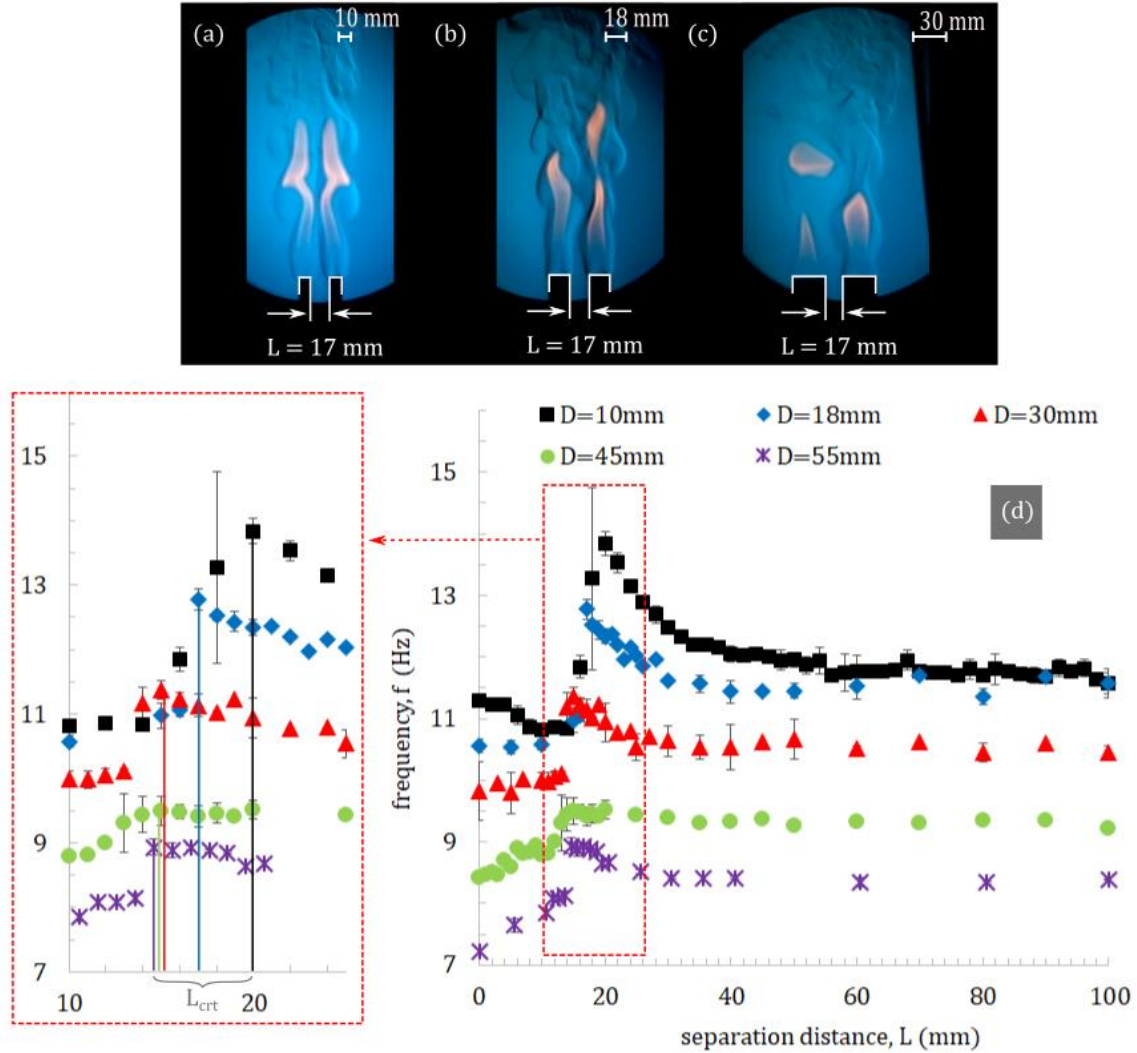


Fig. 4.14 A typical Schlieren images at various burner diameter (above):  $D = 10$  mm, (b):  $D = 18$  mm, (c):  $D = 30$  mm, with constant flowrate  $Q = 900$  cc/min. Effect of burner separation distance on flickering frequency for varying of fuel flowrate (bottom). Cases ( $D = 10, 18$  and  $30$  mm) shown here are at the constant fuel flow rate at  $Q = 1000$  cc/min, but  $D = 45$  and  $55$  mm of  $2000$  and  $3000$  cc/min.

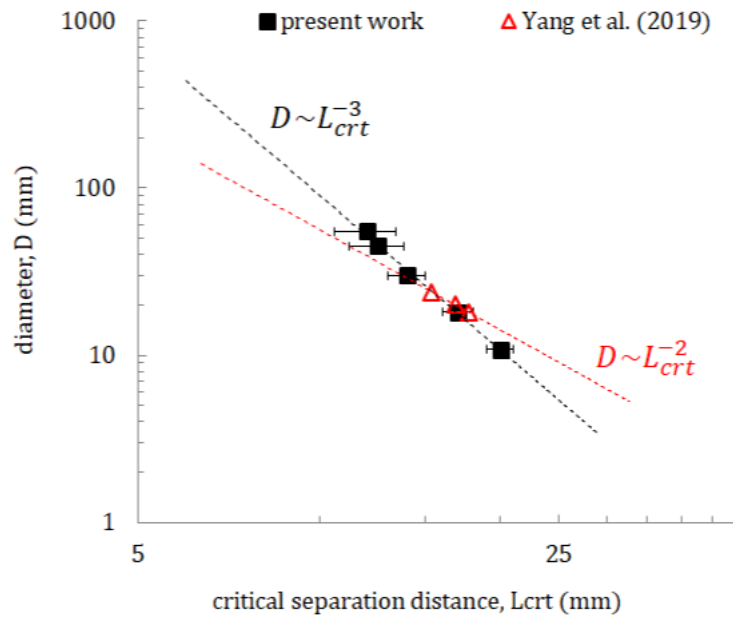


Fig. 4.15 Relation between  $L_{crit}$  and  $D$  based on the measured data in this study. Predicted values by Yang et al. (2019) are also embedded in the figure.

Figure 4.15, Relation between  $L_{crit}$  versus  $D$  at critical conditions of mode change, confirms that comparisons (previous work and present study) with  $f$ - $L$  plane is a solid strategy for examining the characteristics of oscillation behavior. Nevertheless, it is necessary to find a similar trend in  $f$ - $L$  plane for all tested cases. Most importantly, as noted in Fig. 4.14 (d), there is a clear dependency of  $L_{crit}$  on the adopted burner diameter. For instance, a larger diameter gives a smaller  $L_{crit}$ , under the conditions studied here, confirming that there are two important length scales ( $D$  and  $L_{crit}$ ) in the present system when the mode transition is being studied. Interestingly, these two important scales have clear a dependency, as summarized in Fig. 4.15,  $D \sim L_{crit}^{-3}$  (namely,  $D \times L_{crit}^3 \sim const.$ ). The predicted values (three plots) by Yang et al. (2019) are also embedded in the figure, showing their plots are well-fitted to the trend

obtained by the present experiment. With this respect, our experimental work for wider a range of fire scale ( $D$ ) may reveal a “universal” trend for transition behavior.

#### 4.3.7 Updating the Mode Transition Model

When discussing the update modeling on the mode transition behavior of the two flickering flames, there are several assumptions to apply. (1) The flame sheet model can be adopted (we can assume that Damkohler number is infinity, suggesting that the transition phenomena is far from either ignition/extinction); (2) Lewis number is unity; (3) the presence of a burner plays a minor role on overall flame dynamics (namely, the boundary layer formed by the burner is not really important; (4) radiation does not have a primary role in flame dynamics (see Mochizuki et al., 2017). Further, Grashof number ( $Gr = gD^3/\nu_A^2$ ;  $g$  is gravity acceleration,  $\nu_A$  is dynamic viscosity of air) is the only responsible non-dimensional number to describe the dynamics in the present system. In addition, we have already learned from Fig. 4.14 that there are two important length scales in this system,  $L$  and  $D$ . Hence, we should consider their ratio ( $\alpha = L/D$ ) as the additional non-dimensional number to characterize the target phenomena. Finally, the characteristic parameter to govern flame behavior in the present system (including the transition), say  $\Lambda$ , shall be described as the combination of two non-dimensional groups which has been derived in section 2.4.

$$\Lambda \sim \alpha^n Gr^m = \left[\frac{L}{D}\right]^n \left[\frac{gD^3}{\nu_A^2}\right]^m \quad (4.1)$$

To fulfill the observation, as confirmed in Fig. 4.16, the exponent of  $n$  must be equal to 3 obtained from Fig. 4.15, so that the order of  $4/3$ , regarding this matter, is also the value of the exponent of  $m$  to complete this formula.

$$\Lambda \sim \alpha^3 Gr^{4/3} = \left[ \frac{L}{D} \right]^3 \left[ \frac{gD^3}{\nu_A^2} \right]^{4/3} \quad (4.2)$$

From Eq. (2.5),  $\Lambda_{\text{crt}}$  can be presented in the form of Reynolds number based on the buoyancy-induced flow and the burner separation distance at transition ( $Re_L$ ).

$$\Lambda_{\text{crt}} \sim \alpha^{(n-2)/3} Re_L^{2(n+1)/3} = \alpha^{1/3} Re_L^{8/3} \quad (4.3)$$

This Reynolds number is not the one to characterize the jet flow but the one to characterize the transport between two burners (gap Reynolds number).

Recall that in Yang's work (2019), a modified Grashof number ( $\alpha Gr^{1/2}$ ) was proposed with a characteristic global parameter, to summarize the transition under the range considered, which is the limited range of the fire scale with limited data (see Fig. 4.15). In fact, in their report, Yang et al. found that their global parameter gave some discrepancy and they explained this via temperature dependency on viscosity. An updated global parameter,  $\alpha^3 Gr^{4/3}$ , works better for a wide range of the transition, and discrepancy shall be minimized. To confirm this, we have attempted to summarize all data available into Fig. 4.16, using an updated global parameter, and a comparison indicates that the updated parameter works well in revealing the critical condition in a more precise manner.

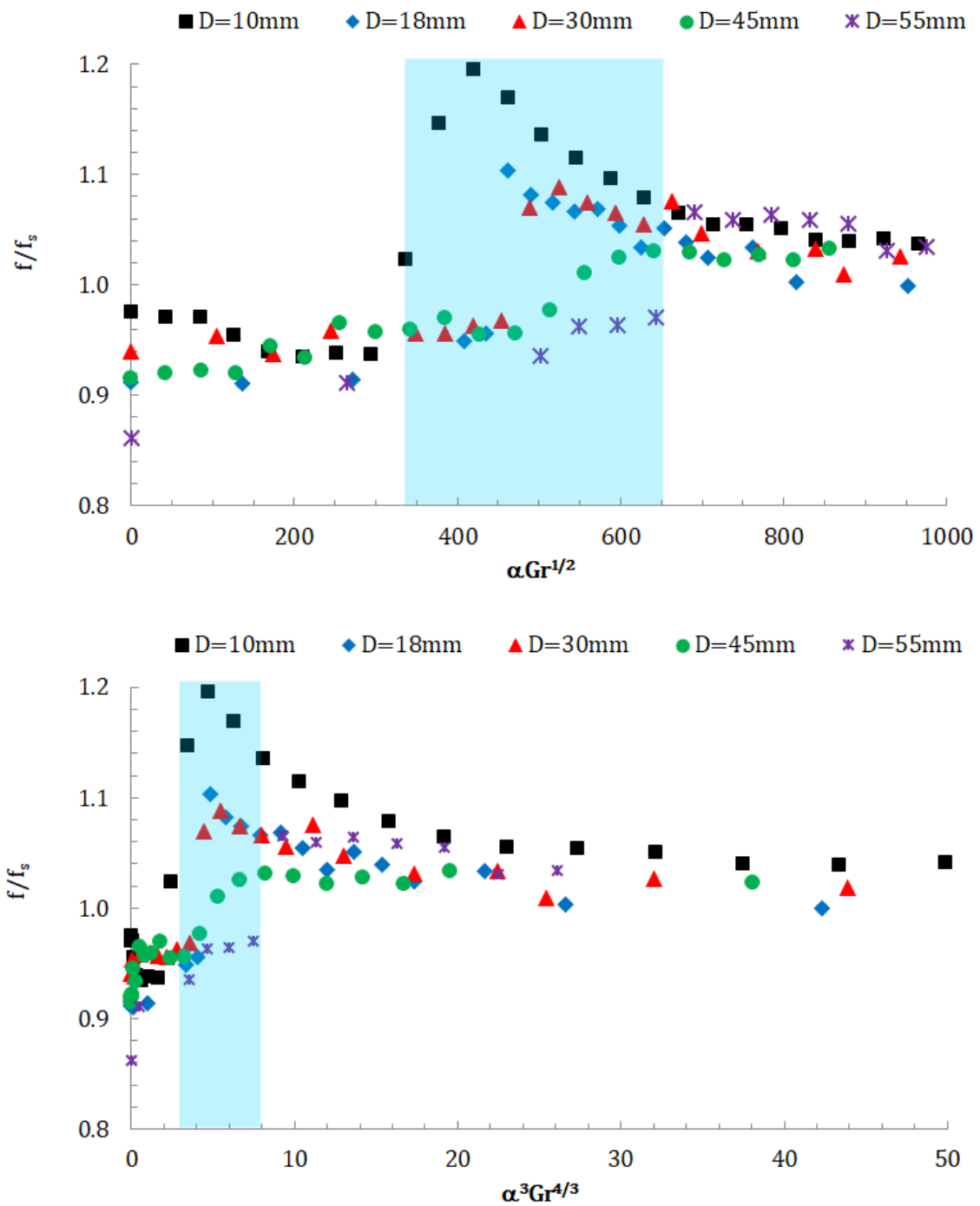


Fig. 4.16 Nondimensional frequency (by frequency at transition:  $f_s$ ) as a function of the characteristic of global parameter (either (a)  $\alpha Gr^{1/2}$  or (b)  $\alpha^3 Gr^{4/3}$ ). The solid symbols correspond to the experimental data.

## 4.4 Conclusions

It was found that the transition of mode change is sensitive to the modified  $L$  and  $D$ . Those were used to scale the target phenomena. The critical condition could be summarized by  $Gr$ -number ( $Gr = gD^3/\nu_A^2$ ) and ratio of length scale ( $\alpha = L/D$ ). An updated correlation as  $D \times L_{\text{crt}}^3 \sim \text{const.}$ , found slightly different from the one recently proposed by Yang et al., (2019), which was given under a narrow range of the fire scale ( $D$ ). The critical condition can also be described by this critical value of the global parameters, such as  $\alpha^3 Gr^{4/3}$ , where  $\alpha$  and  $Gr$  denote the length ratio ( $L_{\text{crt}}/D$ ) and Grashof number based on the inner diameter of burner. Additionally, the target phenomena under the adopted size of burners with the prescribed examining conditions is more pronounced to behave in 2-D plane of twin-flame system.

## Chapter 5

# Similarity of Dynamics Behavior of Buoyant Single and Twin Jet-flames(s)

### 5.1 Introduction

The second target of the research objectives pointed out at section 1.5, is focused on in this section. To understand the transition phenomenon of flame dynamics in single (pool) fire is motivated. This event (transition) was observed by Cetegen and Dong since 2000, but its instability mechanism have not been explained clearly yet. Thus the critical condition to present the transition (having sinuous mode) in the single fire is not easy task in practice. Whereas, the critical Reynolds number bases on the gap winding cold-air can possibly be applicable to the single fire if a proper way of interpretation can be proposed. In order to achieve this purpose, the similarity of the periodically dynamic behavior of both buoyant single- and twin-jet flame(s) is discussed from scientific way. Aside from identifying any similarity in flame dynamics of two different systems, this study highly aims to the applicable way for providing a proper interpretation of mode transition found in single-flame system. The asymmetric motions: sinuous mode for single-jet flame and anti-phase mode for twin-jet flames, are paid attention on detailed physics. In summary, the relation between the frequency difference and (effective) length scale ( $\Delta f - D_{\text{eff}}$ ) is provided nicely by introducing the concept of an equivalent area of momentum diffusion across the middle gap of burners. Therefore the similarity of the asymmetric oscillating flow behavior appearing in the single- and twin-flame systems can be interpreted properly. The  $Re_{\text{crit}}$  (Karman vortex

feature),  $Re_f$  (single jet flame), and  $Re_L$  (middle gap winding cold-flow) are discussed as the ideal candidate to characterize the transition in the different systems.

## 5.2 Methodologies

### 5.2.1 Experimental Apparatus

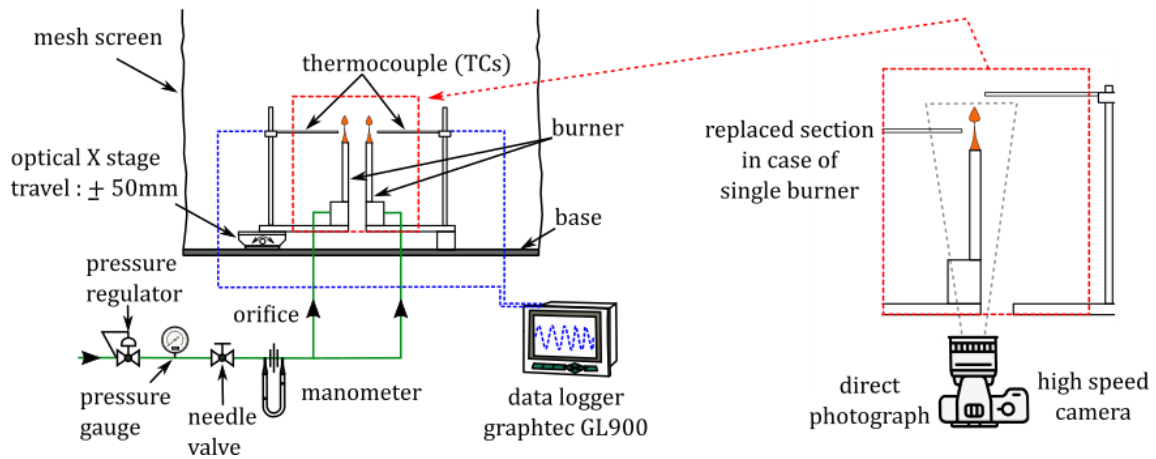


Fig. 5.1 Schematics of experimental apparatus, the burner arrangement for single fire is replaced as shown in the blowup section.

Figure 5.1 shows the schematics of experimental apparatus applied in this section. The setup for twin-flame system is pretty same as pointed out in section 4.2, but slight modification makes the system suit the investigation of single fire so that a brief explanation is made here. All experiments were performed at in the open, in the laboratory. The experiment was repeated for least twice in common cases, whereas, over five times are needed for single fire because of highly unstable oscillating behavior. Sample standard deviation was adopted for

uncertainty. Round-shaped burner was located vertically and research grade methane gas was issued upward at identical flowrate. Flowrate of the methane was controlled by a controlling system through the applied hand-made monometer. Multi-layered mesh screens surrounded the apparatus in order to eliminate any undeniable disturbance from the ambient to modify the fundamental dynamic mode of interaction effect. After ignition by fire torch, the system allowed to stabilize before recording data. Dynamical flame was directly recorded by a high-speed camera, recording through both the direct shooting and optical system. Harmonic frequency of oscillatory motion was tracked by two points of different height equipped thermocouples, i.e. vicinity near the exit and two times height of burner diameter. Its frequency was analyzed by operating the FFT of the input time signals of field-temperature variation collected by data logger at 10 millisecond of the sampling rate. Investigation was performed under the buoyant condition,  $Fr < 1$ . The range of  $Q$ , and  $D$ , including the  $L$ , varied in this study can be observed in Table 5.1.

### **5.2.2 Schlieren Imaging**

The applied visualizing system is physically same as described in section 3.1, but it was slightly modified in here by replacing the modified apparatus of single fire as observed in Fig. 5.2 (the test section). So it is briefly discussed here. One thing should be careful when the apparatus is moved the arrangement of Schlieren system must be retained. If it is even slightly out of the alignment of optical devices, the optical image gets blurred, the more time-consuming is needed for setting up and adjusting the device, especially, adjustment of the light paths. The shooting frequency of light source should perfectly match with the camera filming rate avoiding the black dots (frame overlapping) appearing in the image plate.

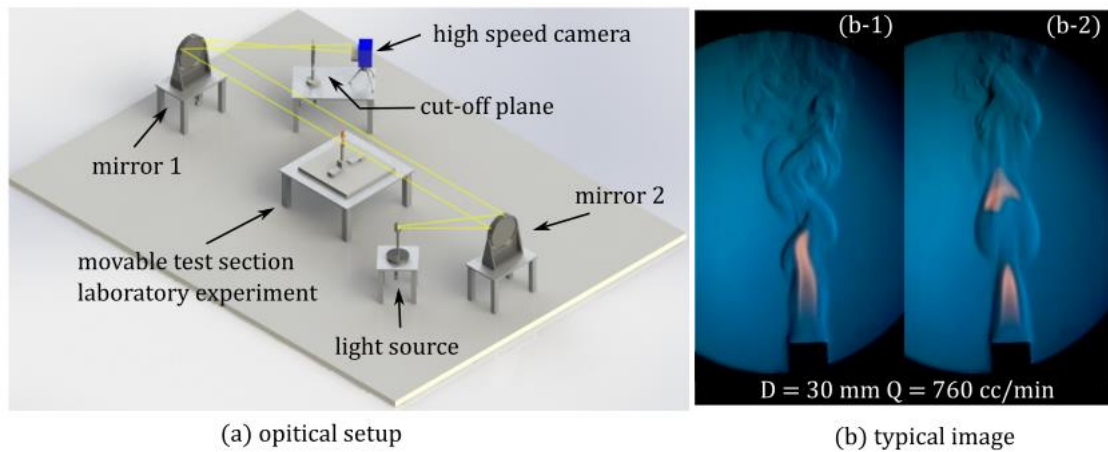


Fig. 5.2 Schlieren optical imaging system (a) and representative images observed at  $D = 30$  mm,  $Q = 760$  cc/min: Sinuous mode (b-1) and Varicose mode (b-2), occurring randomly in time, indicating the representative boundary of thermal layer.

## 5.3 Results and Discussion

### 5.3.1 Single Fire Case: Varicose and Sinuous Modes

Figure 5.3 ( $D = 18$  mm,  $Q = 520$  cc/min) and Figure 5.4 ( $D = 30$  mm,  $Q = 850$  cc/min), show the typical sequential image of direct photograph of fluctuating methane diffusion flame in varicose mode (a) and sinuous mode (b). Reproducibility of the two modes of flame dynamics can be identified. These oscillating fashions are similarly pointed out by past work [Cetegen & Dong, 2000]. Typically three cycles of visible flame oscillation are shown. However, please remember that these found by chance and they are selected at a specific period of the observed time for description. See the (a) of Fig. 5.3 and 5.4, the typical images of varicose mode are shown with axisymmetric motion of visible flame oscillation. On the

contrary, those of the sinuous meandering fashion of flame behavior are found in the (b) of both figures.

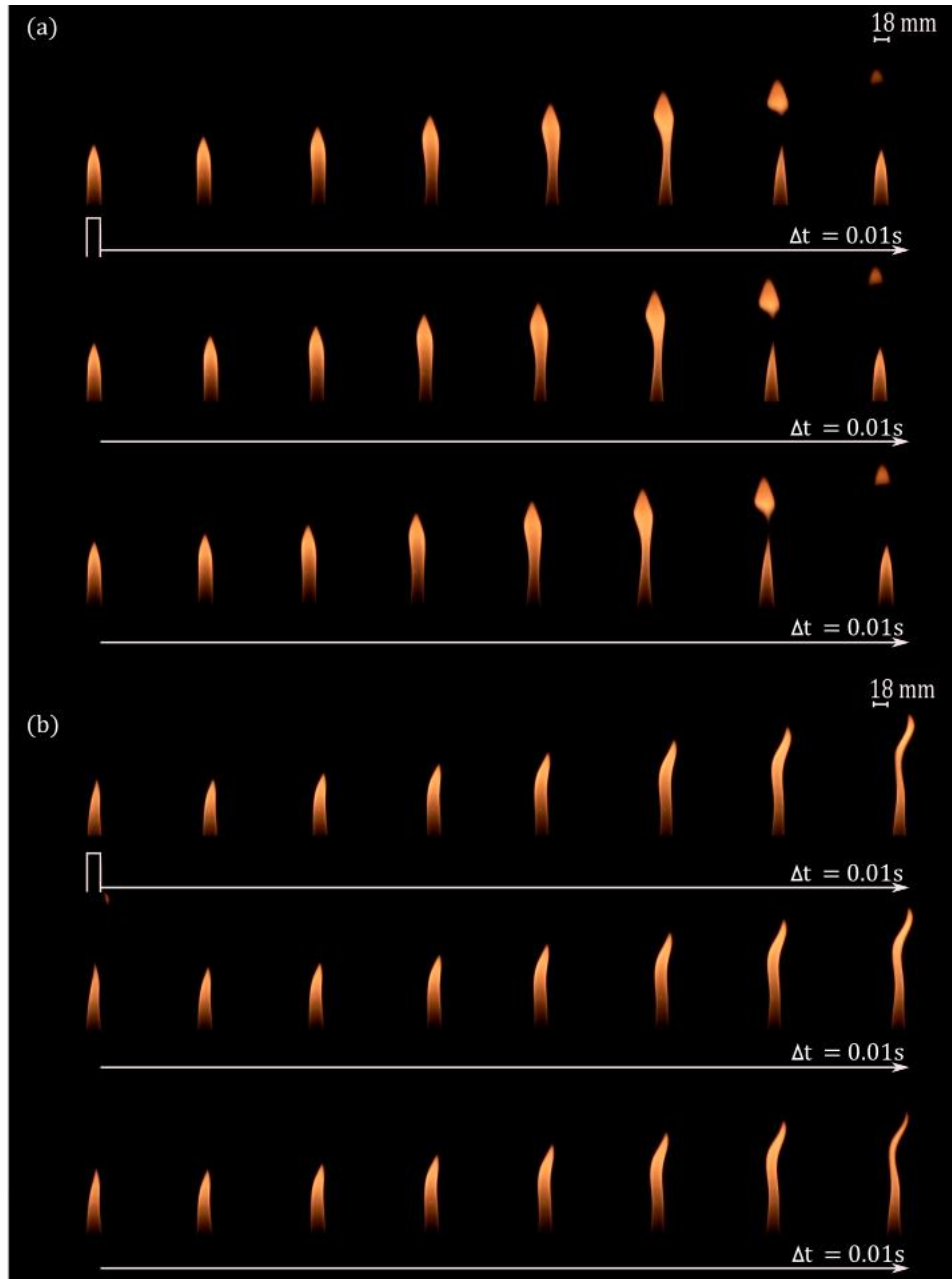


Fig. 5.3 Time-sequence images of direct photograph of fluctuating methane diffusion flame:  $D = 18\text{ mm}$ ,  $Q = 520\text{ cc/min}$ , (a) Varicose mode and (b) Sinuous mode.

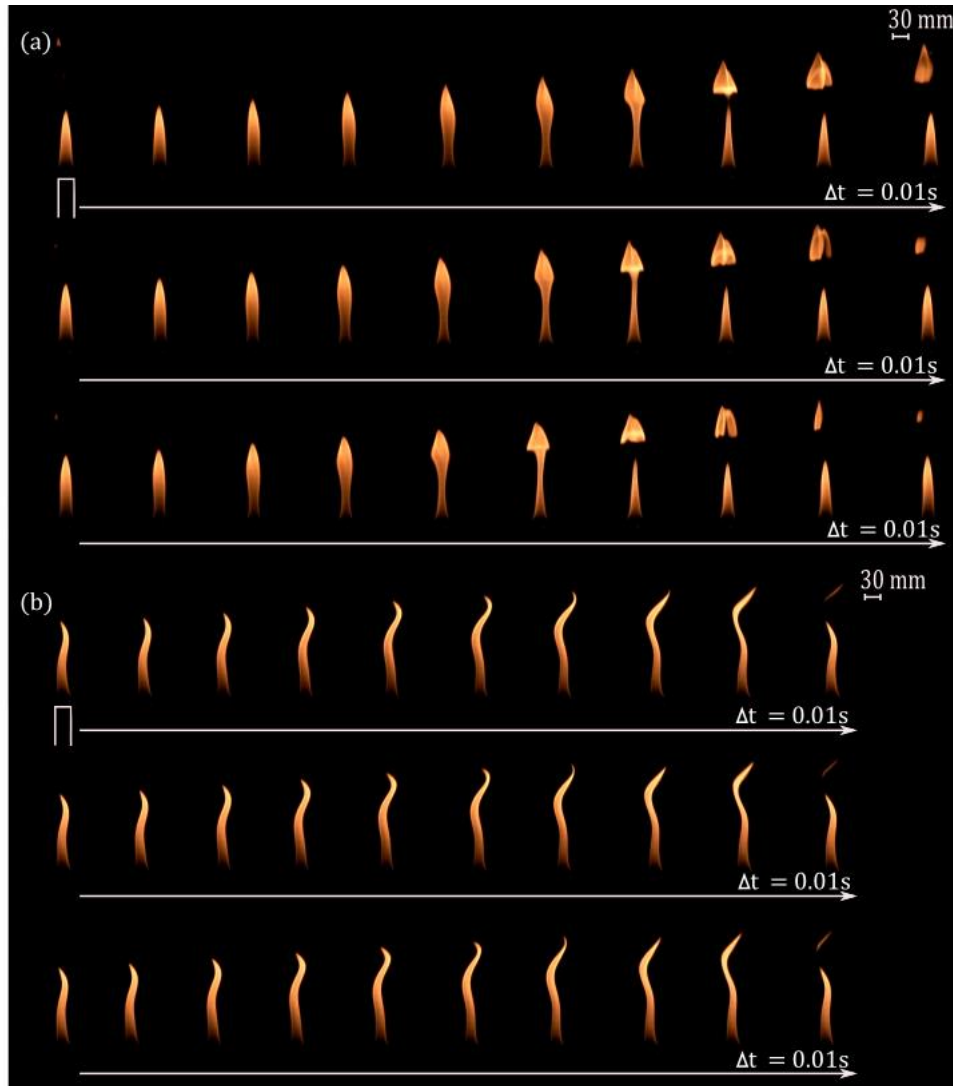


Fig. 5.4 Time-sequence images of direct photograph of fluctuating methane diffusion flame:  $D = 30 \text{ mm}$ ,  $Q = 850 \text{ cc/min}$ , (a) Varicose mode and (b) Sinuous mode.

The visible flame becomes more slender shape when burner becomes larger. This is because the buoyancy due to chemical energy release becomes more intensified bring more the high buoyant acceleration in flow field. Even though the disturbance is satisfactory suppressed by the mesh, it is obviously observed that both modes appear randomly, not even obtain the complete axisymmetric shape. In this regard, there is no preference to present under the

specific condition having been adopted thus far. One thing is very interesting feature that is the presence of peak (frequency jump) when the mode switches another mode as shown in Fig. 5.5, the time-sequence of the TC signals (a), corresponding with the FFT analysis (b)(c), of single methane flame oscillation for  $D = 30$  mm,  $Q = 850$  cc/min picked up the signals at  $2D$  height of burner-exit (a)(b), and (c) at  $3 \times 3$  mm above and offset the tip of the burner.

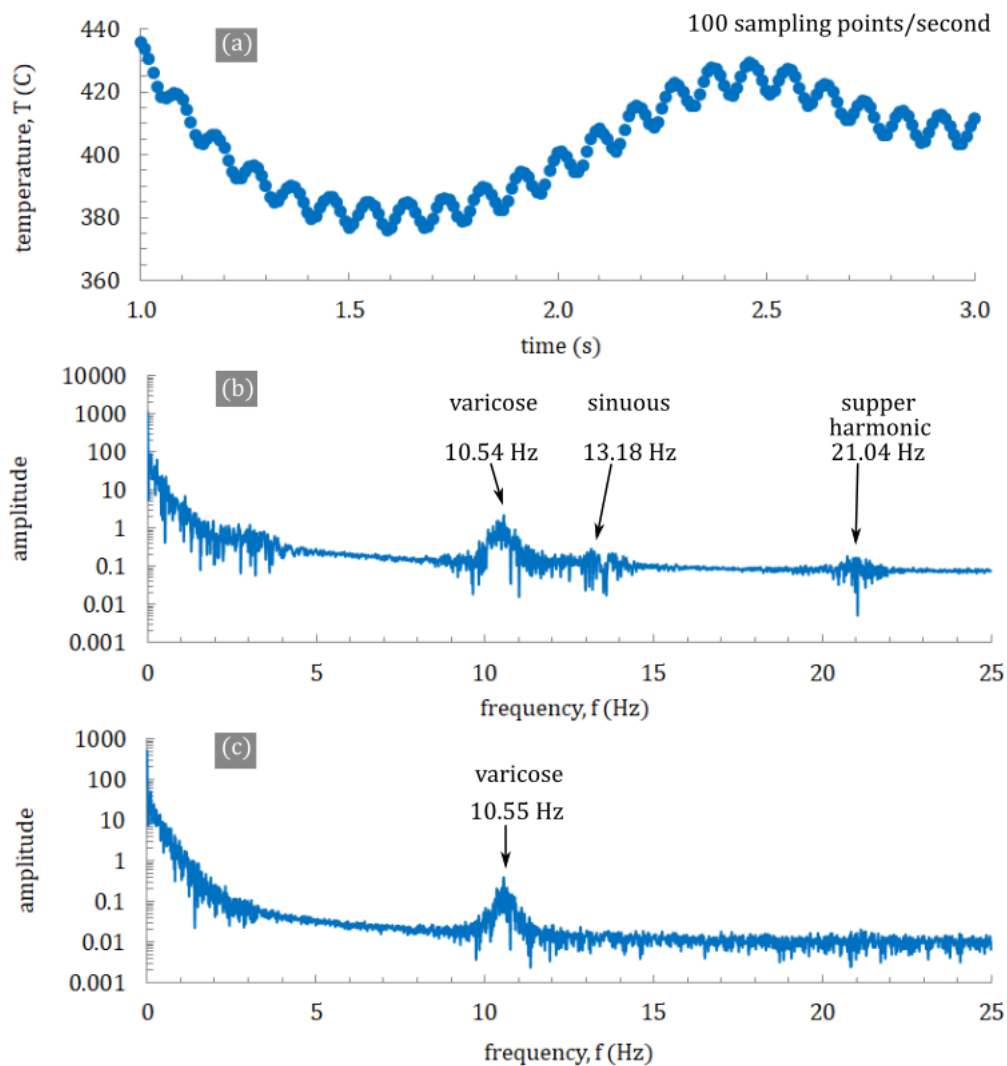


Fig. 5.5 Time-sequence of the TC input signals corresponding the FFT frequency analysis data for single methane flame:  $D = 30$  mm,  $Q = 850$  cc/min picked up the signals at  $2D$  height of burner-exit (a)(b), and (c)  $3 \times 3$  mm above and offset the tip of burner.

The strongest peak shown in here is found at 10.5 Hz showing the varicose mode that often takes longer time to appear, then it comes following the second harmonics, around 21 Hz. Small spire comes additional for TC's signals analysis and the sinuous mode is defined through it. Peak becomes weak but it is observable, around 13.2 Hz, because this mode appears randomly in time and short period is taken when this mode appears. Notice the FFT frequency analysis, only TC at double diameters of height can capture this type of dynamics because of its own nature of asymmetric flow development (the onset of instability). Not likely the sinuous mode, the varicose mode develops at very earlier stage of ejecting fuel, saying that the onset is close to the burner-exit. So this is why we sampled the whole bundle of flame dynamics by two thermocouples equipped at different height. Regarding this analysis, sinuous mode has higher frequency than varicose one when the prescribed condition is adopted and they simultaneously appear in the considered system when the time goes by.

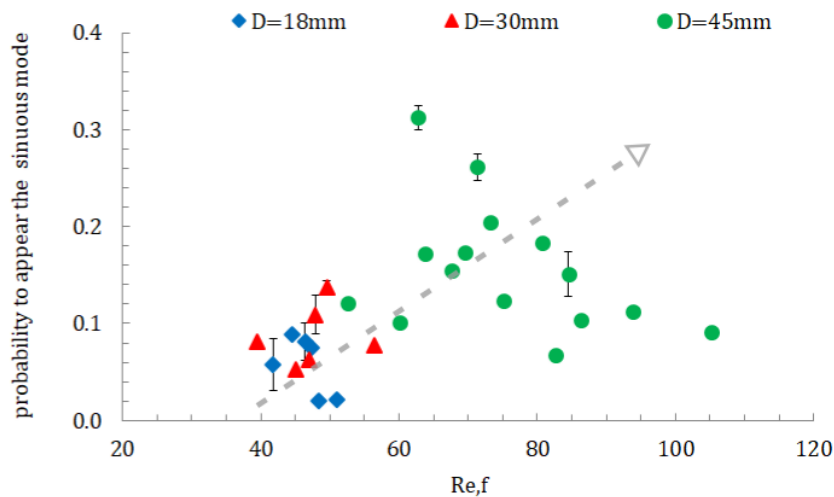


Fig. 5.6 Probability of appearing sinuous mode against the adopted Reynolds number for single methane diffusion fire.

Figure 5.6 shows probability of appearance of sinuous mode in single fire with various sizes of fuel source and ejecting fuel velocities. The observed probability is plotted against the Reynolds number ( $Re_f$ ) based on the velocity of ejecting methane gas. From literature review, Yang and coworker proposed the model to characterize the two synchronized buoyant pool fires. This is highly possible that the Reynolds number can be adopted to describe the mode change found in single fire if the same mechanism occurs in both different systems of flame dynamics. Therefore observation of sinuous meandering occurrence is done under this regard. By our great effort of experimental performing and of tedious image analysis, three different sizes of circular burner and fuel flowrates designated as prescribed conditions ( $D = 18, 30, 45$  mm and  $Q \sim 500-2300$  cc/min) are successfully done. The analyzing data found in Fig. 5.6, seems much fluctuated, but such clear trend of the probability increase can be found out. Increasing the adopted Reynolds number trends to bring more chance having sinuous meandering fashion, but the unity of probability is never achieved because, in reality, this mode does not always appear in the system of single fire. Anyway let's further infer that there must have a certain value of Reynolds number to trigger the sinuous meandering motion frequently appearing in the system so that the  $Re_{crit}$  to promote the sinuous mode must be there, but it cannot be well-determined yet. Hereto, a proper interpretation of appearance of mode change in single-flame system seems very hard to reveal the academically scientific information without some special tricks. Therefore, the twin-flame system is introduced and their flame behavior will be compared both the detailed physics and characteristic quantity bases on the similarity matter from scientific way.

### 5.3.2 Periodic Axisymmetric/Asymmetric Motions in the Single- and Twin-flame(s) Systems

In Figs. 5.7 and 5.8, typical time-sequential images showing periodic axisymmetric (Fig. 5.7) and asymmetric (Fig. 5.8) motions found in the single- and twin-flame systems. For the reference purpose, the flame images from the past work done by Cetegen and Dong (2000) is also added in (a). Figure 5.7 (a), only time-sequential flame images are shown and no other information (e.g., flow pattern, plume shape) is provided. Furthermore, the flame axis is slightly tilted probably due to the environmental disturbance, suggesting that even obtaining “ideal” axisymmetric motion is not an easy task. Nevertheless, it is clearly observed that flame exhibits the typical varicose fashion: namely, clear top-cap detachment as a result of squeezing neck due to the buoyancy-induced flow, then revealing the periodic motion. Figure 5.7 (b), a cycle of flickering at varicose mode is imaged through the Schlieren optical system to visualize the variation of hot plume shape as well as direct flame shape in time. This figure shows that the necking (locally squeezing the hot plume) occurs at upstream to form mushroom-shape of the flame, then travels to downstream in time, eventually the top part of the flame is detached to generate the fragment. It is understood that the hot plume and the flame are similarly deformed in earlier stage, whereas their inconsistency is pronounced when it is close to the detaching process. This suggests that air entrainment induced by the buoyancy would not reduce the temperature much but sufficient to bring the local extinction to separate the flame there. Once the local extinction is experienced, top part of the remained stem stays there although the necking generated at the upstream travels toward to downstream. This becomes the trigger to form mushroom flame as found in the figure to have the periodic “varicose” behavior. With this respect, buoyancy flow shall be

responsible for the whole dynamics appeared in the gas-phase and control periodic frequency of the system.

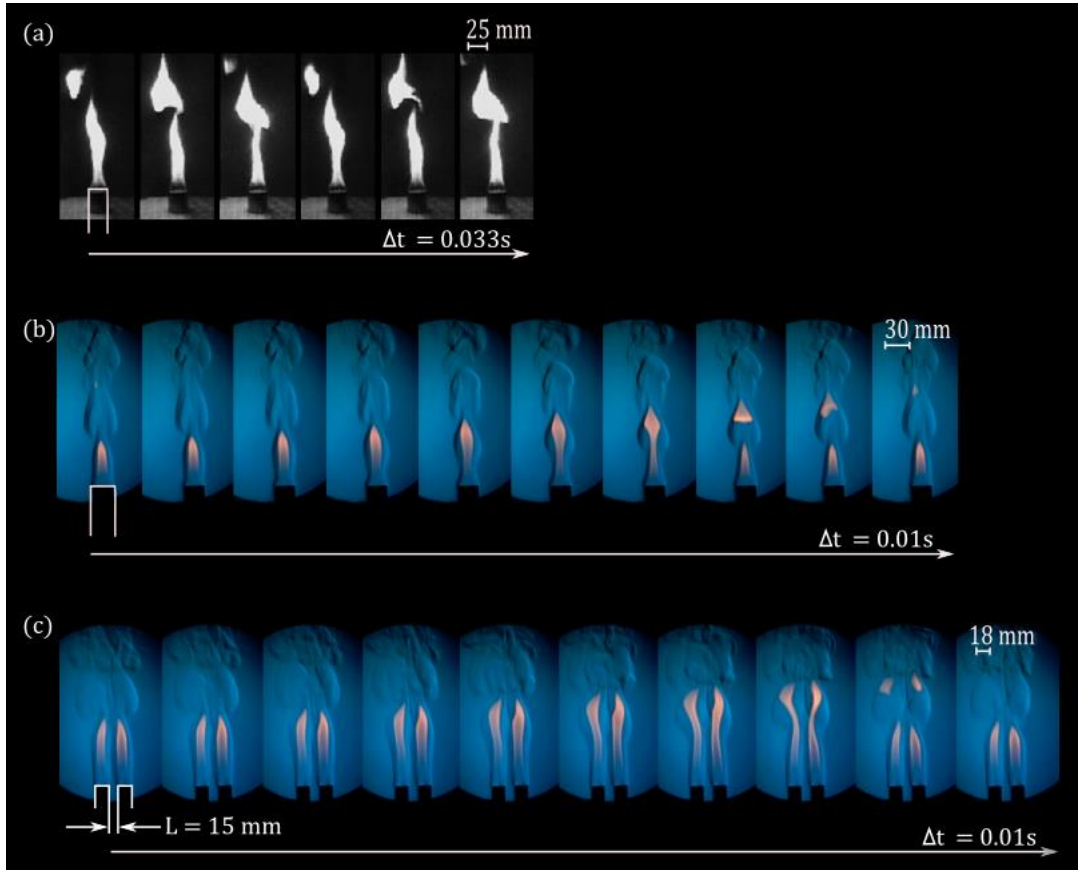


Fig. 5.7 Time-sequential images of pulsating fire(s) with varicose (a)(b) and in-phase (c) modes, respectively. (a) is referred from the work by Cetegen and Dong (2000); single propane-air flame with  $D = 25$  mm and fuel flowrate is 570 cc/min. (b) Schlieren images of single methane-air flame with  $D = 30$  mm and  $Q = 760$  cc/min, (c) Schlieren images of twin methane-air flame with  $D = 18$  mm,  $Q = 1000$  cc/min,  $L = 15$  mm.

Figure 5.7 (c), a cycle of the in-phase oscillation presented at shorter burner-separation distance is shown (15 mm in this case) for twin-flame system. Although the flame shape is

different to that observed in Fig. 5.7 (b), essential physics are basically identical. On the contrary, the outer layer of hot plumes are strongly deformed to cause the necking. It is noted that the hot plume over the flames merged satisfactorily to form the (unified) cluster of the hot product gases. Although it is not very clear, hot plume zone between the flames merges relatively observed through the laboratory experiment. The numerical prediction will be introduced to confirm this hypothesis which is shown in next chapter (Chapter 6) as well.

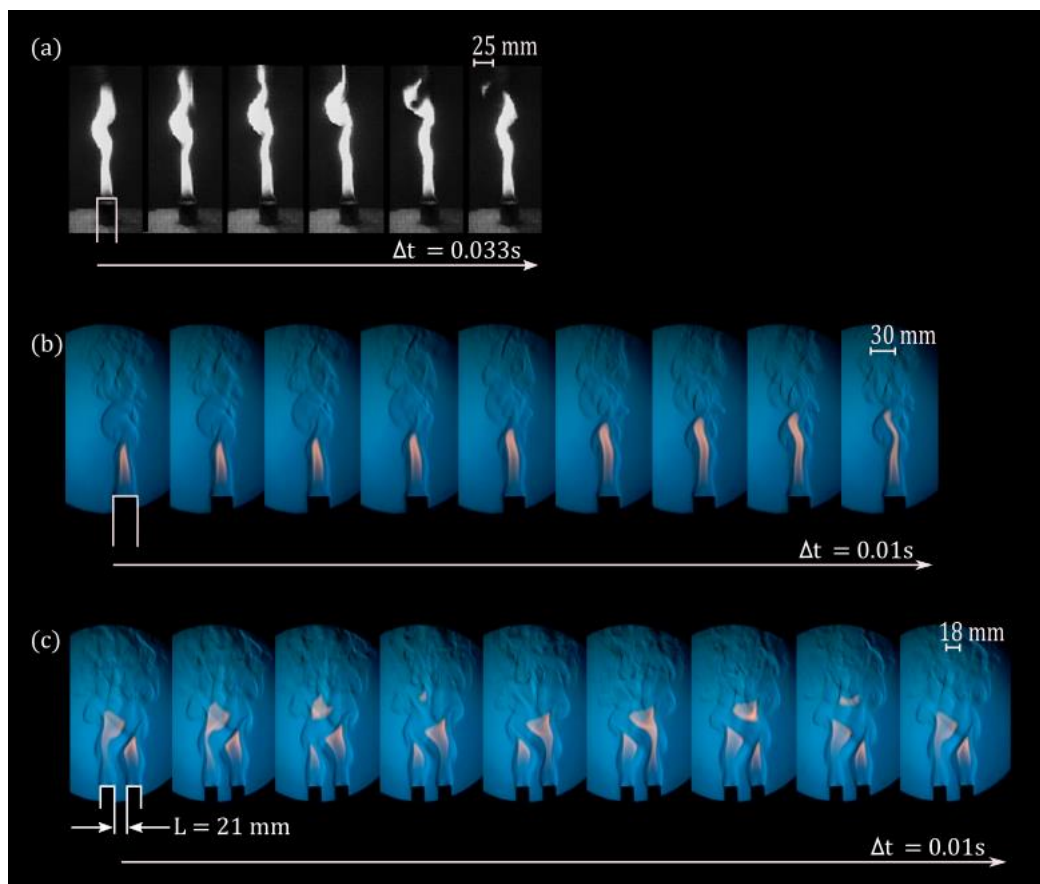


Fig. 5.8 Time-sequential images of pulsating fire(s) with sinuous (a)(b) and anti-phase (c) modes, respectively. (a) is referred from the work by Cetegen and Dong (2000); single propane-air flame with  $D = 25$  mm and fuel flowrate is 570 cc/min. (b) Schlieren images of single methane-air flame with  $D = 30$  mm and  $Q = 760$  cc/min, (c) Schlieren images of twin methane-air flames with  $D = 18$  mm,  $Q = 1000$  cc/min,  $L = 21$  mm.

Figure 5.8 shows the detail time-response during the asymmetric flame behaviors (sinuous mode in single-flame system, whereas anti-phase mode in twin-flame system). Figure 5.8 (a), similar to Figure 5.7 (a), time-sequential images of sinuous mode reported by Cetegen and Dong (2000) is added for the reference purpose. Flame exhibits winding shape although it is not very clear, suspecting that such flame behavior might be considered as the random perturbation. Figure 5.8 (b), evolution process to achieve the sinuous meandering is taken through the Schlieren optical system. Note that the hot plume formed over the flame exhibits asymmetry even though the flame does not show as such behavior. Triggered by the asymmetric perturbation over the flame (traveling to the upstream), flame tip starts to winding, then eventually whole flame achieves sinuous mode. Figure 5.8 (c), a cycle of the anti-phase oscillation presented at (relatively) larger burner separation distance (21 mm in this case) is shown using twin-flame system. Clearly two flames flicker asymmetry fashion with detaching the cap alternatively, which is not found in the single-flame system (Fig. 5.8 (b)). Interestingly, its shape exhibits sinuous meandering motion, which is similar to the flame shape exhibited in Fig. 5.8 (b). The hot plume over the flames is noted to severely fluctuate. Although it is not observed clear by the present, the cold-air can find the gap and it ought to penetrate through the interface plane of two flickering flames eventually. This scene will also be confirmed again by the computational results in the next (Chapter 6).

### 5.3.3 Transition in Single- and Twin-flame(s) Systems

Figure 5.9 compares the sequential images during the mode transition in single-flame system (a) and twin-flame system (b). As reported previously, the appearance of the sinuous mode is not well controllable and it is found by chance (the (a)). Hence the pictures presented here are extracted at the specific period of the event of interest. It is true that the time interval presented here cannot completely cover the whole dynamics of flame oscillation; nevertheless, important behavior could be observed the onset of the transition. As seen in the very beginning at the top in (a) ( $0 < t < 0.3$  sec), flame initially shows that the typical laminar fashion and less wrinkled of the hot plume are observed. Gradually the flame height increases, accordingly, the hot plume exhibits “puffing” motion to achieve the varicose mode ( $0.3 \text{ sec} < t < 0.7 \text{ sec}$ ). Although it continues for a while, interestingly, the flame trends to “cease” ( $0.7 \text{ sec} < t < 3.3 \text{ sec}$ ). During such temporal “freezing” behavior in the flame, the post-flame zone (hot plume) is kept exhibited the “puffing” motion. The plume shows axisymmetric (varicose mode) motion, however, it gradually turns into asymmetric (sinuous mode) motion, especially at the downstream (away from the flame). Simultaneously, the remained stem part of the flame gently elongates with time, and the flame top interact the asymmetric dynamics motion in the downstream and re-start to flicker at an asymmetric mode, revealing the sinuous meandering. Once the flame exhibits the sinuous motion, the mode sustains for a while ( $8.8 \text{ sec} < t < 10.2 \text{ sec}$ ) by varying the flame height in time. Although not shown here, after certain time, mode transition occurs (again) to back to varicose mode with some delay time. From this observation, it is understood that the mode transition shall be achieved with the certain “reset” term (i.e. delay time), not just randomly change suddenly one to the other. Hence, it is difficult to tell that which mode is more stable, furthermore, we must admit that having sinuous mode for long time is almost impossible.

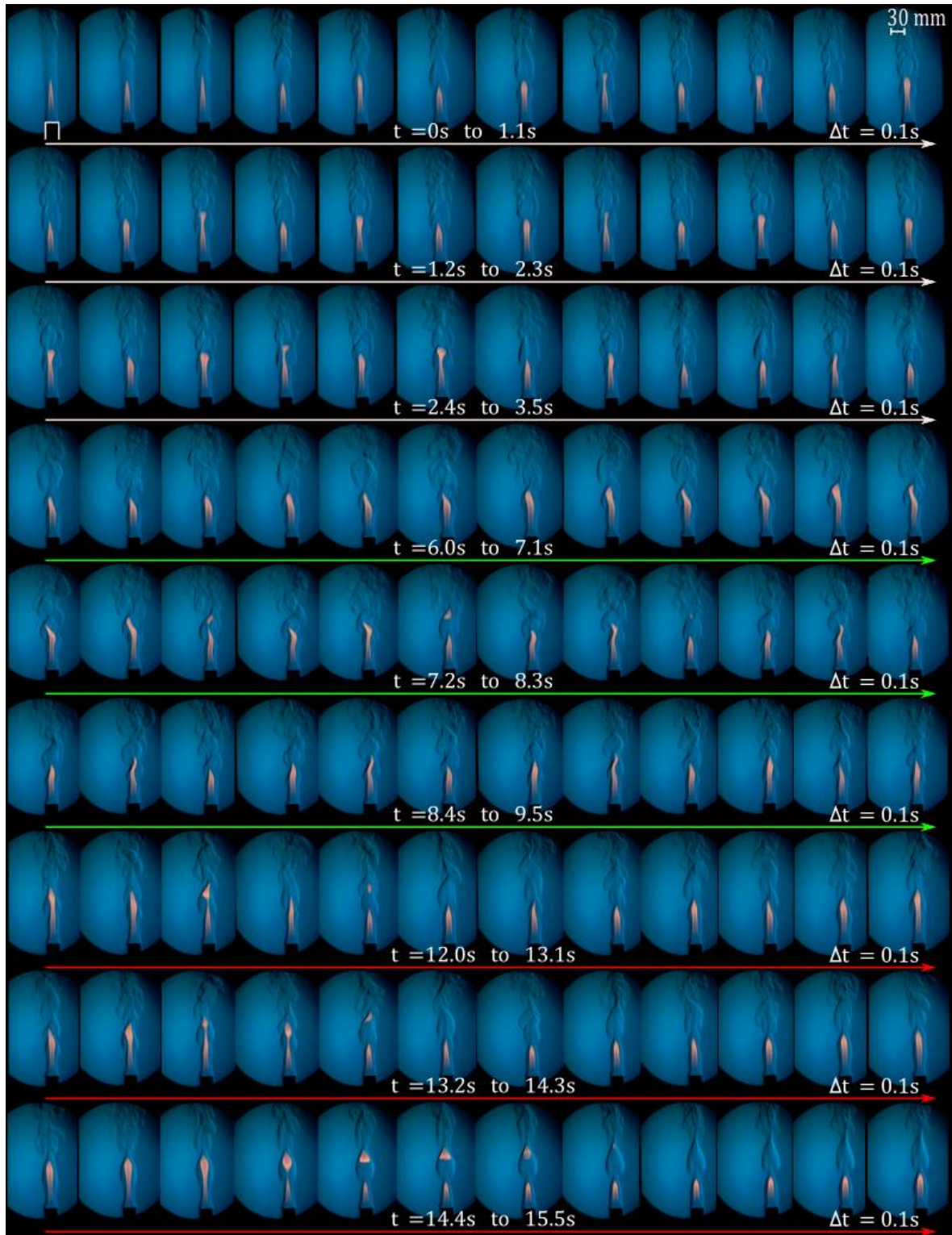


Fig. 5.9 (a) Typical optical image-sequence of coexisting the varicose and sinuous modes for single fire ( $D = 30$  mm,  $Q = 760$  cc/min,  $\Delta t = 0.1$  s).

Figure 5.9 (b), the mode transition in the twin-flame system is shown. As shown in the figure, the transition one mode to the other is rather faster than that in the single-flame system (a) (note that the time interval of the images is not the same order magnitude in (b)). It might be because that the asymmetric plume formation over the flame is rather easy to occur in the twin-flame system. As already understood, having a bit larger burner separation distance, flames exhibits anti-phase mode and no in-phase mode appears. Alternatively, having a bit smaller distance, flames exhibits in-phase mode and no anti-phase mode appears. Hence the controllability of the mode transition one to the other is much better than that of the single-flame system. Before the transition occurs, although the flames are nearly identical (at in-phase), the hot plume over the flame exhibits slightly differently each other. Eventually such asymmetry feature is more pronounced, then complete transition (to anti-phase) is made. As indicated above, when the burner separation distance is fixed, the transition is quickly done and no “cease” during the transition is not found apparently. However, as already presented previously, the mode change from in-phase to the anti-phase can be introduced manually with variation of the burner separation distance, and it is noted that the flame motion is temporary “ceased” during the variation of the distance across the critical value. Such no-motion feature onset of the transition is qualitatively similar to what we observed in transient behavior in single-flame system.

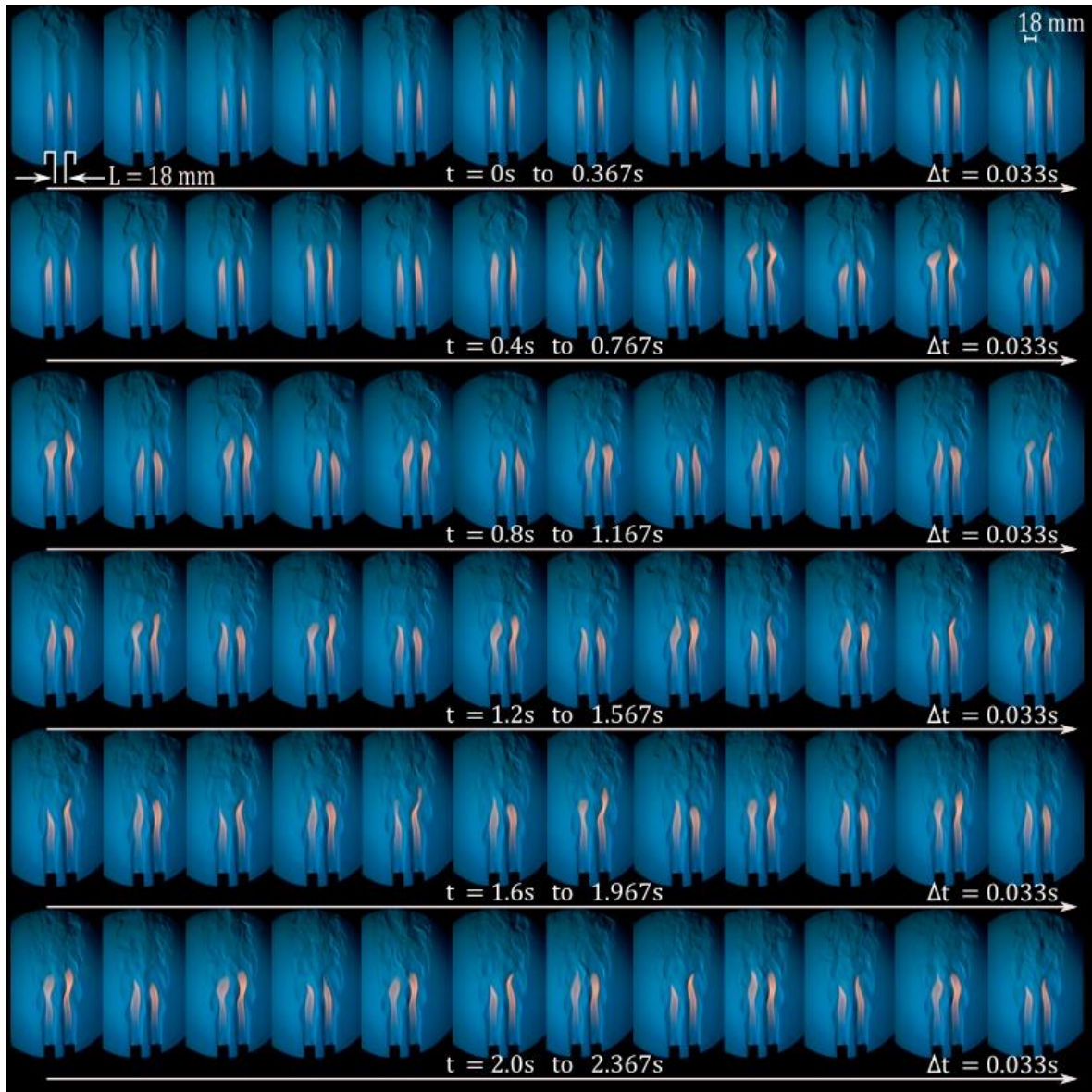


Fig. 5.9 (b) Typical optical image-sequence of coexisting of flame transition from in-phase- to anti-phase mode for twin-flames system ( $L = 18$  mm,  $D = 18$  mm,  $Q = 900$  cc/min,  $\Delta t = 0.033$  s).

### 5.3.4 Characteristic Frequency of Two Modes of Oscillation

Measured temperature fluctuations recorded by TCs and analyzed data are shown in Fig. 5.10 for single-flame system. Figure 5.10 (a), a typical time-variation of TC signal placed at  $2D$  height above the burner exit is presented. A clear periodic motion is successfully captured. It is amazing the measured signal via FFT operation in order to obtain the system frequency ( $f$ ); a pack of characteristic frequencies is obtained (Fig. 5.10 (b)), that is 10.7 Hz, 12.7 Hz, and 21.4 Hz, respectively. The peak of 10.7 Hz is responsible to the varicose mode and its secondary harmonics can be found around 21.4 Hz. Interestingly, the additional peak is found at slightly higher than that of varicose mode around 12.7 Hz, which is responsible to the sinuous mode. Harmonized frequency of the sinuous mode is always higher than the varicose mode that such similar scene is observed in Fig. 5.10 (c) in case of interacting non-premixed jet flames. As presented in our previous work (Mochizuki et al., 2017; Bunkwang et al., 2020), there is critical burner separation distance ( $L_{crit}$ ) for mode change (from the in-phase to anti-phase mode) and sudden discontinuous jump of the frequency is found. Anti-phase oscillation frequency is always higher than that of the in-phase in this regard.

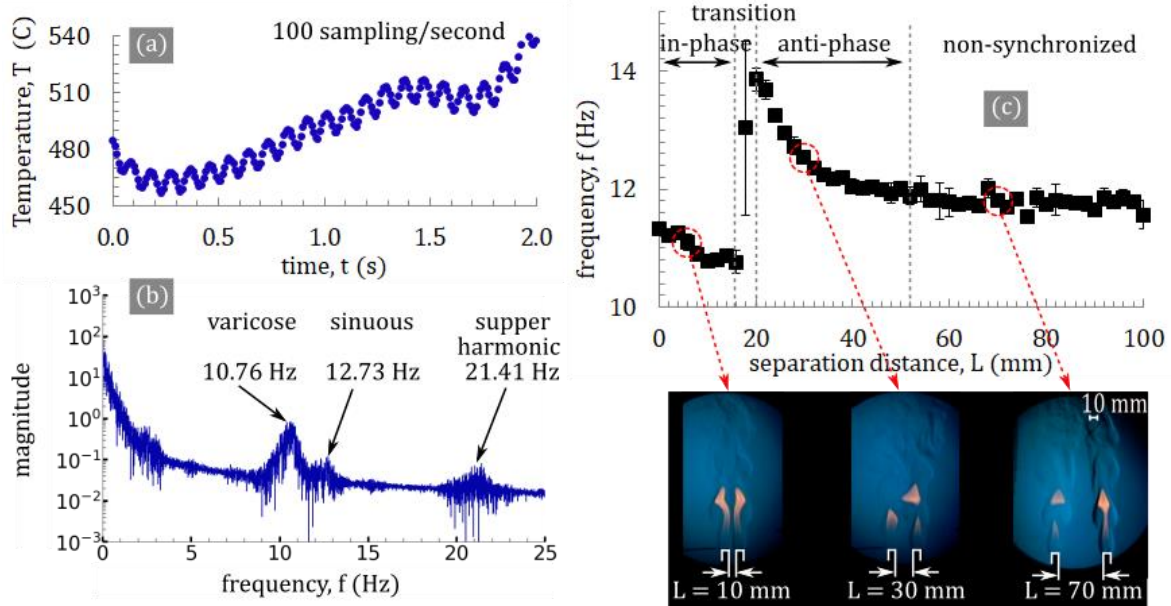


Fig. 5.10 Time-sequence of TC signal (a), corresponding FFT data (b) for single flame case of  $D = 30$  mm and  $Q = 850$  cc/min. The flickering characteristic frequency versus the separate on distance for twin-flames case of  $D = 10$  mm,  $Q = 500$  cc/min.

Frequencies for varicose and sinuous mode(s) oscillation are summarized in Fig. 5.11. Frequency analyses is made many times to ensure the reproducibility. Standard deviation of the typical run is about 0.2 for varicose mode and 0.4 for sinuous mode; which ensures the quality of the data for further discussion. From (a) to (c), sensitivity of oscillation on imposed fuel flowrate is shown for each burner size. Because the current dynamic oscillatory motion is purely buoyancy controlled, it is expected that the characteristics of the oscillation dynamics shall be insensitive to the momentum of the jet (i.e., supplied fuel flowrate). The results clearly confirm the hypothesis, suggesting that the characteristic frequencies for varicose and sinuous modes can be determined by the imposed scale ( $D$ ).

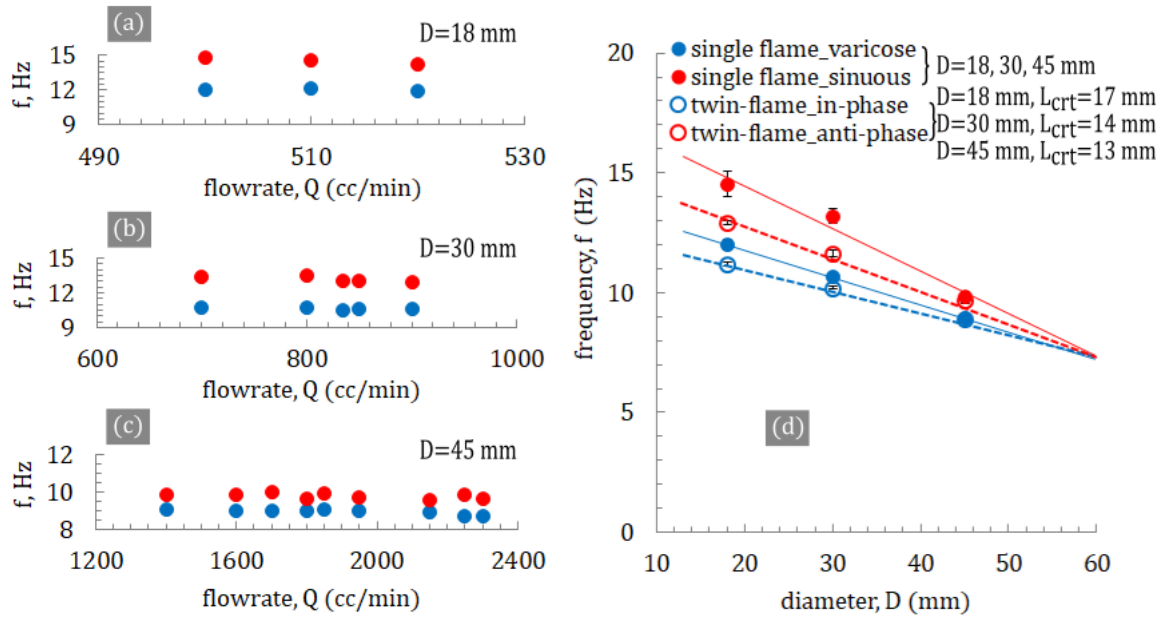


Fig. 5.11 The analysis of flickering characteristic frequency of various fuel flowrate and burner diameter for single-flame system (a-c) and the frequency difference (d) of single-and twin-flam systems.

In (d), these frequencies are plotted against the imposed burner scale (diameter,  $D$ ) to capture the behavior of such characteristic frequency of each oscillation mode. Although the data is limited, it is clearly found that both characteristic frequencies for varicose and sinuous modes decrease as increase of the burner scale. Furthermore, their frequency difference ( $\Delta f$ ) also decreases as the burner scale is larger. Suppose the decreasing trend follows linearly as shown in the dashed line in (d), both mode frequencies are merged at  $D = 60$  mm, where the flame dynamic motion is highly fluctuated and clear two modes oscillation (varicose and sinuous) is hardly identified. Similarly, we also can identify the in-phase and anti-phase oscillation frequencies per given separation distance for twin-flame system. At the transition condition, signals of TCs includes mixed frequencies of minimum of in-phase oscillation

frequency and maximum of anti-phase oscillation frequency. In the same manner, the difference of the frequency for both dynamic mode are obtained. In the next, we shall discuss about the similarity in difference of the two-mode frequencies ( $\Delta f$ ) per given scale of interest.

### 5.3.5 Frequency Difference ( $\Delta f$ ) vs given Burner Scale

First, let's attempt how to summarize the  $\Delta f$ , as the most featured dynamics value in present study, obtained with the single- and twin-flame systems, as shown in Table 5.1.

Table 5.1 Summarized the frequency difference of single- and twin-flame systems

Single-flame system			Twin-flame system				
Diameter	flow rate	Frequency difference	Diameter	flow rate	Critical burner separation distance	Effective diameter	Frequency difference
$D$	$Q$	$\Delta f = f_{\text{sinuous}} - f_{\text{varicose}}$	$D$	$Q$	$L_{\text{crt}}$	$D_{\text{eff}}$	$\Delta f = f_{\text{in-phase}} - f_{\text{anti-phase}}$
[mm]	[cc/min]	[Hz]	[mm]	[cc/min]	[mm]	[mm]	[Hz]
-	-	-	10	500	21	18.3	3.00
18	500 ~ 520	2.88	18	800	17	22.7	1.70
30	700 ~ 900	2.50	30	1000	14	29.6	1.40
45	1400 ~ 2300	0.80	45	2000	13	39.0	0.75

As we learned from obtained results, sinuous meandering for single-flame system is similar to anti-phase oscillation for twin-flame system. When such asymmetric oscillation mode appears, frequency “jump” is identified with the  $\Delta f$  experienced. Appearance of the luminous

flame for single-flame system shows “winding” feature for sinuous mode, whereas “winded” dark-zone formed by two “winding” luminous flames over twin jets is clearly presented for twin-flame system. In other word, winded dark zone is formed over the gap zone between twin burners, which is defined as separated distance,  $L$ . By this comparison, characteristic length of the sinuous meandering for single-flame system is burner scale and corresponding one for twin-flame system is the burner separation distance, not the burner size itself. Recall that the current flame behavior shall be controlled by the buoyancy (either varicose or sinuous for single-flame system; either in-phase or anti-phase for twin-flame system), any feature of oscillation, including the  $\Delta f$ , shall be summarized by the characteristic length scale.

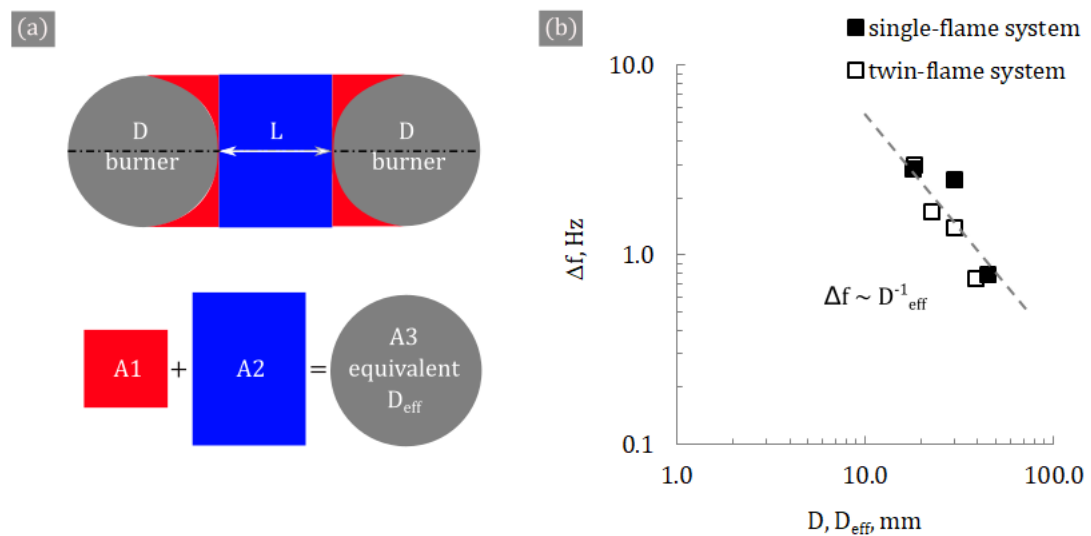


Fig. 5.12 Schematics of the equivalent diameter technique (a), Experimental correlation of the effective length scale for both different systems (b).

In order to calculate “equivalent gap scale” for twin-flame system, we introduce the  $D_{eff}$  (effective diameter) at the gap zone comprising of two particular areas (i.e. red and blue) expressed by the following equation.

$$\frac{D_{eff}}{D} = \left[ \frac{(4-\pi)}{\pi} + \frac{4L}{\pi D} \right]^{1/2} \quad (5.1)$$

First term on the right represents the area of flow distribution as demonstrated by the red in Fig. 5.12 (a), which is approximately 17.4% of cross sectional flow area for twin circular burners. The second term, the blue area is modified through the length scale ratio ( $L/D$ ). The effective diameter is calculated to have the equivalent cross sectional area of opening gap zone between the twin flames (see Fig. 5.12 (a); top view of the twin-flames system). Then both  $\Delta f$  for single- and twin-flame systems are summarized by the  $D_{eff}$  or  $D$  in Fig. 5.12 (b). It is clearly shown that a plot of the  $\Delta f$  (frequency difference between varicose (in-phase) and sinuous (anti-phase) of flame dynamic modes) against  $D$  or  $D_{eff}$  in single- or twin-flame systems are following to the single line and their correlation shows inversely linear relationship. This fact quite resembles with the well-known  $St-Fr^{-1}$  scaling of the flickering flames, where dynamic frequency ( $f$ ) follows inversely correlated to the imposed fire scale ( $D$ ). This similar behavior of sinuous meandering fashion appeared to the sinuous mode for single-flame system and anti-phase mode for twin-flame system gives potential insight how to determine the sinuous mode, which is truly random to appear and hard to control. Because the similar meandering motion occurs by hot flame surrounded by the cold air (for single-flame system) and cold air surrounded by the hot flames (for twin-flames system), we shall consider that sinuous meandering would occur when there are two thermal boundary layers exist at certain length scale. Due to the large temperature variation in the thermal layer, strong shear layer introduced by the buoyancy is formed. Shear layers at the edge of the scale

(gap) generate vortices and they are detached then flowed to downstream. In this regard, the sinuous meandering is basically caused by vortices detached from two edges of the interested scale. This is quite similar to what we observed in, so-called Karman vortex formed downstream of the obstacle. Karman vortex exhibits asymmetry in the crossed flow, which shows sinuous meandering fashion. Although it is also known that there is in-line oscillation mode at double frequency (so called in-line mode), no such mode is observed here. Not likely the Karman vortex which is stably formed in the uniformed flow, the present flames are formed under accelerating flow field. This might be the reason why the clear sinuous motion shall be appeared at the limited range of the imposed conditions. Because the evolved vortices becomes weakened in the (surrounded) hot zone and rather confined in the cold zone for twin-flame system, the clear winding motion can sustain in a solid manner. On the contrary, for single-flame system, vortices are released to the cold ambient and no confined mechanism is presented there, therefore, it is hard to keep sinuous mode stably. This hypothesis supports the observed trend in the experiment. As summarized, it is important to note that the sinuous oscillation behavior might be the essentially the same for single-flame system and twin-flame system; moreover, it might be similar to Karman Vortex structure in fluid motion. To confirm this hypothesis with other angle of view, we shall summarize the motion behavior based on the Reynolds number.

### **5.3.6 Dynamic Similarity of Buoyant Single- and Twin-flame(s)**

The relationship of  $St$  and  $Re$  is plotted instead as shown in Fig. 5.13. The blue and red indicate varicose and sinuous modes of single-flame system. The star and plus signs denote the initial condition to start a pulsation for single-flame system and the transition from the

in-phase to anti-phase mode in twin-flame system which the black circle is the conditions set at the normal open atmosphere ( $g = 9.81 \text{ m/s}^2$ ). Vertical dash-line represents the regions of the characteristic wake flow reported by Taneda (1956), Betchov and Szewczyk (1963), and Williamson (1996). Plot the  $Re$  shows consistency with the previous suggested fundamental studies and a good agreement is found reasonably. The characteristics length is the effective diameter in twin-flame system of calculation, whereas, a normal diameter of burner is for single-flame system. The appearance of the threshold value of flame pulsation appeared in the region 1 for single-flame system, where the vortex ring starts to form behind a bluff body in fluid trajectories for characteristic wake flow compared with the canonical viscous oscillating flow. Notice that the three representatives (single-flame system) and the four representatives (twin-flames system) of different fire sizes, the present investigation show nicely alignment to each study case. All of them falls in the region 2 where the vortices starts to alternatively emit the downstream of the flow. This confirms that the transient condition to trigger the asymmetric motion for single fire should be determined by the critical Reynolds number. Interestingly, this observation fact tells that the mod change of flame dynamics would highly be considered as similar mechanism of both the single- and twin-flame systems. Noticeably, the relevance of this Reynolds number does not mean that it can control the whole flame dynamics. What we suggest in this study is that the critical Reynolds number showing the wake shedding condition may play as “trigger” of the mode transition for buoyancy-controlled flame motion.

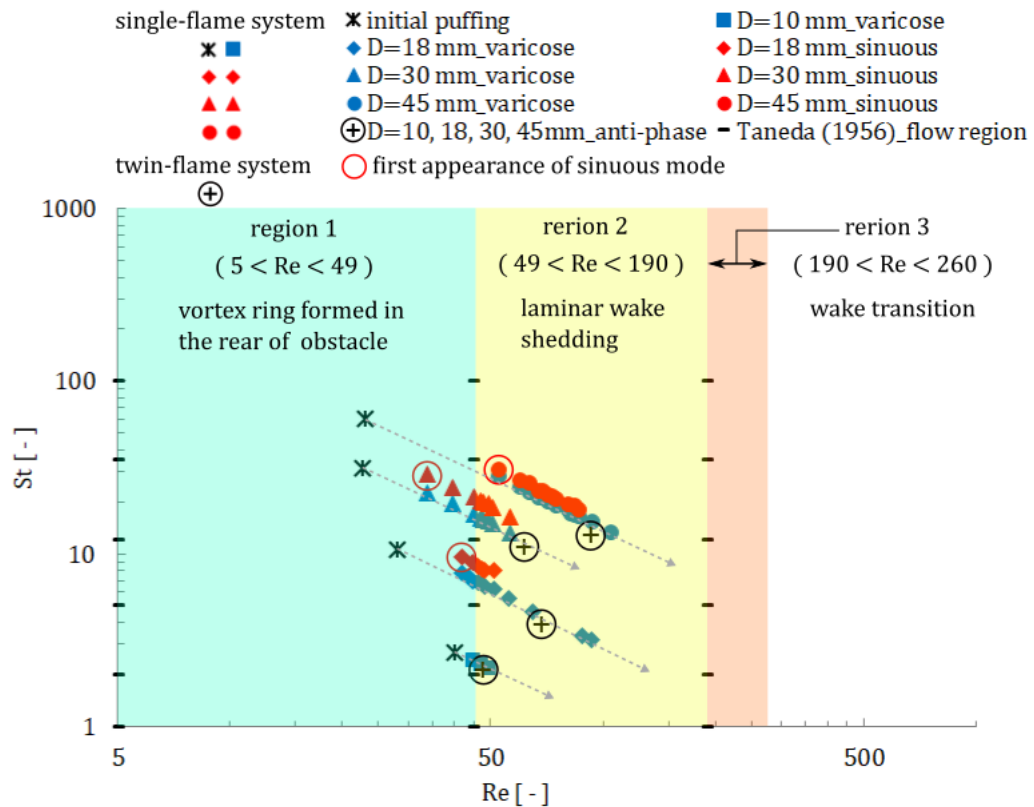


Fig. 5.13 Show the relationship of  $St$  and  $Re$ , the blue and red indicate varicose and sinuous modes of single flame. The star indicates the onset of flame flickering of single-flame system. The plus sign indicates the anti-phase at critical condition (transition) of twin-flames system. The vertical dash-line represents the region of the characteristic wake flow reported by past studies.

## 5.4 Conclusions

It is understood that the physical similarity and the frequency difference when the dynamic mode changes from the axisymmetric to asymmetric motion are found in both the systems. By proposing a proper length scale, the sinuous mode appearing in the single-flame system is characterized by the staggering flow pattern, the winding cold-air found at the middle

spacing-gap between two identical burners of twin-flame system. The inverse relationship can summarize the frequency difference at the critical condition. Through the  $St-Re$  plane, the canonical classical asymmetric flow feature “Karman vortex street”, the critical Reynolds number ( $Re_{L}$ ) based on the gap flow characteristics for twin-flame system (anti-phase mode) is found consistent with the critical Reynolds number ( $Re_{f}$ ) based on the velocity of ejecting fuel for single-flame system. Saying that through the method of similarity, the critical Reynolds number can be one of the potential candidates to describe the transition having the sinuous meandering behavior of single fire. The transition for the single and twin fire(s) is figured out the similar kernel of asymmetric flow mechanism under this concept idea presented in this dissertation.

## Chapter 6

### Results of Numerical Simulation

The transition of flame behaviors and the similarity in dynamics of the different flame system are studied in a systematic manner. In the preceding (Chapters 4 and 5), the investigation based on the laboratory experiment through the modification of the important systematic parameters has been conducted. On this regard, the interpretation of the target phenomena has been further made with the numerical approach to gain more detailed physics with the insightful understanding from scientific way. The axisymmetric/asymmetric motions which are found in the previous chapters have been predicted by the computer software (FDS). The applied simulation appeals the two distinctive dynamic modes of interacting non-premixed jet flames, its transition behavior, including the effect of gravity at prescribed conditions. For computational configurations, in practice, the number of grid cells for all simulations performed in this study is approximately 2.3 million cells in average value (0.7- to 7 million cells were adopted) depending upon the adopted size of cylindrical tubes as mentioned in section 3.2. In necessitation, the impact of mesh size and other influences on the numerical results were carefully checked prior to the productive runs in order to qualitatively confirm the satisfaction.

#### 6.1 Characteristic Frequency of Interacting Two Buoyant Jet Flames

The updated model,  $\alpha^3 Gr^{4/3}$ , found by observing the laboratory experiment of present work is suggested for the more validity of the unified criterion to characterize the dynamics in

twin-flame system. Based on the experimental observations in Fig. 6.1, the region of transition is shrunk compared with the one proposed by Yang and coworkers in 2019. Thus the critical value can be approximated to be about 4 evaluated within the range of prescribed conditions of present study. Four adopted diameters are 10, 18, 30, and 45 mm and methane gas is employed. Noticeably, on the physical plane of the non-dimensional frequency vs. modified Grashof number (the updated model), both experimental (solid symbols) and numerical (empty symbols) results show good agreement. Even though the value is not same, the trend and the essential physics are basically identical. The prediction of transition is satisfactory for relative small sizes of fuel source ( $D = 10, 18, 30$  mm), except the case of 45 mm diameter (the green) of both applied methods (numerical and laboratory experiments).

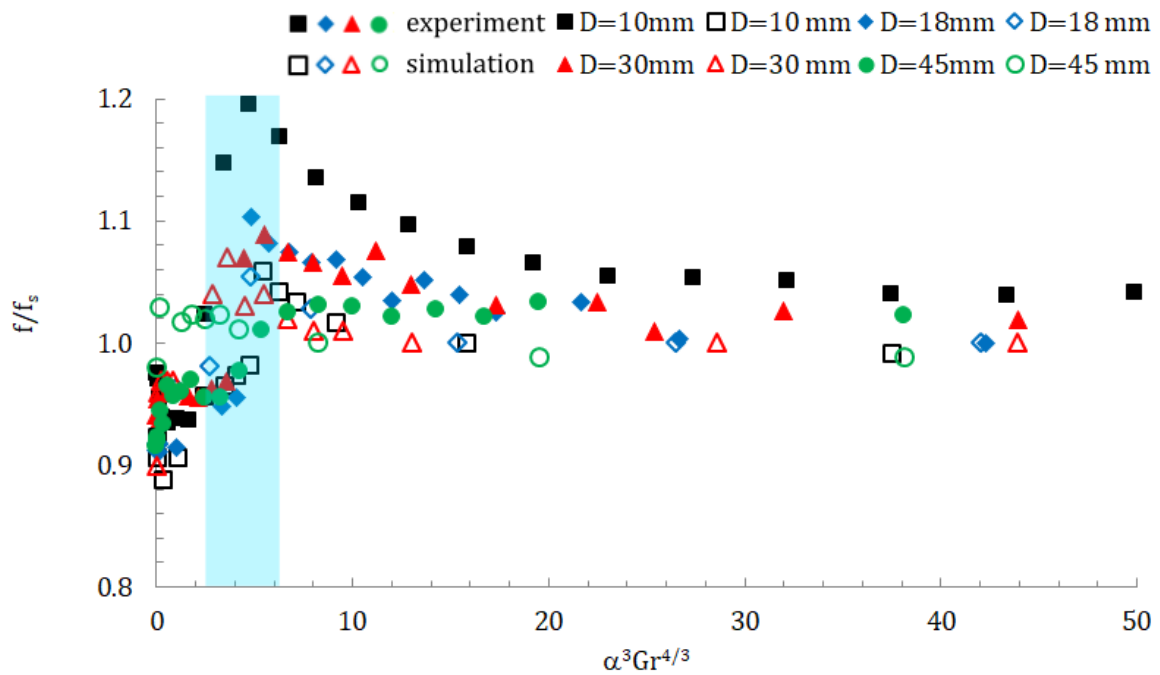


Fig. 6.1 Nondimensional frequency as a function of the modified Grashof number and the ratio of length scales, the solid and empty symbols correspond to the experimental and numerical results.

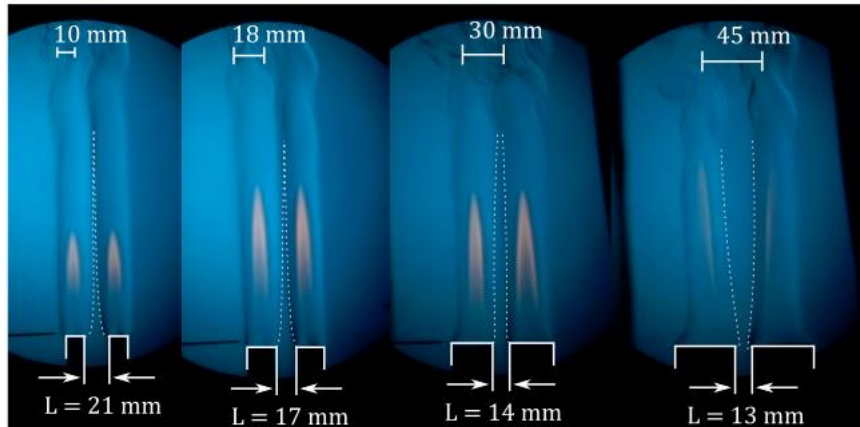


Fig. 6.2 Schlieren images of twin methane-air flame at critical conditions, from left to right:  $D = 10$  mm,  $Q = 500$  cc/min,  $L = 21$  mm;  $D = 18$  mm,  $Q = 900$  cc/min,  $L = 17$  mm;  $D = 30$  mm,  $Q = 1200$  cc/min,  $L = 14$  mm;  $D = 45$  mm,  $Q = 2500$  cc/min,  $L = 13$  mm.

Such similar scenario is observed when the size of fuel source increases; the region of transition becomes broaden. From numerical results, It is more larger compared with the experimental one and it is no longer clear enough because of turbulent feature dominating the flame behavior as mentioned already in Sec. 2.1 (suggested by previous studies). So it is not surprising that repeatability cannot be achieved in the single-flame system. This event probably tells that the higher concave toward the centerline of cylindrical burner due to highly buoyant accelerating flow occurs (see Fig. 6.2), those are induced by the strong buoyancy leading to more turbulent buoyant fashion. Fire scale like size of fire source plays a very important role on the target phenomenon. As seen through the figure above, spacing-gap becomes wider when burner diameter increases. Mechanism (visible flames) to confine the ascending vortices becomes less influence so that the vortex freely rolls and evolves. This may bring more chance the dynamics keep switching and randomly appearing of the

two modes when the time goes by. Thus, clear identification of the transition point becomes difficulty. Such small scale turbulent motion trends to intensively exist when freely-burning surface is enlarged [Maynard, 2013]. Rayleigh number would be properly given a critical value for the multiple thermals formed across the surface. The 2-D problem might not be appropriate any longer and it seems out of the design limit of our laboratory experiment so that problem may be suggested to deal with the 3-D toroidal vortex evolution with highly non-linear instability problem instead.

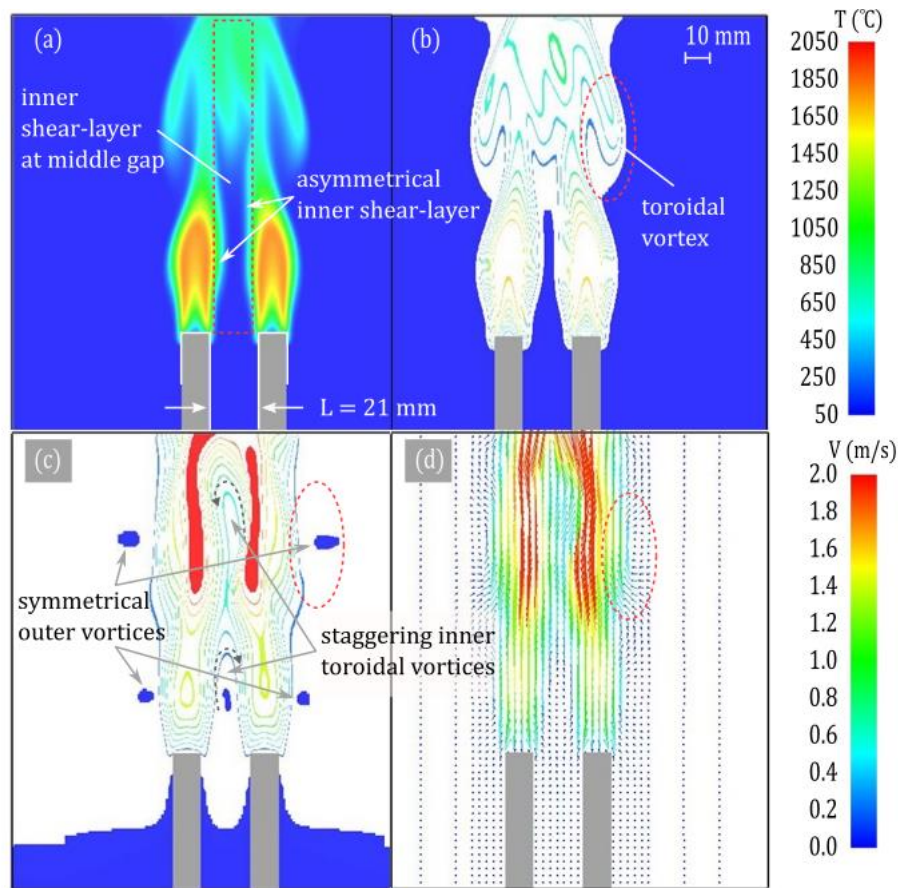


Fig. 6.3 Typical images of instant snapshot of methane jet flames: (a) temperature contour, (b) line-temperature contour, (c) line-velocity contour, and (d) velocity vector :  $D = 10$  mm,  $Q = 500$  cc/min,  $L = 21$  mm.

Figure 6.3 (a) to (d) shows the physical details of flame dynamics during the transition event (in-phase to anti-phase mode). Red circle, (b) to (d), indicates the outer toroidal vortex formed by twin-jet flames. The inner shear-layer (middle spacing-gap) is defined by red rectangle (a), where flow structure is very important to understand the transition scenario. The (c) shows that the shear-layer periodically forms the staggering fashion of flow pattern emitting vortices along the gap with the different orientation in time, whereas, symmetrical vortex pairs (outer shear layers) are still found during this transient process. This confirms that most important flow feature in velocity field would be the inner shear-layer, rather than the outer shear ones. The growth of disturbance becomes naturally involved to characterize the whole flame dynamics in global which the new equilibrium state of instability is found.

## **6.2 Periodic Axisymmetric/Asymmetric Motions in the Twin-flame System**

In previous chapter, the merging fashion of hot plume over the flames was proposed to depict that the unified cluster of the hot gases can be responsible for the whole dynamics behavior of flame oscillation. As shown in Fig. 6.4, the detail time-response during the axisymmetric flame behaviors in twin-flame system, the hot plume merges satisfactorily and the three cycles of non-premixed jet flames presented in the in-phase mode, consecutively. It is observed clear that the mentioned hypothesis sounds physically right for the case considered here that they are found consistency with the observations in laboratory experiment (Fig. 5.7 (c)). In physical essence, the outer toroidal vortex becomes great impact of periodic pinching-off fashion of flame flickers found in the fundamentals. This is basically identical for diffusion flame oscillation in gravimetric field. In addition, the inner shear-layer becomes symmetry and sufficiently merged at very short progressing displacement resulting in an

annihilation of vorticity dissipated by viscous diffusion in the flow as expressed by the fourth-term on right hand-side of Eq. (1.12).

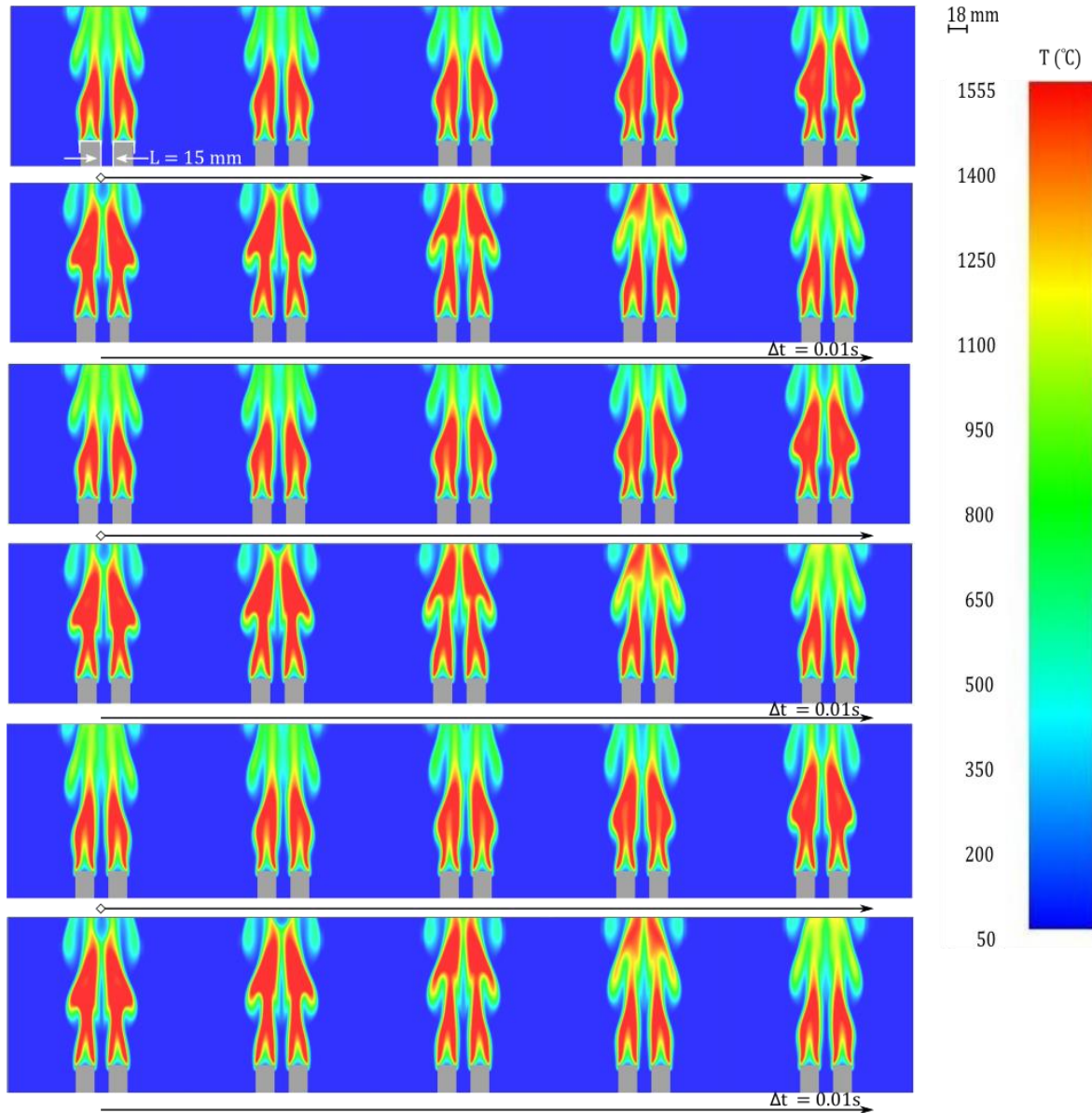


Fig. 6.4 Time-sequential images of pulsating fire(s) with anti-phase modes, predicted temperature contours:  $D = 18\text{ mm}$ ,  $Q = 1000\text{ cc/min}$ ,  $L = 15\text{ mm}$ ,  $\Delta t = 0.01\text{s}$ .

The time-sequential images are used to show the detail time-response during the asymmetric (anti-phase mode) flame behaviors done by computational software. Three cycles of periodic flame oscillation is selected to present the global flame dynamics as shown in Fig. 6.5.

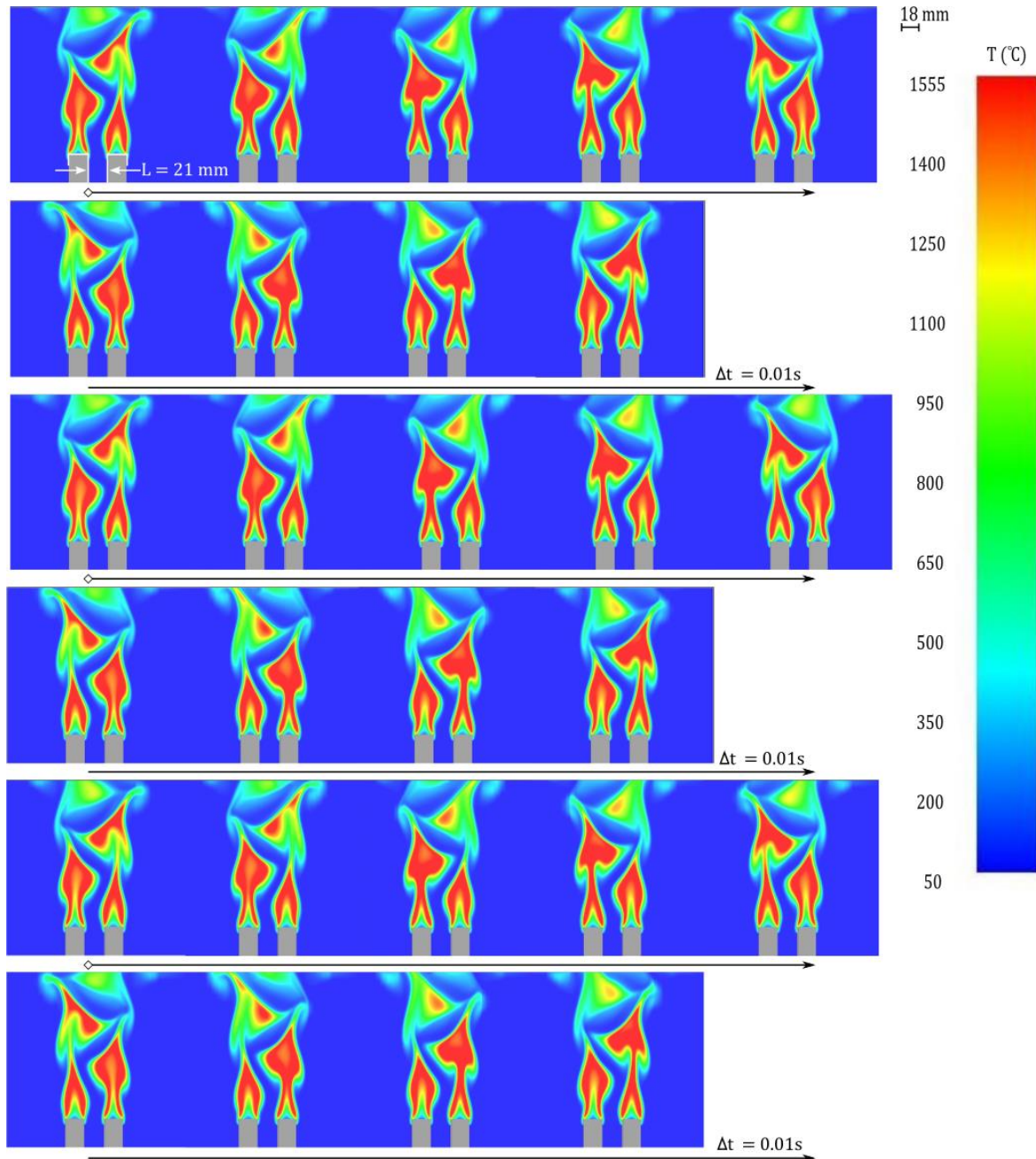
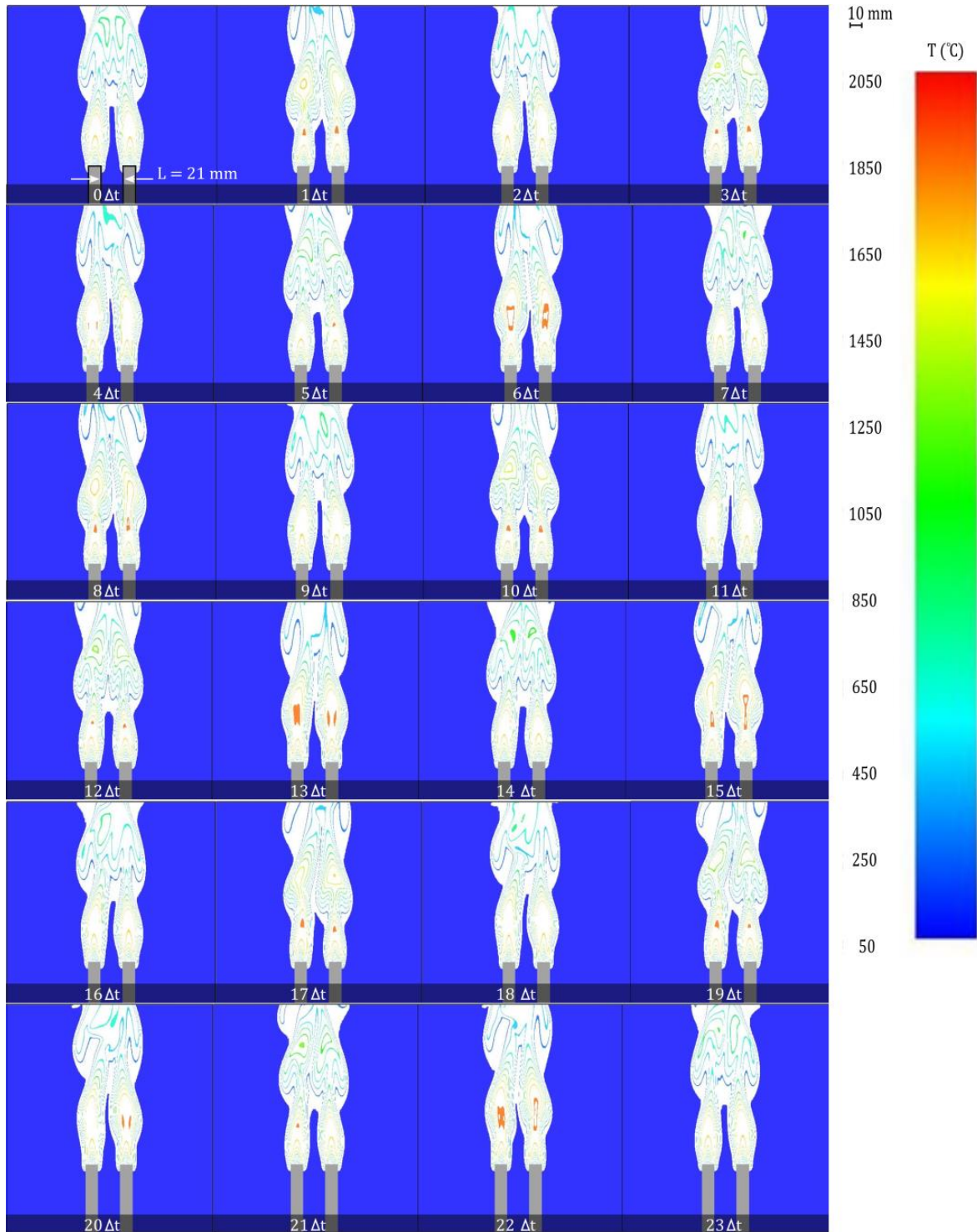


Fig. 6.5 Time-sequential images of pulsating fire(s) with anti-phase modes, predicted temperature contours:  $D = 18$  mm,  $Q = 1000$  cc/min,  $L = 21$  mm,  $\Delta t = 0.01s$ .

This scene shows good agreement with the observations revealed by Schlieren imaging (Fig. 5.8 (c)). Flame clearly exhibits winding fashion and it is highly suspecting that such flame behavior might be considered as the random perturbation. The evolution process to achieve the sinuous meandering fashion similar to the winding cold-air behavior at the spacing-gap is successfully simulated. The surrounding cold-air penetrates the hot zone of gases, this scene is confirmed by the numerical results.

### **6.3 Structures during the Transition Event in Twin-flame System**

Although our computational model might not easily reproduce the transition (from the varicose to sinuous mode) which is usually observed in single flame system (even with the intentional addition of a weak disturbance in technical), the twin-flame system is done satisfactorily. Figure 6.6 shows the transient behavior of flame dynamics from the in-phase to anti-phase mode for the twin-flame system:  $L = 21$  mm,  $D = 10$  mm,  $Q = 500$  cc/min,  $\Delta t = 0.05$  s. For convenience, we intentionally construct the temperature contour plot, where the temperature of the blue zone is less than  $25^{\circ}\text{C}$  (temperature of surroundings). In the early stage, the in-phase motion is fairly reproduced. As depicted by the optical visualization system, Schlieren imaging in Fig. 5.3 (b), the hot plumes above the flames are initially nearly identical, however, their shapes gradually deform and eventually reform asymmetrically. Importantly, the prediction clearly shows that the low-temperature zones between two flames (gap zone) are “winding” and their heights are increasing in time (0.1 – 1.8 sec). This scene is difficult to ascertain through the optical measurement. After the transition completed, the winding cold-air displays such similar behavior to the sinuous mode (1.8 sec ~).



Continue...

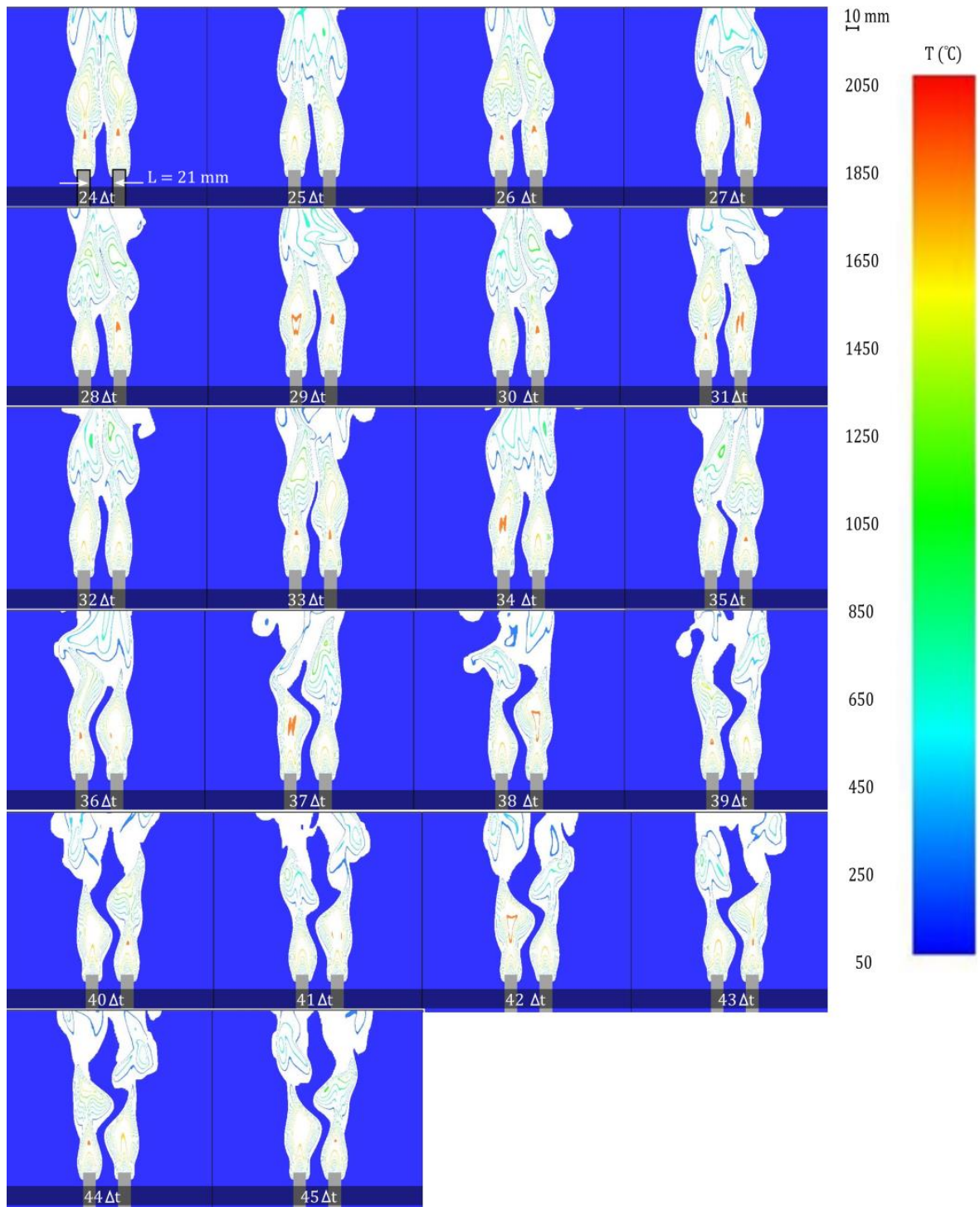
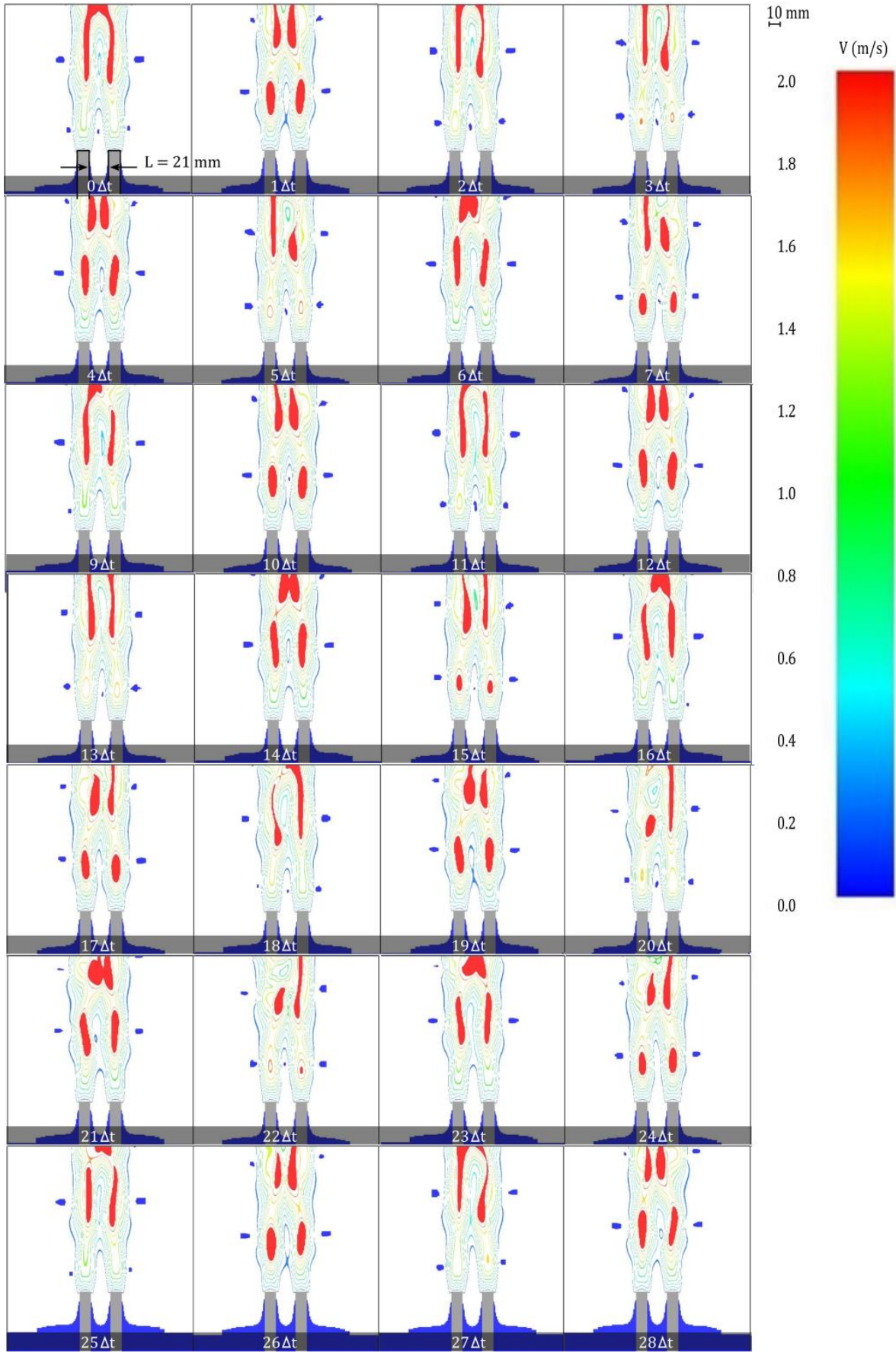


Fig. 6.6 Demonstration of the predicted flame transition from the in-phase to anti-phase mode for the twin-flame system:  $L = 21$  mm,  $D = 10$  mm,  $Q = 500$  cc/min,  $\Delta t = 0.05$  s.

Figure 6.7 demonstrates the transient behavior of flame dynamics from the in-phase to anti-phase mode at prescribed condition: 10 mm diameter of burner, 500 cc/min of ejecting (methane) fuel, and 21 mm of distance between two identical burners. Image are tracked at 0.05 sec from frame to frame. At this separation distance, vortex can grow inside the thermal boundary layer (inner shear-layer) formed by each jet flame and self-sustained event evolves along the flame. Once the completed occurrence of the periodic shedding fashion is found in nature, the global mode of flickering flames behaves in an anti-phase mode as the time goes by. By observation fact (Fig. 6.8), the measurement of thermal layer thickness is found nearly a constant value (~14 mm) at the transition. This implies that the vortices formed by each jet flame at inner shear-layer need to align themselves in zigzagging fashion. As pointed out by Durox and coworkers (1997), this length can be considered as the size of vorticity which found velocity inflection across the length as characteristic scale. Vicinity near the flame (the red coloring in Fig. 6.7), the maximum velocity appears. Whereas the place closed to the outer edge of the layer, cold-surrounding fluid slows down the velocity resulting in the inflection point in the boundary. Large density differences subjected to gravitational force leads to forces in different direction to rotate the fluid in flow field like moment of a couple. This scene can grow the toroidal vortex at the inner layer turns the flow field between the burners with staggering flow fashion like Karman Vortex Street, that is order of 0.21 of  $St$ -number having stability of oscillating flow [Somchai & Kaewnai, Fluid Mechanics (2014); ]. Very closed value was proposed by Christiansen and Zabusky (1973) at approximately 0.281 through computational experiments to study the stability and long-time evolution of two-dimensional wakes. This consistency with numerical experiment done by Yang on coworkers (2019), presented at an order of 0.2 in average value. The vortex-dynamical interpretation of the anti-phase and in-phase flickering of dual buoyant diffusion flames.



Continue...

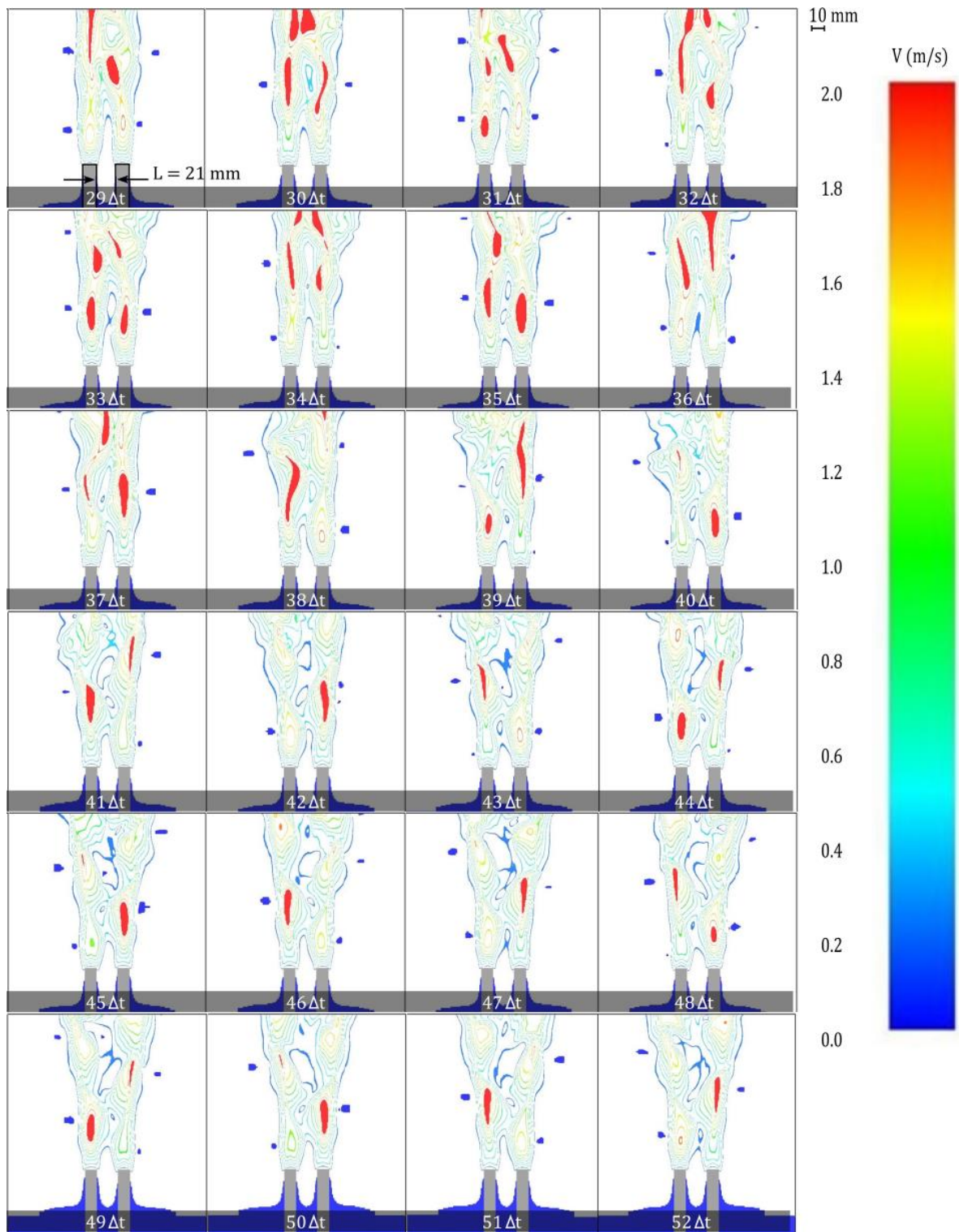


Fig. 6.7 Demonstration of the predicted flame transition from the in-phase mode to the anti-phase mode for the twin-flame system:  $L = 21$  mm,  $D = 10$  mm,  $Q = 500$  cc/min,  $\Delta t = 0.05$

s.

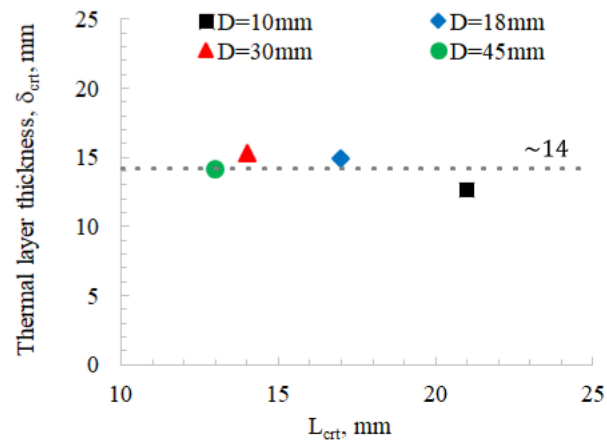


Fig. 6.8 Measurement of thermal layer thickness at the transition.

These numerical observations are evident that the fluid dynamics induced by buoyancy played an important role having asymmetric motion and this ascertain the hypothesis proposed in the preceding chapters is insisted by these numerical results. Let's take a look from frame to frame (see Fig. 6.7). Observe the first frame of velocity contour plots corresponding to Fig. 6.3 (c), the blue, especially two pairs aside the buoyant flows, represents flowing fluid nearly zero velocity in motion. Interestingly, the symmetry achievement can be found at the outer shear-layer side by side during transient process ( $0 < t < 1.9$  sec), but the inner shear-layer shows slightly difference of asymmetric fashion. Meanwhile, the turbulent hot-plume over the flames distorts the winding cooled air at middle gap. It is obvious to support the idea that the disturbance can be one of trigger of the appearance of the mode change. It is interesting to notice that the mode change is attained by the disturbance only traveling toward the upstream and the deformation at inner shear-layer turns the whole dynamics to asymmetric fluid in motion. At  $t = 1.9$  sec, ( $38 \Delta t$ ) flame achieves the anti-phase mode. Clear observation found at  $t = 1.5$  sec (frame  $30 \Delta t$ ), the outer

symmetry layers become asymmetry (indicated by the blue zone aside). Quick appearance of staggering fashion is found at  $t = 2$  sec (frame 40  $\Delta t$ ). Such disturbance observed in this case is a stabilizing mechanism of this dynamic system of twin flickering flame interaction. The results showed that the behavior of the hot plume is important for triggering the transition observed in the laboratory experiment. Thus, the promotion of buoyant-flow intensity ought to promote the result in modifying the transition condition.

#### **6.4 Effect of Gravity on Transition in Twin-flame System**

In considering of utilizing the beneficial part of numerical method, Computer (FDS) software was introduced. The influence of gravity on the interaction effect can be observable and its value can be changeable indecently regarding the observed detailed physics of flickering flame dynamics at prescribed condition. Figures 6.9 and 6.10 show the transient motion of flame behaviors for the prescribed gravities (2g and 0.5g) at prescribed conditions: 10 mm diameter of burner, 500 cc/min of fuel flowrate, and 16 mm (25 mm) of separation distance(s). The numerical results show the change of dynamic mode from the in-phase to anti-phase mode at the transition that is significantly affected by this factor. High gravity brings more a high buoyancy force. This make the move quickly change another mode, and it takes about 3 seconds which it is faster than the one observes in Fig. 6.10. However the target phenomenon can still be observed with different characteristic frequency.

The transition seems disappeared and the critical separation distance getting wider when a low gravitational value is configured to the environment in computational domain. This scene tells clearly that this factor broadens the thermal shear-layer formed by jet flames. If

the gravity gets decreasing, the merging behavior and losing the interaction effect are eventually occur. This scenario is illustrated by Fig. 6.10. On the contrary, the characteristic frequency increases with increasing the gravity value and the critical separation distance shrinks to small value (see Fig. 6.9). This observation evidence tells further us that thermal thickness become thinner and it is inversely promotional to the gravitational acceleration. This similar trend is found by changing the fire scale (burner diameter, Fig. 6.2). This trend also implies that the buoyancy force becomes highly intensified with increasing the gravity. To have the interaction effect to make the mode of flame dynamics change, the outer edges of thermal boundary layer must be at a critical point. Thus critical vertex can be formed at the inner shear-layer and the vortices can align themselves like staggering flow pattern which is confined by visible flames. Infer to interpret that thus Froude number depends on the buoyant induced fluid flow in velocity field which parameter was varied independently. Thus buoyancy force is highly necessary for flickering phenomena. Its effect is more pronounced to have great effect at high Reynolds number (a high value of gravity) which promotes a quick occurrence of the transition phenomenon. This suggests that the transition of flame dynamics could become disappeared/suppressed in microgravity. Though the classical fundamentals of pool fire-puffing phenomenon, the observed characteristics frequency of the transition shows such similar trend. Regarding this observation fact, the transition of flame dynamics would not occur when the gravity diminishes at a significantly relatively small value [Hiroki et al., 2014].

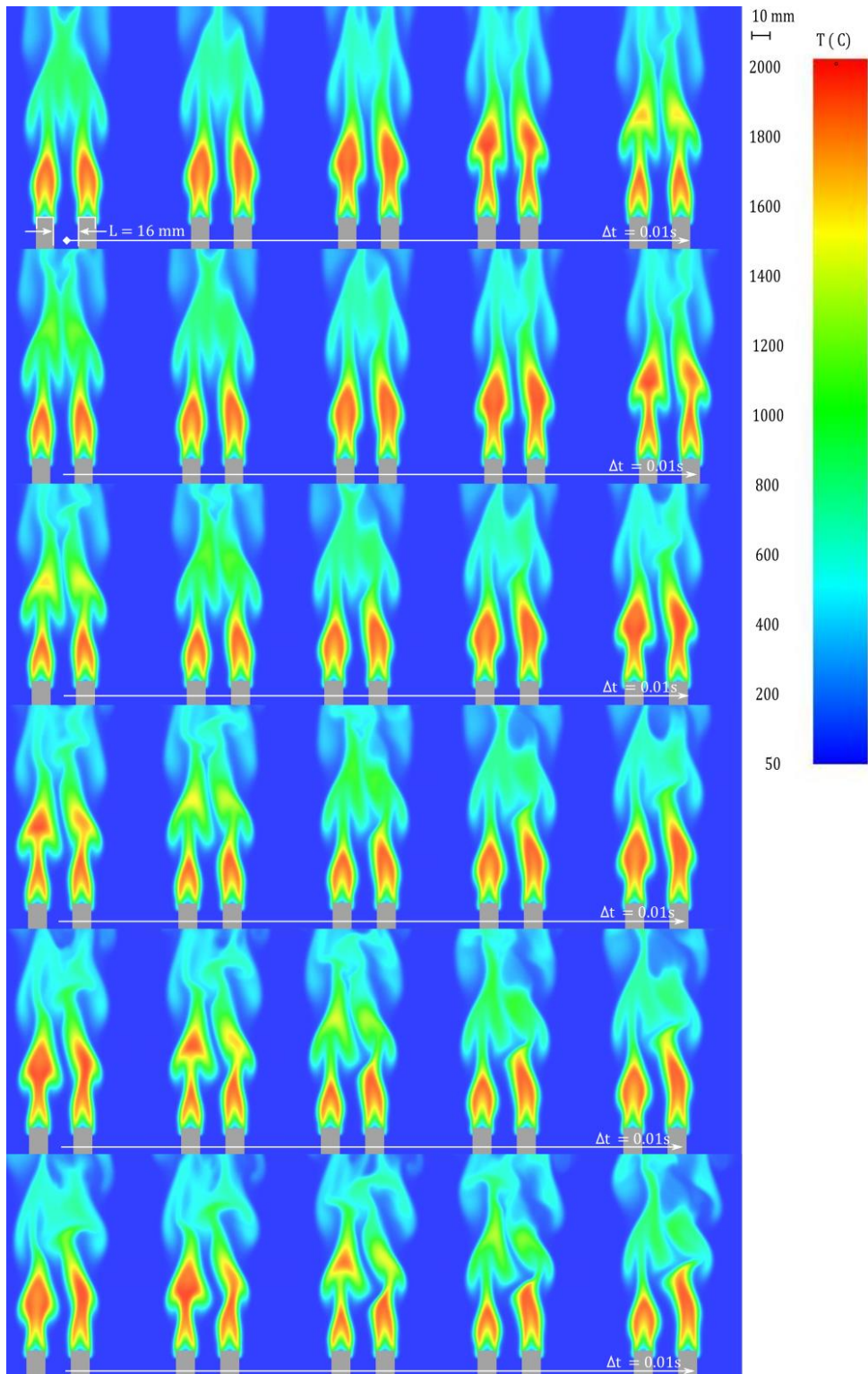
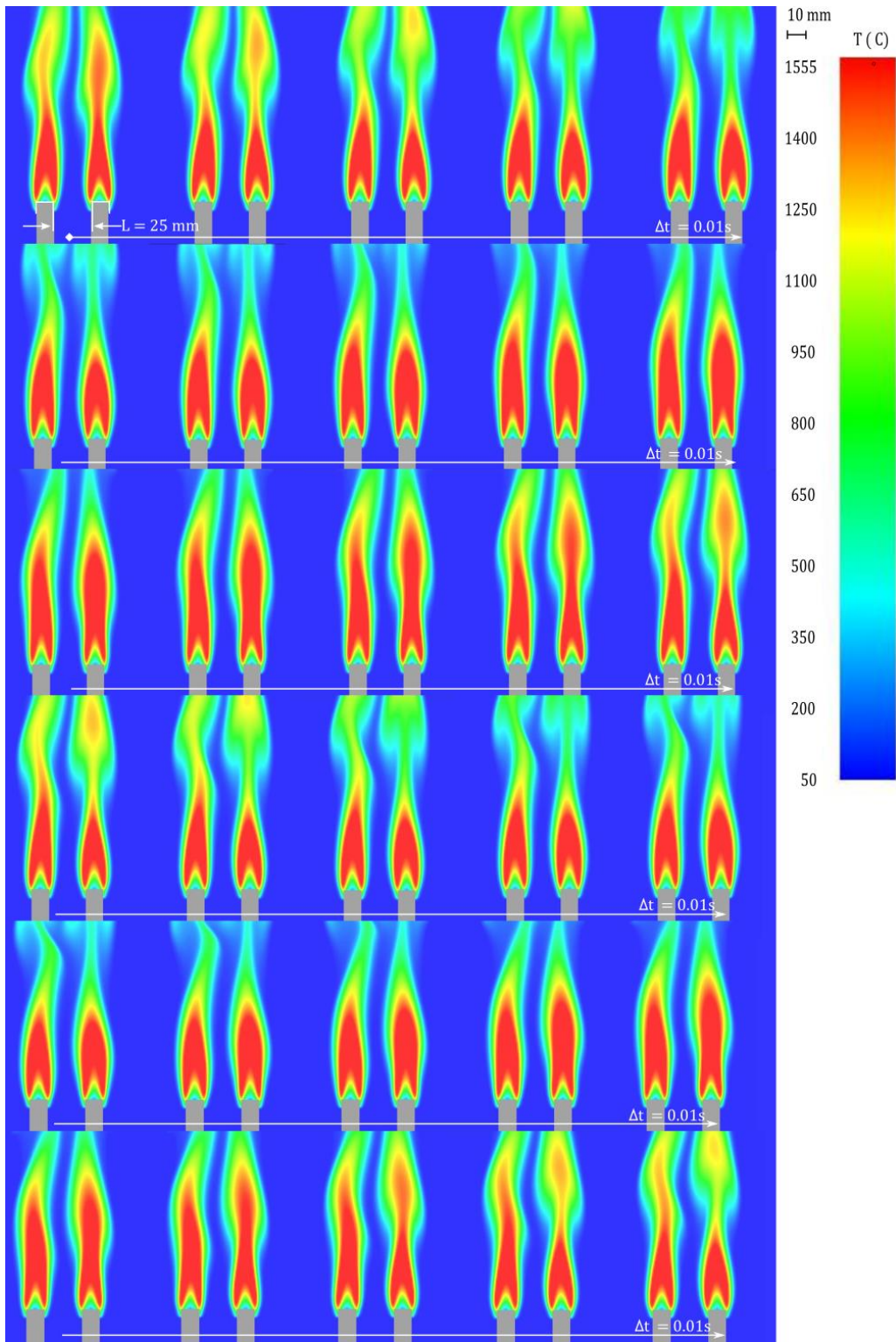


Fig. 6.9 Prediction of flame behaviors at the transition from the in-phase to the anti-phase mode for the twin-flame system with high-gravity (2g):  $L = 16$  mm,  $D = 10$  mm,  $Q = 500$  cc/min,  $\Delta t = 0.01$  s.



Continue...

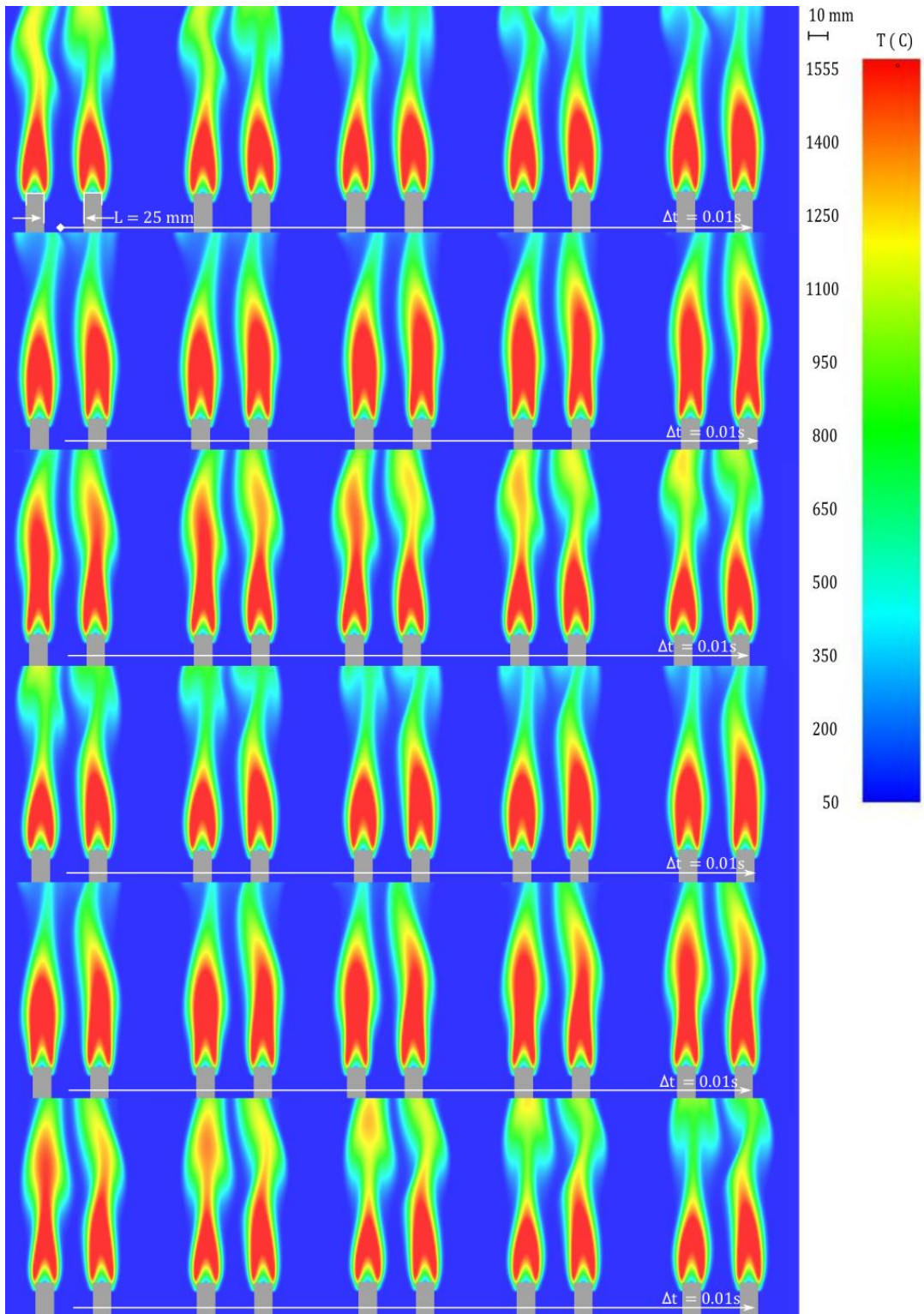


Fig. 6.10 Prediction of flame behaviors at the transition from the in-phase to the anti-phase mode for the twin-flame system with low-gravity ( $0.5g$ ):  $L = 25 \text{ mm}$ ,  $D = 10 \text{ mm}$ ,  $Q = 500 \text{ cc/min}$ ,  $\Delta t = 0.01 \text{ s}$  (continue).

Figure 6.11 shows the relationship of  $St-Re$  plane for many fire scale with varying gravity observed from laboratory and numerical experiments at the critical condition. The effect of gravity on the dynamics of interacting flickering flames is focused on and the summary is made at the transition. The solid rectangle with dash-line represents the prescribed conditions at normal gravity which are summarized by the experiment, but the empty ones are the one that is over the normal gravity; whereas, the diamond indicates the case of under the normal one. They have been finished by numerical simulation. The vertical dash-line represents the regions of the characteristic wake flow being adopted from the past works: Taneda (1956), Betchov and Szewczyk (1963), and Williamson (1996). All plots (laboratory and numerical experiments) fall into the region 2, the consistency finds well with the previous suggested fundamental studies. Even though the value has slightly difference, the physical essence is identical. Regarding the observation fact thought the present study, we can say that therefore the physical details of transition mechanism (different values of the  $g$ ) can be considered the same, as long as the phenomena are controlled by buoyancy force. Additionally, the interaction effect on the transition phenomenon showing various gravity results does not alter the mechanism, rather, the values of one-dimensional parameter are changed because the inner shear-layer is dramatically modified by changing of gravity. The gravity intensities/diminishes the characteristic frequency of the system. Saying that swelling outward scenario is observed when the small value of the gravity is set, the frequency becomes small and vice versa. This obeys the prominent relationship,  $f \sim (g/D)^{0.5}$ , which the frequency is proportional to the  $g$  as shown by the symbols: diamond, triangle, and circle, respectively.

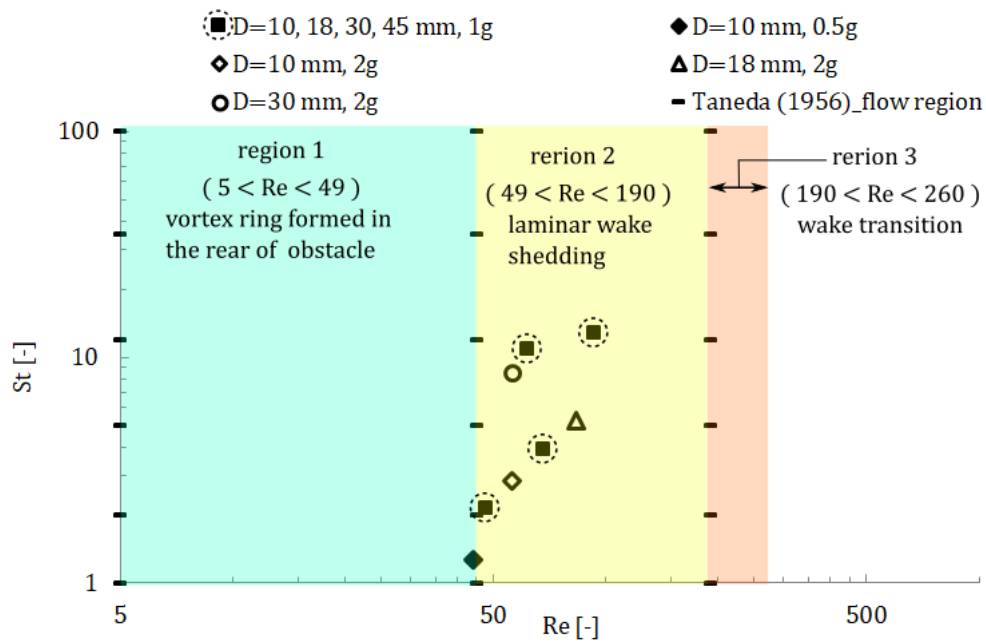


Fig. 6.11 The effect of gravity on the dynamics of interacting flickering flames is shown on the plane of  $St$  and  $Re$ . Solid rectangle with dash-line represents the prescribed condition at normal gravity, but the empty ones are over the normal gravity. The diamond indicates the case of under the normal gravity. Most cases shown here are at the transition (from the in-phase to anti-phase mode) of twin-flames system. The vertical dash-line represents the region of the characteristic wake flow reported by past studies.

## 6.5 Conclusions

By introducing the numerical method, transient behavior during the mode change of flame dynamics can be observed in details. A hot-plume cluster formed over the flames can drive the whole flame dynamics. The most important dynamics having the transition (e.g. to appear asymmetric motion like in-phase mode) is region in-between the two identical burners. Thermal shear-layer formed by each jet flame does not merge at the earlier stage,

rather it is separated allowing to the fully-developed of inner vortex growth resulting in interaction matter. The cold-air successfully penetrates the hot-zone between two flames and the winding cold-air presents in significant. The effect of gravity clearly modifies thermal boundary thickness which similar scene is found by increasing fire scale. The time-delay of changing the dynamics mode (new equilibrium state) is depending upon the effects of gravity and fire scale. Also it is understood that at critical condition the thermal boundary thickness becomes constant that is approximately 4 under prescribed conditions.

## Chapter 7

### Conclusions

These two objectives in this dissertation: 1) the critical condition of mode transition of twin-flame system, and 2) the interpretation of mode transition of single-flame system: similarity approach, are concluded as follows:

*Firstly*, a dynamic behavior of interacting two buoyant-jet flames was studied experimentally by varying fuel flowrate, burner diameter and burner separation distance as systematically experimental parameters. The experimental hardware was updated in order to identify the transition of oscillation dynamic modes (in-phase and anti-phase) for larger burner cases. Orthogonal flame images were additionally taken to confirm the dynamic motion occurring in the two-dimensional plane. Schlieren imaging was introduced to identify the relationship between the disturbance in a hot plume and the visible flame. Dynamic frequency was measured by a thermocouple signal placed near the burner exit. FFT analyses provided the clear transition condition depending on the adopted experimental parameters. The results confirm that there is critical condition giving the transition at specific burner separation distance. This confirm that burner separation distance is the important length scale in mode transition behavior. It is found that the fuel flowrate is insensitive to the mode transition, suggesting that the transition is purely governed by buoyancy, not the jet momentum. When a larger burner is used, the frequency “jump” to identify the transition became less pronounced, although we track the point clearly for the larger burner case. Importantly it is clearly observed that variation of burner diameter is sensitive to the point of mode change, revealing that the burner diameter is an additional, important length scale.

Interestingly we figure out these two length scales are well-correlated each other, suggesting that there is (at least) one constrained condition connecting their relation. Based on the dimensional analysis, we can successfully propose the updated global parameter to describe the transition as  $\alpha^3 Gr^{4/3}$  where  $\alpha$  and  $Gr$  stand for the ratio of two length scales ( $L/D$ ) and Grashof number. This is somewhat different from the one proposed by Yang et al. (2019) because their prediction is based on the limited range of the fire scale. Regarding the critical value found out by studying the interacting flickering flames, next studying series comes consequently. In order to reveal the appearance of the sinuous meandering motion in single fire, the upgraded model is applied to further interpretation the transition in single-flame system. We have experimentally and numerically compared two different flame systems (single and twin flame(s)). We have successfully demonstrated the physical similarity of the flame dynamics and the frequency jump when the mode changes from the axisymmetric to asymmetric motions. There is a close resemblance between the sinuous mode (asymmetric flowing characteristics) of single-flame system and the anti-phase mode of twin-flame system. Observed the alternately staggered flowing pattern of the anti-phase mode exhibiting the winding cold-air at the middle gap between the two identical burners. When a proper length scale is introduced, the frequency jump can be summarized accordingly by the characteristic length scale following to the inverse relationship. Furthermore, the asymmetric dynamics somewhat resembles the Karman vortex feature, the canonical oscillatory viscous flow pattern. Therefore, we have also attempted to prove the similarity between the different systems by examining the critical Reynolds number taken at transient prescribed conditions of single fire and of twin flickering flames. It is found that the appearance of this type of flow oscillation (asymmetric dynamic behavior) observed from the different systems could properly be shared the similar mechanism.

## References

Anderson J. D., Ludwig Prandtl's boundary layer, *Physics Today*, Vol. 58(12):42-48, 2005.

Betchov R., Szewczyk A., Stability of a Shear Layer between Parallel Streams, *The Physics of Fluids*, Vol.6 (10): 1391-1396, 1963.

Baldwin, R., Thomas, P.H., Wraight, H.G.G., The merging of flames from separate fuel beds, *Fire Research Note 551* (1964), Boreham Wood Fire Research Station, (Boreham Wood, Hertfordshire), London.

Baldwin R., Flame merging in multiple fires, *Combustion and Flame*, Vol. 12(4): 318-324, 1968.

Buckmaster J., Nachman A., Taliaferro S., The fast-time instability of diffusion flames, *Physica 9D* (1983) 408-424, North-Holland Publishing Company.

Buckmaster J., Peter N., The infinite candle and its stability—a paradigm for flickering diffusion flames, *Twenty-first Symposium (International) on Combustion*, The Combustion Institute, Pittsburgh, PA, 1986, pp. 1839-1836.

Bray, K. N. C., The challenge of turbulent combustion, *Twenty-sixth Symposium (International) on Combustion*, The Combustion Institute, Pittsburgh, PA, 1996, pp. 1-26.

BUZZCarrot's NEWS (2016). OMG! A Woman from Fort McMurray Loses House to Fire, 3 Weeks Later Wins \$324,786.00 Online...Truly Amazing!. Accessed January 4th 2021 through <http://www.buzzcarrot.com/omg-a-woman-from-fort-mcmurray-loses-house-to-fire-3-weeks-later-wins-324-786-00-online-truly-amazing/>

Bunkwang A., Matsuoka T., Nakamura Y., Mode Transition of Interacting Flickering Flames, The 27<sup>th</sup> International Colloquium on the Dynamics of Explosions and Reactive Systems 28 July – 02 August 2019, Peking University, Beijing, China.

Christiansen J. P., Zabusky N. J., Instability, coalescence and fission of finite-area vortex structures, *Journal of Fluid Mechanics*, Vol.61:219-243 (part2), 1973.

Corlett R.C., “Velocity distribution in fires”, *Heat Transfer in Fires* (1974), edited by P.L. Blackshear, John Wiley and Sons, New York

Chen L. D., Seaba J. P., Roquemore W. M., and Goss L. P., Buoyant diffusion flames, Twenty-second Symposium (International) on Combustion, The Combustion Institute, Pittsburgh, PA, 1988, pp. 677-684.

Cetegen B. M., Ahmed T. A., Experiments on the periodic instability of buoyant plumes and pool fires, *Combustion and Flame*, Vol.93: 157-184, 1993.

Coats C. M., Coherent structures in combustion, *Progress in Energy and Combustion Science*, Vol.22: 427-509, 1996.

Cetegen B. M., Kasper K. D., Experiments on the oscillatory behavior of buoyant plumes of helium and helium-air mixtures, *Physics of Fluids*, Vol.8 (11): 2974-2984, 1996.

Cetegen B. M., Dong Y., Experiments on the instability modes of buoyant diffusion flames and effects of ambient atmosphere on the instabilities, *Experiments in Fluids*, Vol.28:546-558, 2000.

Clement J.M., Experimental verification of the Fire Dynamics Simulator (FDS): Hydrodynamic model, Ph.D. diss. University of Canterbury, 2000.

Chitsomboon T., Construction and interpretation of dimensionless variables in a new way, The 15<sup>th</sup> Conference of Mechanical Engineering Network of Thailand (ME-NETT 2001), Thailand.

Clement J.M., Fleischmann, C.M., Experimental Verification Of The Fire Dynamics Simulator Hydrodynamic Model, International Association for Fire Safety Science, Fire Safety Science 7:839-850 (2003), DOI:10.3801/IAFSS.FSS.7-839

Cengel Y. A., Cimbala J. M., Fluid Mechanics—Fundamentals and Applications (2006), McGraw-Hill Higher Education, New York.

Carpio J., Sánchez-Sanz M., Fernández-Tarrazo E., Pinch-off in forced and non-forced, buoyant laminar jet diffusion flames, Combustion and Flame, Vol. 159:161-169, 2012.

Chakravarthy R. V. K., Lesshafft L., Huerre P., Global stability of buoyant jets and plumes, Journal of Fluid Mechanics, Vol.835:654-673, 2018.

Chen T., Guo X., Jia J., Xiao J., Frequency and phase characteristics of candle flame oscillation, Scientific Reports 9, 342 (2019), DOI:10.1038/s41598-018-36754-w

Changchun L., Xinlei L., Hong G., Jun D., Shasha Z., Xueyao W., Fangming C., On the influence of distance between two jets on flickering diffusion flames, , Combustion and Flame, Vol. 201:23-30, 2019.

Dyke M.V., An album of fluid motion (1982), The Parabolic Press, Stanford, California.

Delichatsios M. A., Transition from momentum to buoyancy-controlled turbulent jet diffusion flames and flame height relationships, *Combustion and Flame*, Vol.92:349-364, 1993.

Durox D., Yuan T., Villermaux E., The effect of buoyancy on flickering in diffusion flames, *Combustion Science and Technology*, Vol.124: 277-294, 1997.

Drazin P. G., *Introduction to Hydrodynamic Stability* 1<sup>st</sup> edition (2002), Cambridge University Press.

DiNenno P. J., Drysdale D., Craig L. Beyler C. L., Walton W. D., Hall J. R., Watts J. M., *SFPE Handbook of Fire Protection Engineering* 3<sup>rd</sup> edition (2002), National Fire Protection Association, Inc.

Drysdale D., *An introduction to fire dynamics* (2011), John Wiley & Sons, West Sussex.

De Ris J. L., Mechanism of buoyant turbulent diffusion flames, *Procedia Engineering*, Vol.62:13-27, 2013.

Dange S., Pawar S. A., Manoj K., Sujith R. I., Role of buoyancy-driven vortices in inducing different modes of coupled behaviour in candle-flame oscillators, *AIP Advances* 9, 015119 (2019); <https://doi.org/10.1063/1.5078674>

Fukuda Y., Kamikawa D., Hasemi Y., Kagiya K., Fire characteristics of group fires, *Fire Science and Technology*, Vol. 23(2):164-169, 2004.

Fukuda M., Kudo Y., Ito A., Fire characteristics of subsisting multiple fire sources in three dimensions, *Bulletin of Japan Association for Fire Science and Engineering*, Vol. 56(3):45-52, 2006.

Finney M. A., McAllister S. S., A Review of Fire Interactions and Mass Fires, *Journal of Combustion*, Volume 2011: 548328, doi:10.1155/2011/548328

Fujisawaa N., Imaizumib K., Yamagata T., Synchronization of dual diffusion flame in co-flow, *Experimental Thermal and Fluid Science* 110,109924 (2020), <https://doi.org/10.1016/j.expthermflusci.2019.109924>

GoKunming, page of Articles. Accessed January 4th 2021 through <https://www.gokunming.com/en/blog/image/small/8111.jpg>

Gebhart B., Jaluria Y., Mahajan R. L., Sammakia B., *Buoyancy-induced flows and transport* (1988), Hemisphere Publishing Corporation, USA.

Guyon E., Hulin J. P., Petit L., Mitescu C. D., *Physical-Hydrodynamics* 2<sup>nd</sup> edition (2017), Oxford University Press.

Hottel H. C., Hawthorne W. R., Diffusion in laminar flame jets, *Symposium on Combustion and Flame, and Explosion Phenomena*, Vol. 3(1):254-266, 1948.

Huerre P., Monkewitz P. A., Absolute and convective instabilities in free shear layers, *Journal of Fluid Mechanics*, Vol.159:151-168, 1985.

Huerre P., Monkewitz P. A., Local and global instabilities in spatially developing flows, *Annual Review of Fluid Mechanics*, Vol.22:473-537, 1990.

Hamins A., Yang J. C., Kashiwagi T., An experimental investigation of the pulsation frequency of flames, Twenty-fourth Symposium (International) on Combustion, The Combustion Institute, Pittsburgh, PA, 1992, pp. 1695-1702.

Hewitt G. F., Shires G. L., Bott T. R., Process Heat Transfer 1<sup>st</sup> edition (1994), CRC Press-Taylor & Francis, Boca Raton, USA.

Halliday D., Resnick R., Walker J., Fundamentals of Physics 9<sup>th</sup> edition (2011), John Wiley & Sons, Inc., USA.

Hu L., Hu J., De Ris J. L., Flame necking-in and instability characterization in small and medium pool fires with different lip heights, Combustion and Flame, Vol.162:1095-1103, 2015.

Jiang X., Luo K. H., Combustion-induced buoyancy effects of an axisymmetric reactive plume, Proceedings of the Combustion Institute, Vol.28:1989-1995, 2000.

Juniper M. P., Hanifi A., Theofilis V., Modal stability theory, Applied Mechanics Reviews (ASME), Vol.66 (2): 024804, 2014.

Kimura I., Stability of laminar-jet flames, Tenth Symposium (International) on Combustion, The Combustion Institute, Pittsburgh, PA, 1965, pp. 1295-1300.

Ko Y. C., Hou S. S., Lin T. H., Laminar diffusion flames in a multiport burner, Combustion Science and Technology, Vol.177: 1463–1484, 2005.

Kuo K. K., Principles of Combustion 2<sup>nd</sup> edition (2005), John Wiley & Sons, Inc., Hoboken, New Jersey.

- Kunda K. K., Cohen I. M., Fluid-Mechanics 4<sup>th</sup> edition (2008), Elsevier Inc., USA.
- Katta, V. R., Roquemore W. M., Menon A., Lee S. Y., Santoro R. J., Litzinger T. A., Impact of soot on flame flicker, Proceedings of the Combustion Institute, Vol.32: 1343–1350, 2009.
- Kitahata H., Taguchi J., Nagayama M., Sakurai T., Ikura Y., Osa A., Sumino Y., Tanaka M., Yokoyama E., Miike H., Oscillation and Synchronization in the Combustion of Candles, Journal of Physical Chemistry A, Vol. 113:8164–8168, 2009.
- Kheradvar A., Pedrizzetti G., Vortex Formation in the Cardiovascular System (2012), Springer-Verlag London Limited.
- Kumar N., Spatio-Temporal Stability Analysis of Shear Flows—Using analytical and non-analytical approaches, M.Sci. thesis. Delft University of Technology, 2016
- List E. J., Turbulent jets and plumes, Annual Review of Fluid Mechanics, Vol. 14(1): 189-212, 1982.
- Lingens A., Neemann K., Meyer J., Schreiber M., Instability of diffusion flames, Twenty-sixth Symposium (International) on Combustion, The Combustion Institute, Pittsburgh, PA, 1996, pp. 1053-1061.
- Lingens A., Reeker M., Schreiber M., Instability of buoyant diffusion flames, Experiments in Fluids, Vol.20: 241-248, 1996.
- Lars-Göran B., Enclosure fire (2001), Swedish Rescue Services Agency, <https://www.ctif.org/library/enclosure-fires>

Lee S. H., Park S., Kim T., Review on investment direction of green technology R&D in Korea, *Renewable and Sustainable Energy Reviews*, Vol.50:186–193, 2015.

Linan A., Vera M., Sanchez A. L., Ignition, liftoff, and extinction of gaseous diffusion flames, *Annual Review of Fluid Mechanics*, Vol. 47:293–314, 2015.

Ling S. J., Sanny J., Moebs W., *University Physics Vol.1* (2017), OpenStax, Rice University, USA.

Milne-Thomson., *Theoretical Hydrodynamics 5<sup>th</sup>* (1968), Dover Publications, Inc., New York.

Maxworthy T., Some experimental studies of vortex rings, *Journal of Fluid Mechanics*, Vol.81:465-495, 1977.

McCaffrey B. J., Momentum implications for buoyant diffusion flames, *Combustion and Flame*, Vol. 52:149-167, 1983.

Monkewitz P. A., Bechert D. W., Barsikow B., Lehmann B., Self-excited oscillations and mixing in a heated round jet, *Journal of Fluid Mechanics*, Vol.213:611-639, 1990.

Moses E., Zocchi G., Procaccia I., Libchaber A., The Dynamics and Interaction of Laminar Thermal Plumes, *Europhysics Letters*, Vol.14(1):55-60, 1991.

Malalasekera W. M. G., Versteeg H. K., Gilchrist K., A review of research and an experimental study on the pulsation of buoyant diffusion flames and pool fires, *Fire and Materials*, Vol.20:261-271, 1996.

Mell W. E., McGrattan K. B., Baum H. R., Numerical simulation of combustion in fire plumes, Twenty-sixth Symposium (International) on Combustion, The Combustion Institute, Pittsburgh, PA, 1996, pp. 1523-1530.

MAIL FOREIGN SERVICE (2009). Five killed and 150 injured as massive fire rages through Indian oil depot. Accessed January 4th 2021 through <https://www.dailymail.co.uk/news/article-1224018/Five-killed-150-injured-massive-rages-Indian-oil-depot.html>

McAllister S.M., Chen J. Y., Fernandez-Pello A. C., Fundamentals of Combustion Processes (2011), Springer.

Maynard T., Fire Interactions and Pulsation—Theoretical and Physical Modeling, Ph.D. diss. University of California, Riverside, 2013.

McGrattan K., McDermott R., Forney G., Overholt K., Weinschenk C., Fire Modeling for the Fire Research, Fire Protection, and Fire Service Communities, Fire Protection Engineering Journal, September 8, 2014. <https://www.nist.gov/publications/fire-modeling-fire-research-fire-protection-and-fire-service-communities>

Majid Bahrami. “Natural Convection”, ENSC 388 (F09), 30 Sep. 2015. Simon Fraser University. Lecture note and example.

Moreno-Boza D., Coenen W., Sevilla A., Carpio J., Sanchez A. L., Linan A., Diffusion-flame flickering as a hydrodynamic global mode, Journal of Fluid Mechanics, Vol.798:997-1014, 2016.

Miklavcic M., Wichman I., Theoretical and numerical analysis of oscillating diffusion flames, *Combustion and Flame*, Vol. 173: 99–105, 2016.

News Mobile State Bureau (2017). What to do if you are stuck in a high rise. Accessed January 4th 2021 through <http://newsmobile.in/articles/2017/06/14/what-to-do-if-you-are-stuck-in-a-high-rise/>

Mochizuki K., Matsuoka T., Nakamura Y., Study on oscillation and transition behavior of interacting flickering flames, *Bulletin of Japan Association for Fire Science and Engineering*, Vol. 67(2):77-85, 2017.

McGrattan K., Hostikka S., McDermott R., Floyd J., Weinschenk C., Overholt K., *Fire Dynamics Simulator User's Guide Volume 1, 6th 2017 (FDS Version 6.5.3)*, National Institute of Standards and Technology (NIST), U.S.

McGrattan K., Hostikka S., McDermott R., Floyd J., Weinschenk C., Overholt K., *Fire Dynamics Simulator Technical Reference Guide Volume 1: Mathematical Model, 6<sup>th</sup> 2017 (FDS Version 6.5.3)*, National Institute of Standards and Technology (NIST), U.S.

Moreno-Boza D., Coenen W., Carpio J., Sánchez A. L., Williams F. A., On the critical conditions for pool-fire puffing, *Combustion and Flame*, Vol. 192:426-438, 2018.

Nakamura Y., Mochizuki K., Matsuoka T., Interaction-induced flickering behavior of jet-diffusion flames, *The 27<sup>th</sup> International Symposium on Transport Phenomena 20-23 September 2016, Honolulu, USA.*

Nagamine Y., Otaka K., Zuiki H., Miike H., Osa A., Mechanism of candle flame oscillation—detection of descending flow above the candle flame, *Journal of the Physical Society of Japan* 86, 074003 (2017).

Norbert Ebeling. “Boundary\_Layer\_Theory”: Boundary Layer Analysis, *Fluid Mechanics (MEC12) 2018/2019*. University of Delhi. Lecture note and example.

Orloff L., De Ris J. L., Markstein G. H., Upward turbulent fire spread and burning of fuel surface, *Fifteenth Symposium (International) on Combustion*, The Combustion Institute, Pittsburgh, PA, 1975, pp. 183-192.

Quintiere J. G., Scaling applications in fire research, *Fire Safety Journal*, Vol.15:3–29, 1989.

Reynolds O., An Experimental Investigation of the Circumstances which determine whether the Motion of Water shall be Direct or Sinuous, and of the Law of Resistance in Parallel Channels, *Philosophical Transactions of the Royal Society of London*, Vol. 174:935-982, 1883.

Sreenivasan K. R., Raghu S., Kyle D., Absolute instability in variable density round jets, *Experiments in Fluids*, vol. 7:309-317, 1989.

Samimy M., Breuer K. S., Leal L. G., Steen P. H., *A gallery of fluid motion* (2003), Cambridge University Press.

Saito K., Impact of "Scale Modeling" on Research and Development, *JSME TED Newsletter*, No.55, 2008. [https://www.jsme.or.jp/ted/NL55/Ted\\_Plaza\\_NL55.html](https://www.jsme.or.jp/ted/NL55/Ted_Plaza_NL55.html)

Somchai W., Kaewnai S., *Fluid Mechanics* (2014), ChulaPress, Thailand.

Settles G. S., Hargather M. J., A review of recent developments in Schlieren and shadowgraph techniques, *Measurement Science and Technology*, Vol.28:1-25, 2017.

Taneda S., Experimental investigation of the wakes behind cylinders and plates at low Reynolds numbers, *Journal of the Physical Society of Japan*, Vol. 11 (3):302-307, 1956.

Toong T. Y., Salant R. F., Stopford J. M., Anderson G. Y., Mechanisms of combustion instability, Tenth Symposium (International) on Combustion, The Combustion Institute, Pittsburgh, PA, 1965, pp. 1301-1313.

Terra-Homem, M., Erdelyi R., Absolute and convective instabilities in open shear layers. I. Hydrodynamic equilibrium, *Astronomy and Astrophysics*, Vol.403:425-432, 2003.

Takahashi F., Linteris G. T., Katta V. R., Vortex-coupled oscillations of edge diffusion flames in coflowing air with dilution, *Proceedings of the Combustion Institute*, Vol.31: 1575–1582, 2007.

Takuya Y., Study on limiting behavior of smoldering using low pressure, Ph.D. diss. Toyohashi University of Technology, 2020.

Williams F. A., *Combustion Theory* 2<sup>nd</sup> edition (1995), The Benjamin/Cummings Publishing Company, Inc., California.

Williamson C. H. K., Vortex dynamics in the cylinder wake, *Annual Review of Fluid Mechanics*, Vol.28:477-539, 1996.

White F. M., *Fluid Mechanics* 5<sup>th</sup> edition (2002), McGraw-Hill Higher Education, New York.

Weng W.G., Kamikawa D., Kagiya K., Fukuda Y., Hasemi Y., Study on Flame Merging Behavior in Group Fires, International Association for Fire Safety Science, AOFST Symposiums 6 (2004).

Wen J.X., Kang K., Donchev T., Karwatzki J.M., Validation of FDS for the prediction of medium-scale pool fires, *Fire Safety Journal*, Vol.42: 127–138, 2007.

Wang Q., Darabkhani H. G., Chen L., Zhang Y., Vortex dynamics and structures of methane/air jet diffusion flames with air coflow, *Experimental Thermal and Fluid Science*, Vol. 37: 84-90, 2012.

Weng W., Kamikawa D., Hasemi Y., Experimental study on merged flame characteristics from multifire sources with wood cribs, *Proceedings of the Combustion Institute*, Vol.35: 2597–2606, 2015.

Wu B., Zhao X., Effects of radiation models on steady and flickering laminar non-premixed flames, *Journal of Quantitative Spectroscopy & Radiative Transfer*, Vol. 253:107103, 2020.

Xia X., Zhang P., A vortex-dynamical scaling theory for flickering buoyant diffusion flames, *Journal of Fluid Mechanics*, Vol.855:1156-1169, 2018.

Yu M. H., Monkewitz P. A., The effect of nonuniform density on the absolute instability of two-dimensional inertial jets and wakes, *Physics of Fluids A: Fluid Dynamics*, Vol.2 (7):1175-1181, 1990.

Yuan T., Durox D., Villermaux E., An analogue study for flame flickering, *Experiments in Fluids*, Vol.17: 337-349, 1994.

Yang T., Xia X., Zhang P., Vortex-dynamical interpretation of anti-phase and in-phase flickering of dual buoyant diffusion flames, *Physical Review Fluids* 4, 053202 (2019), DOI: 10.1103/PhysRevFluids.4.053202

Zhu X., Xia X., Zhang P., Near-field flow stability of buoyant methane/air inverse diffusion flames, *Combustion and Flame*, Vol.191:546-558, 2018.

Zhang H., Xia X., Gao Y., Instability transition of a jet diffusion flame in quiescent environment, *Proceedings of the Combustion Institute*, <https://doi.org/10.1016/j.proci.2020.07.086>

# Appendix

## A) Experimental Devices

### A-1 Cylindrical Tube Selection for Burner Design

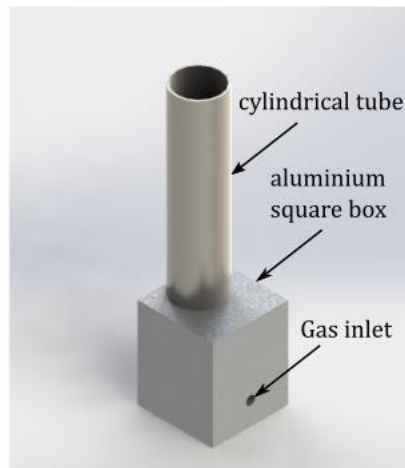


Fig. A-1 Drawing concept of typical burner aspects for construction.

Basically, the burner fabrication and construction of laboratory experiment were undertaken from previous master student [Mochizuki, 2015], which they were very carefully remodified and upgraded by introducing the concept of Toong's laboratory experiment in 1965 at MIT, in order to handle the larger burner diameter and wide range of operation for the present study. In this study, laminar flow regime is most preferable for all cases. To achieve this purpose, the length of cylindrical tube shown in Fig. A-1 must be long enough to serve fully developed of velocity profile, but buoyant criteria is still fulfilled ( $Fr < 1$ ). So, the entry lengths,  $L_{h,laminar} \cong 0.05 Re \cdot D$ , is adopted for finding a proper length of cylindrical tube. A given  $D$  here is diameter of burner. The applied fluid for calculation is methane that is

severed as fluid in this calculation, its dynamic viscosity is 0.000017025 kg/m and density is 0.6604 kg/m<sup>3</sup> at 25°C. The transition region from the laminar to turbulent regime is following to  $2300 < Re < 4000$  [Cengel & Cimbala, Fluid Mechanics (2006) P.326]. From results of calculation (Table A-1), an order of 0.15 m of tube length is enough to work with 3500 cc/min of fluid flowrates, but laminar flow characteristics is retained.

Table A-1 Calculation of Reynolds number and Entry lengths for laminar flow

Flowrate, $Q$ (cc/min)	500	1500	2500	3500
$D=10$ mm				
$Re$ -number	41	123	206	288
$L_{h,laminar}$ (mm)	21	62	103	144
$D=18$ mm				
$Re$ -number	23	69	114	160
$L_{h,laminar}$ (mm)	21	62	103	144
$D=30$ mm				
$Re$ -number	14	41	69	96
$L_{h,laminar}$ (mm)	21	62	103	144
$D=45$ mm				
$Re$ -number	9	27	46	64
$L_{h,laminar}$ (mm)	21	62	103	144
$D=55$ mm				
$Re$ -number	7	22	37	52
$L_{h,laminar}$ (mm)	21	62	103	144

## A-2 Hand-made of Manometer

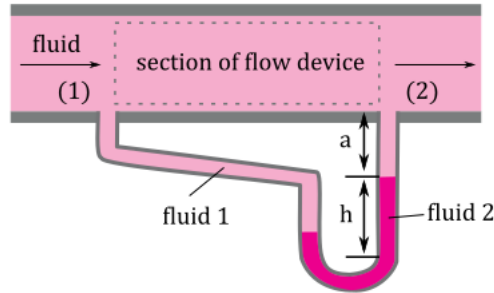


Fig. A-2.1 Measuring the pressure drop across a flow section or a flow device by a differential manometer [Cengel & Cimbala, Fluid Mechanics (2006)].

Hand-made monometer is constructed by analyzing a simple pressure change across a flow device in flow field [Cengel & Cimbala, Fluid Mechanics (2006) P.72]. Let's make some assumptions for calculation: 1) the flow through the pipe is steady, incompressible, and irrotational with negligible frictional effects; therefore, the Bernoulli equation is applicable. 2) The losses in the reducing section are negligible. Taking points 1 and 2 in see Fig. A-2.1, and introduce the Bernoulli equation, the pressure drop is given by

$$\frac{P_1}{\rho g} + \frac{V_1^2}{2g} + z_1 = \frac{P_2}{\rho g} + \frac{V_2^2}{2g} + z_2$$

$$P_1 - P_2 = \frac{\rho}{2}(V_2^2 - V_1^2) \quad (\text{A-1})$$

Balance of force between the two points (1) and (2) in flow section is determined as follows.

$$P_2 = P_1 + \rho_1 g(a + h) - \rho_1 g a - \rho_2 g h$$

$$P_1 - P_2 = (\rho_2 - \rho_1) g h \quad (\text{A-2})$$

Combining Eqs. (A-1) and (A-2), solving for the height (h), then we obtain

$$h = \frac{\rho_1 (V_2^2 - V_1^2)}{2g (\rho_2 - \rho_1)} \quad (\text{A-3})$$

In design the orifice device, diameter is required to know and it is defined as the  $d_2$ . By applying the conservation of mass relation for single stream steady flow device, it can be expressed as

$$V_2^2 = \frac{2gh}{\rho_1} (\rho_2 - \rho_1) + V_1^2$$

$$V_2 = V_1 + \sqrt{\frac{2gh}{\rho_1} (\rho_2 - \rho_1)}$$

$$A_2 = \frac{Q}{A_1} + \sqrt{\frac{2gh}{\rho_1} (\rho_2 - \rho_1)} \quad (\text{A-4})$$

Let's pause to ponder about this  $Q_1 = Q_2 = Q \rightarrow V_1 A_1 = V_2 A_2 \rightarrow Q_1 / A_1 = Q_2 / A_2$  ; therefore, the diameter of orifice can be solved by taking Eq. (A-4). In terms of fulfilling this purpose of the design and fabrication, the typical snapshots of hardware applied in the flowrate controlling section are shown as the following figure.

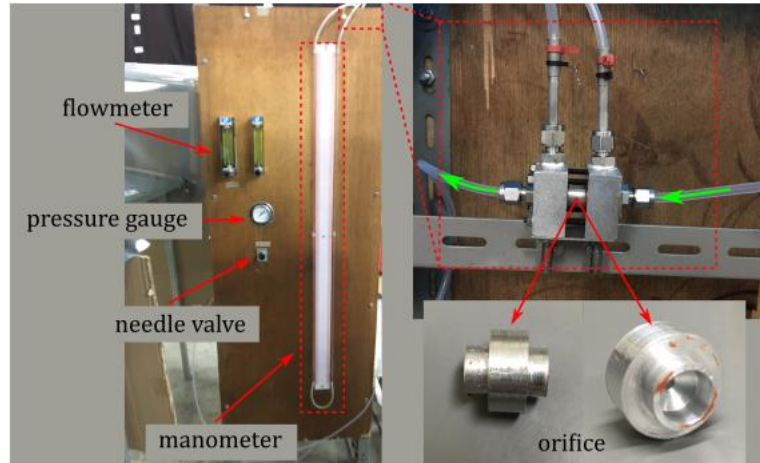


Fig. A-2.2 The applied flow controlling panel and hand-made orifice device.

### A-3 Calibration Graphs of Methane and Helium Flows

Flow-calibration adopted a hand-made manometer was completed by gas meter (Shinagawa DC Series / Dry Gas Test Meter) as figure below. Each flowrate of methane/helium gas was repeated for at least five times to obtain the average value. Calibration was successfully done and it is in satisfaction with more 99% of calibrating accuracy. Please see the following graphs of gaseous flowrate calibration, e.g. methane and helium.



Fig. A-3.1 A typical snapshot of dry test gas meter.

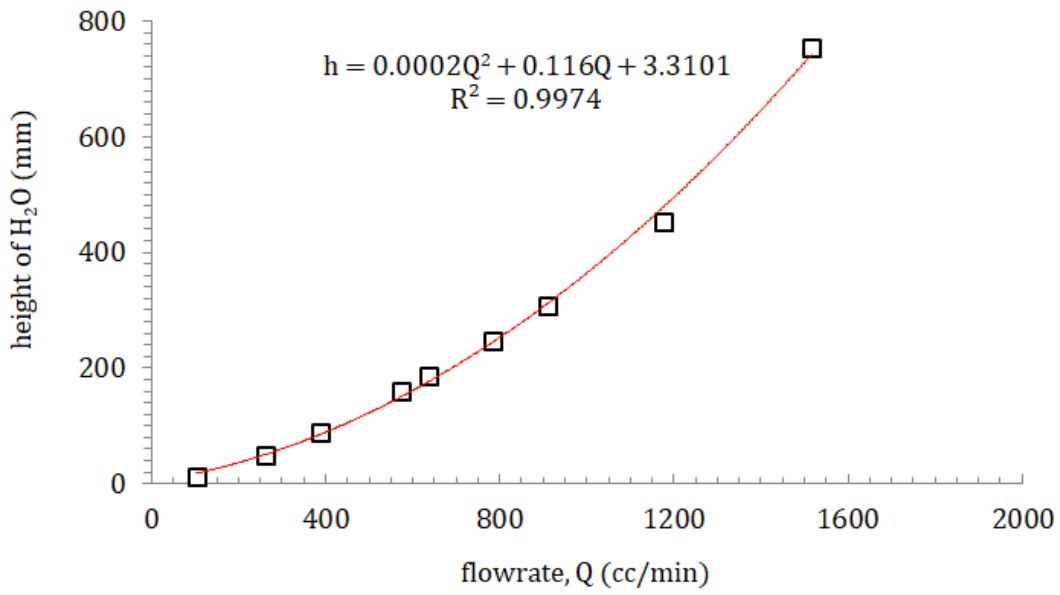


Fig. A-3.2 Flow calibration of methane gas at 0.45 mm diameter of orifice and operating pressure is 0.03MPa.

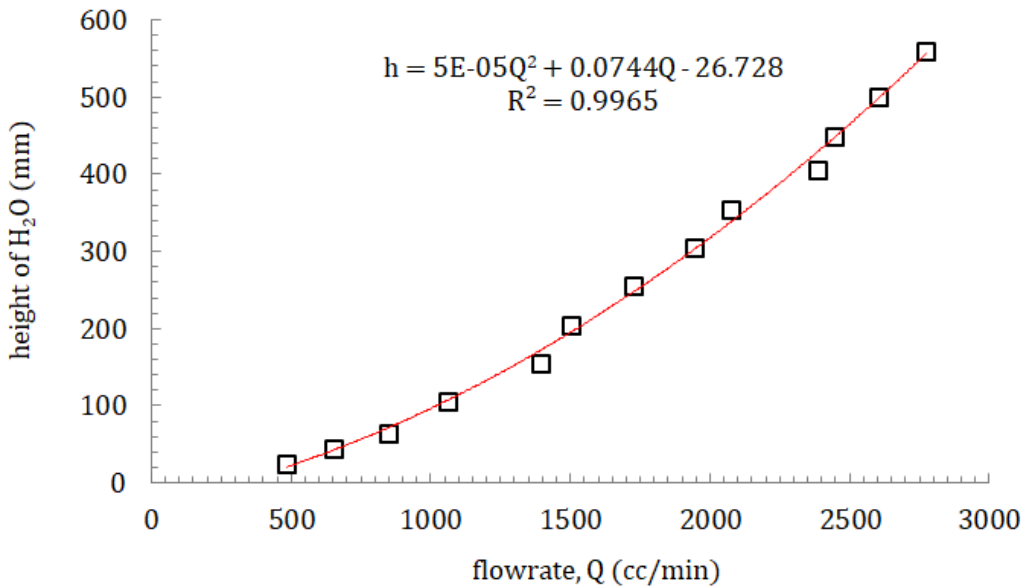


Fig. A-3.3 Flow calibration of methane gas at 0.7 mm diameter of orifice and operating pressure is 0.03MPa.

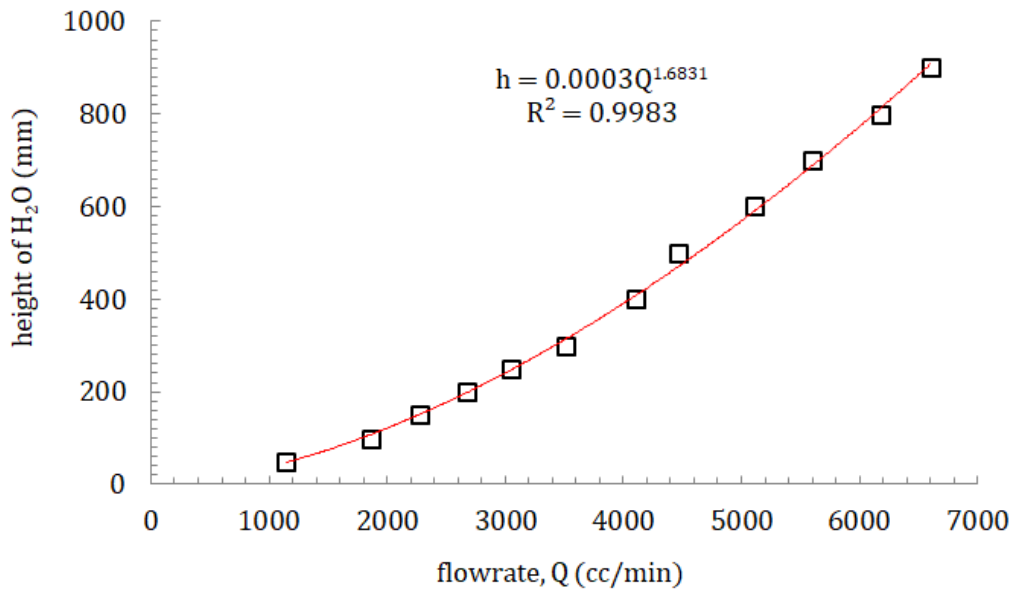


Fig. A-3.4 Flow calibration of helium gas at 0.7 mm diameter of orifice and operating pressure is 0.03MPa.

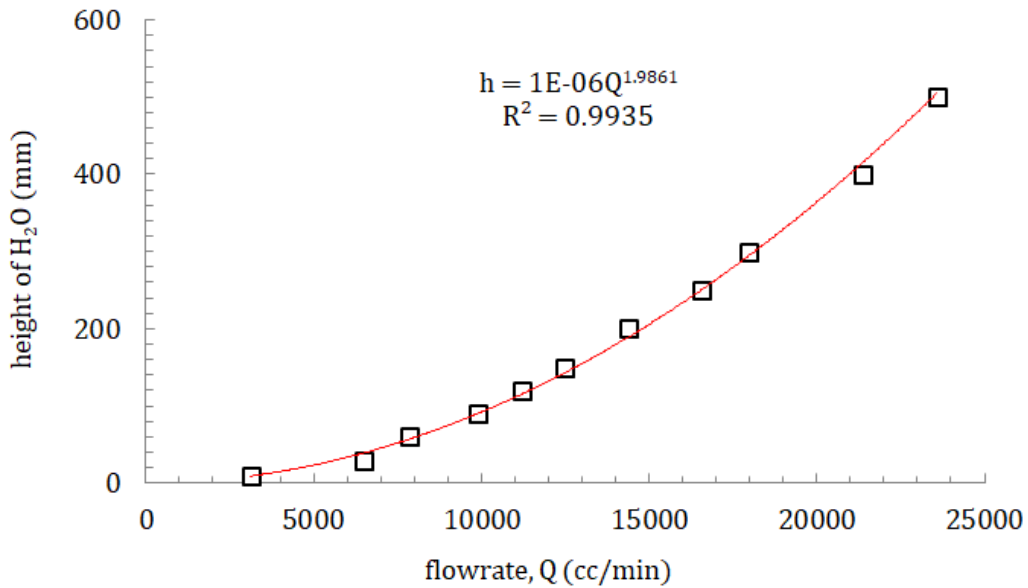


Fig. A-3.5 Flow calibration of helium gas at 1.5 mm diameter of orifice and operating pressure is 0.03MPa.

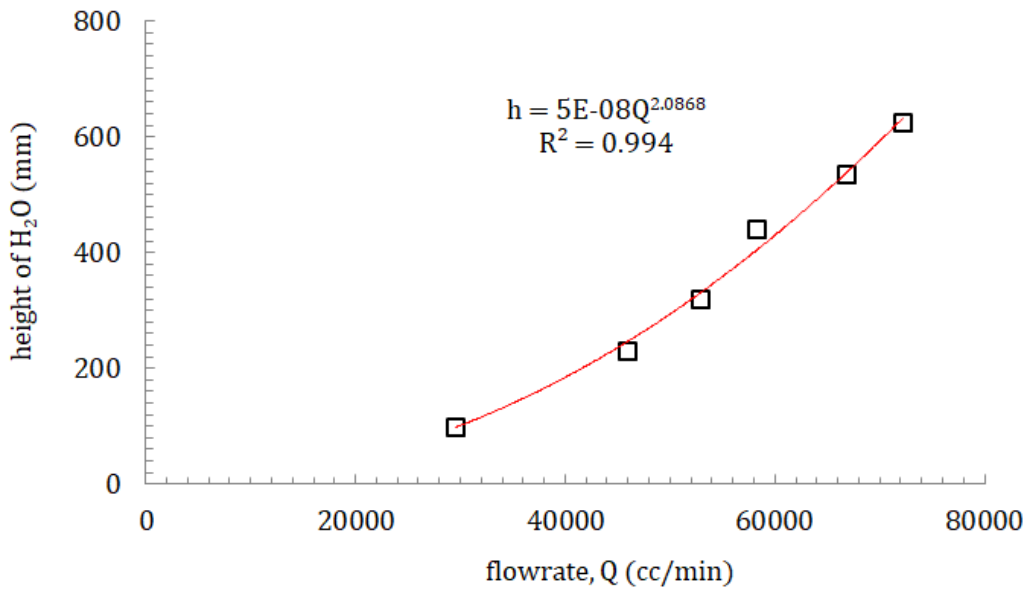


Fig. A-3.6 Flow calibration of helium gas at 2.5 mm diameter of orifice and operating pressure is 0.06MPa.

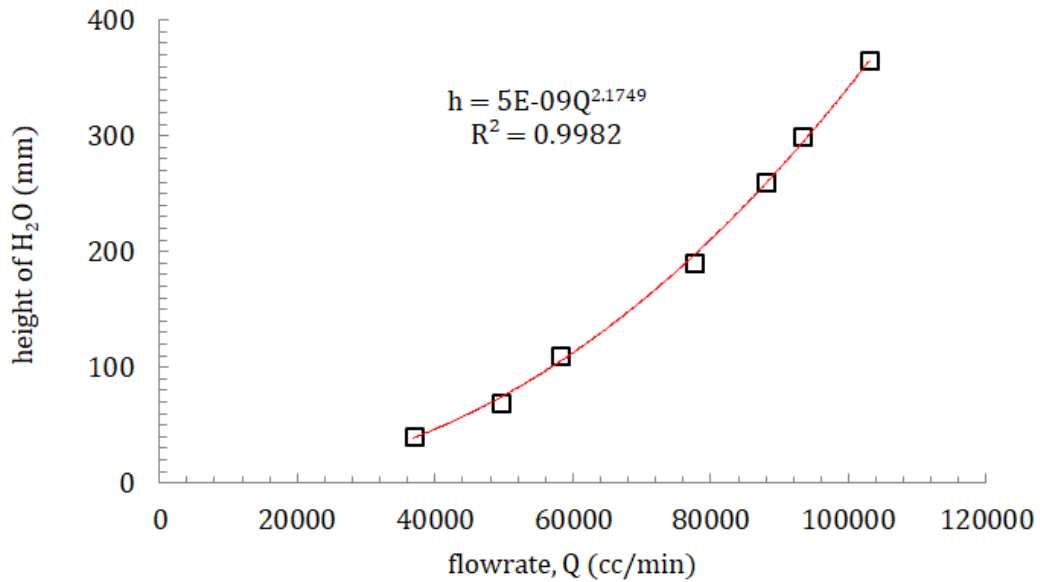


Fig. A-3.7 Flow calibration of helium gas at 3.5 mm diameter of orifice and operating pressure is 0.16MPa.

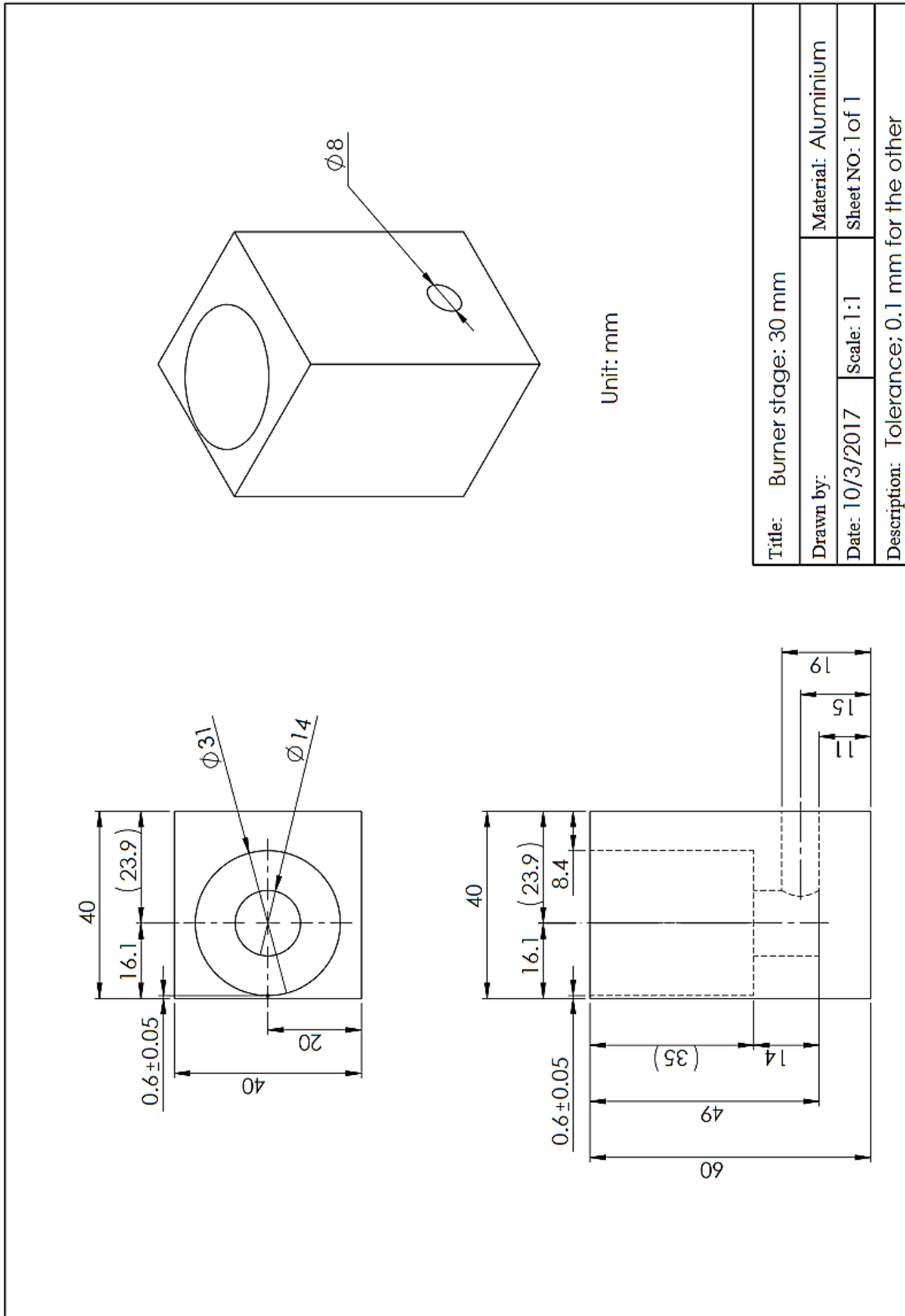
### A-3 Volume Expansion Coefficient

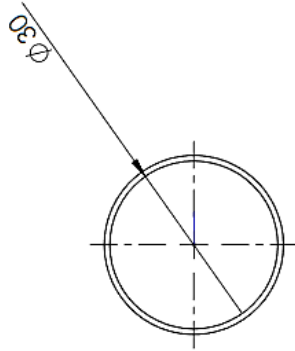
For macroscopic viewpoint of flame dynamic instability, the volumetric thermal expansion coefficient and temperature difference can be ignored. Let's say this is right for most cases of fuel burned in air at normal atmospheric conditions. The adiabatic flame temperature varies in a wide range roughly between 1200 K and 2400 K. The ambient temperature and pressure are 300 K and 101.325 kPa. Through the ideal gas equation, the volume thermal expansion coefficient can be expressed as  $\beta = 1/T$  when the pressure is kept constant and  $T$  has to be absolute temperature. As the conditions mentioned above, the product of volumetric thermal expansion coefficient and temperature difference has minor effect. The approximated value is ranging from 0.75 to 0.88 (Table A-3). This is infinitesimal compared to the product of gravity, characteristic length, and viscosity. For simplification, these factors can be ignored for studying the global instability of flickering flames.

Table A-3 Calculation of volume expansion coefficient  $\beta$  for adiabatic flame temperature

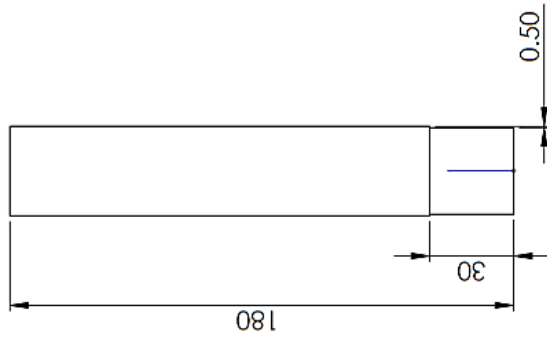
$T_{adi}, K$	$\beta, K^{-1}$	$\Delta T$	$\beta \times \Delta T$
1200	0.0008333	900	0.75
1400	0.0007143	1100	0.79
1600	0.0006250	1300	0.81
1800	0.0005556	1500	0.83
2000	0.0005000	1700	0.85
2200	0.0004545	1900	0.86
2400	0.0004167	2100	0.88

### A-4 Drawings of Some Burner Fabrication (Examples)

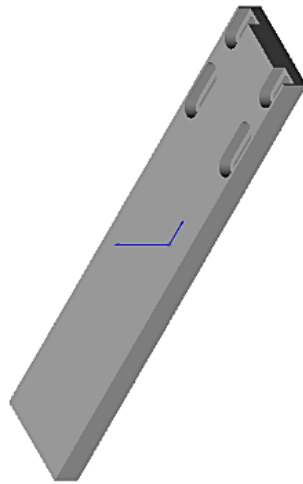
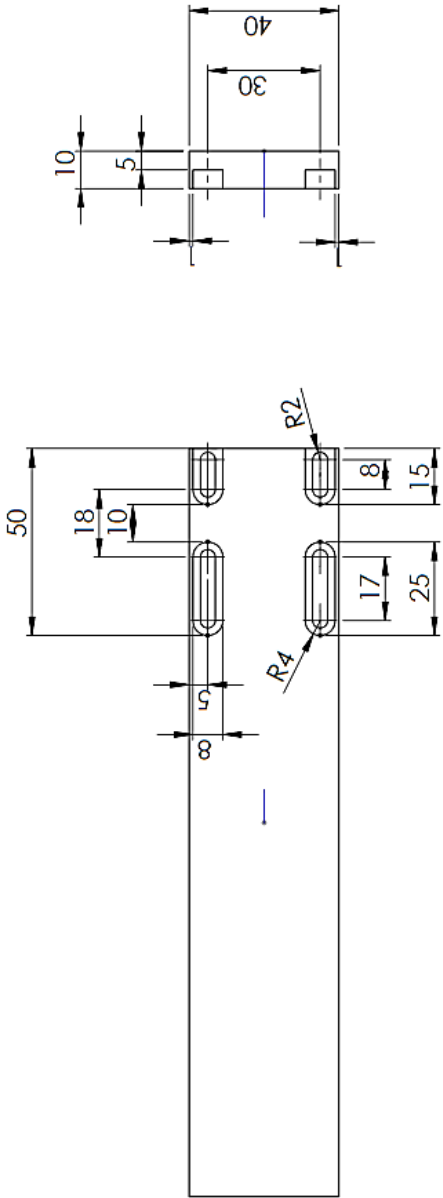




Thickness is 1 mm



Title:	
Drawn by:	Material:
Date: 10/3/2017	Scale: 1:5
Sheet NO: 1 of 1	
Description:	



Title:	
Drawn by:	Material:
Date: 10/11/2017	Scale: 1:1
Sheet NO: 1 of 1	
Description:	

## B) Analysis of Oscillation Frequency

### B-1 Physical Description of Fourier Transform

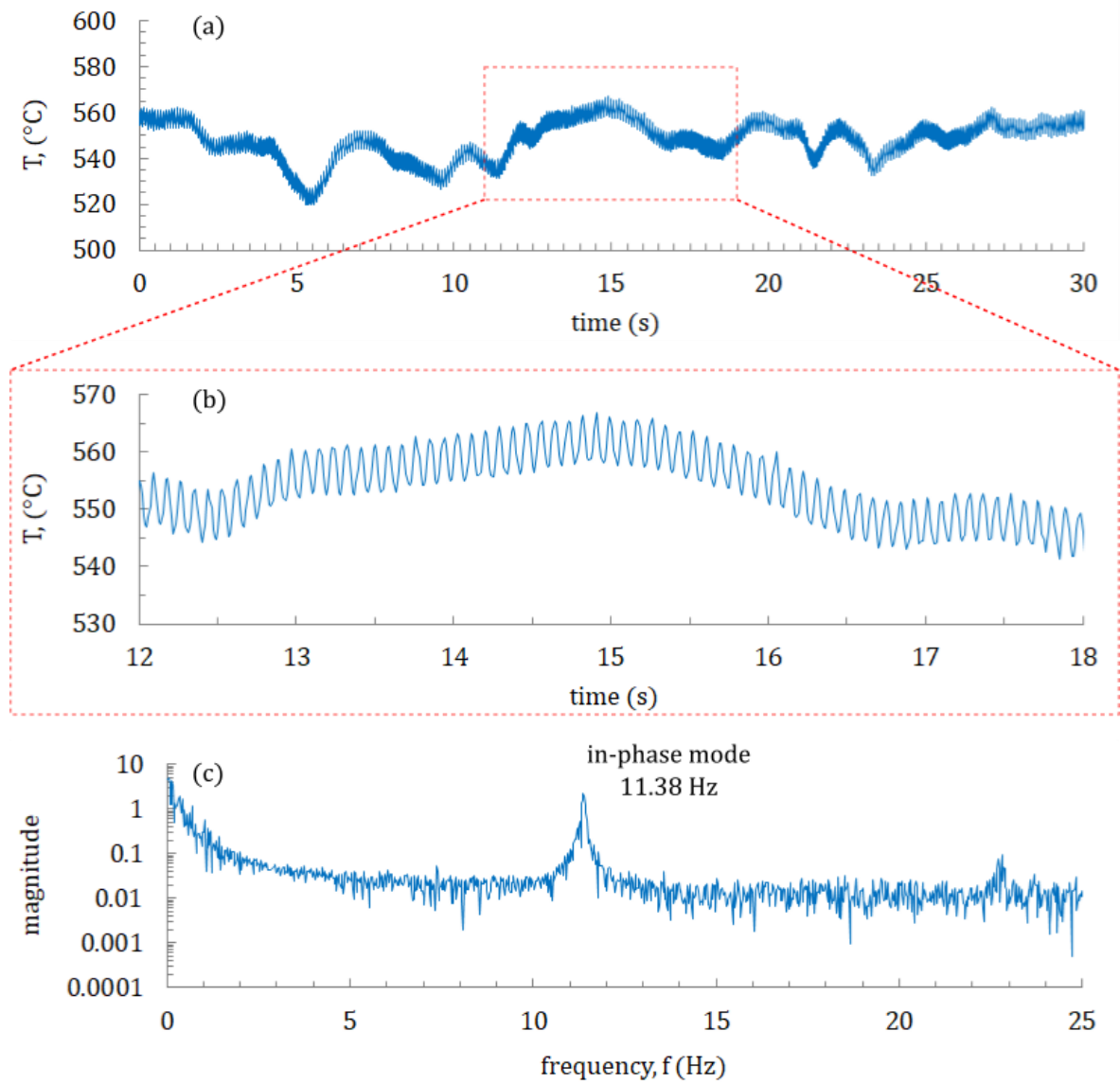


Fig. B-1.1 Time-sequence of TC signal (a)(b), corresponding FFT data (c) for dual flames case of  $D = 10$  mm  $L = 0$  mm,  $Q = 500$  cc/min, and 10 millisecond of sampling frequency.

In reality, a thermocouple records the input signals spatially that just picks up the temperature deviated caused by velocity field fluctuation at many different points in time (figure B-1.1 (a) and (b) blowup portion). The question is how we can take the pure frequency of flame oscillation like figure B-1.1 (c) and decomposed it into a pure frequency that makes it up. Well, through this concept the 11.38 Hz is found out to be of oscillatory frequency for this instance. It is pretty interesting that how this applied method gets real frequency of flame oscillation of the input signals.

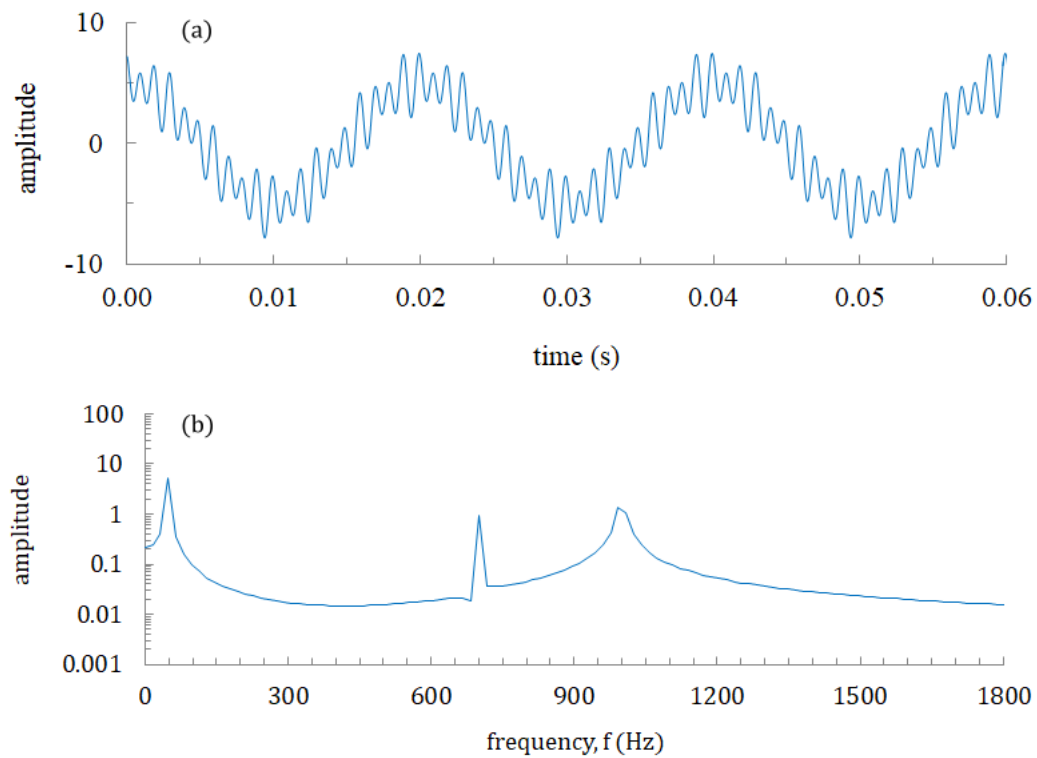


Fig. B-1.2 Typical combined decomposition of an arbitrary input signals through the applied Fourier transform.

The key idea is the signal is going to be wrapped around the circle. Let's get example as shown in Fig. B-1.2, there are three waves (b), e.g. 50 Hz, 700 Hz, and 1000 Hz, compounding of this arbitrary input signals (a). Physically what this concretely means by that the highest point corresponds to the origin of the graph and the lowest point of the graph is closed to the origin. Imagine that this wire of signal (a) has some kind of mass and the center of mass (CM) is on it. When the wrapping/wiring frequency is changed, the CM changes differently and spreads out around the origin, but pretty close to the origin, once the wiring frequency is the same frequency as the same as the frequency (first wave) of the signal. In this case, it is 50 Hertz and then it becomes like the CM unusual far from the origin and the steeple occurs upward (Fig. B-1.3 (a)(b)). So keep changing the wrapping frequency, once this designated frequency matches the original frequency (second and third waves) of the signals. Then the two spires left can be found out as shown in Fig. B-1.3 (c) to (f). This thing is almost called "the Fourier transform". Noticeably, this is relatively idea that the wire is wrapping around the circle to get its real frequency. However, what happens (see Fig. B-1.3) if we take three signals and then apply the Fourier transform to each of them individually? The adding-up results of this matter becomes the same results as we add up the signals and then apply the Fourier transform as shown in Fig. B-1.2. In final, the transformed graphs are the same physically.

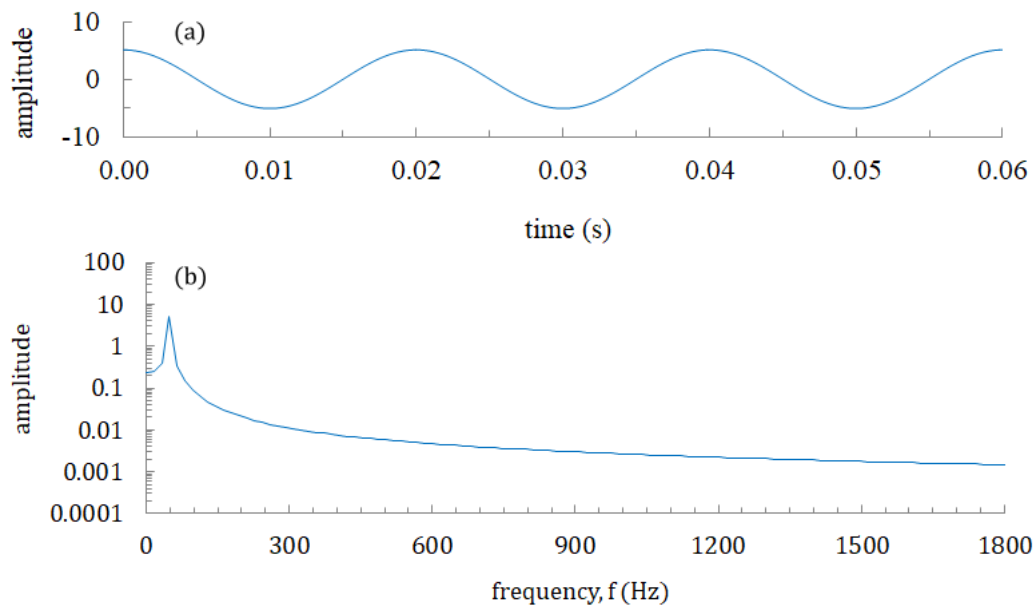
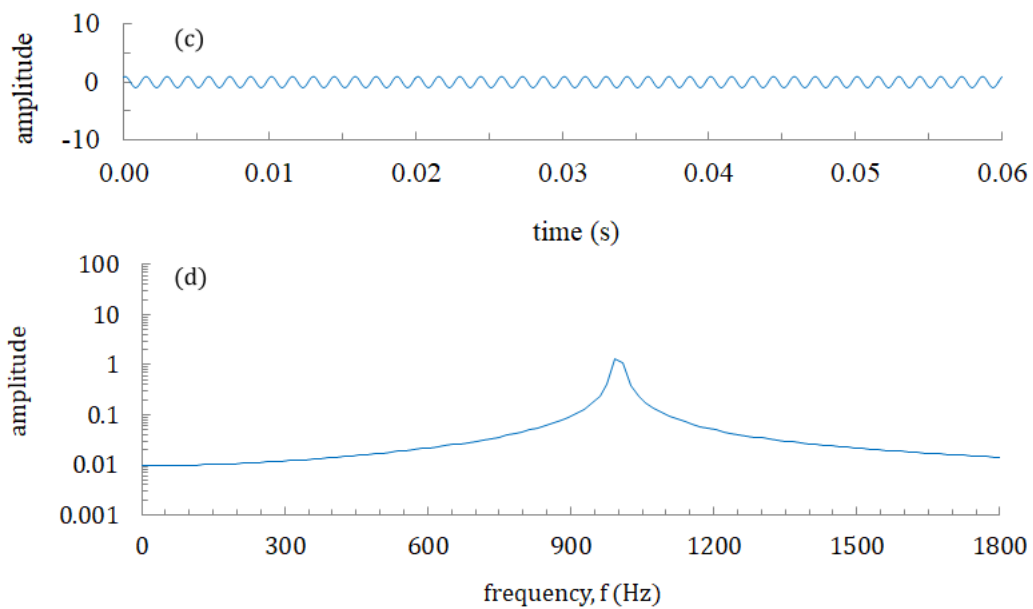


Fig. B-1.3 Typical decomposition of an arbitrary input signals by applying Fourier transform.



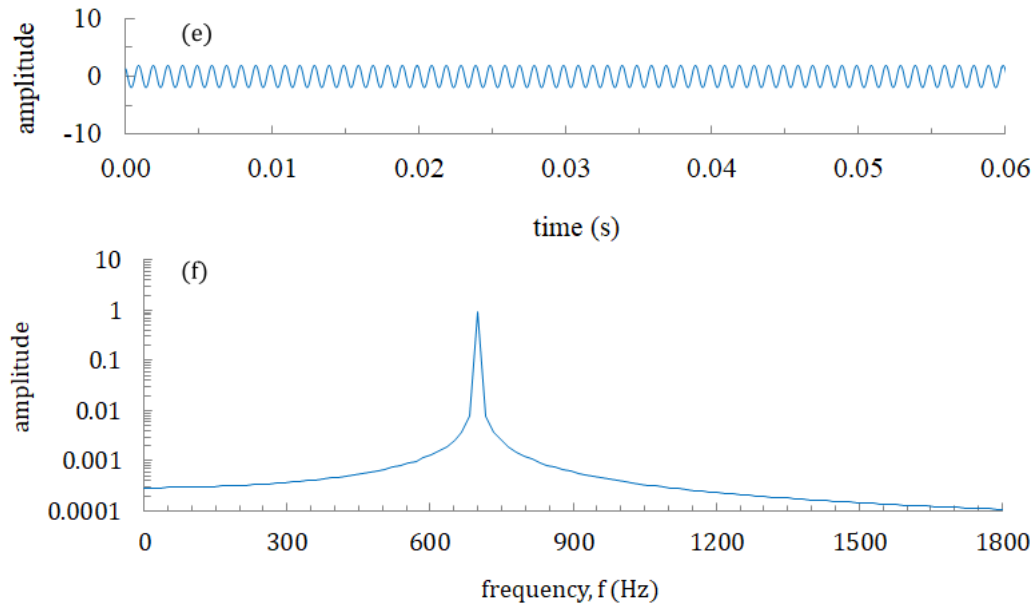


Fig. B-1.3 Typical decomposition of an arbitrary input signals by applying Fourier transform (continue).

Reversely, the transformed graph is taken to wire it around the circle, then it gives us back something closed to the original function found in Fig. B-1.3 (a)(c)(e). So what exactly the Fourier transform is. Let's consider the Euler equation that famously tells us the idea of wiring up the signal around the circle. In this graph (Fig. B-1.4 (a)) the direction is counterclockwise (the red) but if we put  $e^{-2\pi if t}$ , the direction turns into the clockwise (the blue) which is used in the Fourier transform.

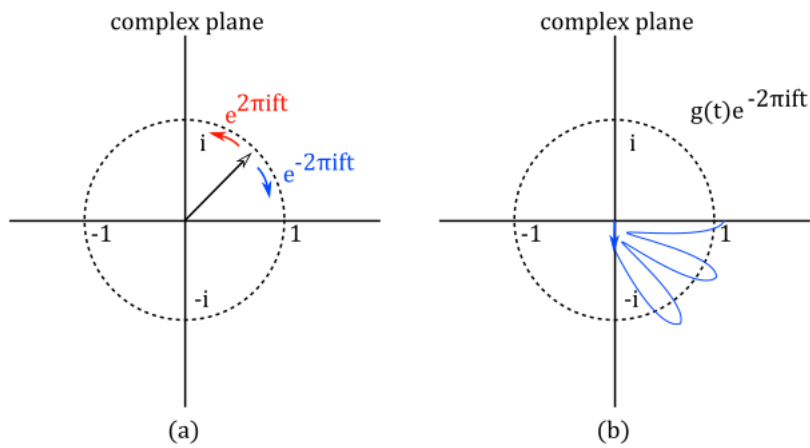


Fig. B-1.4 The complex plane and Euler's Formula.

Let's take some function describing signal intensity versus time like that cosine wave and let's call this  $g(t)$ . If we multiply this exponential expression by this  $g(t)$ , that mean we are rotating the complex number resulting in the scale up and down fashions according the value of this function around the origin point with designated frequency as shown in the (b).

$$g(t)e^{-2\pi if t} \rightarrow \frac{1}{N} \sum_{k=1}^N g(t) e^{-2\pi if t} \quad (\text{B-1})$$

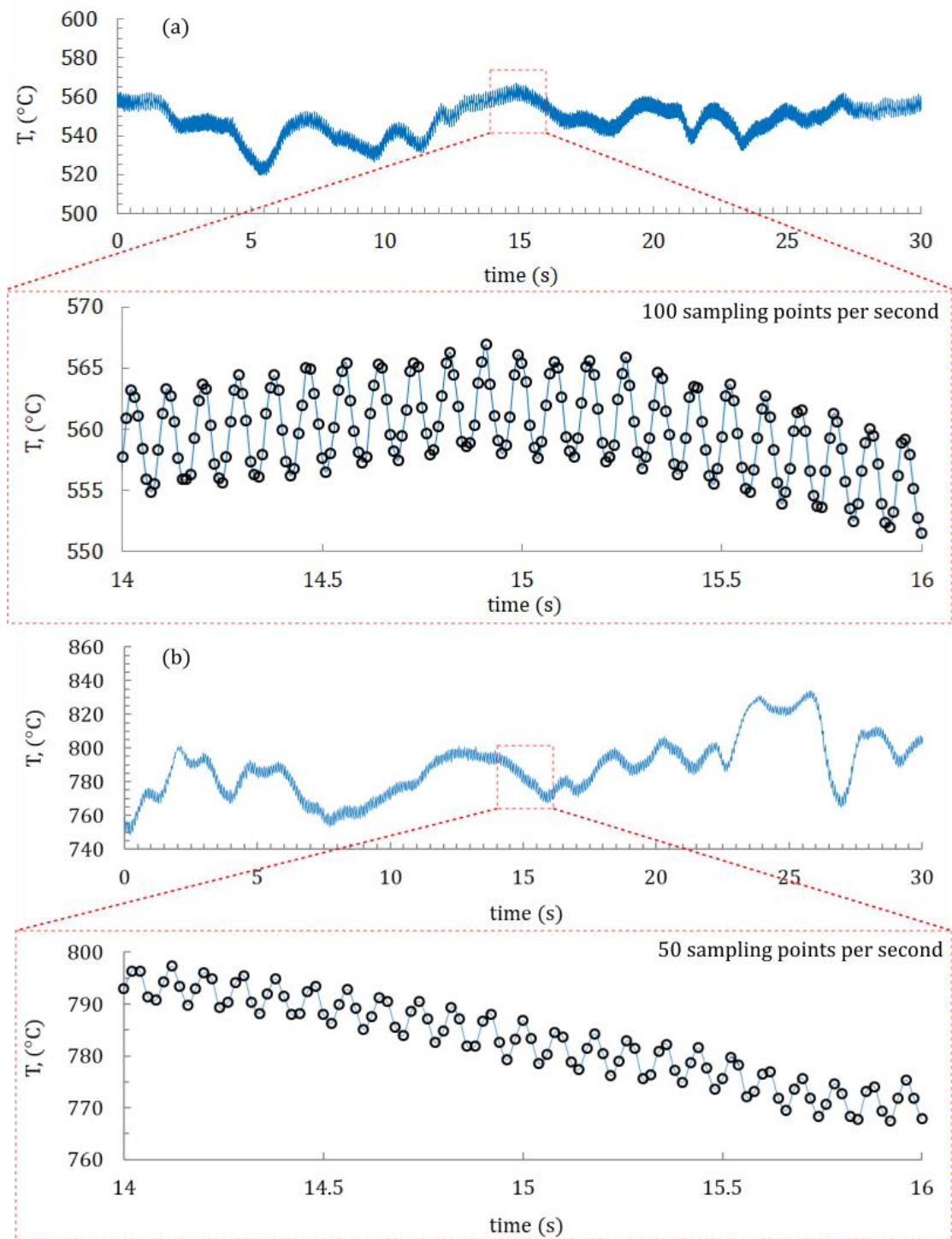


Fig. B-1.5 Time-sequence of TC signal (top) and its blowup sampling points (bottom) for twin jet flames:  $D = 10$  mm  $L = 0$  mm,  $Q = 500$  cc/min, and 10 millisecond of sampling frequency. (a) Sampling order is of 100 points per second and is of 50 points per second for (b).

Through this super arrogant way to encapsulate the whole idea of wiring a graph around the circle with variable frequencies. So let's think about what formula to capture that track CM. Well, to get it approximately, we might sample a whole bundle points of time from the original signal (all sampling points, N as expressed by Eq. (B-1)). More accurately, the more points are then sampled and make sampling points more close together as seen in the following figures (Fig. B-1.5 (a) and (b)).

The limit, rather than looking at the sum of the whole bundle points divided by the number of the sampling points (N), we take an integral of this function divided by the sign of the time interval ( $\Delta t$ ) that we are looking at.

$$\frac{1}{t_2-t_1} \int_{t_1}^{t_2} g(t) e^{-2\pi i f t} dt \rightarrow \int_{t_1}^{t_2} g(t) e^{-2\pi i f t} dt = F(2\pi i f) \quad (\text{B-2})$$

Well, so now there is one final distinction to point out between this and the actual function of Fourier transform, namely, just do not divide out by the time interval. Thus the actual Fourier transform is just integral part of Eq. (B-2). Output of this function is a complex number some point in the 2-D plane that corresponds to the string of giving frequency of the original signal. The plot that we have been graphing for the Fourier transform is just the real component of that output the x-axis in Cartesian coordinate.

## **B-2 Image Analysis Software: Spotlight-16**

Set up Area of Interest (AOI) is used to select an area of the image to which image processing operations will be applied, to which the object is tracked from frame to frame in time. Tracking AOI choiced in this example for explanation of an overview of use is the simplest type of a fully automated tracking. It is designed to move themselves around, attempting to follow object identified in the images. Fig. B-2.1 presents how tracking AOI (threshold tracking) is configured. On the left, instant photograph of twin jet flames flickers in an in-phase mode adopted. While the right-hand side, image is turned to black and white (a binary form) when AOI is applied. Through the threshold tracking option, specific tracking direction is set in vertical by “constrain AOI to line option”, and then search for the farthest white pixel along the dash-line. The location of this brightest pixel is recorded in the result file and then the AOI is moved. These processes are begun again for the next oncoming image. In terms of finding off the line, AOI is allowed to freely search for the track point, not only along the specified direction, but also the areas away from the constraint dash-line, whereas, that areas are still inside the AOI. If the new track point is found elsewhere, not on the dash-line, then AOI will move to the point along the dash-line that is closet to the track point. Fig. B-2.2 typically demonstrates how the AOI moves with the object along the constraint line. Clearly observe in Fig. B-2.3 that the applied tracking AOI for frequency analysis of twin-flame system shows good agreement with k-type thermomocuple measuring temperature variation shown in Fig. B-1.1, qunatitatively.

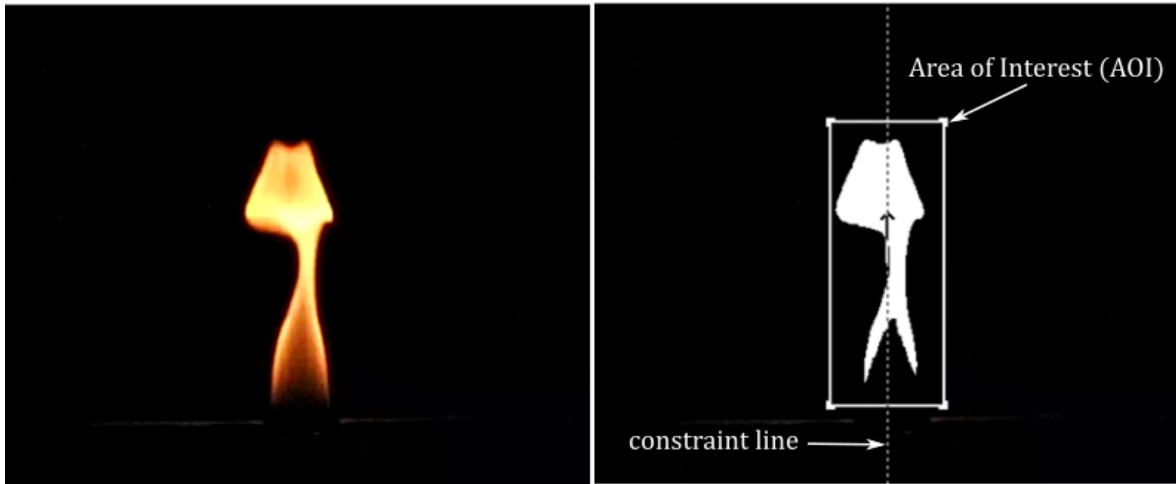


Fig. B-2.1 Typical instant photograph of buoyant non-premixed jet flames in an in-phase mode (left) and the applied AOI image represented in a binary form (black and white) inside a rectangle.

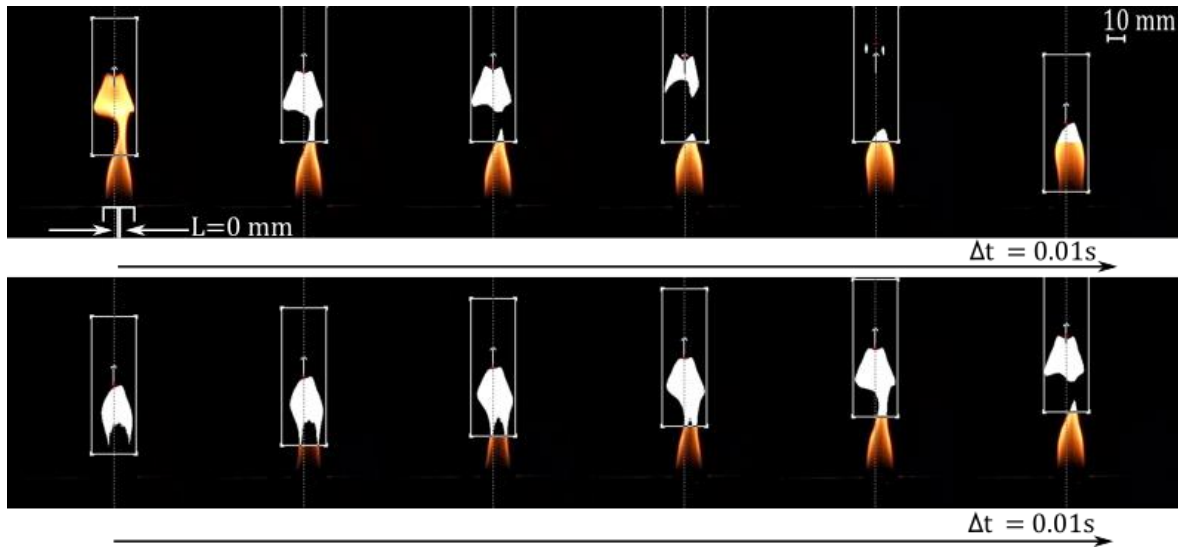


Fig. B-2.2 Pulsation cycle of a 10 mm diameter of circular burner for methane non-premixed flame with the applied spotlight-16, image analysis software tracking in time [Klimek & Wright, 2004].

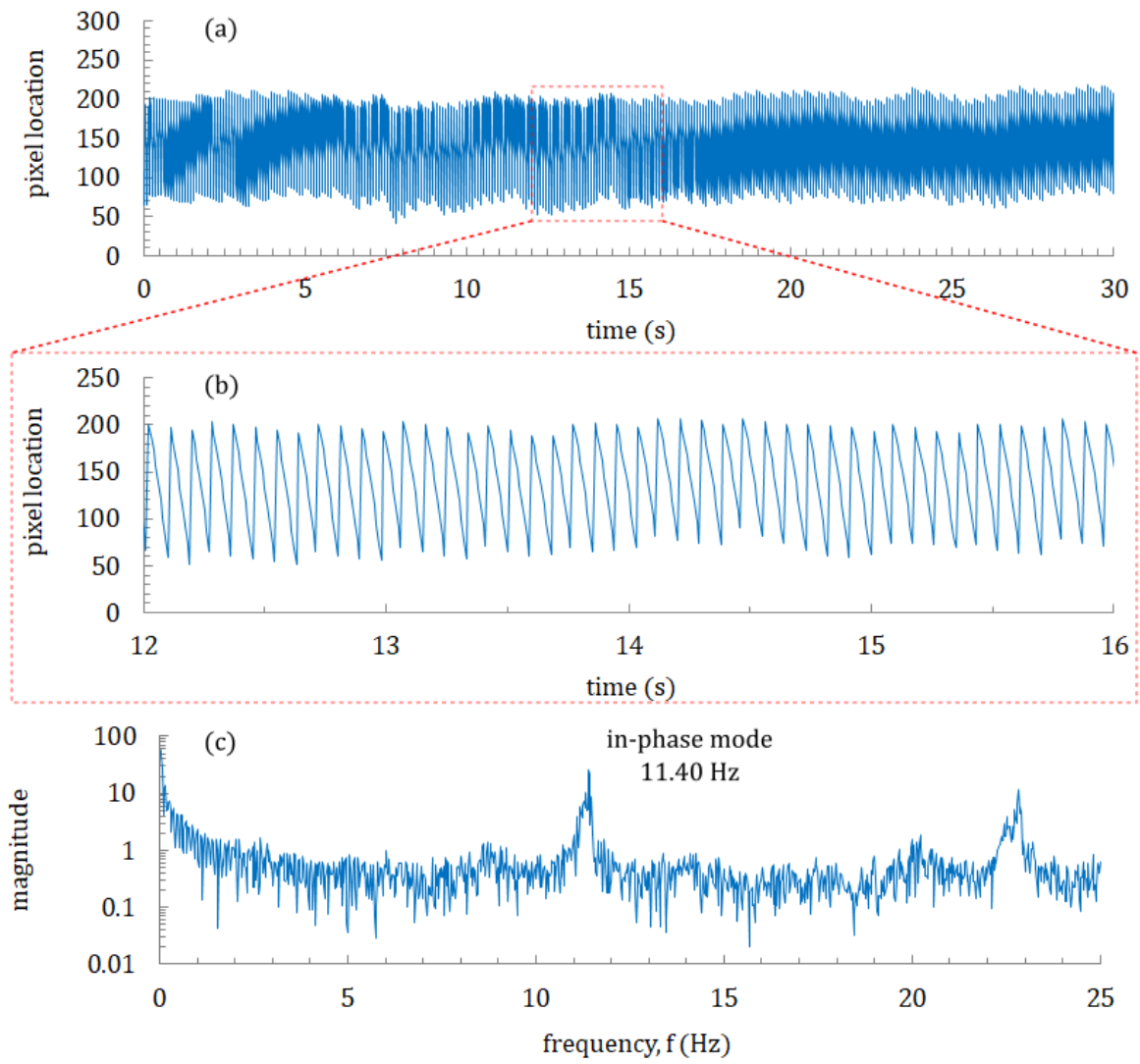


Fig. B-2.3 Time-sequence of TC signal (a)(b), corresponding FFT data (c) for twin-flame case of  $D = 10 \text{ mm}$   $L = 0 \text{ mm}$ ,  $Q = 500 \text{ cc/min}$ , and 10 millisecond of sampling frequency.

## References

Cengel Y. A., Cimbala J. M., Fluid Mechanics—Fundamentals and Applications (2006), McGraw-Hill Higher Education, New York.

Klimek R., Wright T., Spotlight–16 Image Analysis Software (16-bit) version 2004.4.27, NASA Technical Reports Server, U.S.

Mochizuki K., Study on Synchronous Oscillation of Two Adjacent Diffuse Flames, M.Eng. thesis. Toyohashi University of Technology, 2015

Toong T. Y., Salant R. F., Stopford J. M., Anderson G. Y., Mechanisms of combustion instability, Tenth Symposium (International) on Combustion, The Combustion Institute, Pittsburgh, PA, 1965, pp. 1301-1313.

## List of Publications

1. Bunkwang, A., Matsuoka, T., and Nakamura, Y. "Mode Transition of Interacting Buoyant Non-premixed Flames", Journal of Thermal Science and Technology, Vol.15, No.1, JTST0003 (2020.2), DOI: 10.1299/jtst.2020jtst0003.
2. Bunkwang, A., Matsuoka, T., and Nakamura, Y., "Similarity of Dynamic Behavior of Buoyant Single and Twin Jet-Flame(s)", Journal of Thermal Science and Technology, Vol.15, No.3, JTST0028 (2020.9), DOI: 10.1299/jtst.2020jtst0028.

## International Conference

1. Bunkwang, A., Matsuoka, T., and Nakamura, Y., "Dynamic Behavior of Interacting Flickering Flames", 11th Pacific Symposium on Flow Visualization and Image Processing (PSFVIP-11), Kumamoto (2017.12), #025, 5 pages (on USB).
2. Bunkwang, A., Matsuoka, T., and Nakamura, Y., "Mode Transition of Interacting Flickering Flames", Proc. 27th International Colloquium on Dynamics of Explosion and Reactive Systems (27th ICDERS), Beijing China (2019.7), paper# 49, 5 pages.
3. Bunkwang, A., Matsuoka, T., and Nakamura, Y., "Resonance Behavior of Interacting Diffusion Flames", 6th International Conference of Global Network for Innovative Technology and International Conference on Vibration, Sound and System Dynamics (IGNITE-ICVSSD 2019) (will be published at IOP Conference Series: Materials Science and Engineering), Penang Malaysia (2019.12), IGNITEMECH19\_005, 8 pages.